ISSN 0233-7584

Vol. 32, Iss. 4 July – August 2025

Physical Oceanography

http://physical-oceanography.ru/

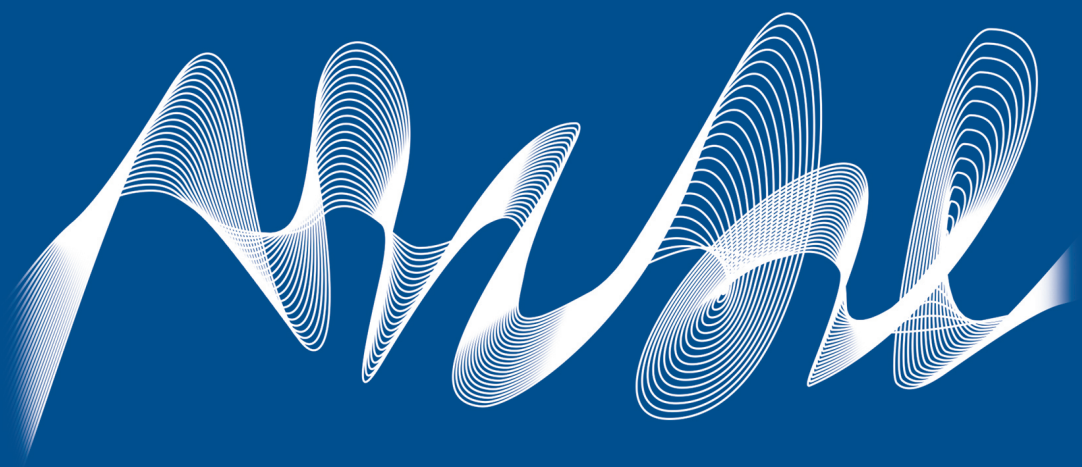

ISSN 1573-160X

Vol. 32, no. 4. 2025
July – August
Founded in January 1987
Publication frequency:
6 issues per year

Physical Oceanography

Scientific and theoretical journal

FOUNDER AND PUBLISHER:

Federal State Budget Scientific Institution
Federal Research Centre
"Marine Hydrophysical Institute of RAS"

Peer reviewed scientific journal.

The Journal publishes original research results, review articles (at the editorial board's request) and brief reports on the following sections of hydrophysics:

- thermohydrodynamics of the ocean and atmosphere;
- analysis of observational results and methods of calculation of ocean hydrophysical fields;
- experimental and expeditionary studies;
- satellite hydrophysics;
- mathematical modelling of marine systems;
- automation of scientific research of the seas and oceans.

Objectives
- familiarisation of the world and Russian scientific community with the results of theoretical, experimental and expeditionary studies of the World Ocean;
- exchange of scientific information, experience, research and observation data with specialists from different regions of the country and abroad;
- increase of publication activity of national authors, rating of scientific organisations of Russia and level of national publications in the world scientific community according to their citation data;
- the oretical and practical assistance to scientists in preparing articles for printing that meet modern requirements of publication and scientific ethics;
- strengthening the popularity and authority of the publication, increasing the number of regular subscribers

The Journal is indexed in:

Google Scholar
Web of Science (ESCI)
Scopus

journal@mhi-ras.ru **http://physical-oceanography.ru/**

Founder, Publisher and Editorial Office address:
2, Kapitanskaya St., Sevastopol, 299011
Russia
Phone, fax: + 7 (8692) 54-02-23

CONTENTS

Vol. 32, no 4. 2025 **July – August, 2025**

ISSN 1573-160X, *PHYSICAL OCEANOGRAPHY*, Vol. 32, Iss. 4, pp. 429-445 (2025)
Original Russian Text © M. E. Lee, E. B. Shybanov, 2025,
published in *Morskoy Gidrofizicheskiy Zhurnal*, 2025, Vol. 41, Iss. 4, pp. 399–416

Original article

A New Differential Method for Determining the Light Spectral Absorption by Suspended and Dissolved Organic Matter Directly in Seawater

M. E. Lee ✉, E. B. Shybanov

Marine Hydrophysical Institute of RAS, Sevastopol, Russian Federation
✉ *michael.lee.mhi@gmail.com*

Abstract
Purpose. The purpose of the study is to introduce a new method for measuring the spectral absorption of light using suspended and dissolved organic matter directly in seawater, without its prior concentration or filtration onto a substrate.
Methods and Results. A new method is proposed for determining light absorption by impurities in seawater. It is based on the application of two reflective double-walled conical cuvettes of large length (connected at the input to an integrating sphere) and assembled according to the optical scheme of a two-beam differential spectrophotometer. The cuvettes are identical thin-walled quartz cones coaxially inserted inside the same outer cones, the latter having a mirror coating. When seawater is placed in the measuring channel and the deionized water is placed in the reference channel for comparison, only the total absorption by suspended matter and colored dissolved organic matter will be defined. It is necessary to pour the filtrate of the same seawater that was passed through the 0.2 μm-pore filter into the reference cuvette to determine only the light absorption by suspended matter in seawater. The seawater filtrate placed in the measuring channel and compared to the optically pure water in the reference channel permits determination of the spectrum of dissolved organic matter absorption in the original seawater.
Conclusions. For the first time, the spectral characteristics of light absorption by suspended matter in an aqueous medium are being defined directly in its natural state. This is being achieved by significantly increasing sensitivity, provided that all the scattered rays are collected completely by the receiving device. This is made possible by a method that uses double-walled conical quartz glass cuvettes, which increase the reflection angle by the value of the cone apex with each subsequent reflection. Therefore, the combination of conical cuvettes in the optical scheme of a two-beam differential photometer with an integrating sphere allows to obtain accurate data that require no more corrections for the influence of scattered rays. The principle of a two-beam differential spectrophotometer proposed and applied in the study makes it possible to perform spectral analyses of the absorption characteristics of various suspended matter components separately from all other substances and the properties of the seawater in which they are present.

Keywords: suspended particles, dissolved organic matter, light absorption, scattering medium, total internal reflection, double-walled cone cuvette, scattering angle

Acknowledgments: The study was conducted as part of the state assignment FNNN-2024-0012, funded by FSBSI FSC MHI, titled “Analysis, Diagnosis and Operational Forecast of the State of Hydrophysical and Hydrochemical Fields of Marine Waters Based on Mathematical Modeling Using the Data of Remote and Contact Measurement Methods”.

For citation: Lee, M.E. and Shybanov, E.B., 2025. A New Differential Method for Determining the Light Spectral Absorption by Suspended and Dissolved Organic Matter Directly in Seawater. *Physical Oceanography*, 32(4), pp. 429-445.

Introduction

The propagation of natural sunlight in the ocean is determined by the patterns of its penetration into the aquatic environment and depends primarily on

the aggregate properties of spectral absorption and scattering by the water itself, as well as on suspended particles and dissolved organic matter (DOM). For this reason, the optical properties of suspended particles and impurities in seawater significantly impact the transformation of the light field and its spectral properties as light penetrates deeper into the ocean. The selective spectral absorption of light by suspended particles and DOM also triggers photosynthesis in the ocean, which impacts the global carbon dioxide cycle and the ecological state of aquatic areas. The optical properties of water impurities provide important information about the taxonomic composition and size distribution of phytoplankton communities, as well as the influence of pigments in algal cells on photosynthesis and heat transfer [1–3]. Precise quantitative data on the spectral absorption and scattering of light by suspended particles and DOM are necessary for parametric representation of radiative transfer equations in bio-optical ecological models of the ocean [4].

Suspended particles in seawater are subdivided into suspended particles, consisting primarily of cells of various phytoplankton species, and sinking particles, composed of mineral solids and detritus. The spectral absorption features of phytoplankton pigments are of particular interest among all the optical properties of suspended matter because they exert a decisive influence on primary production and the life activities of marine organisms, making them important for studying many oceanographic, biological, and biogeochemical processes in the ocean [5]. The sinking component of suspended matter, consisting of non-algal solid particles, participates in the exchange between surface waters and the deep ocean. This component includes non-living organic and mineral particles, as well as heterotrophic microorganisms. The microbial populations responsible for remineralizing sinking particles are likely free-living in the water column. During the slow settling process in seawater, these populations deliver the necessary substances for the life activities of organisms inhabiting the depths [6].

Colored dissolved organic matter (CDOM), also known as the yellow substance, is a complex of substances that strongly absorb the short-wavelength part of light in water. This class of substances includes all impurities in seawater passing through a 0.2 μm filter. Their proportion in the ocean is ~ 10–90% [7]. The selective strong absorption of ultraviolet and blue radiation by CDOM promotes aquatic photochemistry, which has important consequences for biogeochemical processes that influence the carbon cycle. One can also infer the composition and variability in concentration of DOM based on its characteristic spectral absorption signatures. Knowing the precise shape of the spectral absorption curve is necessary for modeling the role of DOM in many of these processes. In semi-analytical ocean color models, light absorption by phytoplankton and other suspended particles is determined by extrapolating DOM absorption from the blue region into the rest of the visible spectrum [8].

The optical properties of light absorption in natural waters are highly variable. This necessitates regular comprehensive interdisciplinary research in the fields of ocean optics, biophysics, and biogeochemistry during marine expeditions on research vessels, oceanographic platforms, and other floating craft. Global studies using satellite data are now possible because the spectral characteristics of upwelling radiation from the ocean – observed as ocean color – depend on the presence of light-absorbing impurities in the water. This upwelling radiation

can be used for remote sensing of the surface layer of aquatic environments and provides information on the global distribution of suspended matter components and CDOM from ocean color satellite images [9, 10]. In order to verify data from spaceborne ocean color scanners, subsatellite determinations of the spectral absorption coefficient of various suspended matter components – especially phytoplankton and cyanobacterial cells – should be carried out with the highest possible accuracy and spectral resolution at the ocean surface level. The isolation of absorption by planktonic cells is justified by the unique spectral features of pigments in phytoplankton, in contrast to the simple, monotonous decrease in absorption spectra of mineral particles and DOM with increasing wavelength. Further advances in the bio-optics and optical oceanography of the upper ocean layer could significantly benefit from fundamentally new approaches to accurately determining light absorption by suspended matter and DOM in seawater, which is essential for improving light radiation transfer models in the sea.

The aim of the present study is to demonstrate a novel method for determining the spectral absorption of light by seawater impurities and to substantiate its high accuracy.

Materials and methods for determining light absorption by seawater impurities

Direct determinations of the spectral absorption coefficients for total absorption by suspended matter and CDOM are conducted based on seawater sample measurements collected from various ocean depths. This methodology has several advantages: it ensures environmental stability, allows for the preliminary preparation of concentrated seawater suspensions with specified characteristics, and increases particle concentration on the filter substrate through filtration. The main drawback of this methodology, however, lies in the inability to study the fine structure of the spatial and vertical distributions of the optical properties of seawater due to the discreteness of the samples.

The most common method for determining the spectral absorption of light by suspended particles is to filter a seawater sample through a paper filter, which acts as a substrate, to deposit solid particles onto it. Then, absorption is measured using a spectrophotometer. This method is called the filter pad method or the quantitative filter technique. There are three configurations: transmission of directed light through the filter [11]; illumination of the filter with direct light and measurement of its reflection [12]; and placement of the filter inside an integrating sphere, where it is illuminated by direct and diffuse light [13]. The transmission configuration is the simplest to apply, but the obtained results are significantly distorted due to losses of scattered rays. Consequently, this approach does not allow for quantitative assessment of significant errors in determining light absorption by suspended matter. The transmission-reflection configuration largely circumvents these limitations, but this method is more labor-intensive and is therefore rarely used in routine practice. The configuration involving the irradiation of the filter substrate inside an integrating sphere is the most preferable, as it avoids errors in measurements resulting from losses of scattered radiation [14].

In addition to determining the total absorption by all organic suspended particles, the quantitative filter technique provides the possibility for

the experimental determination of absorption by phytoplankton cells and detrital particles separately. Typically, this separation is carried out by treating the filter sample with an organic solvent or bleaching agent to extract or bleach the pigments present in phytoplankton cells [15, 16].

As measurement technology improves and methods employing integrating spheres are adopted, the drawbacks of the quantitative filter technique are mitigated by eliminating uncertainties in absorption measurements caused by methodology. Although the method of measuring spectral light absorption on a filter inside an integrating sphere yields superior results, the data obtained using this method still require correction for the influence of multiple light scattering paths through the suspended particles. Though it has some limitations, it has been shown that this method is practically independent of strong scattering by suspended solid particles and provides acceptable sensitivity. One limitation is the sufficiently complex and labor-intensive measurement procedure, as well as the inability to separate absorption by phytoplankton cells, detritus, and mineral particles [17].

Methods for determining the spectral absorption characteristics of seawater have proven more promising. In these methods, seawater is collected from different depths in the studied areas without preliminary preparation and poured into a spherical quartz flask, which is lined over its entire external surface with diffusely reflecting Fluorilon (Fluorilon 99-W™) possessing a very high reflectance. A careful analysis showed that, with the appropriate calibration using a reference aqueous solution, this method can yield satisfactory data on the absorption spectra of seawater. According to the method, light absorption by particles suspended in water is calculated as the difference between the measured spectral absorption coefficients of the seawater and the water after its filtration through a 0.4 μm pore size filter [18].

The primary sources of error in all light absorption determination methods are the pathlength amplification factor for scattered rays and the zero baseline offset. The pathlength amplification factor is associated with the increase in the distance photons travel through a filter containing suspended particles, resulting in an overestimation of the measured absorption coefficient. Most studies aimed at determining corrections for these factors were conducted using the light transmission method through a filter-substrate on a standard spectrophotometer. However, the pathlength amplification factor proved inconsistent across studies and depended on the sample type [19, 20]. For this reason, to obtain quantitative absorption values, data must be corrected by applying a predetermined pathlength amplification factor for scattered rays, which is defined as the ratio of the optical pathlength to the geometric pathlength [21].

The correction for the pathlength amplification factor is usually derived from experiments with algal cultures. It is calculated as the ratio of the optical density of the filter containing suspended particles to the optical density of the same suspension in a dilute solution. This establishes a functional relationship that can be subsequently applied to field samples [22].

Nevertheless, a comprehensive analysis of various experimental and analytical methods conducted to obtain reliable estimates of errors in determining absorption by suspended particles revealed significant variability between different approaches for different water types [23]. In this regard, existing methods for

determining absorption by suspended matter and phytoplankton pigments currently do not allow for the unambiguous selection of a single method for applications in optical oceanography.

A new method for determining light absorption by impurities directly in seawater

Seawater is a weakly absorbing scattering medium with concentrations of suspended matter and impurities that allow light beams to travel significant distances through single scattering. Single scattering, which requires that scattering particles are not too close to each other and are separated by at least three times their radius, is the primary necessary condition for correctly determining the optical properties of a scattering medium [24]. This condition means that the optical properties of suspensions and impurities in seawater must be determined in their natural state, without any concentration or thickening procedures. Currently employed methods for determining absorption in suspensions and filter substrates do not meet the single scattering condition, necessitating unreliable corrections to the obtained data. Therefore, these methods cannot fully satisfy the modern requirements of solving a wide range of bio-optical problems in oceanography and limnology. Completely different approaches to determining light absorption by suspended matter and DOM are needed. These approaches must be free of the aforementioned drawbacks and must not require the introduction of theoretical and experimental numerical corrections into the final result. In order to measure light absorption directly in natural seawater without first thickening it into a suspension or concentrating it by filtration, the sensitivity would need to be increased by a factor of ten while simultaneously ensuring that all scattered rays are completely collected by the receiving device.

A new method has been proposed based on the use of previously developed reflective, double-walled, long-path cone cuvettes [25]. These cuvettes are connected to an integrating sphere and assembled according to the optical scheme of a dual-beam differential spectrophotometer. This method positions the measuring and reference conical reflecting cuvettes outside the integrating sphere, directly in front of its input apertures, ensuring that all rays exiting the cuvettes enter the sphere. The seawater under investigation is placed into the measuring cuvette, while the reference cuvette contains either ultrapure water with no impurities or filtered seawater with DOM. The new method uses elongated cone cuvettes with light beams that diverge at the cone angle to increase sensitivity, which may allow for the determination of spectral light absorption across a broader range of seawater transparencies. Additional sensitivity enhancement is achieved by significantly reducing instrumental error through the application of the dual-beam differential spectrophotometer optical scheme. Both cuvettes are identical and consist of coaxially nested thin-walled quartz cones that ultimately form unique double-walled cone cuvettes. The small air gap between the cuvette walls ensures total internal reflection on the inner wall. It also allows for the application of a stable, air-stable multilayer mirror coating with a very high reflection coefficient on the outer wall. Cone cuvettes are notable because the angle of reflection of rays from the walls increases by the value of the cone’s apex angle with each reflection event. Using this property of cone cuvettes in the new method

for determining the spectral absorption of light by suspended matter and DOM offers the following advantages and reveals new photometric properties:

– substantial increase in sensitivity for determining spectral light absorption of impurities across a wide range of seawater transparencies;

– capability to perform spectral determination of light absorption by suspended matter in natural seawater without thickening it into suspensions or concentrating it by filtration;

– minimization of errors caused by the strong influence of scattering on the results of determining light absorption by impurities in seawater;

– elimination of the influence on the absorption magnitude caused by the mutual penetration of diffuse radiation from the sphere into the double-walled cone cuvette and back.

Fig. 1 shows the optical scheme of the dual-beam differential spectrophotometer used to determine light absorption by suspended matter and DOM directly in seawater in its natural state, without any concentration or thickening procedures. The dual-beam scheme consists of two channels: a measuring channel and a reference channel (subscripts ^{m} and ^{r} respectively). These channels are identical, and in Fig. 1, they both have the same numerical designations for the elements of the double-walled cone cuvettes and the same letter designations for the ray paths.

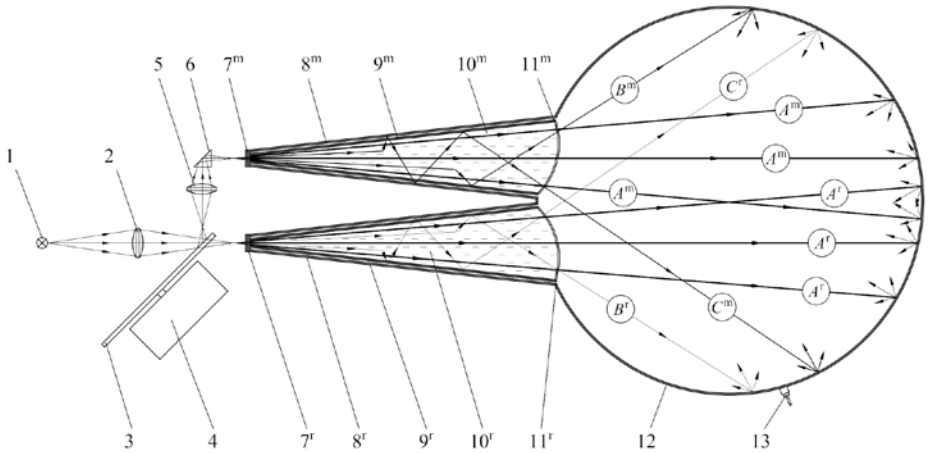

F i g. 1. Scheme for determining the light spectral absorption by suspended DOM in seawater: *1* – light source; *2* – light source lens; *3* – rotating mirror disk with notches; *4* – electric motor; *5* – measuring beam objective; *6* – rectangular prism; 7^{m}–7^{r} – entrance illuminators; 8^{m}–8^{r} – external conical reflectors with mirror coating; 9^{m}–9^{r} – conical quartz cuvettes providing total internal reflection of scattered rays in forward direction; 10^{m}–10^{r} – measuring and reference mediums; 11^{m}–11^{r} – output illuminators; *12* – integrating sphere, *13* – receiving light guide of spectrometer; A^{m}–A^{r} – direct rays that weakened as a result of absorption in the medium and passed through the measuring and reference cuvettes, B^{m}–B^{r} – rays scattered in the range of angles of total internal reflection of a quartz cuvette, C^{m}–C^{r} – rays scattered at large angles beyond the total internal reflection angles

The operation of the scheme proceeds as follows: light from source *1* is formed by lens *2* into a diverging beam at an angle matching that of the double-walled cuvettes' cone. This beam is then directed to mirrored disk *3*, which has

mirrored sectors that alternate with identical sectors containing cutouts. Therefore, as this disk rotates via electric motor *4*, the beam is sequentially switched between the measuring and reference channels. When a mirrored sector of disk *3* passes in front of the light beam from source *1*, the light reflected by lens *5* and rectangular prism *6* is directed to the double-walled cuvette of the measuring channel. Here, the beam passes sequentially through the input illuminator 7^{m}, the seawater sample under investigation 10^{m}, the output illuminator 11^{m}, and then enters the integrating sphere *12*. Inside the sphere, multiple reflections from the diffusely reflecting spherical surface transform the beam into isotropic light for the measuring channel. During the next phase, when a cutout in the disk is positioned in front of the light source, the beam passes through the cutout and is directed to the double-walled cuvette of the reference channel.

Similarly to the measuring channel, the beam passes sequentially through all elements of the reference channel, including the illuminator 7^{r}, the comparative aqueous medium 10^{r}, and the output illuminator 11^{r}. Inside sphere *12*, *the* beam forms isotropic light for the reference channel. The isotropic light fluxes formed by integrating sphere *12*, from the measuring and reference channels, sequentially pass through receiving light guide *13* to the input of a precision spectrometer with a data acquisition system based on a personal computer.

As evident from the ray paths shown in Fig. 1, the double-walled cuvettes in the measuring and reference channels very effectively redirect all light scattered within the aquatic environment towards the integrating sphere. This occurs because the reflecting cones increase the reflection angle by the value of the cone's apex angle with each subsequent reflection. Consequently, inside the cone, rays of any direction reflecting multiple times from the cone walls gradually turn towards the cone's axis. As a result, rays scattered at small angles (B^{m}–B^{r}) are efficiently redirected towards the sphere via total internal reflection within the conical quartz cuvettes (9^{m}–9^{r}), while those scattered at larger angles (C^{m}–C^{r}) are redirected via reflections from the outer mirrored wall (8^{m}–8^{r}). In the cone cuvettes, the number of reflections from the walls is drastically reduced. Rays are redirected from the point of light scattering to the input apertures of the integrating sphere along an expanding zigzag path with a gradually increasing step size. The reduction in reflections and straightening of scattered rays' zigzag paths within conical cuvettes results in the beam traversing a much shorter path length than with existing methods. Thereby, this minimizes the error associated with the path length amplification factor. Within the inner cone cuvettes, the main light flux is dominated by rays that pass through the water without contacting the walls, as well as by rays that are scattered at small angles and experience one or a few reflections. Due to the elongation of the scattering phase function of seawater, ~ 93% of all scattered rays pass through the inner cuvettes and enter the integrating sphere [25]. This phenomenon is explained by the scattering phase function of seawater, which exhibits a pronounced peak at small angles (0–10°) [26].

A small fraction of C^{m}–C^{r} photons scattered at large angles that exit the cuvette into the air gap are reflected from the mirrored coating of the outer cone walls 8^{m}–8^{r}. These photons also follow a gradually straightening zigzag trajectory. After several reflections from the outer cones 8^{m}–8^{r}, the C^{m}–C^{r} rays scattered at large angles return to the cuvettes 9^{m}–9^{r} at the angle of total internal reflection.

They are then redirected towards the integrating sphere, along with the main flux of direct rays A^m–A^r and rays scattered at small angles B^m–B^r. Since the reflection and refraction of rays at the surface of the quartz cuvette occur with virtually no losses, all rays scattered at large angles (~ 6%) are redirected into the sphere. As a result, ~ 93% of rays from the small-angle scattering region and ~ 6% from the large-angle region are redirected from the double-walled cone cuvettes into the sphere for detection by the photodetector. In other words, more than 99% of all rays scattered in seawater are redirected [25]. Fewer than 1% of scattered rays are irretrievably lost due to minor absorption on the mirrored coating of the outer cones and on microscopic inhomogeneities of the quartz glass during total internal reflection. Therefore, combining cone cuvettes with an integrating sphere can overcome the challenges associated with the strong influence of scattering on determining light absorption by suspended matter and DOM. This is achieved by the receiving device simultaneously registering both the direct rays transmitted through the medium without absorption and all photons scattered along this path. Consequently, only the rays absorbed within the medium fail to reach the sphere, while all rays scattered along the length of the cuvette and the direct rays not absorbed throughout the cuvette end up inside the integrating sphere. However, it should be noted that diffuse radiation from the sphere returning into the measuring cone cuvette would cause an unknown change in absorption. In a dual-beam scheme, though, this change is compensated for by normalization relative to the reference channel. Once inside the integrating sphere, all these rays create uniform illumination throughout its internal volume after multiple diffuse reflections. The spectral absorption of light in the studied marine environment governs this illumination in both the measuring and reference channels.

The use of the optical scheme of a dual-beam differential spectrophotometer in the proposed new method enables the spectral analysis of the optical absorption properties of various impurities in seawater. This is achieved by selecting the appropriate aqueous media for the measuring and reference channels. When seawater extracted from the study depth is placed in the measuring channel and ultrapure water is placed in the reference channel, the total absorption by suspended matter and CDOM can be determined. To determine light absorption by suspended matter alone in seawater, it is necessary to fill the reference cuvette with a filtrate of the same seawater that has been passed through a 0.2 μm pore filter. Placing seawater filtrate in the measuring channel and comparing it with ultrapure water in the reference channel allows for determining the absorption spectrum of DOM in the original seawater.

Theoretical analysis of using double-walled cone cuvettes with an integrating sphere

Within the double-walled cone cuvettes, we distinguish three light beams directed toward the entrance of the integrating sphere. These beams are shown in Fig. 1 by lines of different thickness, which correspond to the light ray intensities. The beams are direct light, light scattered at small angles or reflected from the cone wall without energy loss, and scattered light that has lost energy through one or several reflections from the mirrored coating.

In the single-scattering approximation, the measured signal can be represented as follows:

$$I = I_0\left(1+\frac{bL_0}{4\pi}\int\limits_0^{\Omega_1} p(\theta)d\Omega+\frac{bL_0}{4\pi}\int\limits_{\Omega_1}^{\Omega_2} R^n \exp\left[-(a+b)\Delta L\right]p(\theta)d\Omega\right)\cdot\exp\left[-(a+b)L_0\right], \quad (1)$$

where I_0 is the intensity generated by the light source; b is the scattering coefficient; L_0 is the measurement path length; Ω_1 is the solid angle within which a ray enters the integrating sphere entrance after total internal reflection or without reflection from the cone wall; $L(\theta)$ is the phase function of angle θ; R is the reflection coefficient of the cone cuvette wall; Ω_2 is the solid angle within which rays can enter the integrating sphere entrance after multiple reflections from the wall of the cone reflector and the quartz cuvette; n is the number of reflections; a is the absorption coefficient; ΔL is the additional path length of the ray in water depending on the scattering angle.

For small values of optical thickness $(a+b)L_0$, it is more convenient to rewrite expression (1) in the following form:

$$I = I_0\exp\left[-(a+\Delta b)L_0\right], \quad (2)$$

where $\Delta b = \frac{b}{4\pi}\int\limits_{\Omega_3}^{4\pi} p(\theta)d\Omega$ is a quantity determining light loss due to scattering. The Ω_3 angle is smaller than Ω_2 and depends on the R reflection coefficient. Using the calculation algorithm presented in [27, 28], the average path length of light in the $L(\theta)$ cuvette and the amount of light incident on the entrance of the $I(\theta)$ integrating sphere were computed as a function of the given θ angle for the following parameters: measurement path length – 250 mm; apex angle – 8° of the outer cone reflector and quartz cuvette; input diameter of the cone cuvette – 5 mm; output diameter – 40 mm; combined thickness of the glass and air gap – 2 mm; reflection coefficient of the mirrored coating of the outer cone reflector – 0.95. Integration over the angle, taking into account the scattering phase function, shows what fraction of the scattered rays can be collected by the optical scheme under consideration. If the path length of a ray in the medium increases due to scattering, additional excess absorption will occur. For a given phase function $p(\theta)$ and the calculated function $I(\theta)$, the integral was computed:

$$\frac{1}{4\pi I_0}\int\limits_{4\pi} I(\theta)\,p(\theta)\exp\left[-a\Delta L(\theta)\right]\sin\theta d\theta d\varphi, \quad (3)$$

where $\Delta L(\theta) = L(\theta) - L_0$.

According to the conducted estimates, with low absorption and a mirror coating reflection coefficient R_m = 0.95, using the Petzold phase function [29], light loss after scattering will be 0.91%, while with the molecular phase function it will be 22.8%. In calculations using the Petzold phase function, this value decreases from 0.99 at $a = 0$ to 0.977 at $a = 1$ m^{-1}. In reality, the asymmetry of the scattering

phase function in the Black Sea is higher than the Petzold phase function. Therefore, the influence of scattering on absorption measurement in the long-wavelength region will be less. Moreover, the improvement in the mirror coating quality has a diminishing effect as absorption increases. This pattern is explained by the elongation of the ray path in water upon multiple reflections from the wall of the cone reflector. Thus, the scattered light reaching the integrating sphere travels a path whose length depends on the scattering phase function. For molecular scattering and $a = 1$ m^{-1}, approximately half of the scattered light is lost. It should be noted that purely molecular scattering does not occur in natural water (for example, in the clearest waters of the World Ocean, the light scattering coefficient minus molecular scattering at a wavelength of 515 nm is 0.023 m^{-1} [30], which is almost three times higher than the theoretical value of molecular scattering at a wavelength of 400 nm). In seawater, the higher the absorption in a given spectral interval, the smaller the contribution molecules make to scattering.

Fig. 2 shows how the fraction of scattered light detected by the photometer changes with increasing water absorption.

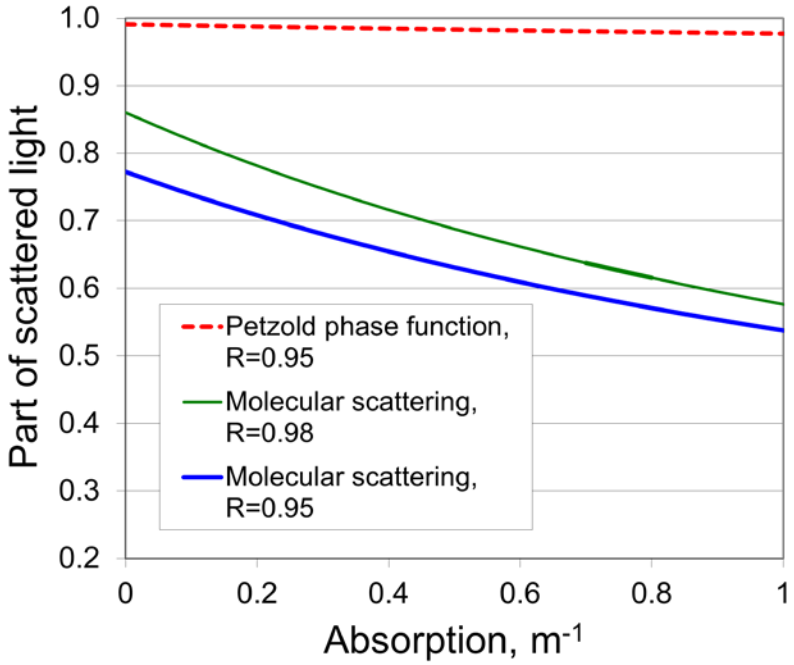

F i g. 2. Relative amount of scattered light leaving a cone cuvette depending on the water absorption coefficient for molecular scattering (reflectance coefficients of the mirror coating of a cone wall are 0.95 and 0.98), and for highly anisotropic light scattering in water with the Petzold phase function (reflectance coefficient of the mirror coating is 0.95)

Calculations demonstrated that the average path length of scattered light in seawater with the Petzold phase function is $\overline{L}_{\mathrm{p}} = 1.027 L_0$, where L_0 is the measurement path length, while for molecular scattering it is $\overline{L}_{\mathrm{m}} = 1.6 L_0$.

Let us express the intensity of light incident on the entrance of the integrating sphere as

$$I = I_0 \exp[-a\bar{L}_0 - \delta_p b_p \bar{L}_p - \delta_m b_m \bar{L}_m], \quad (4)$$

where δ_p, δ_m are the fractions of light loss due to scattering by particles and water molecules, respectively; b_p, b_m are the light scattering coefficients for particles and water molecules. $\bar{L}_0$ is close to the measurement path length, since a significant portion of the total intensity consists of direct light. In calculations using formula (4), the main uncertainty is introduced by δ_p, δ_m, as they significantly depend on the actual reflection coefficient of the cuvette walls. At the same time, the δ_m multiplier is responsible for the strong spectral dependence of the measurement error and depends more strongly on the reflection coefficient of the mirror coating, which also depends on the wavelength. Note that if the I_0 reference intensity is the intensity obtained by measuring a sample of filtered seawater or purified freshwater, then the molecular component will be compensated. Instead of expression (4), taking into account the path length estimates, we obtain

$$I = I_0 \exp[-(a + 1.027\delta_p \Delta b_p) L_0], \quad (5)$$

where Δb_p is the difference between the light scattering coefficients by hydrosol particles in the measured sample and in the reference water. Henceforth, we will assume that the error in determining absorption is 1% of the scattering coefficient by hydrosol particles.

The next problem in determining the intensity of the optical signal arises due to the strong spatial non-uniformity of the light field exiting the measurement volume. According to expression $\exp(-cL_0)$ the main light energy is contained in the direct beam. The remaining part is also distributed non-uniformly due to the anisotropy of scattering and reflection from the cuvette wall. In the proposed scheme, the integrating sphere, performing the function of an ideal collector, is used to measure the intensity of the light flux, which has a spatial-angular non-uniformity of brightness distribution. After multiple reflections from the spherical wall, the uniform distribution of light throughout the volume of the sphere leads to an increase in its intensity and to the fact that part of the light rays is redirected back towards the conical cuvette from the sphere. Due to the high reflectivity of the conical cuvette wall and the property of the cone to redirect rays towards its apex, part of the light energy will return to the sphere, while another part will be absorbed by the medium or the mirror coating of the conical reflector. As the ray propagates in the conical cuvette, a sufficient number of reflections and a distance in the medium exceeding the length of the cuvette are required for it to be redirected back towards the sphere. Because of this, uncertainty arises in calculating the main characteristic of the photometric sphere – its gain coefficient.

Let us substantiate this conclusion with analytical expressions. Let $\bar{a}$ be the average albedo of the sphere surface, a_c – the albedo of the double-walled conical cuvette when illuminated from its wide end, and δ – the fraction of the sphere surface occupied by the cone insert. The gain coefficient is equal to the sum of the geometric progression $\bar{a} + \bar{a}^2 + \bar{a}^3 + \ldots = \frac{\bar{a}}{1-\bar{a}}$. For a perfectly reflecting surface

$$\bar{a} = \frac{1}{4\pi \cdot r^2} \int_S a(s)ds = 1 - \delta(1 - a_c), \tag{6}$$

$$K = \frac{1 - \delta(1 - a_c)}{\delta(1 - a_c)}. \tag{7}$$

Since the light flux entering from the conical cuvette is proportional to $\exp\left(-a\bar{L}\right)$, where $\bar{L} \approx L_0$, determining absorption in transparent water requires specifying the gain coefficient with high accuracy, which depends on a_c. The albedo of the double-walled cone cuvette for rays entering the cuvette at different angles will be a function of the angle, as it depends on the number of reflections from the walls of the outer cone with the mirror coating and on the attenuation of the ray along the path traveled in the water from the sphere into the cuvette and back. The estimation formula for the albedo of the double-walled cone cuvette will include n – the average number of reflections, l_{avg} – the average path length of rays reflected from the walls and exiting back into the sphere, as well as a_w – the light absorption coefficient of water:

$$a_c = r^n \exp(-a_w \cdot l_{avg}). \tag{8}$$

The estimative nature of the formula does not imply precise determination of the albedo of the double-walled cone cuvette. From formulas (7) and (8), it is evident that the gain coefficient fundamentally depends on the optical properties of the water sample. This dependence, as well as the insufficient accuracy in determining the gain coefficient, is eliminated by normalization relative to the reference channel. Here, the property that each ray entering the sphere is amplified equally is used. Then, by dividing the measured isotropic light flux by the value in the reference channel, we obtain the expression $\exp\left(-a_w \bar{L}\right)$ equal to the attenuation of light due to its absorption by water in the cuvette.

Let us consider and analyze three methods for determining light absorption in seawater.

1. The method for determining absorption based on the use of a double-walled cone cuvette connected to an integrating sphere and a reference channel via an air path [27].

2. The method for studying the spectral absorption properties of seawater by sequentially determining the absorption of reference water and a sample using this

approach. The reference can be either ultrapure freshwater obtained by various means or filtered seawater.

3. The method under consideration, based on the use of two long conical cuvettes connected to an integrating sphere in a differential spectrophotometer scheme, for determining light absorption by suspended matter and CDOM directly in seawater.

In the first case, the total light absorption by seawater will be measured. Then to obtain the light absorption by suspended matter and dissolved substances, the absorption of pure water should be subtracted. It is known from the literature that laboratory experiments have failed to obtain values of the spectral absorption of pure water that are closely matched with high accuracy. In the short-wavelength region (according to [31]), the absorption values are strongly influenced by the degree of water purification, while in the long-wavelength region, where the influence of impurities is significantly less (according to [32]), a noticeable spread in the values of the light absorption coefficient of pure water is observed. The long-wavelength region of the visible spectrum is most susceptible to errors in determining absorption by impurities, because besides methodological errors, random measurement errors will also have an influence. Fig. 3 shows the difference between two absorption spectra of pure water according to the data from [31] and [32], compared to the absorption of yellow substance in the central part of the Black Sea. The data on the yellow substance absorption are taken from the work [1].

It is evident from Fig. 3 that the error from using tabulated values from the cited works can exceed light absorption by DOM. Furthermore, the non-monotonic nature of the error could be misinterpreted as a phytoplankton pigment absorption peak in measurements.

Using the second method, two sequential measurements are performed, resulting in two signals proportional to $\exp(-a_w \overline{L})$ and $\exp(-a_r \overline{L})$, where a_r is the light absorption in the reference water. Logarithm of the ratio of the two signals, divided by the average path length $\overline{L}$, is precisely the absorption by those particles and molecules not present in the reference water ($a_w - a_r$). The advantage of determining the analyzed sample and the reference water using this method lies in the compensation of systematic error and the reduction of errors caused by differences in spectral resolution. However, this method is sensitive to random errors in measurements, since they are performed at different times, which requires high stability of the photodetector and the power supply voltage.

In the third method, continuous comparison is achieved through the use of a differential dual-beam scheme with two rapidly switching sequential signals. Since these signals are proportional to $\exp(-a_w \overline{L})$ and $\exp(-a_r \overline{L})$, the light absorption by suspended matter in seawater can be easily calculated continuously via the logarithm of the ratio of the measuring and reference signals, divided by the average path length $\overline{L}$.

[1] Mankovsky, V.I., Soloviev, M.V. and Mankovskaya, E.V., 2009. *Hydro-Optical Characteristics of the Black Sea. Reference Book.* Sevastopol: ECOSI-Gidrofizika, 90 p. (in Russian).

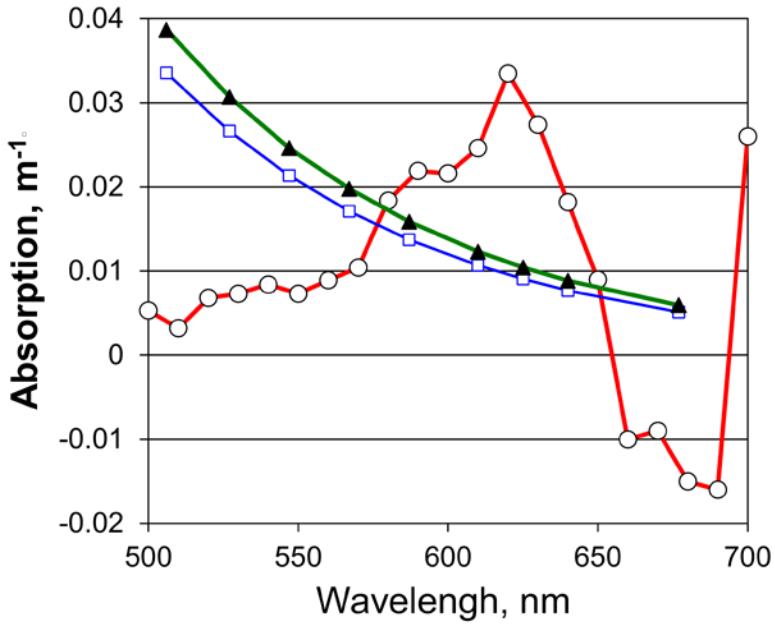

F i g. 3. Difference in the coefficients of pure water light absorption based on the data of two experiments, and the values of light absorption by CDOM in the central part of the Black Sea. ○ – difference between the coefficients of pure water light absorption given in [31] and [32]; ■ – typical values of CDOM absorption [1] for low values of beam attenuation (c = 0.28 м$^{-1}$); ▲ – CDOM absorption for high values of beam attenuation (c = 0.60 м$^{-1}$)

As we see, the third method does not differ mathematically in its formulas from the previous one, but due to the application of the differential dual-beam scheme, it achieves two orders of magnitude higher measurement accuracy.

Conclusion

The primary condition for correctly determining the optical properties of a scattering medium is single scattering, where scattering particles are not too close to each other and are separated by a distance greater than three times their radius. For seawater, this condition implies that the spectral absorption properties of suspended phytoplankton cells, detritus, and mineral particles must be determined in their natural state, without any preliminary procedures such as depositing particles on a filter or concentrating samples extracted from the sea. Currently, in none of the methods for determining light absorption by suspended matter satisfy the single scattering condition. Since seawater is a weakly absorbing medium dominated by scattering, directly measuring light absorption by suspended matter in an aqueous medium would require increasing sensitivity by tens of times while simultaneously ensuring complete collection of all scattered rays by the receiving device. It has been demonstrated for the first time that this can be achieved using the method proposed in this work. This method is based on the use of double-walled cone cuvettes made of quartz glass connected to an integrating sphere.

Integrating these elements into the optical scheme of a differential dual-beam photometer also facilitated this process. Consequently, the new method enables spectral analysis of the optical absorption properties of all impurities collectively and of each component separately, independently of the other substances in the mixture and the properties of the seawater in which they are present.

REFERENCES

1. Ciotti, A.M., Lewis, M.R. and Cullen, J.J., 2002. Assessment of the Relationships between Dominant Cell Size in Natural Phytoplankton Communities and the Spectral Shape of the Absorption Coefficient. *Limnology and Oceanography*, 47(2), pp. 404-417. https://doi.org/10.4319/lo.2002.47.2.0404
2. Marra, J., Trees, C.C. and O'Reilly, J.E., 2007. Phytoplankton Pigment Absorption: A Strong Predictor of Primary Productivity in the Surface Ocean. *Deep Sea Research Part I: Oceanographic Research Papers*, 54(2), pp. 155-163. https://doi.org/10.1016/j.dsr.2006.12.001
3. Torrecilla, E., Stramski, D., Reynolds, R.A., Millán-Núñez, E. and Piera, J., 2011. Cluster Analysis of Hyperspectral Optical Data for Discriminating Phytoplankton Pigment Assemblages in the Open Ocean. *Remote Sensing of Environment*, 115(10), pp. 2578-2593. https://doi.org/10.1016/j.rse.2011.05.014
4. Mobley, C.D., 1994. *Light and Water. Radiative Transfer in Natural Waters.* San Diego: Academic Press, 592 p.
5. Behrenfeld, M.J. and Falkowski, P.G., 1997. *A* Consumer's Guide to Phytoplankton Primary Productivity Models. *Limnology and Oceanography*, 42(7), pp. 1479-1491. https://doi.org/10.4319/lo.1997.42.7.1479
6. Karl, D.M., Knauer, G.A. and Martin, J.H., 1988. Downward Flux of Particulate Organic Matter in the Ocean: A Particle Decomposition Paradox. *Nature*, 332, pp. 438-441. https://doi.org/10.1038/332438a0
7. Blough, N.V. and Del Vecchio, R., 2002. Chromophoric DOM in the Coastal Environment. In: D. A. Hansell and C. A. Carlson, eds., 2002. *Biogeochemistry of Marine Dissolved Organic Matter*. San Diego: Academic Press, pp. 509-546. https://doi.org/10.1016/B978-012323841-2/50012-9
8. Twardowski, M.S., Boss, E., Sullivan, J.M. and Donaghay, P.L., 2004. Modeling the Spectral Shape of Absorption by Chromophoric Dissolved Organic Matter. *Marine Chemistry*, 89(1-4), pp. 69-88. https://doi.org/10.1016/j.marchem.2004.02.008
9. Lee, Z.P., Carder, K.L. and Arnone, R.A., 2002. Deriving Inherent Optical Properties from Water Color: A Multiband Quasi-Analytical Algorithm for Optically Deep Waters. *Applied Optics*, 41(27), pp. 5755-5772. https://doi.org/10.1364/ao.41.005755
10. Woźniak, S.B. and Stramski, D., 2004. Modeling the Optical Properties of Mineral Particles Suspended in Seawater and Their Influence on Ocean Reflectance and Chlorophyll Estimation from Remote Sensing Algorithms. *Applied Optics*, 43(17), pp. 3489-3503. https://doi.org/10.1364/ao.43.003489
11. Mitchell, B.G., 1990. Algorithms for Determining the Absorption Coefficient for Aquatic Particulates Using the Quantitative Filter Technique. In: R. W. Spinrad, ed., 1990. *Proceedings of SPIE: Ocean Optics X*. Vol. 1302, pp. 137-148. https://doi.org/10.1117/12.21440
12. Tassan, S. and Ferrari, G.M., 1995. An Alternative Approach to Absorption Measurements of Aquatic Particles Retained on Filters. *Limnology and Oceanography*, 40(8), pp. 1358-1368. https://doi.org/10.4319/LO.1995.40.8.1358
13. Maske, H. and Haardt, H., 1987. Quantitative in Vivo Absorption Spectra of Phytoplankton: Detrital Absorption and Comparison with Fluorescence Excitation Spectra 1. *Limnology and Oceanography*, 32(3), pp. 620-633. https://doi.org/10.4319/lo.1987.32.3.0620

14. Röttgers, R. and Gehnke, S., 2012. Measurement of Light Absorption by Aquatic Particles: Improvement of the Quantitative Filter Technique by Use of an Integrating Sphere Approach. *Applied Optics*, 51(9), pp. 1336-1351. https://doi.org/10.1364/AO.51.001336

15. Kishino, M., Takahashi, M., Okami, N. and Ichimura, S., 1985. Estimation of the Spectral Absorption Coefficients of Phytoplankton in the Sea. *ICES Journal of Marine Science*, 37(2), pp. 634-642.

16. Ferrari, G.M. and Tassan, S., 1999. A Method Using Chemical Oxidation to Remove Light Absorption by Phytoplankton Pigments. *Journal of Phycology*, 35(5), pp. 1090-1098. https://doi.org/10.1046/j.1529-8817.1999.3551090.x

17. Röttgers, R., Schönfeld, W., Kipp, P.-R. and Doerffer, R., 2005. Practical Test of a Point-Source Integrating Cavity Absorption Meter: The Performance of Different Collector Assemblies. *Applied Optics*, 44(26), pp. 5549-5560. https://doi.org/10.1364/AO.44.005549

18. Glukhovets, D.I., Sheberstov, S.V., Kopelevich, O.V., Zaytseva, A.F. and Pogosyan, S.I., 2017. Measuring the Sea Water Absorption Factor Using Integrating Sphere. *Light & Engineering*, 26(1), pp. 120-126. https://doi.org/10.33383/2016-079

19. Neukermans, G., Reynolds, R.A. and Stramski, D., 2014. Contrasting Inherent Optical Properties and Particle Characteristics between an Under-Ice Phytoplankton Bloom and Open Water in the Chukchi Sea. *Deep Sea Research Part II: Topical Studies in Oceanography*, 105, pp. 59-73. https://doi.org/10.1016/J.DSR2.2014.03.014

20. Lohrenz, S.E., 2000. A Novel Theoretical Approach to Correct for Pathlength Amplification and Variable Sampling Loading in Measurements of Particulate Spectral Absorption by the Quantitative Filter Technique. *Journal of Plankton Research*, 22(4), pp. 639-657. https://doi.org/10.1093/plankt/22.4.639

21. Stramski, D., Reynolds, R.A., Kaczmarek, S., Uitz, J. and Zheng, G., 2015. Correction of Pathlength Amplification in the Filter-Pad Technique for Measurements of Particulate Absorption Coefficient in the Visible Spectral Region. *Applied Optics*, 54(22), pp. 6763-6782. https://doi.org/10.1364/AO.54.006763

22. Hoepffner, N. and Sathyendranath, S., 1993. Determination of the Major Groups of Phytoplankton Pigments from the Absorption Spectra of Total Particulate Matter. *Journal of Geophysical Research: Oceans*, 98(C12), pp. 22789-22803. https://doi.org/10.1029/93JC01273

23. Neeley, A.R., Freeman, S.A. and Harris, L.A., 2015. Multi-Method Approach to Quantify Uncertainties in the Measurements of Light Absorption by Particles. *Optics Express*, 23(24), pp. 31043-31058. https://doi.org/10.1364/OE.23.031043

24. Van de Hulst, H.C., 1981. *Light Scattering by Small Particles*. New York: Dover Publications, 470 p.

25. Lee, M.E. and Shybanov, E.B., 2023. The Concept of a New Approach to the Determination of the Spectral Absorption of Light in Clear Seawater. In: SIO RAS, 2023. *Proceedings of the XII All-Russian Conference with International Participation "Current Problems in Optics of Natural Waters"*. Moscow: Shirshov Institute Publishing House, pp. 97-102 (in Russian).

26. Mankovsky, V.I., 1971. [On the Relationship between the Integral Indicator of Light Scattering of Sea Waters and the Indicator of Scattering in a Fixed Direction]. *Marine Hydrophysical Research*, (6), pp. 145-154 (in Russian).

27. Lee, M.E. and Shybanov, E.B., 2024. New Method for Determining Spectral Absorption of Light in the Sea. *Physical Oceanography*, 31(2), pp. 178-193.

28. Lee, M.E. and Shybanov, E.B., 2024. A New Approach to Determining the Spectral Light Absorption of Seawater by a Conical Reflecting Cuvette with an Integrating Sphere. *Fundamental and Applied Hydrophysics*, 17(3), pp. 9-20. https://doi.org/10.59887/2073-6673.2024.17(3)-1

29. Petzold, T.J., 1972. *Volume Scattering Functions for Selected Ocean Waters*. UC San Diego: Scripps Institution of Oceanography, 82 p.

30. Kullenberg, G., 1968. Scattering of Light by Sargasso Sea Water. *Deep Sea Research and Oceanographic Abstracts*, 15(4), pp. 423-432. https://doi.org/10.1016/0011-7471(68)90050-8

31. Pope, R.M. and Fry, E.S., 1997. Absorption Spectrum (380–700 nm) of Pure Water. II. Integrating Cavity Measurements. *Applied Optics*, 36(33), pp. 8710-8723. https://doi.org/10.1364/AO.36.008710

32. Smith, R.C. and Baker, K.S., 1981. Optical Properties of the Clearest Natural Waters (200–800 nm). *Applied Optics*, 20(2), pp. 177-184. https://doi.org/10.1364/AO.20.000177

Submitted 14.11.2024; approved after review 02.02.2025;
accepted for publication 15.05.2025.

About the authors:

Michael E. Lee, Chief Researcher, Head of the Optics Department, Marine Hydrophysical Institute of RAS (2 Kapitanskaya Str., Sevastopol, 299011, Russian Federation), DSc. (Phys.-Maths.), Professor, **ORCID ID: 0000-0002-2292-1877**, **ResearcherID (WOS): R-4344-2018**, **Scopus Author ID: 56142710400**, **SPIN-code: 2479-6915**, michael.lee.mhi@gmail.com

Evgeniy B. Shybanov, Leading Researcher, Optics Department, Marine Hydrophysical Institute of RAS (2 Kapitanskaya Str., Sevastopol, 299011, Russian Federation), DSc. (Phys.-Math.), **ORCID ID: 0000-0001-7943-305X**, **ResearcherID: ABB-9097-2021**, **Scopus Author ID: 6507075380**, **SPIN-code: 9906-9983**, e-shybanov@mail.ru

Contribution of the co-authors:

Michael E. Lee – scientific supervision of the research, formulation of goals and objectives, development and justification of the new concept, literature review, analysis of materials, preparation of the manuscript

Evgeniy B. Shybanov – participation in development and justification of the new concept, development of the mathematical algorithm, writing of the computer program to perform calculations, visualization of the results, qualitative and quantitative analysis of the results, making conclusions, discussion of the article materials, editing and revising the manuscript

The authors have read and approved the final manuscript.
The authors declare that they have no conflict of interest.

ISSN 1573-160X, *PHYSICAL OCEANOGRAPHY*, Vol. 32, Iss. 4, pp. 446-463 (2025)

published in *Morskoy Gidrofizicheskiy Zhurnal*, 2025, Vol. 41, Iss. 4, pp. 417–435

Original article

Extreme Events of Marine Heat Waves off the Eastern Coast of Kamchatka Peninsula and in the Adjacent Areas under Conditions of Modern Global Warming

I. D. Rostov ✉, E. V. Dmitrieva, I. A. Zhabin

V. I. Il'ichev Pacific Oceanological Institute, Far Eastern Branch of Russian Academy of Sciences, Vladivostok, Russian Federation
✉ *rostov@poi.dvo.ru*

Abstract
Purpose. The purpose of the study is to determine the characteristics and trends of inter-annual variability of marine heat wave parameters off the Kamchatka Peninsula eastern coast and in the adjacent areas over the past four decades and to analyze their cause-and-effect relationships with the large-scale and regional processes in the ocean and atmosphere in the context of global warming, as well as to investigate the possible role of coastal wind upwelling in the chain of events of a large-scale environmental disaster in the study region in the fall 2020 under conditions of intensification of marine heat waves and outbreak of harmful algal blooms.
Methods and Results. Standard methods for identifying the variability of marine heat waves and for determining the amplitude-frequency parameters at the regular grid nodes were used to analyze the NOAA climate data array. The results enabled detailed characterization of the spatiotemporal variability of marine heat waves in the region under study including the frequency of events, their duration, intensity, integral indicators (cumulative intensity and composite intensity index), as well as the trends in inter-annual and seasonal variations. The cases of wind-driven upwelling of deep-sea waters in the coastal zone accompanied by a surge in chlorophyll a concentration on the ocean surface during the harmful algal bloom outbreak were also identified.
Conclusions. The marine heat wave events developed against the background of stable positive trends in sea surface temperature. During the last two decades of global warming, a significant increase in all the marine heat wave indicators has been observed. Statistically significant correlations were identified between fluctuations in various marine heat wave parameters and changes in characteristics of anomalies of the surface air temperature field, geopotential height of the 500 mbar isobaric surface as well as climate indices indicating the local and remote influence of large-scale atmospheric processes. During the outbreak of harmful algal bloom off the Kamchatka coast observed after the marine heat waves impact, an increase in wind upwelling in the coastal zone was noted that facilitated the entry of nutrients and dinoflagellates into the photic layer, and also an increase in their numbers and chlorophyll a concentration. The conducted studies confirm the assumption about the role of extreme marine heat waves in the chain of events of the environmental disaster that took place in the region under study in the fall 2020.

Keywords: northwestern Pacific Ocean, Kamchatka, climate change, marine heat waves, upwelling, chlorophyll concentration, climate indices, correlations

Acknowledgments: This work was conducted under the state assignment of POI FEB RAS, titled "Response and Potential Change of Coastal Ecosystems of Kamchatka under Conditions of Global Climatic and Local Catastrophic Impacts" (registration number 124072200009-5).

For citation: Rostov, I.D., Dmitrieva, E.V. and Zhabin, I.A., 2025. Extreme Events of Marine Heat Waves off the Eastern Coast of the Kamchatka Peninsula and in the Adjacent Areas under Conditions of Modern Global Warming. *Physical Oceanography*, 32(4), pp. 446-463.

Introduction

Amid ongoing global warming, extreme climatic phenomena in both the atmosphere and ocean are becoming increasingly frequent, prolonged, and intense. In the ocean, such phenomena include marine heatwaves (MHWs), recognized as one of the most serious extreme events caused by climate change [1]. These waves can be defined as prolonged, discrete, anomalously warm events characterized by duration, intensity, rate of evolution, and spatial extent [1, 2]. Qualitatively, MHWs are defined [3] as discrete periods of prolonged anomalously warm surface water in a specific location, while quantitative definitions are based on ocean temperatures exceeding fixed seasonally varying or cumulative thresholds that differ across regions. Based on a standardized methodology [2], most studies define an MHW event as a prolonged anomalously warm period at the ocean surface lasting at least five consecutive days with temperatures above the 90th percentile for a chosen time period.

The occurrence of MHWs can be triggered by a combination of local oceanic and atmospheric processes, such as air-sea heat fluxes and horizontal advection. These processes can be modulated by large-scale climate variability through teleconnections and interactions [3, 4]. MHWs are typically identified using sea surface temperatures (SSTs), although they can extend to greater depths. Alongside extreme thermal anomalies, the opposite phenomena – extreme marine cold spells – are also periodically observed, with their metrics decreasing in most regions [1, 5], though their intensity may increase in some locations.

Over the past few decades, MHWs have been observed in all ocean basins [1, 2, 4], and their frequency and intensity are projected to increase throughout the 21st century [5]. Notably, over the last 40 years, the average intensity of MHWs in the Arctic marginal seas has become comparable to that observed in other regions of the World Ocean [6]. MHW events can last from several days to several months and cover tens to hundreds of kilometers of water area. They pose a significant threat to marine ecosystems, coastal biological communities, and the economies of coastal regions [2, 6, 7], but can also create favorable conditions for the spread of invasive species.

The factors determining the onset and termination of individual MHW events are diverse and can vary depending on the region, season, and event scale [4]. Oceanic advection plays a key role in regulating the characteristics of small-scale MHWs, while atmospheric processes are the primary driver for larger-scale MHW events. Generally, as the spatial scale increases, MHWs become less intense, occur less frequently, and last longer [8]. During periods of extreme warming, a weakening of vertical water mixing processes and enhanced stratification are observed, reducing the supply of nutrients to the surface, causing water acidification, and decreasing dissolved oxygen levels to critical values [9, 10].

The main risks associated with the impact of MHWs on marine biota [10] arise from disruptions to natural habitat conditions and life cycles of aquatic organisms when their adaptive limits are exceeded. This also leads to disruptions in food

chains, deterioration of oxygen conditions, and the emergence of toxicological threats associated with harmful algal blooms (HABs) [11]. Temperature and nutrient supply are key factors controlling ocean productivity [12, 13]. According to research [14], MHWs can both decrease chlorophyll concentration (an indicator of phytoplankton biomass) [9] and promote its increase across different latitudes. The magnitude of the chlorophyll response to temperature rise increases with the intensity and duration of the MHWs and the rate of nutrient supply to the upper mixed layer. However, the links between these processes are complex and ambiguous.

Numerous studies have shown that MHWs have caused mass HAB events in various regions around the world [15]. Such events have become increasingly frequent in recent decades and have expanded both temporally and spatially, exerting unprecedented impacts on marine ecosystems [1, 16, 17]. In some cases, these phenomena have led to catastrophic consequences for coastal aquaculture and fisheries. For instance, in late September – early October 2020, an ecological disaster occurred in the waters of Avacha Gulf and other areas along the southeastern coast of Kamchatka. It was accompanied by massive phytoplankton development and an anomalous increase in chlorophyll *a* concentration. These changes led to the appearance of foam, films of biogenic surfactants on the water surface, and mass mortality of marine organisms (up to 95% of benthos) [18, 19]. Research indicated that the cause was a massive and prolonged bloom of the dinoflagellate species *Karenia selliformis* [19], whose abundance closely correlated with chlorophyll *a* concentration but was not linked to anthropogenic eutrophication [18, 20], characteristic of Avacha Bay adjacent to Avacha Gulf. The HAB lasted two months and covered an extensive area exceeding 300 × 100 km [19].

Among the probable factors contributing to this phenomenon were strong positive water temperature anomalies, which can be regarded as intense MHWs [15]. Other contributing factors include the supply of nutrients from deep water layers due to wind-wave mixing triggered by the passage of three deep cyclones between September 19 and October 7, 2020 [21], as well as the influence of Typhoon Dolphin, which may have intensified these processes. Additionally, the influence of wind-driven upwelling, promoting the rise of dinoflagellates to the surface, was considered as a possible cause of the HAB outbreak [19], but this hypothesis was not conclusively confirmed during the study. Similar phenomena associated with massive HABs are known as “red tides” and have been recorded in Kamchatka bays before [21]. A year later, in September – November 2021, similar events occurred in the southern part of the region, off the Pacific coast of Hokkaido, where intense MHWs were also observed [16]. A massive dinoflagellate bloom [20] was recorded in this region as well, accompanied by marine organism mortality. These events were linked to features of mesoscale water dynamics and intensification of horizontal and vertical mixing processes that followed intense and extensive MHW manifestations in the area [15]. Overall, the retrospective

analysis of toxic HAB events and laboratory experiments confirm the link between sharp water temperature increases and increased toxin production rates [17].

It should be noted, however, that the multifactorial biological impacts on marine ecosystems associated with various MHW characteristics can vary significantly. The mechanisms of these processes, as well as their causal relationships, remain insufficiently studied [15, 22]. It has been established that the ecosystem response depends significantly on the duration, intensity, and timing of extreme events [23]. At the same time, reliable data on the frequency of HAB occurrences and on MHW characteristics off the eastern coast of Kamchatka, similar to those available for the Bohai Sea [16], are lacking. Overall, in recent years, a certain dependence of HAB occurrence and dynamics on MHW characteristics has been observed in both the northeastern and northwestern Pacific Ocean.

Several key factors influencing HAB development can be highlighted:

– more frequent HAB outbreaks are associated with anomalously warm thermal conditions arising from MHW influence [17, 20]. However, subsequently, these conditions can exert a negative impact on sustaining such algal populations, acting as a stressor for their growth [24];

– in years with “red tides” (HAB period), the total number of days with MHWs is generally higher than in years without them. “Red tides” occur more frequently in areas with higher MHW frequency and duration compared to neighboring waters [25];

– even in locations where such algae are rare, recurrent HAB events can occur in subsequent years following an outbreak [20];

– formation of areas of extreme temperature anomalies on the ocean surface and enhanced stratification caused by MHWs one month [15] or more prior to the onset of HABs facilitate the initiation and acceleration of HAB development processes;

– HAB outbreaks occur when algae encounter optimal ecological conditions [15]. Processes such as wind-wave mixing, upwelling, horizontal advection, and mesoscale water dynamics, leading to the influx of nutrients from deep layers into the photic zone, are necessary for phytoplankton nutrition and sustaining HABs [17, 18];

– expansion of the area affected by HABs is linked to the deepening of the mixed surface layer and the entrainment of nutrients from river runoff [15, 18, 21] and adjacent waters.

The marine areas adjacent to the eastern coast of the Kamchatka Peninsula represent one of the most dynamically active and productive regions of the Pacific Ocean, providing essential conditions for the reproduction and fishery of numerous fish species and other aquatic organisms. At the turn of the 20th – 21st centuries, the study area was dominated by unidirectional trends in thermal conditions towards increasing water and air temperatures, primarily due to changes in heat exchange with the atmosphere, manifested in ice cover characteristics,

thermohaline structure, and water heat content [26]. These processes are characterized by significant spatiotemporal variability and exert a noticeable influence on the ecological state and biota of the region. The waters of the region exhibited the highest warming rate within the entire Pacific basin, with the trend contribution to the total variance of annual mean SST reaching 30–40% [26]. The largest trends in air temperature (T_a) and SST were observed in the western Bering Sea and off the eastern coast of Kamchatka [27]. The features of their interannual variability are determined by surface forcing and the internal dynamics of the ocean. They include seasonal changes, as well as decadal and multidecadal oscillations superimposed on monotonic trends under changing climatic regimes and specific phases of global warming.

Currently, the metrics of MHW events – quantitative indicators (such as intensity, duration, frequency, spatial coverage [2]), their statistical characteristics, as well as cause-and-effect relationships with atmospheric and oceanic processes in the northwestern Pacific region off the eastern coast of Kamchatka remain insufficiently studied.

The aim of this work is to determine the characteristics and trends of interannual variability of MHW parameters off the eastern coast of Kamchatka and adjacent areas, analyze cause-and-effect relationships with large-scale and regional processes in the ocean and atmosphere over the past 40 years, and investigate the potential role of coastal wind-driven upwelling in the chain of events of the large-scale ecological disaster in the study region amid intensifying MHWs and the HAB outbreak.

Data and methods

The study area is bounded by coordinates 51–63° N, 156–180° E, and the temporal period covers four decades from 1982 to 2023. Optimally interpolated daily SST data (NOAA-OI SST V2) on a 0.25° × 0.25° grid, available at https://www.psl.noaa.gov/data/gridded/data.noaa.oisst.v2.highres.html, and the standard MHW identification method [2] are used in the present paper. An MHW event was defined as an anomalously warm phenomenon on the ocean surface lasting at least five consecutive days (two consecutive events separated by less than three days are considered a single event) with SSTs exceeding the 90th percentile, based on a 30-year baseline climatological period (1988–2018) using Matlab software [28]. According to the method [2], the 90th percentile was calculated for each calendar day using daily SST values within an 11-day window centered on the data across all years within the climatological period and smoothed by applying a 31-day moving average. To describe, comparatively analyze, and classify MHW characteristics in each grid cell and averaged over the region, various metrics [2] were calculated, defined based on the extent to which actual temperature values exceed the local climatology of the 90th percentile for the baseline period [22]:

– frequency – the number of MHW events per year (F);

– duration – the number of days between the start and end of an MHW event period when SST exceeds the 90th percentile threshold (D, days);
– intensity – the deviation of the daily mean SST relative to the 90th percentile of the baseline period on a selected day (I, °C);
– mean intensity, representing the average intensity (temperature anomaly) for the entire MHW event under consideration (I_{mean}, °C);
– maximum intensity – the largest temperature anomaly during the MHW event period (I_{max}, °C);
– cumulative intensity – an indicator summing the temperature anomaly values over the MHW event duration (I_{cum}, °C);
– cumulative intensity (composite) index, which integrates the frequency (number) of events, their intensity, and duration over the entire period (ICI, °C·days).

Reanalysis data for surface air temperature (T_a), pressure, and wind, along with time series of CI (*AMO, NPGO, PDO, SOI, WP, NINO.WEST*) [26, 29] were obtained from NOAA websites: https://psl.noaa.gov/data/gridded/index.html and https://psl.noaa.gov/data/climateindices/list/. Satellite data on chlorophyll a concentration and high-resolution SST were taken from the ERDDAP NOAA CoastWatch server at https://coastwatch.noaa.gov/erddap/griddap/index.html?page=1&itemsPerPage=1000.

Statistical calculation and analysis of the spatio-temporal variability of the used data characteristics were carried out according to a unified methodology [29]. Taking into account the duration of the summer and winter monsoons and the intra-annual cycle of T_a and SST, conditionally warm, summer (June – September), and conditionally cold, winter (November – March), seasons (periods) of the year were selected. Calculations were carried out both for the entire 42-year period of 1982–2023 and for its first (1982–2002) and second (2003–2023) halves. The 95% significance level for trends in time series and correlation coefficients was assessed using Student's *t*-test with effective degrees of freedom.

A wind-based upwelling index allowing for quantitative estimates of the offshore-directed Ekman transport in the surface friction layer [30] was used to study the possibility of manifestation and characteristics of seasonal coastal upwelling in the study area. The index was calculated from the wind field in coastal ocean areas using the data obtained from satellite scatterometers, which capture the short-period variability of the wind field [31]. For the coastal areas of the southeastern coast of Kamchatka and Avacha Gulf, the equation for calculating the wind-based upwelling index can be presented as follows:

$$UI = -Q_x \sin(a - \pi/2) + Q_y \cos(a - \pi/2),$$

where a is the angle between the corresponding parallel and the straight line approximating the average coastline; Q_x and Q_y are the values of the zonal and meridional components of the wind-driven transport. In this case, $Q_x = \tau_y/\rho f$, $Q_y = -\tau_x/\rho f$, where τ_x and τ_y are the values of the zonal and meridional components of the wind stress, ρ is the density of seawater (1025 kg·m^{-3}), f is the Coriolis parameter. Wind stress was calculated using the equations proposed in [32].

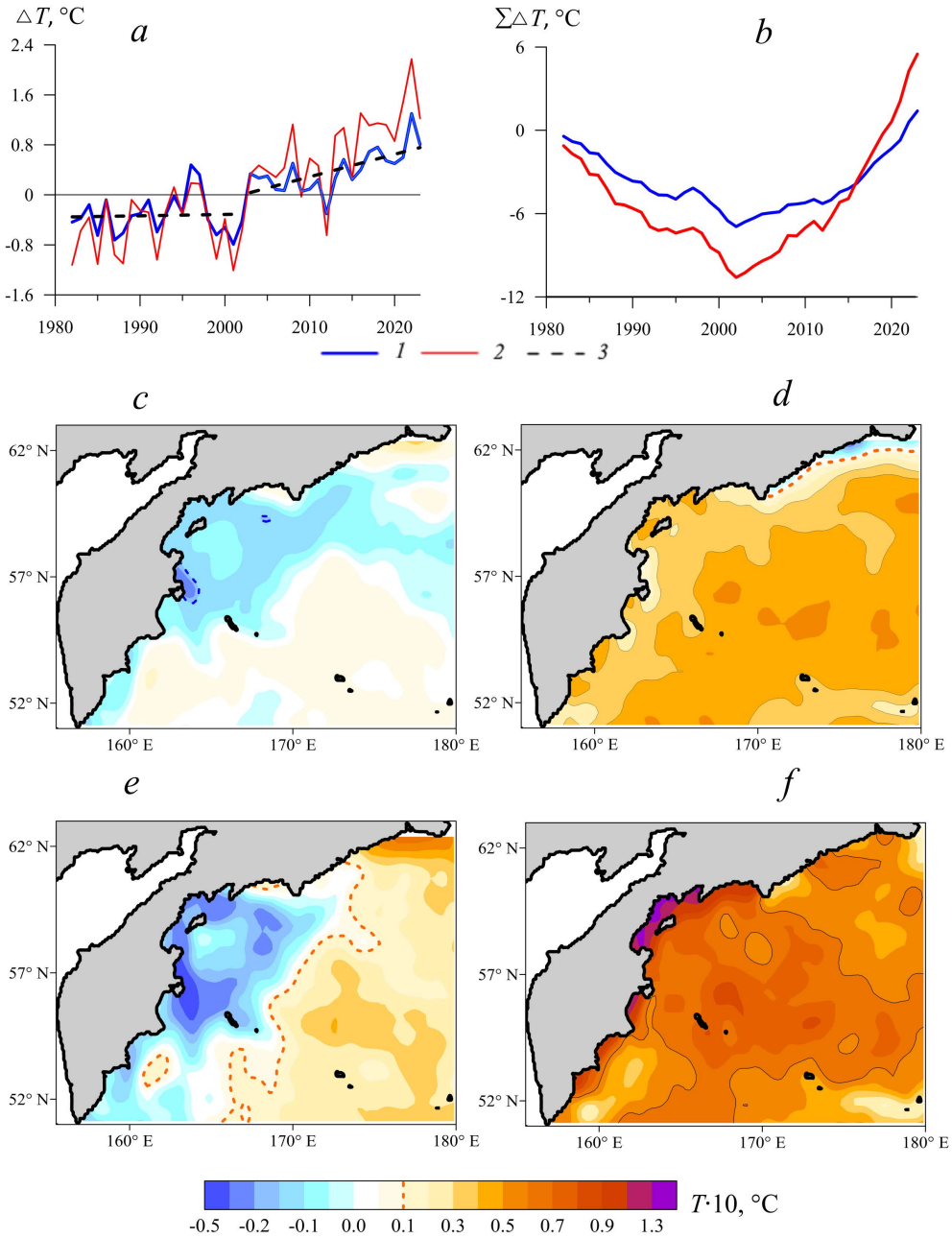

F i g. 1. Inter-annual variability of annual average SST (ΔT) anomalies (*a*) and accumulated ($\sum\Delta T$) anomalies (*b*) in 1982–2023; trends of annual average SST anomalies (*c*) and warm period SST anomalies (*e*) in 1982–2002; the same is for 2003–2023 (*d, f*). Legend at the fragments a and *b*: *1* – annual average SST anomalies; *2* – warm period SST anomalies; *3* – linear trends for two periods; dashed lines delimit the areas statistically significant at the 95% level in fragments *c*, *d* and *e*

Warming trends in the waters off the eastern coast of the Kamchatka Peninsula and adjacent areas

Overall, a statistically significant positive trend in mean annual SST anomalies (ΔT) was observed for the region during 1982–2023, amounting to 0.31 °C per decade. The anomaly and cumulative anomaly plots reveal two distinct phases (periods) of climatic change: 1982–2002, characterized by predominantly negative SST anomalies, and 2003–2023, characterized by predominantly positive anomalies (Fig. 1, *a*, *b*).

The mean annual SST trend value in the first phase was 0.02 °C per decade and was not statistically significant, whereas in the second phase it increased to a significant 0.36 °C per decade. During the warm period of the year in the first phase (1982–2002), a moderate increase in SST of up to 0.12 °C per decade was observed across the entire region. However, in the subsequent period (2003–2023), the SST trend sharply intensified, reaching 0.64 °C per decade. This is associated with a transition to a new climatic regime and changes in atmospheric circulation characteristics in the region. Moreover, as previously shown [26], the identified trends also differ in the northern and southern sectors of the waters throughout the extratropical zone of the northwestern Pacific Ocean. As seen in Fig. 1, *c* – *f*, in the last two decades, the sign of the SST trend in the waters of the western and northwestern parts of the study area changed from negative to positive. Furthermore, during the warm period of the year, a band of extreme SST trends formed off the coast of the eastern part of the Kamchatka Peninsula (Fig. 1, *f*), which, according to our estimates, reached unprecedented values for the entire Pacific basin – up to 1.45 °C per decade.

Average characteristics of marine heat waves

Fig. 2 shows the temporal changes in some MHW characteristics across the entire region. Over the last 40 years, the figure indicates a gradual increase in the area of the water body affected by this process (number of grid points, N_g – Fig. 2, *c*). These events are recorded throughout all months of the year; however, a sharp increase in their number was observed mid-period (Fig. 2, *d*, *e*). Overall, the total number of MHW events (N_e) at grid points over this period increased from 213 in 1987 to 19.7 thousand in 2018 (an average of ~ 6.5 thousand events per year occurred during the period), showing a significant trend of ~ 3.5 thousand events per decade. The amplitude-frequency characteristics of the intra-annual dynamics of these events also vary across the region and exhibit specific features depending on the year within each period (Fig. 2, *a*, *b*). The interannual course of the N_e curve reflects the general warming trends in the region and two main periods marking key climate changes (Fig 1, *a*; 2, *d*).

The main peaks on this curve correspond to peak El Niño values that occurred in recent decades, and the overall trend coincides with global climate changes [1, 29, 33]. Further analysis of MHW characteristics in the region focused on the most recent 20-year time interval (2003–2023). Fig. 3 shows the frequency of events, their duration, intensity, and integral indices, highlighting significant regional differences in these indicators over the last two decades.

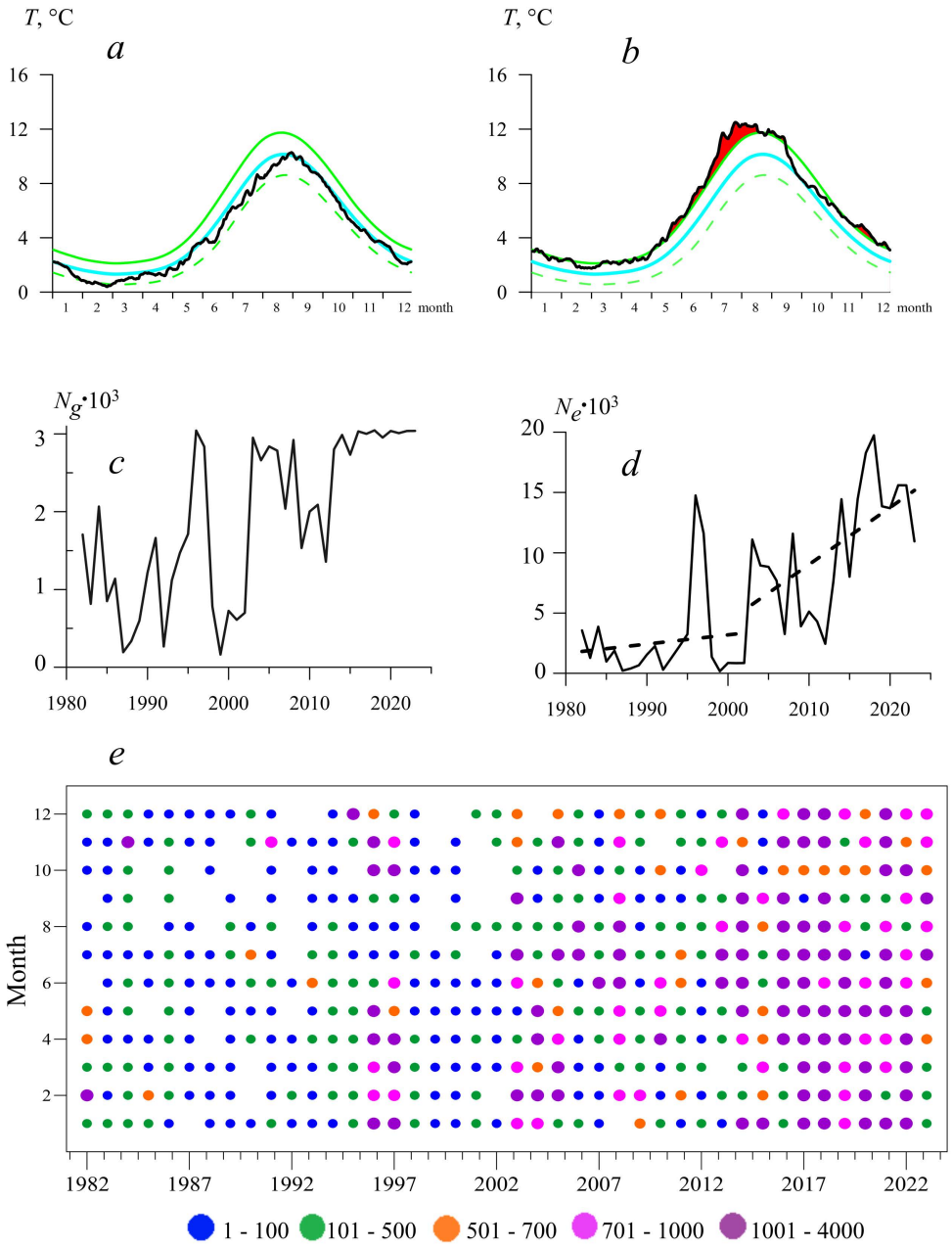

F i g. 2. General indicators of MHW events in the region under study. Changes of daily average SST (black curve), climatological average SST (blue curve), and the 90th (solid green curve) and 10th (dashed green curve) percentile thresholds in 2002 (*a*) and 2023 (*b*); number of grid nodes N_g (*c*) where the MHW events were observed, and a number of MHW events N_e at the grid nodes (*d*); differentiated changes in the number of MHW events over the entire region for different years by months (*e*)

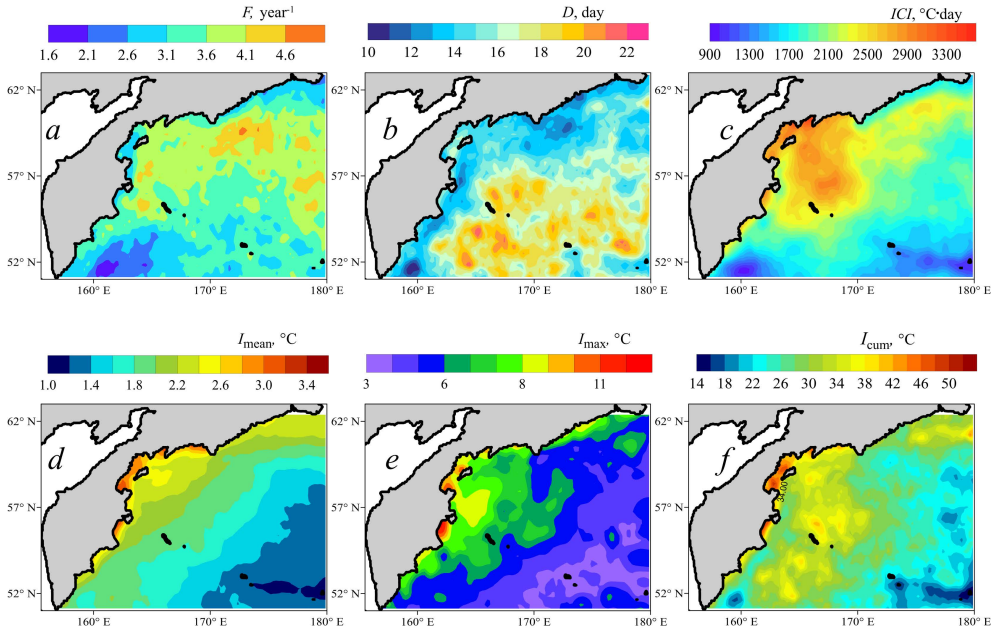

F i g. 3. Spatial distribution of long-term averaged annual mean MHW characteristics in 2003–2023: MHW events frequency (*a*); duration (*b*); composite intensity index (*c*); mean (*d*), maximum (*e*) and cumulative (*f*) intensities

The zone with the lowest frequency of MHW events (fewer than two per year) is located southeast of Kamchatka in the open ocean part, while the highest frequency (more than four per year) was observed near the shelf edge of the Bering Sea (Fig. 3, *a*), as previously noted [34]. The mean event frequency (F) was 3.4 per year. The mean duration of each MHW event (D) in the region's waters was 16 days. However, the duration of these events increases with distance from the continent. In the northwest, the duration is 10–12 days, whereas in the deep-water areas of the southeastern part of the region, it is 20–25 days (Fig. 3, *b*).

Over 20 years, the mean and maximum mean of MHW intensities in the study area were 1.8 °C and 5.2 °C, respectively. The mean cumulative intensity was 28.2 °C. The highest values of these characteristics (I_{mean} ~ 3.4 °C, I_{max} ~ 11.5 °C and I_{cum} ~ 50 °C) were recorded in a narrow coastal zone in the northeastern part of the Kamchatka Peninsula and in adjacent ocean waters near the continent (Fig. 3, *d* – *f*). The composite intensity index (*ICI*), which combines the three main MHW variables (F, D, I_{mean}), provides a more comprehensive picture of MHW manifestation. The spatial distribution of the *ICI* (Fig. 3, *c*) shows higher index values in the western Bering Sea basin and lower values in the southern region.

These general trends in the dynamics of daily MHW characteristics, on the one hand, are an expected consequence of rising mean ocean surface temperature under global warming [33], and on the other hand, reflect selective sensitivity to sea surface temperature changes and may serve as both precursors to and causes of interannual temperature fluctuation trends [34].

Interannual and seasonal changes in MHWs

Fig. 4 shows the interannual changes in the main characteristics of MHWs, averaged across the entire study area. MHW indicators exhibit peak values towards the end of the 1982–2023 period. A positive linear trend is clearly visible (Fig. 4, table). The relationships between changes in MHW characteristics, anomalies of various regional climate indicators, and climate indices demonstrate relatively close correlations.

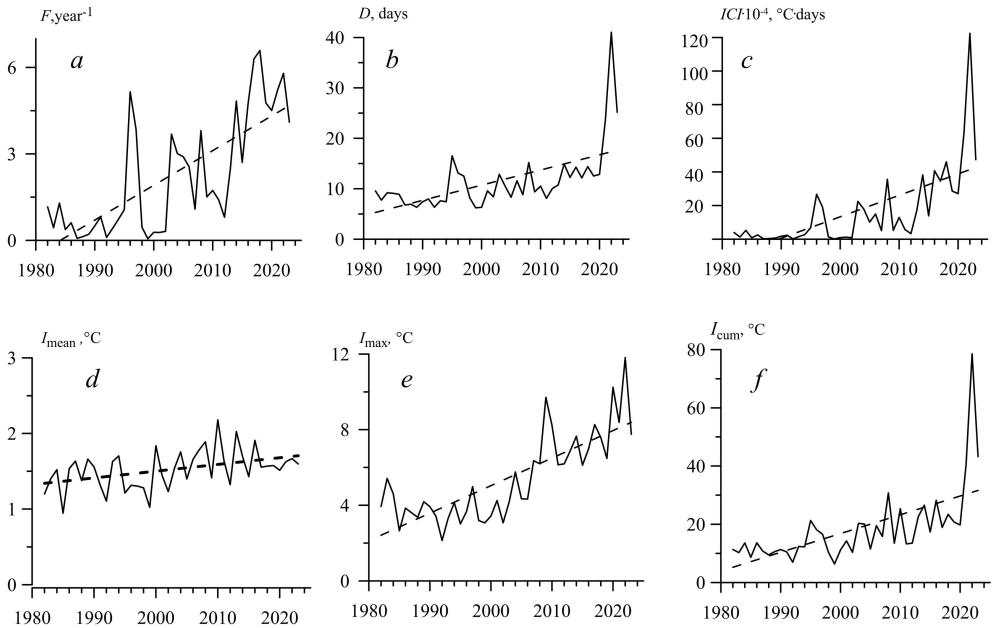

F i g. 4. Regionally averaged annual mean values of frequency F (*a*), duration D (*b*), composite intensity index ICI (*c*), mean I_{mean} (*d*), maximum I_{max} (*e*) and cumulative I_{cum} (*f*) intensities of MHW events for 1982–2023. Legend: solid line denotes MHW index, dashed line – linear trend

Trends in MHW indicators across the region are characterized by the following features. The number of MHW events per year increases by 1.2 per decade (table). The mean duration of each event increased by 3.7 days per decade, reaching a record 49 days in 2022 (Fig. 4, *b*). This explains the presence of peaks in the distribution of cumulative intensity (Fig. 4, *f*) and the composite MHW index for that year (Fig. 4, *c*). On average, the largest water temperature anomalies relative to climatic norms increased by 1.5 °C per decade (table), consistent with the findings of other studies [33]. The dependence of MHW event duration on their frequency and maximum intensity is characterized by a high correlation ($R = 0.6$).

The data in the table show the presence of average statistically significant correlations between the interannual fluctuations of various MHW indicators and the characteristics of changes in surface air temperature anomalies (overall for the region ($R = 0.61$), T_a anomalies at the nearest coastal meteorological station ($R = 0.61$), geopotential height at the 500 mb level ($R = 0.50$)), as well as with various climate indices. Trends in interannual changes of CIs are mainly

determined by the position, intensity, and interaction of the main baric formations, which are seasonal centers of atmospheric action, and depend on the selected time period. Correlations between fluctuations of *AMO* – *IPO* indices reflect the influence of various large-scale processes, which are part of the global climate variability regime, on the structure of pressure, wind fields, and thermal conditions in the subarctic region through long-range relations [26].

Inter-annual trend (*b*/10 years) values of annual average MHW indicators, and correlation coefficients (*R*) of MHW events with climatic parameters for 1982–2023

Parameters	*F*	*D*	*ICI*	I_{mean}	I_{max}	I_{cum}
b	**1.2**	**3.7**	**12.5×10^3**	**0.1**	**1.5**	**6.4**
R/SST_a	**0.81**	**0.57**	**0.76**	**0.33**	**0.55**	**0.59**
R/T_a	**0.76**	**0.63**	**0.74**	**0.36**	**0.52**	**0.65**
R/H_{500}	**0.52**	**0.47**	**0.51**	**0.38**	**0.57**	**0.53**
R/AMO	**0.35**	**0.53**	**0.38**	**0.44**	**0.50**	**0.44**
R/SOI	0.22	**0.36**	**0.32**	0.29	**0.38**	**0.42**
R/NINO.W	**0.61**	**0.45**	**0.57**	**0.39**	**0.69**	**0.52**
R/NPGO	**−0.47**	**−0.31**	**−0.35**	0.12	−0.19	−0.22
R/IPO	−0.21	**−0.38**	**−0.40**	−0.23	**−0.38**	**−0.42**

N o t e. SST_a is annual average anomalies of surface air temperature based on reanalysis data; T_a is annual average anomalies of air temperature at the coastal weather station Apuka (Olyutorka) taken from the website http://portal.esimo.ru/portal; H_{500} – anomalies of geopotential height of the 500 mbar surface; *AMO* – *IPO* are climatic indices [26, 29]. Statistically significant (95%) estimates are highlighted in bold

As shown in Fig. 5, the maximum number of MHW events on individual days at the region's grid points, on average for 2003–2023, corresponds to events of short duration (5–10 days per year) (Fig. 5, *a*). The largest number of events of various durations is observed during the warm period of the year. In the intra-annual dynamics, the total number of MHW events averaged over the region increased sharply during the second phase of the study period (Fig. 5, *a* – *d*).

Thus, local atmospheric influences are a key factor in MHW variability in the region under consideration. These influences can be modified by large-scale climate variability regimes.

Marine heat waves and the 2020 HAB off the Kamchatka coast

As mentioned earlier, a trend of accelerated warming has been observed in the study waters over the last two decades, and marine heat wave events have

spread throughout the entire region (Figs. 1–4). By the end of this period, MHWs and anomalously high temperatures had severely impacted the biota of the coastal zone and adjacent marine areas. In the context of the Kamchatka ecological disaster of late September – early October 2020, these processes were accompanied by the mass development of microalgae and a significant increase in chlorophyll a concentration [18, 19, 21], which apparently contributed to the HAB outbreak. Processes of mixing in the upper ocean layer, which promote the supply of nutrients and dinoflagellates to the photic layer, were also considered among the causes of this phenomenon [18, 19, 21]. One such process is coastal upwelling, which is the rise of deep waters to the surface caused by wind forcing.

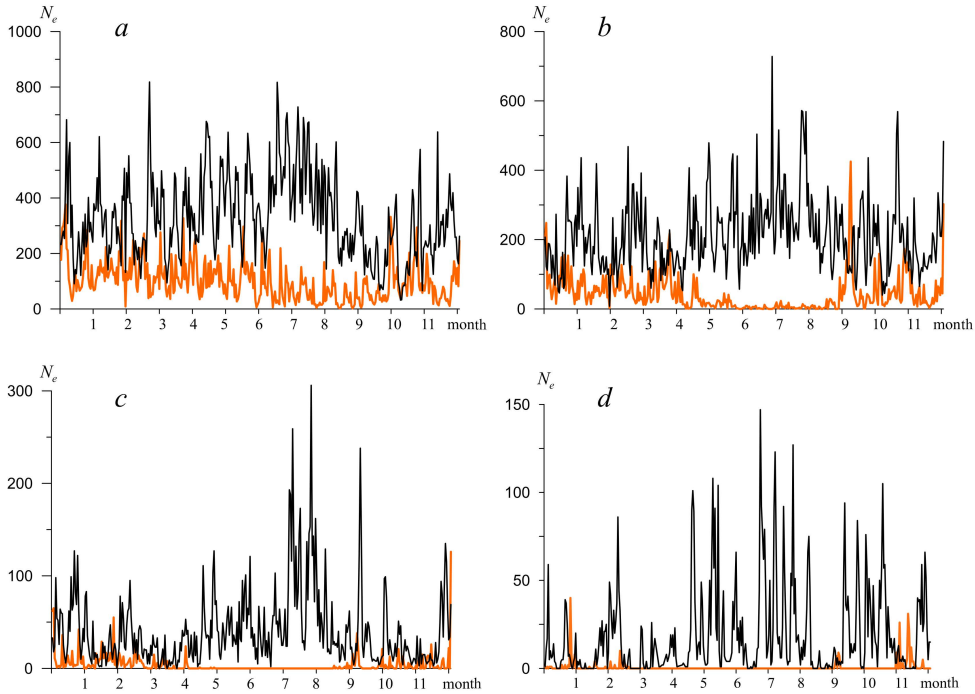

F i g. 5. Number of MHW events (N_e) of different durations for 1982–2002 (orange curve) and 2003–2023 (black curve) averaged for the entire region for different days and seasons of a year: 5–10 days per year (*a*), 11–32 days (*b*), 33–62 days (*c*), and more than 62 days (*d*)

It should be noted that the influence of wind-driven upwelling on the thermal structure of the waters off the eastern coast of the Kamchatka Peninsula during the period of sharp environmental deterioration in September – October 2020 had not been previously studied. To analyze this process, satellite maps of SST distribution can be used. These maps highlight upwelling zones as areas of colder waters near the coast. Additionally, results from calculating the wind-based upwelling index (Fig. 6, *b*, *d*) can be used.

The wind-based upwelling index is used to evaluate the intensity of upwelling in coastal waters. Positive index values indicate upwelling and negative values

indicate downwelling (sinking of waters). Our calculations showed that favorable conditions for the development of seasonal coastal upwelling can form during the summer-autumn period when western and southwestern winds with an average speed of 4–9 m·s^{-1} [27] prevail over the coastal strip and the region's waters. Maximum positive upwelling index values in the coastal zone of Kamchatka within the 52–53° N latitude band (Fig. 6, *b*) indicate intense upwelling and are observed in fall, following spring-summer MHW events (Fig. 6, *a*). These events are accompanied by the formation of a belt of colder waters in the coastal zone (Fig. 6, *d*), as well as a sharp increase in chlorophyll a concentration in the intra-annual course (Fig. 6, *c*) and a change in its spatial distribution (Fig. 6, *f*) compared to periods without pronounced wind-driven upwelling (Fig. 6, *e*). It should be noted that besides the impact of toxins on biota causing the death of marine organisms during HAB outbreaks, another negative factor is the decrease in dissolved oxygen levels to critical values in the bottom layers [11] during the death and decomposition of microalgal biomass. In the context of the Kamchatka ecological disaster, such cases of hypoxia have not been sufficiently studied.

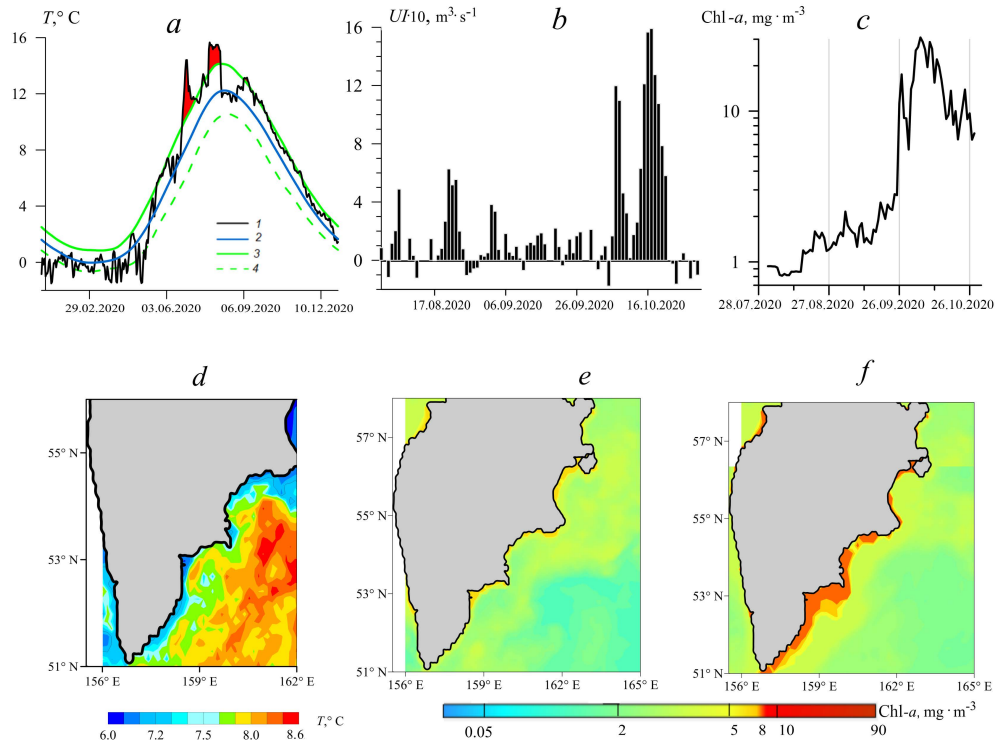

F i g. 6. Changes in daily average SST (*1*), climatological average SST (*2*), and the 90th (*3*) and 10th (*4*) percentile threshold values in temperature seasonal variation in the study area off the coast of Avacha Gulf in 2020 (*a*); temporal variability of daily upwelling index values in the same area in summer – fall, 2020 (*b*); intra-annual variability of surface chlorophyll a concentration off the coast of Avacha Gulf in August – October, 2020 (*c*); SST for 10.28.2020 (*d*); distribution of chlorophyll a concentration on the ocean surface on 08.15.2020 (*e*) and 10.15.2020 (*f*)

Conclusion

1. During 1982–2023, extreme marine heat wave phenomena developed and intensified amid positive sea surface temperature trends. Throughout the first 20-year period (1982–2002), the linear trends in interannual changes of SST and various MHW indicators were small and statistically insignificant. In the second phase (2003–2023), these characteristics demonstrated significant positive interannual trends, confirming the steady intensification of MHW phenomena in terms of event frequency, duration, intensity, and integral indices, highlighting significant regional differences in these indicators over the past few decades.

2. The number of MHW events increased from 213 in 1987 to 19.7 thousand in 2018, corresponding to a significant trend of 3.5 thousand events per decade. On average, ~ 6.5 thousand such events occurred per year in the region, with peaks coinciding with El Niño phases. The maximum number of MHW events on individual days corresponded to a short duration (5–10 days per year). The mean event frequency was 3.4 per year, and the mean event duration was 16 days. In 2003–2023, the highest values of various MHW indicators were recorded in the narrow coastal zone of northeastern Kamchatka and its adjacent waters.

3. Statistically significant correlations were identified between the fluctuations of various MHW indicators and the changes in the characteristics of surface air temperature anomalies, geopotential height of the 500 mb isobaric surface, as well as climate indices (*AMO, NINO.WEST, NPGO* and *IPO*), indicating the influence of air temperature field anomalies and large-scale atmospheric processes on MHW development.

4. During the HAB outbreak off the Kamchatka coast, wind-driven upwelling intensified in the coastal zone, promoting the supply of nutrients and dinoflagellates to the photic layer. The conducted research supports the hypotheses that upwelling played an important causal role in the chain of events that led to the ecological disaster in the study region in fall 2020.

REFERENCES

1. WMO, 2024. *State of the Global Climate 2023*. World Meteorological Organization. WMO-No. 1347. WMO, 48 p.
2. Hobday, A.J., Alexander, L.V., Perkins, S.E., Smale, D.A., Straub, S.C., Oliver, E.C.J., Benthuysen, J.A., Burrows, M.T., Donat, M.G. [et al.], 2016. A Hierarchical Approach to Defining Marine Heatwaves. *Progress in Oceanography*, 141, pp. 227-238. https://doi.org/10.1016/j.pocean.2015.12.014
3. Oliver, E.C.J., Benthuysen, J.A., Darmaraki, S., Donat, M.G., Hobday, A.J., Holbrook, N.J., Schlegel, R.W. and Sen Gupta, A., 2021. Marine Heatwaves. *Annual Review of Marine Science*, 13(1), pp. 313-342. https://doi.org/10.1146/annurev-marine-032720-095144
4. Vogt, L., Burger, F.A., Griffies, S.M. and Frölicher, T.L., 2022. Local Drivers of Marine Heatwaves: A Global Analysis with an Earth System Model. *Frontiers in Climate*, 4, 847995. https://doi.org/10.3389/fclim.2022.847995
5. Yao, Y., Wang, C. and Fu, Y., 2022. Global Marine Heatwaves and Cold-Spells in Present Climate to Future Projections. *Earth's Future*, 10(11), e2022EF002787. https://doi.org/10.1029/2022EF002787

6. He, Y., Shu, Q., Wang, Q., Song, Z., Zhang, M., Wang, S., Zhang L., Bi, H., Pan, R. and Qiao F., 2024. Arctic Amplification of Marine Heatwaves under Global Warming. *Nature Communication*, 15(1), 8265. https://doi.org/10.1038/s41467-024-52760-1

7. Joyce, P.W.S., Tong, C.B., Yip, Y.L. and Falkenberg, L.J., 2024. Marine Heatwaves as Drivers of Biological and Ecological Change: Implications of Current Research Patterns and Future Opportunities. *Marine Biology*, 171(1), 20. https://doi.org/10.1007/s00227-023-04340-y

8. Bian, C., Jing, Z., Wang, H. and Wu, L., 2024. Scale-Dependent Drivers of Marine Heatwaves Globally. *Geophysical Research Letters*, 51(3), e2023GL107306. https://doi.org/10.1029/2023gl107306

9. Le Grix, N., Zscheischler, J., Rodgers, K.B., Yamaguchi, R. and Frölicher, T.L., 2022. Hotspots and Drivers of Compound Marine Heatwaves and Low Net Primary Production Extremes. *Biogeosciences*, 19(24), pp. 5807-5835. https://doi.org/10.5194/bg-19-5807-2022

10. Frölicher, T.L. and Laufkötter, C., 2018. Emerging Risks from Marine Heat Waves. *Nature Communications*, 9(1), 650. https://doi.org/10.1038/s41467-018-03163-6

11. Anderson, D.M., Fensin, E., Gobler, C.J., Hoeglund, A.E., Hubbard, K.A., Kulis, D.M., Landsberg, J.H., Lefebvre, K.A., Provoost, P. [et al.], 2021. Marine Harmful Algal Blooms (HABs) in the United States: History, Current Status and Future Trends. *Harmful Algae*, 102, 101975. https://doi.org/10.1016/j.hal.2021.101975

12. Falkowski, P.G. and Oliver, M.G., 2007. Mix and Match: How Climate Selects Phytoplankton. *Nature Reviews: Microbiology*, 5(10), pp. 813-819. https://doi.org/10.1038/nrmicro1751

13. Krishnapriya, M.S., Varikoden, H., Anjaneyan, P. and Kuttippurath, J., 2023. Marine Heatwaves during the Pre-Monsoon Season and Their Impact on Chlorophyll-a in the North Indian Ocean in 1982–2021. *Marine Pollution Bulletin*, 197, 115783. https://doi.org/10.1016/j.marpolbul.2023.115783

14. Noh, K.M., Lim, H.-G. and Kug, J.-S., 2022. Global Chlorophyll Responses to Marine Heatwaves in Satellite Ocean Color. *Environmental Research Letters*, 17(6), 064034. https://doi.org/10.1088/1748-9326/ac70ec

15. Kuroda, H., Azumaya, T., Setou, T. and Hasegawa, N., 2021. Unprecedented Outbreak of Harmful Algae in Pacific Coastal Waters off Southeast Hokkaido, Japan, during Late Summer 2021 after Record-Breaking Marine Heatwaves. *Journal of Marine Science and Engineering*, 9(12), 1335. https://doi.org/10.3390/jmse9121335

16. Song, N.-Q., Wang, N., Lu, Y. and Zhang, J.-R., 2016. Temporal and Spatial Characteristics of Harmful Algal Blooms in the Bohai Sea during 1952–2014. *Continental Shelf Research*, 122, pp. 77-84. https://doi.org/10.1016/j.csr.2016.04.006

17. McCabe, R.M., Hickey, B.M., Kudela, R.M., Lefebvre, K.A., Adams, N.G., Bill, B.D., Gulland, F.M.D., Thomson, R.E., Cochlan, W.P. [et al.], 2016. An Unprecedented Coastwide Toxic Algal Bloom Linked to Anomalous Ocean Conditions. *Geophysical Research Letters*, 43(19), pp. 10366-10376. https://doi.org/10.1002/2016GL070023

18. Bondur, V., Zamshin, V., Chvertkova, O., Matrosova, E. and Khodaeva, V., 2021. Detection and Analysis of the Causes of Intensive Harmful Algal Bloom in Kamchatka Based on Satellite Data. *Journal of Marine Science and Engineering*, 9(10), 1092. https://doi.org/10.3390/jmse9101092

19. Orlova, T.Y., Aleksanin, A.I., Lepskaya, E.V., Efimova, K.V., Selina, M.S., Morozova, T.V., Stonik, I.V., Kachur, V.A., Karpenko, A.A. [et al.], 2022. A Massive Bloom of Karenia Species (Dinophyceae) off the Kamchatka Coast, Russia, in the Fall of 2020. *Harmful Algae*, 120(2), 102337. https://doi.org/10.1016/j.hal.2022.102337

20. Kuroda, H., Taniuchi, Y., Watanabe, T., Azumaya, T. and Hasegawa, N., 2022. Distribution of Harmful Algae (Karenia spp.) in October 2021 off Southeast Hokkaido, Japan. *Frontiers in Marine Science*, 9, 841364. https://doi.org/10.3389/fmars.2022.841364

21. Tskhay, Zh.R. and Shevchenko, G.V., 2022. Distribution Features of Chlorophyll a Concentration off the East Coast of Kamchatka in Autumn 2020 from Satellite Data. *Sovremennyye Problemy Distantsionnogo Zondirovaniya Zemli iz Kosmosa*, 19(1), pp. 226-238. https://doi.org/10.21046/2070-7401-2022-19-1-226-238 (in Russian).

22. Hobday, A.J., Oliver, E.C.J., Sen Gupta, A., Benthuysen, J.A., Burrows, M.T., Donat, M.G., Holbrook, N.J., Moore, P.J., Thomsen, M.S. [et al.], 2018. Categorizing and Naming Marine Heatwaves. *Oceanography*, 31(2), pp. 162-173. https://doi.org/10.5670/oceanog.2018.205

23. Spillman, C.M., Smith, G.A., Hobday, A.J. and Hartog, J.R., 2021. Onset and Decline Rates of Marine Heatwaves: Global Trends, Seasonal Forecasts and Marine Management. *Frontiers in Climate*, 3, 801217. https://doi.org/10.3389/fclim.2021.801217

24. Lim, Y.K., Park, B.S., Kim, J.H., Baek, S.-S. and Baek, S.H., 2021. Effect of Marine Heatwaves on Bloom Formation of the Harmful Dinoflagellate Cochlodinium Polykrikoides: Two Sides of the Same Coin? *Harmful Algae*, 104, 102029. https://doi.org/10.1016/j.hal.2021.102029

25. Yao, Y., Wang, J., Yin, J. and Zou, X., 2020. Marine Heatwaves in China's Marginal Seas and Adjacent Offshore Waters: Past, Present, and Future. *Journal of Geophysical Research: Oceans*, 125(3), e2019JC015801. https://doi.org/10.1029/2019JC015801

26. Rostov, I.D., Dmitrieva, E.V. and Rudykh, N.I., 2023. Interannual Variability of Thermal Characteristics of the Upper 1000-meter Layer in the Extratropical Zone of the Northwestern Part of the Pacific Ocean at the Turn of the XX–XXI Centuries. *Physical Oceanography*, 30(2), pp. 141-159. https://doi.org/10.29039/1573-160X-2023-2-141-159

27. Rostov, I.D., Dmitrieva, E.V. and Vorontsov, A.A., 2018 Tendencies of Climate Changes for Thermal Conditions in the Coastal Waters of the Western Bering Sea and Adjacent Areas in the Last Decades. *Izvestiya TINRO*, 193(2), pp. 167-182. https://doi.org/10.26428/1606-9919-2018-193-167-182 (in Russian).

28. Zhao, Z. and Marin, M., 2019. A MATLAB Toolbox to Detect and Analyze Marine Heatwaves. The *Journal of Open Source Software*, 4(33), 1124. https://doi.org/10.21105/joss.01124

29. Rostov, I.D., Dmitrieva, E.V. and Rudykh, N.I., 2023. Changes in the Thermal Condition Trends in the Tropical Zone of the Pacific Ocean in 1982–2021. *Oceanology*, 63(6), pp. 755-768. https://doi.org/10.1134/S0001437023060127

30. Bakun, A., 1990. Global Climate Change and Intensification of Coastal Ocean Upwelling. *Science*, 247(4939), pp. 198-201. https://doi.org/10.1126/science.247.4939.198

31. Gonzalez-Nuevo, G., Gago, J. and Cabanas, J.M., 2014. Upwelling Index: A Powerful Tool for Marine Research in the NW Iberian Upwelling System. *Journal of Operational Oceanography*, 7(1), pp. 47-57. https://doi.org/10.1080/1755876x.2014.11020152

32. Large, W.G. and Pond, S., 1981. Open Ocean Momentum Flux Measurements in Moderate to Strong Winds. *Journal of Physical Oceanography*, 11(3), pp. 324-336. https://doi.org/10.1175/1520-0485(1981)011<0324:OOMFMI>2.0.CO;2

33. Cheng, Y., Zhang, M., Song, Z., Wang, G., Zhao, C., Shu, Q., Zhang, Y. and Qiao, F., 2023. A Quantitative Analysis of Marine Heatwaves in Response to Rising Sea Surface Temperature. *Science of The Total Environment*, 881, 163396. https://doi.org/10.1016/j.scitotenv.2023.163396

34. Carvalho, K.S., Smith, T.E. and Wang, S., 2021 Bering Sea Marine Heatwaves: Patterns, Trends and Connections with the Arctic. *Journal of Hydrology*, 600, 126462. https://doi.org/10.1016/j.jhydrol.2021.126462

Submitted 09.12.2024; approved after review 15.01.2025;
accepted for publication 15.05.2025.

About the authors:

Igor D. Rostov, Leading Researcher, Laboratory of Informatics and Ocean Monitoring, V.I. Il'ichev Pacific Oceanological Institute, Far Eastern Branch of Russian Academy of Sciences

(43 Baltiyskaya Str., Vladivostok, 690041, Russian Federation), CSc. (Geogr.), **ORCID ID: 0000-0001-5081-7279**, **Scopus Author ID: 6603588318**, **SPIN-code: 2329-0391**, rostov@poi.dvo.ru

Elena V. Dmitrieva, Senior Researcher, Laboratory of Informatics and Ocean Monitoring, V.I. Il'ichev Pacific Oceanological Institute, Far Eastern Branch of Russian Academy of Sciences (43 Baltiyskaya Str., Vladivostok, 690041, Russian Federation), CSc. (Tech.), **ORCID ID: 0000-0002-0094-5296**, **Scopus Author ID: 36788322900**, **SPIN-code: 6818-1898**, e_dmitrieva@ poi.dvo.ru

Igor A. Zhabin, Leading Researcher, Laboratory of Hydrological Processes and Climate, V.I. Il'ichev Pacific Oceanological Institute, Far Eastern Branch of Russian Academy of Sciences (43 Baltiyskaya Str., Vladivostok, 690041, Russian Federation), CSc. (Geogr.), **ORCID ID: 0000-0002-0294-7156**, **Scopus Author ID: 6701652344**, **SPIN-code: 5881-2713**, zhabin@ poi.dvo.ru

Contribution of the co-authors:

Igor D. Rostov – development of the article structure, processing and analysis of the data, writing the article text

Elena V. Dmitrieva – collection and processing of oceanographic data, calculations, drawing design, text editing

Igor A. Zhabin – upwelling problem statement and data analysis

The authors have read and approved the final manuscript.
The authors declare that they have no conflict of interest.

ISSN 1573-160X, *PHYSICAL OCEANOGRAPHY*, Vol. 32, Iss. 4, pp. 464-478 (2025)

published in *Morskoy Gidrofizicheskiy Zhurnal*, 2025, Vol. 41, Iss. 4, pp. 436-452

Original article

Features of Forming the Water Abnormal Thermal Regimes in the Kuril-Kamchatka Region

V. V. Moroz [1, ✉], T. A. Shatilina [2], N. I. Rudykh [1]

[1] *V. I. Il'yichev Pacific Oceanological Institute, Far Eastern Branch of Russian Academy of Sciences, Vladivostok, Russian Federation*
[2] *Russian Federal Research Institute of Fisheries and Oceanography, Pacific Branch of VNIRO (TINRO), Vladivostok, Russian Federation*
✉ *moroz@poi.dvo.ru*

Abstract

Purpose. The study aims to identify the cause-and-effect relations and mechanisms forming the water abnormal thermal regimes in the western and eastern water areas off the Kamchatka Peninsula as well as in the northern straits of the Kuril Ridge with regard to the influence of regional atmospheric processes during the warm season over the past four decades.

Methods and Results. Data from long-term observations performed at the coastal hydrometeorological stations (Hydrometeorological Centre of Russia) and NCEP/NCAR reanalysis data for the adjacent water areas permitted to study the interannual variability of thermal conditions in the region adjacent to Kamchatka in June–September period in 1980–2022. Cluster and correlation analysis were used to assess the variability of water and atmospheric circulation temperature regimes. An increase in extreme positive monthly mean values of surface water temperature has been revealed for the past two decades. The cause-and-effect relations between the anomalous changes in atmospheric field structure, their impact on water areas and the formation of abnormal thermal conditions were demonstrated.

Conclusions. Formation of the water abnormal thermal conditions in the Kamchatka Peninsula coastal regions and in the adjacent northern Kuril Ridge region is related to the intensity variability in development of such centres of atmospheric impact as the Okhotsk and Hawaiian Highs, the changes in their positions (including the spread of the North Pacific branch of the Hawaiian maximum to the northwest) and the local influence.

Keywords: Kamchatka Peninsula, northern Kuril Straits, hydrological conditions, temperature anomalies, atmospheric circulation

Acknowledgments: The study was carried out within the framework of state assignment of POI FEB, RAS on theme No. 124022100079-4, within the framework of Comprehensive Interdepartmental Program "Ecological Safety of Kamchatka: Study and Monitoring of Hazardous Natural Phenomena and Human Impacts" (NIOKTR 122012700198-9). The authors are thankful to the software developers for the opportunity of using the data posted on the websites of Global Meteorological Network, JMA and NOAA as well as to the reviewer for his useful remarks.

For citation: Moroz, V.V., Shatilina, T.A. and Rudykh, N.I., 2025. Features of Forming the Water Abnormal Thermal Regimes in the Kuril-Kamchatka Region. *Physical Oceanography*, 32(4), pp. 464-478.

Introduction

The study region, encompassing waters off the southeastern and southwestern coasts of the Kamchatka Peninsula and the northern part of the Kuril Ridge (Fig. 1), is an economically significant area in eastern Russia.

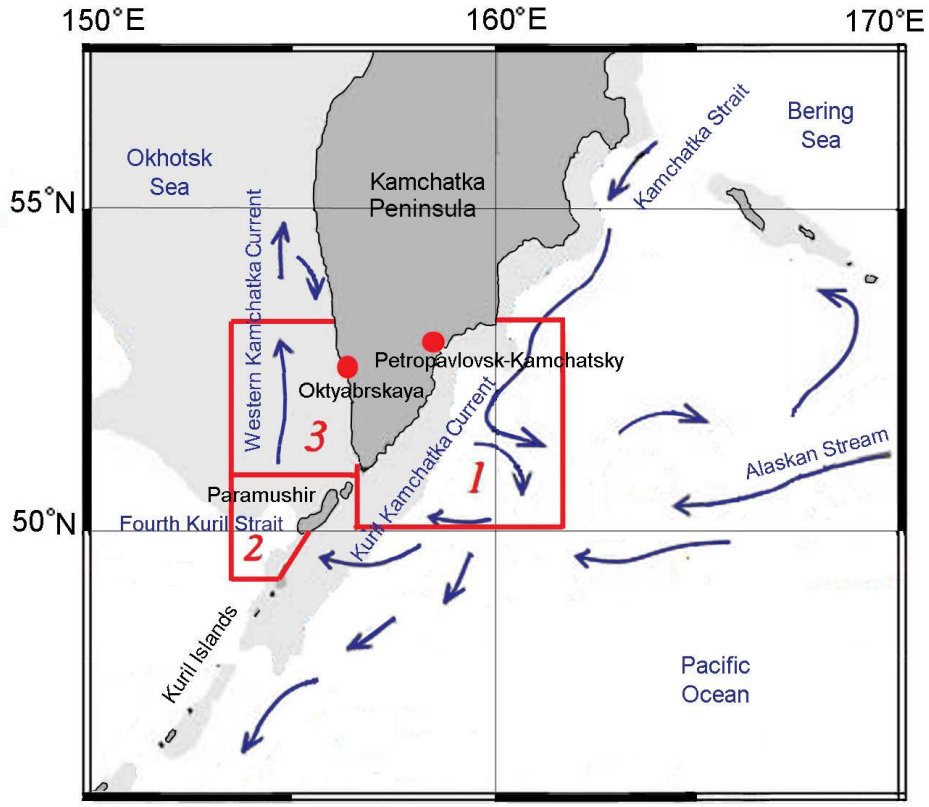

F i g. 1. Region under study: *1* – Kamchatka eastern coast, *2* – northern Kuril, *3* – Kamchatka western coast (points denote hydrometeorological stations)

Amid ongoing global warming and the increasing frequency of extreme hydrometeorological events [1–4], concerns arise regarding the impact of changing temperature conditions on biological resources and fisheries in the waters of the Russian Far East. The response of aquatic organisms to optimal temperatures and food availability increases the migratory activity of commercially important species, resulting in shifts in fishing areas and complicating fisheries forecasting [5]. Therefore, studying the factors driving variability in thermal conditions, particularly the formation of anomalous thermal conditions that impact ecosystem productivity, is increasingly important.

It is well-established that the hydrological conditions of the study area are influenced by various water masses, including the Pacific waters from the Kuril-Kamchatka Current, transformed in the northern straits of the Kuril Ridge, and the Okhotsk Sea waters, as well as variability in water exchange through the ridge

straits and the interaction of island and coastal currents [6, 7]. Key factors influencing temperature variability across the region and its water areas include variations in synoptic processes, climatic patterns, and monsoon-driven atmospheric processes with seasonal wind shifts.

Recent studies indicate that several areas of the Far Eastern seas have demonstrated correlations between variations in the thermal regime and changes in the intensity (pressure variability) and positions of regional atmospheric action centres (AACs) as well as changes in their local impact on water areas [8, 9]. Studies have identified differences in pressure field formation during years with anomalous thermal regimes and proposed methods for detecting and characterizing precursor pressure structures that drive extreme thermal conditions of waters impacting fishing conditions [10]. Concurrently, studies on climatic trends in thermal conditions of coastal water areas have revealed a complex response of the underlying surface to atmospheric circulation impacts [11]. As previously noted, to solve the problem of fishery forecasting for specific water areas has still been relevant and associated with regional peculiarities in the formation of anomalous thermal conditions [5, 8, 9].

This study is purposed at determining the cause-and-effect relations in the mechanisms of forming anomalous thermal conditions in specific zones of the Kuril-Kamchatka region caused by atmospheric processes.

In this study, the following tasks were addressed:

– analysis of interannual variability in the thermal regime of waters at hydrometeorological stations (HMSs) and adjacent areas, assessment of trend variability, and identification of years with anomalous thermal conditions in June – September for each region;

– investigation of interannual variability in the intensity (pressure variability) and position of seasonal AACs;

– evaluation of the role of seasonal AACs in the mechanisms underlying the formation of anomalous thermal regimes in water areas, taking into account hydrological conditions in each region.

Data and methods

Long-term variability of thermal conditions in the coastal waters of Kamchatka was investigated using water temperature data from the Unified System of Information on the World Ocean (ESIMO) (available at: http://portal.esimo.ru/portal/), the All-Russian Research Institute of Hydrometeorological Information – World Data Center (VNIIGMI-MCD) (available at: http://meteo.ru) and Roshydromet HMS data for 1980–2022.

Sea surface temperature data for 1980–2022 at grid nodes of 0.25° × 0.25° from the website http://ds.data.jma.go.jp/gmd/goos/data/rrtdb/jma-pro/cobe_sst_glb_M.html and the NOAA ERDDAP internet resource (available at: https://coastwatch.pfeg.noaa.gov/erddap/griddap/) were analyzed to study the thermal conditions of adjacent water areas. The *ODV* program was applied for data processing and visualization [1].

[1] Schlitzer, R. *Ocean Data View*. [online] Available at: https://odv.awi.de [Accessed: 17 June 2025].

Atmospheric circulation over the second natural synoptic region (2nd N. S. R.) was analyzed using reanalysis archives (NCEP/NCAR Reanalysis Monthly Means and Other Derived Variables [2]) of surface atmospheric pressure P_o and geopotential H_{500} at grid nodes of 2.5° × 2.5° for 1980–2022. Data on the intensity of the Okhotsk High (OH) were obtained from the Pacific Branch of the Russian Federal Research Institute of Fisheries and Oceanography (TINRO) (available at: https://tinro.vniro.ru). Anomalies (deviations of monthly average pressure values from long-term averages) were used to assess changes in the intensity of AACs. Surface pressure P_o and geopotential H_{500} maps for 2000–2022 compiled by the Japan Meteorological Agency (JMA) were used to analyze pressure fields. Correlation analysis was applied to evaluate the relations between the variability of thermal conditions and the intensity of AACs.

Monthly average anomalies of all parameters used in the study were calculated relative to the climatic norm for the period 1991–2020.

Results and discussion

Formation and variability of the thermal regime of waters

Area 1 — Eastern Pacific Coast of Kamchatka (Fig. 1). The formation of temperature characteristics of waters in this area is determined by the effect of waters of various origins. From the north, cold Bering Sea waters flow southward through the Kamchatka Strait with the Kamchatka Current, while a warmer branch of the Alaska Current influences the region from the east. During the warm season, the Kamchatka and Alaska Currents are characterized by the formation of predominantly anticyclonic eddies, which exhibit distinct thermohaline characteristics and contribute to the formation of the water area thermal regime [7, 12]. The thermal conditions of the area are highly variable, as evidenced by their interannual course (Fig. 2, *a*).

Area 2 – Northern Kuril. The straits among the northern Kuril Islands are narrow and shallow. However, active sea–ocean water exchange occurs through the relatively wide and deep (over 500 m) Fourth Kuril Strait. A bidirectional current pattern is observed in the strait [7]. From the Pacific Ocean side, the strait is influenced by the waters of the Kuril Kamchatka Current propagating from the north. The inflow of the Pacific waters into the northern part of the strait is confirmed by oceanographic observations from Argo floats. Some floats from the Pacific Ocean enter the Okhotsk Sea through the strait [12, 13]. Cold Okhotsk Sea waters enter the southern part of the strait. The dynamics of waters in the strait and the adjacent water area determine the formation of thermal conditions. As in the previous area, thermal conditions here demonstrate significant interannual variability (Fig. 2, *b*).

Area 3 – Western Okhotsk Sea Coast of Kamchatka. According to water circulation in this area, the Pacific waters entering through the northern straits spread northward with the West Kamchatka Current along the southwestern coast

[2] APDRC. *NCEP/NCAR Reanalysis, Monthly*. [online] Available at: https://apdrc.soest.hawaii.edu/datadoc/ncep_mon.php [Accessed: 17 June 2025].

of the Kamchatka Peninsula [14]. Thus, the thermal conditions of the water area off the southwestern coast (including HMS Oktyabrskaya) are also formed under effect of waters of various origins: partly the Kuril Kamchatka Current, the Okhotsk Sea waters and waters transformed by tidal mixing in the strait (Fig. 2, *c*).

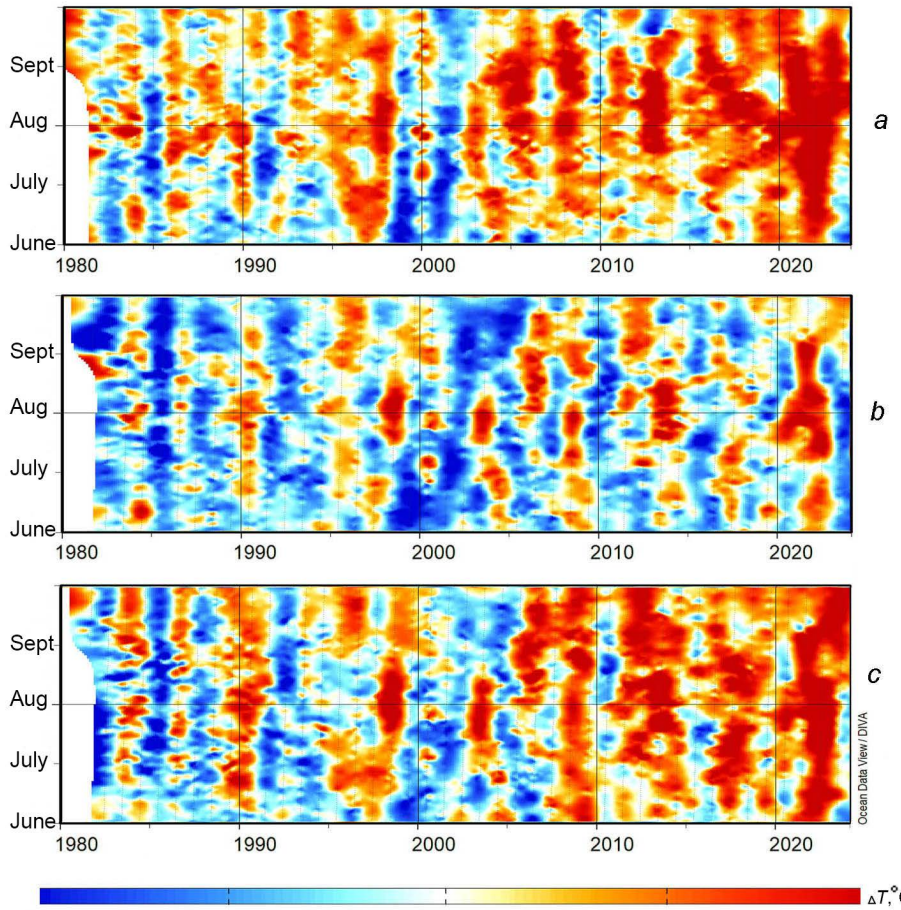

F i g. 2. Interannual variability of water temperature anomalies in June – September in the areas: *1* – Kamchatka eastern coast (*a*), *2* – northern Kuril (*b*) and *3* – Kamchatka western coast (*c*)

The variability in the development of current system components largely determines the redistribution of incoming heat and cold, shaping the long-term variability of the temperature background in each area.

The course of long-term changes in the thermal regime of waters (Fig. 2) indicates a warming trend in the study area as a whole over the past four decades, which is confirmed by previous studies [1]. According to the assessments of temperature condition variability, positive trends were found in each subarea for the period 1980–2022. Significant trends in July and August were observed in the eastern and western water areas (areas *1* and *3*) (Table 1).

Table 1

Linear trend coefficients for water temperature time series for June – September in 1980–2000, 2001–2022 and 1980–2022

Period	Area *1*	HMS Petropavlovsk	Area *2*	Area *3*	HMS Oktyabrskaya
			June		
1980–2022	0.02	0.02	0.01	0.03	0
1980–2000	0.01	−0.03	−0.02	0.02	0.03
2001–2022	**0.06**	**–0.06**	**0.06**	**0.09**	−0.01
			July		
1980–2022	**0.04**	**0.05**	0.03	**0.04**	0.02
1980–2000	−0.01	−0.03	0.02	−0.03	**0.08**
2001–2022	**0.11**	**0.05**	**0.08**	**0.09**	0.03
			August		
1980–2022	**0.05**	**0.06**	0.02	**0.05**	0.02
1980–2000	**0.05**	−0.04	0.04	**0.09**	**0.08**
2001–2022	**0.07**	0.03	0.04	**0.07**	0.02
			September		
1980–2022	0.03	0.04	0.03	0.03	0
1980–2000	**0.05**	**0.08**	0.01	**0.05**	0.03
2001–2022	**0.05**	0.04	0.04	**0.05**	−0.01

N o t e. Statistically significant (95%) estimates are highlighted in bold.

Furthermore, statistical estimates reveal differences in thermal variability between two twenty-year phases of the study period. For the 1980–2000 phase, trends in June – July were mostly insignificant and negative in all three areas, reflecting high frequency of cold thermal regimes during this period and indicating a relatively well-developed first stage of the Far Eastern summer monsoon and the OH effect [8, 9]. In contrast, for the second twenty-year period (2001–2022), significant positive trends indicate a weakening of the first cold stage of the monsoon and predominantly early formation of warm thermal regimes, characteristic of the second monsoon stage in July – August, occasionally September, influenced by the Hawaiian High (HH). However, no significant positive trends are observed in August–September in the northern Kuril zone (area *2*). Apparently, vertical tidal mixing in the ridge straits [7] "masks" the inflow of warmer waters with the branch of the Kuril Kamchatka Current.

The dynamics of anomalies at the HMSs reflect the long-term thermal variability off the eastern and western coasts of the Kamchatka waters. In the Pacific water area off the eastern coast of Kamchatka in Avacha Bay (HMS Petropavlovsk-Kamchatsky) and in the Okhotsk Sea water area off the western coast (HMS Oktyabrskaya), thermal conditions also vary significantly during the two twenty-year phases of the study period. Negative extremes of thermal regimes predominate in 1980–2000 contrasting with the positive anomalies observed in the following twenty years (Fig. 3).

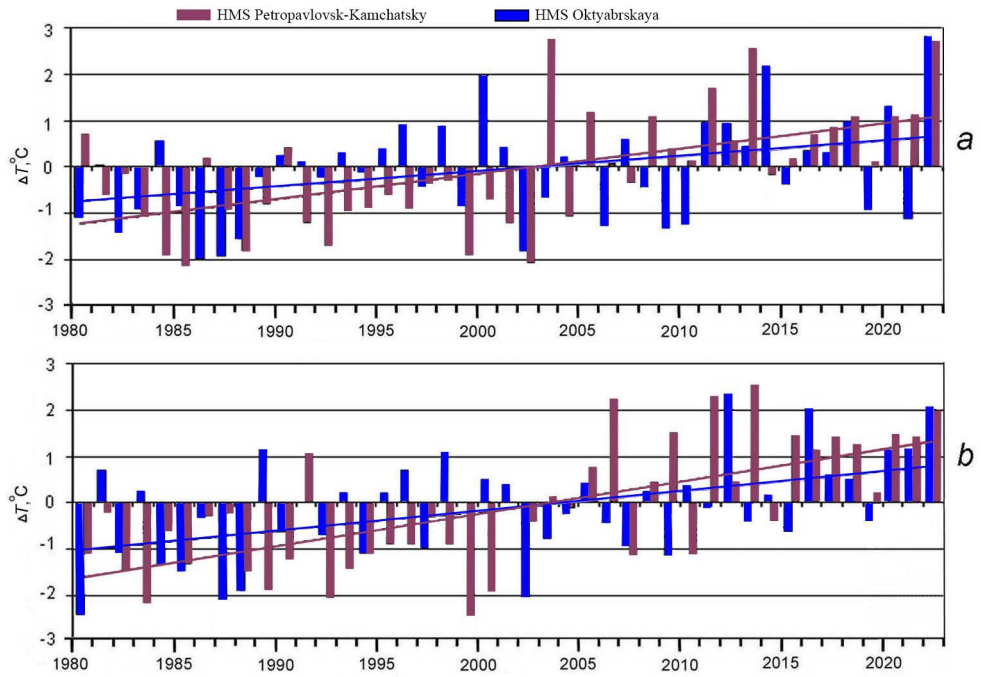

F i g. 3. Interannual variability of water temperature anomalies in July (*a*) and August (*b*) and corresponding linear trends

Analysis of long-term variability of thermal conditions in the eastern (HMS Petropavlovsk-Kamchatsky) and western (HMS Oktyabrskaya) coastal areas of Kamchatka shows significant fluctuations in water temperature anomalies. In accordance with the assessment of interannual variability of thermal regimes at the HMSs off the western and eastern coasts of Kamchatka in June – September over the entire study period (1980–2022) performed using cluster analysis (K-means method), years with extreme thermal regimes were revealed. The study identified thermally homogeneous year groups categorized as follows: years with near-normal conditions demonstrating temperature anomalies with absolute values below 1.0°C, cold and warm regime years showing anomalies ranging between 1.0–1.5°C, extremely cold and warm thermal regimes defined by anomalies exceeding 1.5°C in absolute value (Table 2).

As shown in Table 2, the water areas adjacent to both western and eastern Kamchatka coasts are characterized by the formation of anomalously cold thermal regimes during 1980–1999. The period 2000–2022 marks a transition toward years with anomalously warm thermal regimes, with this trend becoming particularly pronounced during July – September of the most recent five-year period. The maximum temperature anomalies (reaching up to 3°C) were recorded at HMSs and adjacent water areas in July 2022 (Figs. 2, 3).

The thermal state and hydrodynamics of the sea surface are largely determined by surface wind conditions including direction and intensity of air mass transport. In turn, they are associated with the variability of atmospheric circulation and its local impact [2, 8, 9].

Table 2

Years with anomalous thermal regimes at HMSs during 1980–2022

HMS	Thermal regime	
	cold	warm
June		
Petropavlovsk	1985, 1994, 1999, 2000, 2001, 2018	2003, 2009, 2013, 2014
Oktyabrskaya	1980, 1985, 2017	–
July		
Petropavlovsk	1984, 1985, 1988, 1992, 1999, 2002	2003, 2011, 2013, 2022
Oktyabrskaya	1986, 1987, 1988, 2002	2000, 2014, 2022
August		
Petropavlovsk	1983, 1988, 1989, 1992, 1999, 2000	2006, 2009, 2011, 2013, 2022
Oktyabrskaya	1980, 1985, 1987, 1988, 2002	2012, 2016, 2022
September		
Petropavlovsk	1999, 2001, 2012	2008, 2014, 2015, 2020, 2021
Oktyabrskaya	1983, 2002	2006, 2020, 2022

To identify the mechanisms responsible for the formation of anomalous thermal conditions in specific years across the study area, we analyzed variability in regional atmospheric processes and their impact on the underlying sea waters.

Role of atmospheric circulation in the formation of anomalous thermal conditions in water areas

Atmospheric circulation and air mass transport in the Kamchatka region during the Far Eastern summer monsoon period characterized by winds of southern directions are mainly determined by such AACs as the OH forming over the Okhotsk Sea, the tropospheric depression (TD) in upper-level fields, and the HH from the Pacific Ocean side. In June–July, during the first stage of the Far Eastern summer monsoon, cold air masses, predominantly of Arctic origin, emerge over the Okhotsk Sea in the rear part of the TD. They can be observed on synoptic maps as small anticyclones that support the high-pressure area (OH) over the Okhotsk Sea. It was determined that under a developed OH, cold air masses generated reduced thermal background conditions in the underlying sea surface. Conversely, with intensification of the HH influence (characteristic of the monsoon second phase), a warming effect occurs forming positive thermal background conditions [8, 9].

Analysis of long-term surface pressure variability over the studied forty-year period reveals a steady trend toward increasing intensity of the HH (Fig. 4), while the OH is characterized by significant fluctuations. In the period 1980–2000, years with positive pressure anomalies (OH intensive development) predominated while the second phase was characterized by the formation of predominantly negative anomalies. The resulting negative trend indicates a weakening of this AAC.

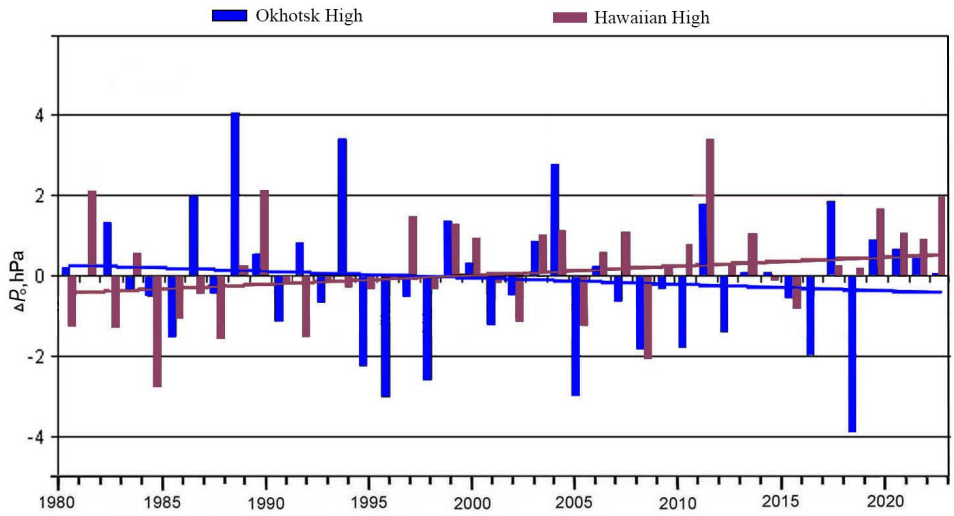

F i g. 4. Interannual variability of near-land pressure anomalies (ΔP_o) in July and corresponding linear trends

T a b l e 3

Correlation coefficients between the anomalies of water temperature and H_{500} geopotential over the Okhotsk Sea for June–September in 1980–2022, 1980–2000 and 2001–2022

HMS, Area	June	July	August	September
1980–2022				
Area *1*	0.23	**0.45**	0.28	0.26
Petropavlovsk	**0.54**	**0.47**	0.27	0.13
Area *2*	0.25	**0.49**	**0.32**	0.23
Area *3*	0.16	**0.44**	**0.39**	0.28
Oktyabrskaya	**0.32**	0.13	0.14	−0.14
1980–2000				
Area *1*	0.36	0.29	0.21	0.11
Petropavlovsk	**0.59**	0.13	0.06	0.10
Area *2*	0.30	**0.50**	0.06	0.21
Area *3*	**0.47**	**0.43**	0.15	0.26
Oktyabrskaya	0.37	0.12	−0.17	−0.09
2001–2022				
Area *1*	0.08	**0.48**	0.22	0.37
Petropavlovsk	**0.60**	**0.53**	0.30	0.14
Area *2*	0.20	**0.48**	**0.43**	0.24
Area *3*	−0.06	0.32	**0.46**	0.28
Oktyabrskaya	0.27	0.15	0.34	−0.19

N o t e. Statistically significant (95%) estimates are highlighted in bold.

Correlation analysis between water temperature anomalies and pressure anomalies over the Okhotsk Sea showed a significant correlation (June – July period) between water temperature anomalies and H_{500} geopotential anomalies, characterizing the development of the TD (Table 3). Maximum correlation coefficients (~ 0.6) were observed in June at the HMS Petropavlovsk-Kamchatsky. High correlation coefficients (~ 0.4–0.5) were also noted in July in almost all studied water areas.

Concurrently, correlation analysis of water temperature anomalies with pressure anomalies in the HH showed low correlation and no significant relations. However, ambiguous relation between thermal regimes and pressure variability in regional AACs was previously identified: along with the intensity of development, the variability in the positions of such atmospheric pressure formations and their corresponding local impact play an important role [8, 9]. This can be one of the causes for low correlation between the occurrence of temperature extremes in water areas and intensity of development of such a large-scale pressure formation as the HH.

The study of pressure patterns during years with anomalous cold or warm thermal conditions in the investigated water areas corroborates prior findings from other regions of the Far Eastern seas [9]. These results confirm distinct differences in both structure of pressure fields and positioning of AACs during such years. Consequently, this leads to varying localized impacts and fundamentally different mechanisms governing the formation of thermal water regimes.

As noted above, in the study period 1980–2000, anomalously cold temperature conditions were formed in certain years in the Kamchatka coastal water areas (see Table 2). A characteristic example is the structure of pressure fields in July 1988 (Fig. 5, *a*). In the near-land pressure field, a developed OH localized over the northeastern water area of the Okhotsk Sea is observed. In the mid-troposphere, the 500-mbar geopotential height (AT_{500}) map reveals a cold trough positioned over the Kamchatka Peninsula and extending toward the Kuril Islands. The trough delta features an extreme geopotential height (H_{500}) minimum where descending air currents accumulate cold air near the surface creating conditions for extreme cold thermal anomalies. Such a structure of atmospheric fields contributes to the transport of cold air masses from the north and northwest over the entire study area. The temperature background of the underlying surface decreases. Negative temperature anomalies in July 1988 in the eastern and western Kamchatka coastal water areas were ~ −2°C (see Fig. 3). Under dynamic wind impact from the north and northwest, the Kuril Kamchatka Current intensifies, increasing the inflow of the cold Bering Sea and Pacific waters into the northern Kuril area [15–17], which collectively contributes to the formation of an anomalously cold thermal regime in the studied water area.

The mechanism of forming anomalously warm thermal regimes in the entire water area (characteristic of the second phase of the study period) is due to the absence of cold depressions over the Okhotsk Sea and Kamchatka. An example

is 2022, the year with extremely warm thermal regime (see Figs. 2, 3). Differences in the structure of pressure fields in 1988 and 2022 should be noted. In 2022, zonality of isohypses in the H_{500} field is evident, reflecting the westerly transport of air masses (Fig. 5, *b*). The HH ridge, at the vertex of which a zone of increased H_{500} geopotential is observed, spreads over the entire study area. As the North Pacific branch of the HH stretched northwestward, it generated a surface-level center of extreme positive air temperature anomalies over the region, accompanied by record warm water temperatures throughout the areas. Such a structure of atmospheric fields with significant northwestward spread (into the Okhotsk Sea water area) of the HH North Pacific branch, transport of warm air masses along its western periphery and formation of anomalously warm thermal regimes in the Kamchatka coastal water areas is characteristic of the last five years. Easterly and southeasterly winds, weakening the Kuril-Kamchatka Current, contribute to the westward inflow of warmer waters with eddies of the Alaska Current extension, which also influences the thermal regime of waters in this area [12, 13].

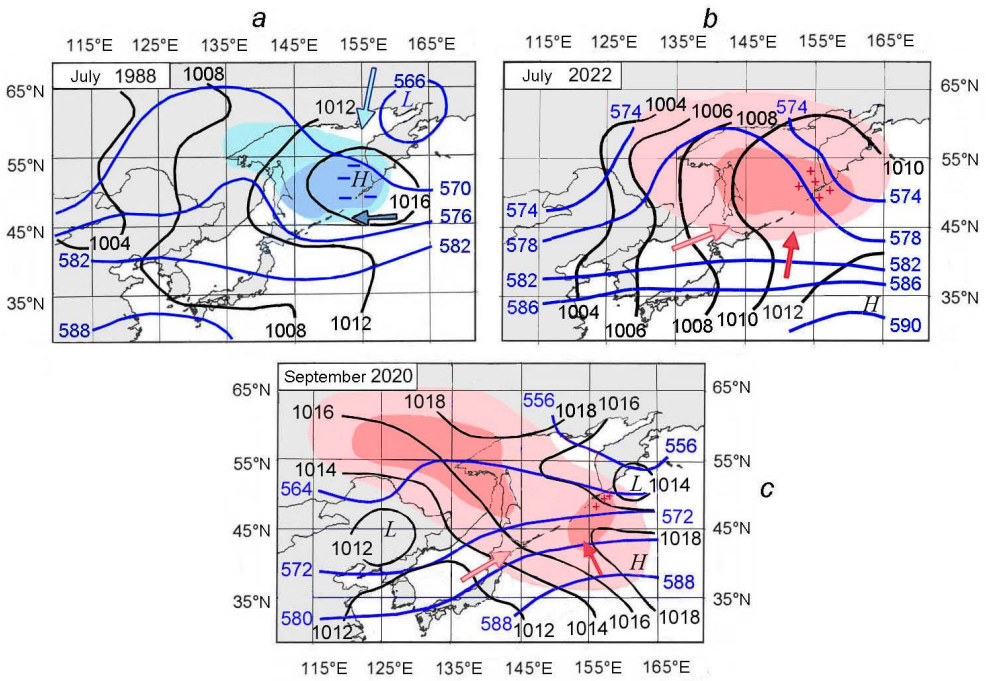

F i g. 5. Structures of the fields of near-surface pressure P_o, hPa (black isobars) and geopotential H_{500}, hPa (blue isohypses) in the years of forming the negative (*a*) and positive (*b*, *c*) anomalies in thermal regimes. *H* is high pressure, *L* is low pressure; "–" and "+" are negative and positive water temperature anomalies, respectively; centres of negative and positive anomalies of the H_{500} geopotential are shown in blue and pink, respectively; centres of anomalously low and high air temperature – in blue and red; arrows indicate the movement of cold and warm air masses (blue and pink – in the mid troposphere, blue and red – in the near-land layer, respectively)

As discussed, thermal anomalies in the coastal waters, which influence the ecosystem productivity, are critical to their functioning. Anomalously warm thermal regimes can be associated with the formation of anomalous hydrological conditions that affect ecosystems and hydrobionts negatively, as observed in September and October 2020 [18]. Fig. 5, *c* shows the structures of atmospheric fields in September 2020. Against the background of the formed anomalously warm thermal regime of waters (increase in positive temperature anomalies up to 1.5°C), cyclones passed off the southeastern coast of Kamchatka causing changes in the structure of the surface pressure field. Such changes led to a local shift in wind direction near the coast from southeasterly to northeasterly and northerly. The passage of cyclones apparently contributed to the formation of upwelling and, as noted in [19], the influx of nutrients from deeper layers, causing blooms of toxic microalgae under favorable anomalously warm temperature conditions in the surface photic layer. The spread of such microalgae blooms along the coast according to water circulation and further toward the northern Kuril straits resulted in adverse effects on the ecosystem of a significant part of the water area.

These studies highlight the importance of considering surface pressure variability, positions of AACs and corresponding local impacts when analyzing the formation of the anomalous thermal conditions.

Analysis of regional atmospheric variability and its impact on the underlying water area revealed cause-and-effect relations. The formation of anomalous thermal conditions is associated with regional atmospheric circulation patterns, including anomalous changes in the development and positions of seasonal AACs and their local effects on thermal conditions.

Conclusion

Analysis of long-term variability of temperature conditions in the studied water areas in June – September for the period 1980–2022 revealed positive trends, with statistically significant increases in July and August.

Differences in the variability of temperature conditions during two twenty-year phases of the study period were identified. From 1980 to 2000, trends in June–July were mostly negative in all areas of the region. This reflects high frequency of cold thermal regimes during this phase and indicates a relatively well-developed first stage of the Far Eastern summer monsoon and the OH influence. During this period, anomalously warm regimes were not observed in the water areas off the western and eastern Kamchatka coasts. Analysis of the second phase (2001–2022) revealed significant positive trends, indicating a weakening of the first cold stage of the monsoon and predominantly early formation of warm thermal regimes. In this phase, we note a transition to the occurrence of years with anomalously warm thermal regimes most clearly manifested in July – September of the past five years.

A significant correlation was found between water temperature anomalies and H_{500} geopotential anomalies, characterizing the intensity of the TD development

which, in turn, supports the OH development. For the first twenty-year phase of pressure variability in the OH area, the formation of positive anomalies (intensive development) was typical but the second phase was characterized by the formation of predominantly negative anomalies, indicating a weakening of this AAC.

Correlation analysis of interannual variability of water temperature anomalies and pressure anomalies in the HH area revealed no significant relations. The formation of temperature extremes in water areas is local in nature, which can be one of the causes for the low correlation with the intensity of development of such a large-scale pressure formation as the HH, despite a relatively good correlation with the OH regional AAC. It is shown that, along with the intensity of development of these AACs, their positions play a key role in the thermal regime formation. It is established that the HH has a steady trend toward increasing intensity of development. Under conditions of the OH weakening and the northwestward propagation of the HH North Pacific branch, the thermal and dynamic impact of this high on the studied water areas increases, contributing to the formation of water thermal regimes with positive anomalies.

It is shown that the formation of anomalous thermal conditions is associated with regional features of atmospheric circulation: anomalous changes in the development and positions of seasonal AACs and in their local impacts.

Findings from this study can be used in fisheries oceanography and incorporated into regional predictive models.

REFERENCES

1. Rostov, I.D., Dmitrieva, E.V., Rudykh, N.I. and Vorontsov, A.A., 2020. Climatic Changes in Thermal Conditions of Marginal Seas in the Western Pacific. *Russian Meteorology and Hydrology*, 45(3), pp. 169-178. https://doi.org/10.3103/S1068373920030048

2. Byshev, V.I., Neiman, V.G., Ponomarev, V.I., Romanov, Yu.A., Serykh, I.V. and Tsurikova, T.V., 2014. The Influence of Global Atmospheric Oscillation on Formation of Climate Anomalies in the Russian Far East. *Doklady Earth Sciences*, 458(1), pp. 1116-1120. https://doi.org/10.1134/S1028334X14090025

3. Johnson, G.C. and Lyman, J.M., 2020. Warming Trends Increasingly Dominate Global Ocean. *Nature Climate Change*, 10(8), pp. 757-761. https://doi.org/10.1038/s41558-020-0822-0

4. Jiang, X., Li, Y., Yang, S. and Wu, R., 2011. Interannual and Interdecadal Variations of the South Asian and Western Pacific Subtropical Highs and Their Relationships with Asian-Pacific Summer Climate. *Meteorology and Atmospheric Physics*, 113(3-4), pp. 171-180. https://doi.org/10.1007/s00703-011-0146-8

5. Shuntov, V.P. and Ivanov, O.A., 2019. Climate Changes and Current State of Biota in the Russian Waters of the Far-Eastern Seas. *Izvestiya TINRO*, 197, pp. 83-107. https://doi.org/10.26428/1606-9919-2019-197-83-107 (in Russian).

6. Terziev, F.C., ed., 1998. [*Gidrometeorology and Gidrochemistry of Seas. Vol. 9. Okhotsk Sea. Iss. 1. Gidrometeorological Conditions*]. Saint Petersburg: Gidrometeoizdat, 398 p. (in Russian).

7. Bogdanov, K.T. and Moroz, V.V., 2004. The *Kuril-Kamchatka Current and Oyashio Currents Water*. Vladivostok: Dalnauka, 141 p. (in Russian).

8. Shatilina, T.A., Tsitsiashvili, G.Sh. and Radchenkova, T.V., 2019. Features of the Summer Atmospheric Force Centers Variability over the Far East and Climatic Extremes in the Period

1980–2017. *Proceedings of the Russian State Hydrometeorological University*, (56), pp. 61-80. https://doi.org/10.33933/2074-2762-2019-56-61-80 (in Russian).

9. Moroz, V.V. and Shatilina, T.A., 2022. Features of Forming the Water Extreme Thermal Regimes in the Kuril Ridge Region in Summer under the Impact of the Changeable Atmospheric Processes. *Physical Oceanography*, 29(5), pp. 435-448. https://doi.org/10.22449/1573-160X-2022-5-435-448

10. Shatilina, T.A., Tsitsiashvili, G.Sh. and Radchenkova, T.V., 2021. Application of Interval Approach to Pattern Recognition for Identification of Preceeding Baric Structures that Determine Extreme Thermal Modes in the South-Kuril Area in Summer. *Izvestiya TINRO*, 201(2), pp. 470-483. https://doi.org/10.26428/1606-9919-2021-201-470-483 (in Russian).

11. Rostov, I.D., Dmitrieva, E.V. and Vorontsov, A.A., 2018. Tendencies of Climate Changes for Thermal Conditions in the Coastal Waters of the Western Bering Sea and Adjacent Areas in the Last Decades. *Izvestiya TINRO*, 193(2), pp. 167-182. https://doi.org/10.26428/1606-9919-2018-193-167-182 (in Russian).

12. Rogachev, K.A. and Shlyk, N.V., 2018. The Role of the Aleutian Eddies in the Kamchatka Current Warming. *Russian Meteorology and Hydrology*, 43(1), pp. 43-48. https://doi.org/10.3103/S1068373918010065

13. Andreev, A.G. and Zhabin, I.A., 2015. Impact of Continuation of the Alaskan Stream Flux Changes on the Water Dynamics in the Eastern Okhotsk Sea. *Vestnik of Far Eastern Branch of Russian Academy of Sciences*, (2), pp. 87-92 (in Russian).

14. Zhigalov, I.A., 2012. Seasonal and Year-to-Year Variability of Geostrophic Currents at West Kamchatka. *Izvestiya TINRO*, 169, pp. 94-99 (in Russian).

15. Rogachev, K.A. and Shlyk, N.V., 2005. Multiyear Variability of the Wind Stress Curl and Sea Level in the Kamchatka Current. *Oceanology*, 45(3), pp. 317-326.

16. Zhabin, I.A., Lobanov, V.B., Watanabe, S., Wakita, M. and Taranova, S.N., 2010. Water Exchange between the Bering Sea and the Pacific Ocean through the Kamchatka Strait. *Russian Meteorology and Hydrology*, 35(3), pp. 218-224. https://doi.org/10.3103/S106837391003009X

17. Isoguchi, O. and Kawamura, H., 2006. Seasonal to Interannual Variations of the Western Boundary Current of the Subarctic North Pacific by a Combination of the Altimeter and Tide Gauge Sea Levels. *Journal of Geophysical Research: Oceans*, 111(C4), C04013. https://doi.org/10.1029/2005JC003080

18. Pichugin, M.K., Gurevich, I.A., Khazanova, E.S. and Salyuk, P.A., 2020. Some Features of Oceanological Conditions of the Microalgae Autumn-Flowering near the Southeast Shore of Kamchatka. *Underwater Investigations and Robotics*, 4(34), pp. 70-73. https://doi.org/10.37102/24094609.2020.34.4.010 (in Russian).

19. Tskhay, Zh.R. and Shevchenko, G.V., 2022. Distribution Features of Chlorophyll a Concentration off the East Coast of Kamchatka in Autumn 2020 from Satellite Data. *Sovremennye Problemy Distansionnogo Zondirovaniya Zemli iz Kosmosa*, 19(1), pp. 226-238. https://doi.org/10.21046/2070-7401-2022-19-1-226-238 (in Russian).

Submitted 05.02.2025; approved after review 20.02.2025;
accepted for publication 15.05.2025.

About the authors:

Valentina V. Moroz, Senior Research Associate, Laboratory of Informatics and Ocean Monitoring, V.I. Il'ichev Pacific Oceanological Institute, Far Eastern Branch of Russian Academy of Sciences (43 Baltiyskaya Street, Vladivostok, 690041, Russian Federation), CSc. (Geogr.), **ORCID ID: 0000-0001-5937-4080**, **Scopus Author ID: 7102508049**, **ResearcherID: K-1520-2018**, moroz@poi.dvo.ru

Tatyana A. Shatilina, Leading Research Associate, Laboratory of Fishing Oceanology, Russian Federal Research Institute of Fisheries and Oceanography, Pacific Branch of VNIRO (TINRO) (4 Shevchenko Alley, Vladivostok, 690091, Russian Federation), CSc. (Geogr.), **ORCID ID: 0000-005-7954-9745**, **Scopus Author ID: 6505548902**, **SPIN-code: 8296-4906**, tatiana.shatilina@tinro.vniro.ru

Natalya I. Rudykh, Senior Research Associate, Laboratory of Informatics and Ocean Monitoring, V.I. Il'ichev Pacific Oceanological Institute, Far Eastern Branch of Russian Academy of Sciences (43 Baltiyskaya Street, Vladivostok, 690041, Russian Federation), CSc. (Geogr.), **ResearcherID: N-5821-2018**, **SPIN-code: 8068-7093**, rudykh@poi.dvo.ru

Contribution of the co-authors:

Valentina V. Moroz – paper structure development, collection and processing of oceanographic data, data analysis, drawing design, references, writing the paper text

Tatyana A. Shatilina – collection and processing of meteorological data, data analysis, result interpretation

Natalya I. Rudykh – data collection and processing, calculations

The authors have read and approved the final manuscript.
The authors declare that they have no conflict of interest.

ISSN 1573-160X, *PHYSICAL OCEANOGRAPHY*, Vol. 32, Iss. 4, pp. 479-491 (2025)
Original Russian Text © P. P. Tishchenko, P. Ya. Tishchenko, 2025,
published in *Morskoy Gidrofizicheskiy Zhurnal*, 2025, Vol. 41, Iss. 4, pp. 453–466

Original article

Oxygen in the Bottom Layer of the Amur Bay Waters (Sea of Japan) During the Cold Season 2013–2014

P. P. Tishchenko ✉, P. Ya. Tishchenko

V. I. Il'ichev Pacific Oceanological Institute, Far Eastern Branch of Russian Academy of Sciences, Vladivostok, Russian Federation
✉ *eq15@poi.dvo.ru*

Abstract
Purpose. This study aims to analyze oxygen concentration data from the bottom waters of Amur Bay during the cold season and to identify the causes of its decrease in late February to March, when the bay remains ice-covered.
Methods and Results. Variations in bottom water characteristics during the cold season were investigated in the area of summer hypoxia at a depth of 22 m (1 m above the seafloor) using the Water Quality Monitor autonomous bottom station (Wet Labs). Temperature, salinity (measured by conductivity), dissolved oxygen (*DO*), and chlorophyll a (measured by fluorescence) were recorded every 4 hours. Monitoring data from the cold period of 2013–2014 were compared with the data previously collected at the same station and location in summer 2011. The basic patterns of changes in oxygen content and the periods of dominance of production and organic matter mineralization in the bottom waters of Amur Bay during the cold season were identified.
Conclusions. During the winter season, upwelling of the Japan Sea waters delivers nutrients to the bottom waters of Amur Bay. Enhanced vertical mixing, driven by low water column stability, supplies the euphotic layer with nutrients, enabling photosynthesis throughout the bay's water column. Over four months in winter, the Amur Bay waters become supersaturated with oxygen relative to atmospheric levels. The onset of the summer monsoon (late February to early March) initiates the formation of summer hypoxia in the bottom waters of Amur Bay.

Keywords: Japan Sea, Amur Bay, dissolved oxygen, hypoxia, upwelling, downwelling, nutrients, photosynthesis

Acknowledgements: The study was supported by the state programs of POI FEB RAS (registration numbers 121-21500052-9 and 121021700346-7). The authors express their gratitude to P.Yu. Semkin (POI FEB RAS) for the installation and retrieval of the bottom WQM station.

For citation: Tishchenko, P.P. and Tishchenko, P.Ya., 2025. Oxygen in the Bottom Layer of the Amur Bay Waters (Sea of Japan) During the Cold Season 2013–2014. *Physical Oceanography*, 32(4), pp. 479-491.

Introduction

Deoxygenation of the World Ocean and its continental shelves is a pressing global issue under intensive scientific investigation. There is broad consensus on the causes of hypoxia/anoxia on ocean shelves, with eutrophication of coastal waters being the primary driver [1]. In Peter the Great Bay (PGB), two depressions (Fig. 1) experience hypoxia (oxygen content below 76 μmol/kg) during the summer season. One depression, located near Furugelm Island in the southwestern part of the bay, exhibits irregular hypoxia, while the other, in the central part of Amur Bay, experiences consistent seasonal hypoxia [2]. The primary cause of hypoxia in these areas is nutrient influx during floods from the eutrophic Tumannaya and Razdolnaya Rivers [2].

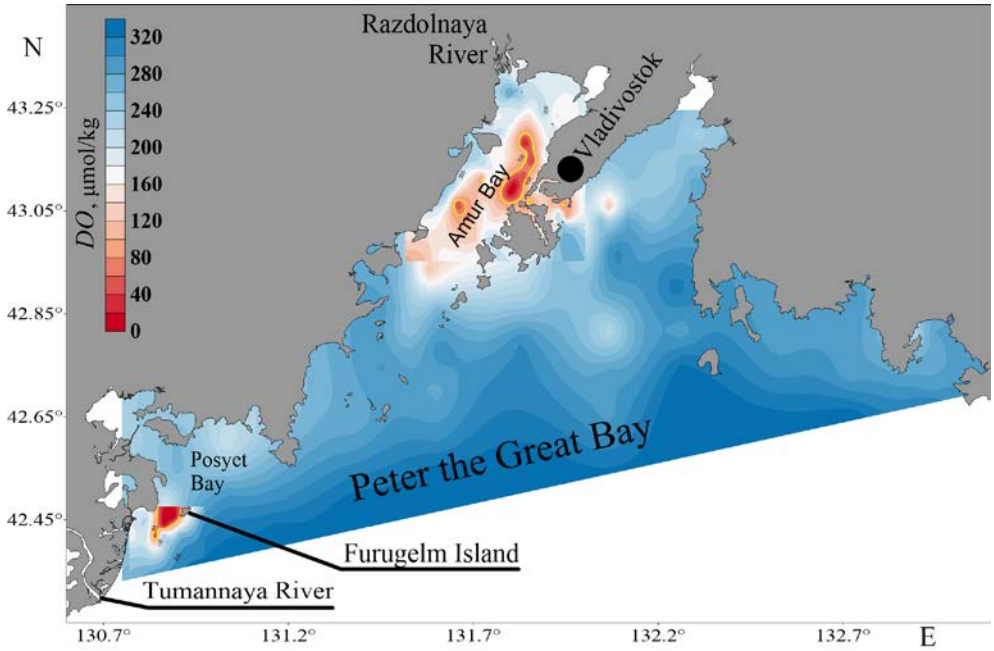

F i g. 1. Hypoxia areas in Peter the Great Bay

Amur Bay, a part of PGB, extends from northeast to southwest. The bay is 70 km long, with a width varying from 10 to 22 km [3]. Its maximum depths, located in the southernmost part, does not exceed 53 m, while the average depth is about 30 m [4]. The northern part of the bay features an extensive shallow zone with depths up to 10 m. The central part contains a deep-water depression with depths of 20–25 m. In the southeast, this depression is bounded by the Muravyov Ridge, which extends southeastward from the Peschaniy Peninsula to Russkiy Island (Fig. 2). During summer, hypoxia develops in the bottom waters of the depression, with its upper boundary at depths of 15–17 m [5]. Hypoxia is defined as an ecosystem state with oxygen levels low enough to cause quantitative and qualitative changes in the ecosystem. Literature sources suggest various threshold values for oxygen concentration as hypoxia criteria, typically ranging from 63 to 89 μmol/kg [6]. In this study, a threshold of 76 μmol/kg is adopted as the hypoxia criterion.

The monsoon climate of Primorye [7] drives downwelling circulation in Amur Bay during the spring-summer season, promoting hypoxia formation, and upwelling circulation during the autumn-winter season, facilitating its dissipation [8].

Numerous hydrochemical studies of Amur Bay have been conducted during the warm season, focusing on the processes of hypoxia formation and dissipation [6]. In contrast, hydrochemical processes during the winter season have received far less attention. Our research reveals high oxygen concentrations (400–500 μmol/kg) in both the surface and bottom waters of Amur Bay during winter [5]. Moreover, the bottom waters are supersaturated with oxygen relative to atmospheric levels,

except in Tavrichanka Estuary and Uglovoy Bay [1]. Winter observations also indicate significant under-ice primary production (0.1–0.3 gC/m²) [9]. At the same time, extensive hydrological studies, including oxygen and chlorophyll measurements using a probe, led the authors of [10] to hypothesize the potential formation of hypoxia in the bottom waters of Amur Bay during winter. This study presents monitoring data collected during the cold season using an anchored station deployed in the area of summer hypoxia in Amur Bay.

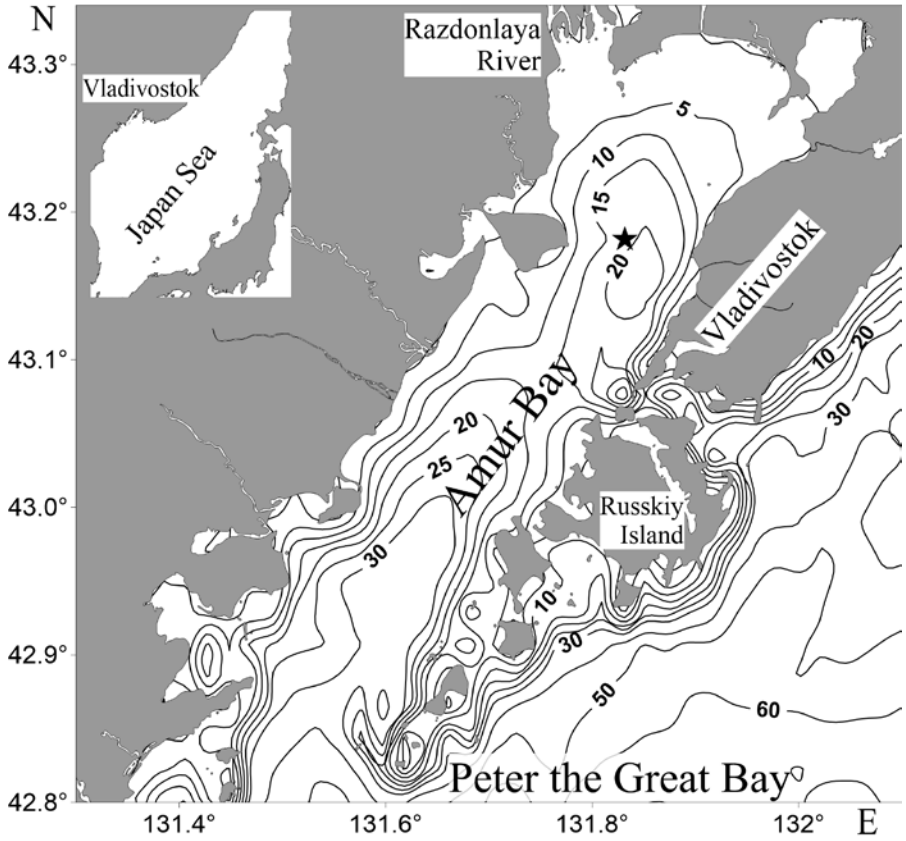

F i g. 2. Geographical location of Amur Bay and depth map. Star indicates the WQM station location

This study aims to examine changes in water parameters and identify the primary causes of oxygen content variations in the bottom waters during the cold season.

Measuring methods

Variability in bottom water characteristics during the cold season was investigated in an area prone to summer hypoxia, at a depth of 22 m (1 m above the seabed), using the Water Quality Monitor (WQM) autonomous bottom station

[1] Tishchenko, P.P., 2013. *Seasonal Hypoxia of Amurskiy Bay*. Thesis Cand. Geogr. Sci. Vladivostok: POI FEB RAS, 166 p. (in Russian).

(Wet Labs). The station was positioned at 43°10.894′N, 131°49.949′E (Fig. 2). Measurements were conducted from September 11, 2013, to May 15, 2014. Temperature, salinity (measured by conductivity), dissolved oxygen (*DO*), and chlorophyll a (measured by fluorescence) were recorded every 4 hours with a 1-second interval over 5-minute periods using the DH4 submersible logger (Wet Labs). To mitigate biofouling, WET Labs employed copper housings, chlorine injection, and pesticide-containing inserts for the WQM station, ensuring stable sensor performance over extended periods [11]. The cited article provides detailed specifications of the WQM sensors. The discrepancy between oxygen measurements obtained by the WQM station and those using the Winkler method ranged from 1.2 to 14.0 μmol/kg [8]. The variation is primary attributed to the spatial mismatch between the WQM station and bathometer sampling locations. Monitoring data from the cold season of 2013–2014 were compared with data from the summer season of 2011, previously collected by the same station at nearly identical coordinates (43°10.881′N, 131°49.893′E) [8].

Summer and winter conditions in Amur Bay were compared using Apparent Oxygen Utilization (*AOU*), as this parameter reflects the balance between oxygen production and respiration processes. *AOU* values were calculated using the following equation:

$$AOU = [O_2]_o - [O_2].$$

Here, *AOU* is calculated as the difference between the oxygen concentration in seawater at equilibrium with the atmosphere ($[O_2]_o$) for a given temperature and salinity and the measured oxygen concentration ($[O_2]$). Oxygen solubility in seawater at specific temperature and salinity was determined using the equation from [12]. Seawater is supersaturated with oxygen relative to atmospheric levels when $AOU < 0$ and undersaturated when $AOU > 0$.

On March 22, 2011, a hydrochemical survey was conducted in the area of summer hypoxia in Amur Bay (43°11.816′N, 131°50.139′E). The survey was performed from a rescue vessel during the ice-melt period, when the northern part of Amur Bay was covered with broken ice, while the southern part was ice-free. Vertical profiles of CO_2 partial pressure (pCO_2), oxygen concentration, ammonium nitrogen, phosphates, and silicates were measured in the summer hypoxia area. Alkalinity was determined by direct titration in an open cell with 0.02N hydrochloric acid using a mixed indicator (methyl red + methylene blue) [2]. pH was measured potentiometrically at 20°C in a cell without liquid junction [13]. pCO_2 was calculated following the method described in [14]. Nutrient concentrations were determined using standard analytical methods [3].

[2] Bruevich, S.V., 1944. [*Instructions for Chemical Investigation of Seawater*]. Moscow: Glavsevmorput, 83 p. (in Russian).

[3] VNIRO, 1988. [Methods of Hydrochemical Studies of Major Biogenic Elements]. Moscow: VNIRO, 120 p. (in Russian).

Results

The detailed variability in the hydrological characteristics of the bottom waters of Amur Bay in the hypoxia formation area during the cold season of 2013–2014 is present in Fig. 3. To analyze a complete annual cycle, the data from the WQM station collected in 2011, previously analyzed in detail [8], were used.

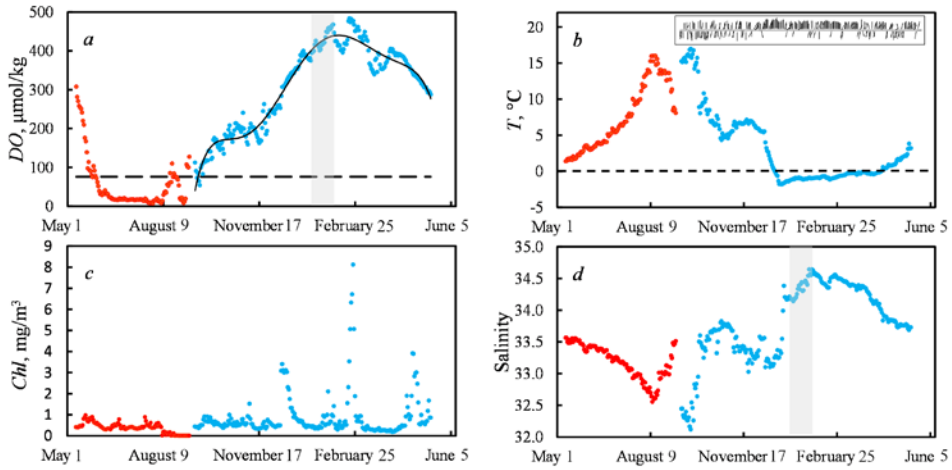

F i g. 3. Temporal variability of dissolved oxygen concentration (dashed line indicates the hypoxia level – 76 µmol/kg) (*a*), temperature (*b*), chlorophyll a content (*c*) and salinity (*d*) in the Amur Bay bottom layer at the location of the WQM autonomous bottom station: in 2011 (●); in 2013–2014 (●). The inset in Fig. 3, *b* shows temporal variability of wind direction in 2013–2014. Grey area corresponds to the period December 27 – February 02 when salinity increases due to brine formation

In late August to autumn, bottom hypoxia in Amur Bay dissipates due to upwelling of the Sea of Japan waters [8], as evidenced by increased *DO*, absence of chlorophyll, decreased water temperature, and increased salinity. Elevated nitrate concentrations, absent in the bottom waters of Amur Bay during summer, indicate the intrusion of the Sea of Japan waters [1] from depths of 250–300 m. At these depths, silicate, nitrate, phosphate, and *DO* concentrations are 29.3, 17.2, 1.36, and 285 µM, respectively [15]. In 2013, the displacement of oxygen-depleted waters by cold, saline Sea of Japan waters occurred between September 12 and October 24 due to autumn upwelling (Fig. 3). This process was accompanied by a decrease in water temperature from 17.0 to 4.3 °C, an increase in salinity from 32.12 to 33.69, and an increase in *DO* from 54 to 213 µmol/kg. During this period, wind direction was variable, alternating between southerly and northerly (inset in Fig. 3, *b*).

The period from October 25 to December 9 marks the transition from the summer to winter monsoon in Amur Bay. This period is characterized by variable wind directions, resulting in altered bay water circulation and temporal variations in measured parameters: *DO* ranging from 159 to 263 µmol/kg, temperature from 4.6 to 7.2 °C, and salinity from 33.03 to 33.79. These significant variations are driven not only by changes in wind direction but also by wind-induced mixing of the Sea of Japan waters with residual summer shelf waters, alongside atmospheric cooling, which enhances the dissolution of atmospheric gases. The increase in oxygen

concentration during this period is partly attributed to higher gas solubility at lower temperatures and enhanced primary production.

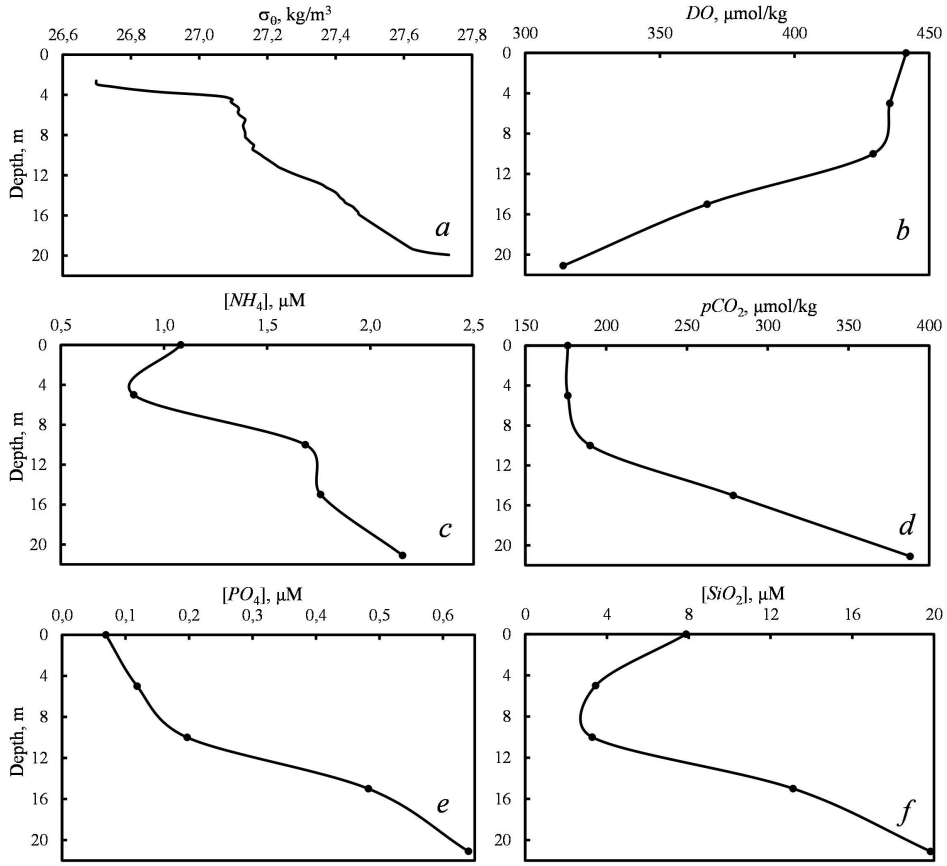

F i g. 4. Vertical profiles of conditional density (*a*), oxygen concentration (*b*), ammonium nitrogen concentration (*c*), partial pressure of carbon dioxide (*d*), and phosphate (*e*) and silicate (*f*) concentrations in the area of hypoxia formation (43°11.816′N, 131°50.139′E) in Amur Bay, March 22, 2011

On December 10, 2013, snowfall occurred along the coast of Amur Bay, initiating intensive ice formation in the bay. Water temperature dropped to the freezing point of seawater, − 1.818 °C, by December 27. Subsequently, salinity increased to 33.323, and oxygen concentration reached 353 μmol/kg. During this period, a peak chlorophyll concentration of 3.4 mg/m³ was recorded on December 17 (Fig. 3, *c*). From December 10 to 27, winter cooling led to the formation of continuous ice cover in the northern part of Amur Bay (north of 43°8.5′N to the mouth of the Razdolnaya River) and triggered winter convection. South of 43°8.5′N, ice formation occurred but remained discontinuous. Dominant northerly winds intensified this effect. On December 8, 2013, the average daily air temperature was 1.15 °C dropping to − 5.51 °C on December 9 (http://www.rp5.ru/). Satellite imagery from https://worldview.earthdata.nasa.gov/ indicates that by December 11, the northern part of Amur Bay was covered with continuous ice, with the WQM station located beneath it. The bottom water temperature reaching the seawater

freezing point on December 27 suggests vertically uniform water parameters throughout the bay, as freezing occurs at the surface. From December 27 to February 2, salinity increased to 34.578 and *DO* rose to 468 μmol/kg (Fig. 3 *a*, *d*, grey area). During the same period, a slight increase in water temperature to −0.878 °C was observed. The maximum salinity of the Sea of Japan waters is 34.070 ± 0.002 [15], while Amur Bay waters exhibit significantly lower salinity during the warm season (Fig. 3, *d*) [3]. The salinity increase to 34.578 is attributed to brine formation during ice formation. The slight temperature increase is likely due to residual summer heat retained by the seabed [16, 10]. This bottom heating enhances vertical mixing, maintaining water column homogeneity with minor temporal variations in *T* and *S* (Fig. 3, *b*, *d*).

February was characterized by minor fluctuations in hydrological parameters. From February 2 to 12, *DO* decreased slightly to 396 μmol/kg, water temperature increased to −0.69 °C, and salinity decreased to 34.413. Conversely, from February 12 to 23, *DO* increased to 477 μmol/kg, water temperature decreased to −0.856 °C, and salinity rose to 34.56. These fluctuations are most likely driven by water advection in the bay, with the *DO* increase attributed to phytoplankton blooms. The peak chlorophyll concentration of 8 mg/m³, observed on February 23, coincided with the maximum *DO* concentration (Fig. 3).

Vertical stratification of Amur Bay waters began forming in March (Fig. 4), driven by ice melt and seasonal temperature increases. During this period, upwelling circulation transitioned to downwelling due to variations in wind direction (Fig. 3, *b*) [8].

Discussion

The monsoon climate of Primorye plays a critical role in the formation and dissipation of hypoxia in the bottom waters of Amur Bay. Southeasterly winds in summer drive downwelling circulation in the bay [8], limiting interaction between subsurface Sea of Japan waters and PGB shelf waters. This season also experiences the highest atmospheric precipitation [7]. In summer, the inflow of eutrophic waters from the Razdolnaya River into Amur Bay increases significantly. This, combined with other factors, establishes river runoff as the primary nutrient source for the bay, triggering phytoplankton blooms in surface waters. Oxygen produced during photosynthesis partially escapes to the atmosphere and partially remains in the upper water column due to stable stratification. Excess phytoplankton biomass, unconsumed by zooplankton and zoobenthos, settles to the bay floor. In the bay's depressions below 15–17 m, where photosynthetically active radiation (PAR) does not penetrate, hypoxia develops due to microbial decomposition of the settled phytoplankton biomass [2].

In the cold season, northwesterly winds drive upwelling circulation in the bay. During this period, atmospheric precipitation decreases significantly [7]. The Razdolnaya River discharge in winter is over 100 times lower than during summer floods. Meanwhile, subsurface Sea of Japan waters, upwelling from depths of 250–300 m, contain high concentrations of nutrients and dissolved oxygen: silicates (29.3 μM), nitrates (17.2 μM), phosphates (1.36 μM), and dissolved oxygen (285 μmol/kg) [15]. In winter, the primary nutrient source for Amur Bay is subsurface Sea of Japan waters. These waters are transparent, allowing PAR to reach

the seafloor in the ice-free southern part of the bay. Photosynthesis occurs actively under ice when it is not snow-covered. Additionally, these waters enter the bottom waters of the bay and are mixed through winter convection. Nutrients from the Sea of Japan waters support winter photosynthesis in Amur Bay, resulting in elevated oxygen concentrations (Fig. 2). Using Redfield stoichiometry [17], the photosynthesis process can be represented as follows:

$$106 \cdot CO_2 + 122 \cdot H_2O + 16 \cdot HNO_3 + H_3PO_4 \leftrightarrow$$
$$(CH_2O)_{106}(NH_3)_{16}H_3PO_4 + 138 \cdot O_2$$

We propose that the Sea of Japan waters fully replace Amur Bay shelf waters during upwelling. If photosynthesis occurs in these waters, the *DO* concentration would be $(285 + 138 \times [PO_4]) = 473$ μmol/kg, comparable to the maximum winter *DO* concentration of 482 μmol/kg (Fig. 3, *a*). An additional nutrient source for the bay is the nutrient flux from the seabed [18].

The comparison of *AOU* between the warm and cold seasons is presented in Fig. 5. In summer, under downwelling conditions, decomposition processes dominate in the bottom waters of Amur Bay, with *AOU* values reaching up to 300 μmol/kg (Fig. 5). The influx of the Sea of Japan waters in autumn significantly reduces this dominance by supplying oxygen to the bottom waters. However, the transition from net decomposition to net production ($AOU < 0$) occurs only on December 29. This delay is attributed to the origin of the Sea of Japan waters from depths of 250–300 m, where photosynthesis is absent, and these waters exhibit an oxygen deficit relative to atmospheric levels. Comparison Figs. 3, *a* and 5 indicates that the shift in production-decomposition balance results solely from intensified organic matter production in December, driven by nutrient supply from the Sea of Japan waters and coinciding with winter convection when the entire water column reaches freezing temperatures. Fig. 5 shows that bottom waters of Amur Bay are supersaturated with oxygen relative to atmospheric levels for nearly four months (December 29, 2013 – April 22, 2014).

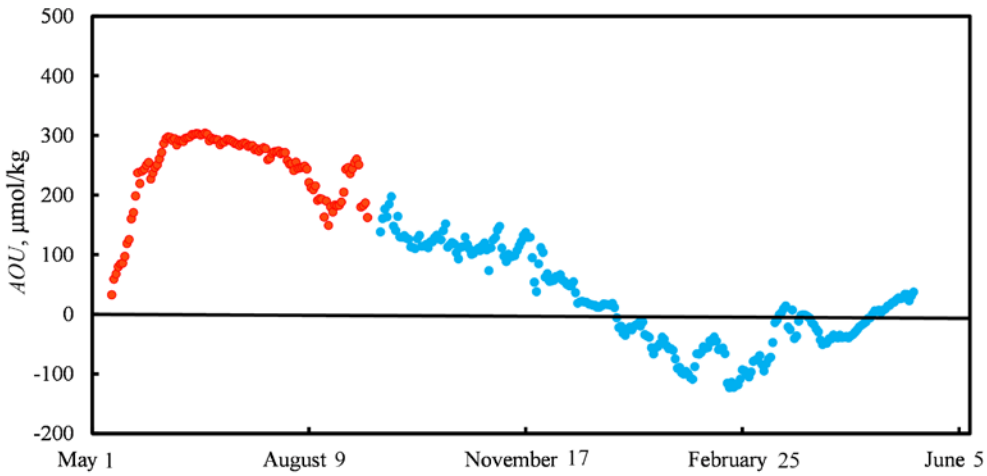

F i g. 5. Temporal variability of AOU in the Amur Bay bottom layer at the location of WQM station: in 2011 (●); in 2013–2014 (●)

The bottom waters at the WQM station exhibit consistently high *DO* concentrations throughout the winter season, exceeding the hypoxic threshold of 76 μmol/kg by 4–6 times. This phenomenon primarily stems from distinct nutrient delivery mechanisms compared to summer conditions. Unlike the stratified summer period, winter nutrient supply to the bottom waters occurs under conditions of high water transparency and the absence of density stratification in the Sea of Japan waters. Winter photosynthesis influences the entire ice-free water column through vertical mixing, delivering waters with $AOU < 0$ to the bottom waters, indicating oxygen supersaturation relative to atmospheric equilibrium. Notably, phytoplankton blooms can develop even under ice cover, as described in [19]. Although ice reduces PAR intensity, photosynthesis persists in shallow basins such as Novgorod Bay (10–15 m depth) and Posyet Bay due to winter convection processes. Winter convection in the shallow waters of Amur Bay facilitates complete vertical mixing, continuously supplying nutrients to the sub-ice layer where photosynthesis occurs. Phytoplankton cells undergo continuous cycling, being transported downward by convection and returning to the photic zone, with the shallow basin depth preventing their permanent export from layers influenced by PAR. We propose that this mechanism applies specifically to ice-covered areas of Amur Bay without snow cover, where sufficient light penetration supports sustained winter productivity despite surface ice conditions.

The observed decrease in oxygen levels after February 23 suggests the presence of mechanisms contributing to oxygen depletion in the bay waters. We propose two primary processes. During the winter season, when $AOU < 0$, gas exchange in ice-free areas of the bay reduces oxygen concentrations. The ice-free area expands from late February to early March, and by early April the bay becomes completely ice-free (https://worldview.earthdata.nasa.gov). This mechanism of oxygen removal from the bay waters is effective only when *DO* concentrations exceed atmospheric levels, i.e., until approximately April 26 (Fig. 5). However, even after the bay ecosystem shifts from dominance by production processes ($AOU < 0$) to dominance by decomposition processes (AOU > 0), *DO* concentrations in the bottom waters continue to decline (Figs. 3, 5). The second process contributing to *DO* reduction is biochemical oxygen consumption during organic matter mineralization at the water-sediment interface. We utilized previously determined rates of biochemical oxygen consumption V_{BOC} (μmol/(L·day)) for the bottom waters of Amur Bay [8]:

$$V_{BOC} = -0.1225 \cdot [O_2].$$

Observational data for oxygen concentration over time (Fig. 2) were processed using least squares method. An empirical equation for $[O_2]$ (μmol/L) was obtained:

$$[O_2] = -2.21703 \cdot 10^{-10} \cdot t^6 + 1.754836 \cdot 10^{-7} \cdot t^5 - 5.246808 \cdot 10^{-5} \cdot t^4 + 7.23196 \cdot 10^{-3} \cdot t^3 - 0.453612 \cdot t^2 + 13.1475 \cdot t + 27.52. \quad (1)$$

Here t represents time in days from the start of observations. The derivative of this equation yields the total rate of oxygen change (V_{tot}) at any given time. The biochemical oxygen consumption rate (V_{BOC}) was calculated using the relation (1), and the ventilation rate (V_{vent}) was derived as the difference between V_{tot} and V_{BOC}. The results are presented in Fig. 6. Biochemical oxygen consumption is

a second-order reaction [8], meaning the consumption rate peaks at maximum *DO* concentrations (Fig. 6; equation (1)).

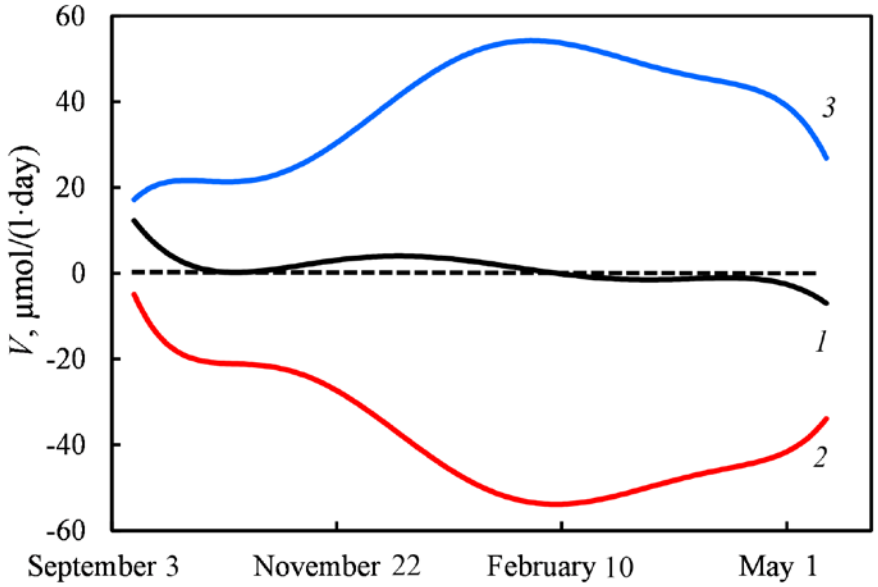

F i g. 6. Dependence of rate of oxygen concentration change on time: *1* – total rate V_{tot} calculated by equation (1); *2* – rate of biochemical oxygen consumption of organic matter V_{BOC}; *3* – rate of water ventilation V_{vent}

In March 2011, profiles of hydrochemical parameters were obtained in Amur Bay (Fig. 4). By March 22, density stratification had developed due to ice melt and seasonal temperature increases. During this period, upwelling transitioned to downwelling, which limited the influence of the Sea of Japan waters on Amur Bay. Consequently, the profiles in Fig. 4 reflect geochemical processes at the bay's bottom. *DO* concentrations decreased toward the bottom, while nutrient concentrations increased, indicating organic matter mineralization at the water – sediment interface. The organic carbon content in sediments at hypoxia sites ranges from 2–3% [20], with mineralization in these sediments occurring via anaerobic pathways. Downwelling resuspends surface sediments in Amur Bay, increasing bottom water turbidity and enhancing the flux of mineralization products from sediments into the water column [8]. Therefore, despite relatively high *DO* concentrations, ammonium was the dominant form of mineral nitrogen (Fig. 4, *c*). Nitrate concentrations were also measured but were 2–3 times lower than those of ammonium. Another possible pathway is the formation of a thin low-oxygen layer [4] at the water – sediment interface in reduced sediments [21]. In this layer, organic

[4] Gurova, Yu.S., 2023. *Features of the Formation of Redox Conditions at the Water-Bottom Sediments Boundary in the Coastal Areas of the Russian Sector of the Azov-Black Sea Basin*. Thesis Cand. Geogr. Sci. Sevastopol, 182 p. (in Russian).

matter mineralization would primarily produce ammonium rather than nitrate [6]. This phenomenon warrants further investigation.

The transition period in late February to early March is crucial: the wind direction shifts from winter to summer monsoon, altering the bay's circulation from upwelling to downwelling. During this period, the interaction between the Sea of Japan waters and the shelf weakens, reducing nutrient supply from the Sea of Japan waters. Photosynthesis in the bay declines, and these factors collectively initiate the formation of summer hypoxia.

Conclusions

The oxygen content in the bottom waters of Amur Bay is shaped by the complex interplay of hydrodynamic processes and biogeochemical transformations.

Two primary natural sources govern nutrient dynamics and ecological conditions in Amur Bay: 1) eutrophic waters discharged by the Razdolnaya River; 2) the deep Sea of Japan waters originating from depths of 250–300 m.

During the winter months, upwelling of the Sea of Japan waters transports nutrients to the bottom waters of Amur Bay. The low static stability of the water column facilitates vertical mixing, effectively supplying the euphotic zone with nutrients. This mixing enables photosynthetic activity to extend throughout the entire water column. As a result, winter waters maintain oxygen supersaturation relative to atmospheric equilibrium for approximately four months, with *DO* concentrations ranging from 353 to 482 μmol/kg.

The Amur Bay ecosystem undergoes transitions twice per year corresponding to shifts in circulation patterns. From February to March, the establishment of downwelling circulation triggers several interconnected processes: increased nutrient input from the Razdolnaya River, the development of pronounced vertical stratification, and a progressive decline in near-bottom *DO* concentrations, ultimately reaching hypoxic conditions (less than 76 μmol/kg) by summer. Conversely, from September to October, the onset of upwelling circulation dissipates summer hypoxia while delivering nutrient-rich subsurface Sea of Japan waters.

REFERENCES

1. Breitburg, D., Levin, L.A., Oschlies, A., Grégoire, M., Chavez, F.P., Conley, D.J., Garçon, V., Gilbert, D., Gutiérrez, D. [et al.], 2018. Declining Oxygen in the Global Ocean and Coastal Waters. *Science*, 359(6371), eaam7240. https://doi.org/10.1126/science.aam7240
2. Tishchenko, P.Ya., Tishchenko, P.P., Lobanov, V.B., Mikhaylik, T.A., Sergeev, A.F., Semkin, P.Yu. and Shvetsova, M.G., 2020. Impact of the Transboundary Razdolnaya and Tumannaya Rivers on Deoxygenation of the Peter the Great Bay (Sea of Japan). *Estuarine, Coastal and Shelf Science*, 239, 106731. https://doi.org/10.1016/j.ecss.2020.106731
3. Gomoyunov, K.A., 1926. A *Hydrological Essay on the Amur Bay and the Suifun River*. Proceedings of Far Eastern State University, Series 3, 1. Vladivostok: Far Eastern State University, 44 p. (in Russian).
4. Grigoriev, R.V. and Zuenko, Yu.I., 2005. Climatic Distribution of Water Temperature and Salinity in the Amur Bay (Japan Sea). *Izvestiya TINRO*, 143, pp. 179-188 (in Russian).
5. Tishchenko, P.Ya., Lobanov, V.B., Zvalinsky, V.I., Sergeev, A.F., Volkova, T.I., Koltunov, A.M., Mikhailik, T.A., Sagalaev, S.G., Tishchenko, P.P. [et al.], 2011. Seasonal Hypoxia in the Amur Bay (Japan Sea). *Izvestiya TINRO*, 165, pp. 136-157 (in Russian).

6. Tishchenko, P.P., Zvalinsky, V.I., Mikhaylik, T.A. and Tishchenko, P.Ya., 2021. Hypoxia in Peter the Great Bay. *Izvestiya TINRO*, 201(3), pp. 600-639. https://doi.org/10.26428/1606-9919-2021-201-600-639 (in Russian).

7. Gaiko, L.A., 2005. *Peculiarities of Hydrometeorological Regime of the Coastal Zone in the Peter the Great Bay (Sea of Japan)*. Vladivostok: Dalnauka, 150 p. (in Russian).

8. Tishchenko, P., Tishchenko, P., Lobanov, V., Sergeev, A., Semkin, P. and Zvalinsky, V., 2016. Summertime in Situ Monitoring of Oxygen Depletion in Amursky Bay (Japan/East Sea). *Continental Shelf Research*, 118, pp. 77-87. https://doi.org/10.1016/j.csr.2016.02.014

9. Sorokin, Yu.I. and Konovalova, I.W., 1973. Production and Decomposition of Organic Matter in a Bay of the Japan Sea during the Winter Diatom Bloom. *Limnology and Oceanography*, 18(6), pp. 962-967. https://doi.org/10.4319/lo.1973.18.6.0962

10. Lazaryuk, A.Yu., Lobanov, V.B. and Ponomarev, V.I., 2013. Evolution of Thermohaline Structure in the Amurskiy Bay in a Cold Season. *Vestnik of the Far East Branch of the Russian Academy of Sciences*, 6(172), pp. 59-70 (in Russian).

11. Orrico, C.M., Moore, C., Romanko, D., Derr, A., Barnard, A.H., Janzen, C., Larson, N., Murphy, D., Johnson, R. [et al.], 2007. WQM: A New Integrated Water Quality Monitoring Package for Long-Term in-Situ Observation of Physical and Biogeochemical Parameters. In: IEEE, 2007. *Proceedings of OCEANS 2007*. Vancouver, BC, Canada, pp. 1-9. https://doi.org/10.1109/OCEANS.2007.4449418

12. Weiss, R.F., 1970. The Solubility of Nitrogen, Oxygen and Argon in Water and Seawater. *Deep Sea Research and Oceanographic Abstracts*, 17(4), pp. 721-735. https://doi.org/10.1016/0011-7471(70)90037-9

13. Tishchenko, P.Ya., Chichkin, R.V., Il'ina, E.M. and Wong, C.S., 2002. The Measurement of pH Values in Seawater Using a Cell without a Liquid Junction. *Oceanology*, 42(1), pp. 27-35.

14. Dickson, A.G. and Goyet, C., eds., 1994. *Handbook of Methods for the Analysis of the Various Parameters of the Carbon Dioxide System in Sea Water. Version 2*. OENL/CDIAC-74. DOE, 198 p.

15. Talley, L.D., Tishchenko, P., Luchin, V., Nedashkovskiy, A., Sagalaev, S., Kang, D.-J., Warner, M. and Min, D.-H., 2004. Atlas of Japan (East) Sea Hydrographic Properties in Summer, 1999. *Progress in Oceanography*, 61(2-4), pp. 277-348. https://doi.org/10.1016/j.pocean.2004.06.011

16. Burov, B.A., Lazaryuk, A.Y. and Lobanov, V.B., 2014. Study of the Heat Flux at the Water-Bottom Sediments in Amurskiy Bay in the Sea of Japan in the Winter Season. *Oceanology*, 54(6), pp. 695-704. https://doi.org/10.1134/S0001437014060022

17. Redfield, A.C., Ketchum, B.H. and Richards, F.A., 1963. The Influence of Organisms on the Composition of Seawater. In: M. N. Hill, ed., 1963. The *Sea: Ideas and Observations on Progress in the Study of the Seas*. New York: Interscience Publishers. Vol. 2, pp. 26-77.

18. Tishchenko, P.Ya., Borisenko, G.V., Barabanshchikov, Yu.A., Pavlova, G.Yu., Riumina, A.A., Sagalaev, S.G., Semkin, P.Yu., Tishchenko, P.P., Ulanova, O.A. [et al.], 2022. Estimation of Nutrient Fluxes on the Interface Bottom Water–Sediments in Shallow Bights of the Peter the Great Bay, Sea of Japan. *Geochemistry International*, 60(9), pp. 891-904. https://doi.org/10.1134/S0016702922090087

19. Vyshkvartsev, D.I. and Konovalova, G.V., 1979. On Mechanism of Winter Blooming of Microalgae in Peter the Great Bay (the Sea of Japan). *Russian Journal of Marine Biology*, (1), pp. 72-73 (in Russian).

20. Tishchenko, P.Ya., Barabanshchikov, Yu.A., Volkova, T.I., Marjash, A.A., Mikhailik, T.A., Pavlova, G.Yu., Sagalaev, S.G., Tishchenko, P.P., Khodorenko, N.D. [et al.], 2018. Diagenesis of Organic Matter in the Top Layer of the Sediments of the Peter the Great Bay in Hypoxia Locations. *Geochemistry International*, 56(2), pp. 171-181. https://doi.org/10.1134/S0016702918010093

21. Fredriksson, J.P., Attard, K., Stranne, C., Koszalka, I.M., Glud, R.N., Andersen, T.J., Humborg, C. and Brüchert, V., 2024. Hidden Seafloor Hypoxia in Coastal Waters. *Limnology and Oceanography*, 69(11), pp. 2489-2502. https://doi.org/10.1002/lno.12607

Submitted 06.12.2024; approved after review 13.12.2025;
accepted for publication 15.05.2025.

About the authors:

Petr P. Tishchenko, Senior Research Associate, Laboratory of Hydrochemistry, V. I. Il'ichev Pacific Oceanological Institute, Far Eastern Branch of Russian Academy of Sciences (43 Baltiyskaya Str., Vladivostok, 690041, Russian Federation), CSc. (Geogr.), **ORCID ID: 0000-0003-2182-5477**, **SPIN-code: 1796-8910**, eq15@poi.dvo.ru

Pavel Ya. Tishchenko, Chief Research Associate, Laboratory of Hydrochemistry, V. I. Il'ichev Pacific Oceanological Institute, Far Eastern Branch of Russian Academy of Sciences (43 Baltiyskaya Str., Vladivostok, 690041, Russian Federation), DSc. (Chem.), **ORCID ID: 0000-0002-3500-2861**, **SPIN-code: 7561-9500**, tpavel@poi.dvo.ru

Contribution of the co-authors:

Petr P. Tishchenko – processing and analysis of natural data, construction of graphic material, generalization of research results, formulation of conclusions, writing of the manuscript text

Pavel Ya. Tishchenko – generalization of research results, formulation of conclusions

The authors have read and approved the final manuscript.
The authors declare that they have no conflict of interest.

ISSN 1573-160X, *PHYSICAL OCEANOGRAPHY*, Vol. 32, Iss. 4, pp. 492-507 (2025)

published in *Morskoy Gidrofizicheskiy Zhurnal*, 2025, Vol. 41, Iss. 4, pp. 467–483

Original article

Colored Dissolved Organic Matter and Total Suspended Matter as the Indicators of Water Pollution in the Kerch Strait

P. D. Lomakin ✉, A. A. Chepyzhenko, A. I. Chepyzhenko

Marine Hydrophysical Institute of RAS, Sevastopol, Russian Federation
✉ *p_lomakin@mail.ru*

Abstract
Purpose. Based on the data collected from expeditions conducted in 2001–2014, this study aims to identify patterns in the structure of concentration fields of colored dissolved organic matter and total suspended matter of anthropogenic origin in the Kerch Strait, to reveal polluted areas in the region under study, to identify the associated sources, and to assess the linear scale of their impact on the aquatic environment. Additionally, the study compares these findings with the existing data on water pollution in the strait, derived from the contact hydrochemical and satellite measurements.
Methods and Results. Polluted areas within the studied water region were identified by locating local maxima in the concentrations of colored dissolved organic matter and total suspended matter. These anthropogenic substances are shown to be localized in the form of individual lenses with elevated concentrations relative to background levels. The concentration profiles of these lenses exhibit a characteristic intrusive shape, with similar empirical concentration distributions for both substances. Thirteen lenses, with horizontal scales of 1–6 miles, were identified. Each lens is associated with a specific anthropogenic source, primarily shipping routes and canals, dredging and dumping of excavated soil, ports, offshore transshipment points, cargo terminals, and landfills. The Tuzla Ravine is examined separately as a source of anthropogenic suspended matter. Data indicate that, even 5–10 years after its formation, the ravine remains a major contributor, increasing suspended matter concentrations in the central strait by an order of magnitude compared to the surrounding background.
Conclusions. The structure regularities of concentration fields of colored dissolved organic matter and total suspended matter of anthropogenic origin in the Kerch Strait have been identified. The polluted areas within the water region, along with their associated sources, have been delineated, and the linear scale of their impact on the aquatic environment has been assessed. Comparison of these findings with existing studies of water pollution in the region demonstrates strong agreement.

Keywords: colored dissolved organic matter, total suspended matter, water structure, pollution, Kerch Strait

Acknowledgments: The study was conducted under the framework of state assignments FNNN-2024-0016 and FNNN-2024-0012.

For citation: Lomakin, P.D., Chepyzhenko, A.A. and Chepyzhenko, A.I., 2025. Colored Dissolved Organic Matter and Total Suspended Matter as the Indicators of Water Pollution in the Kerch Strait. *Physical Oceanography*, 32(4), pp. 492-507.

Introduction

The Kerch region has experienced significant industrial growth since the 1960s. Shipping activity in the Kerch Strait has intensified, accompanied by the development of infrastructure to support vessels of various sizes and purposes. This has led to substantial anthropogenic pressure on the region's aquatic environment, which leading research institutions have been studying systematically since the 1970s using various methods.

These studies include traditional hydrochemical methods: monitoring of water pollution in the Kerch Strait by the State Hydrometeorological Service of Ukraine from 1979 to 2009 [1]; monitoring of water and sediment pollution in the strait and adjacent areas by the Southern Scientific Research Institute of Marine Fisheries and Oceanography (YugNIRO) from 1990 to 2015 [2]; studies of heavy metal pollution in the bottom sediments of the Kerch Strait by Marine Hydrophysical Institute (MHI) based on expeditionary data from 2005 to 2008 [3]; research on water, suspended matter, and sediment pollution by the Shirshov Institute of Oceanology of the Russian Academy of Sciences (IO RAS) from 2019 to 2022 [4]. Currently, IO RAS researchers are monitoring technogenic pollution in the region using optical and radar remote sensing methods [5].

From 2001 to 2015, expeditionary data collected by leading domestic research institutions were used to study water pollution in the Kerch Strait caused by colored dissolved organic matter (CDOM) and total suspended matter (TSM) of anthropogenic origin. These studies employed an oceanographic method of analyzing the structure of concentration fields of these substances. CDOM and TSM are notably considered effective indicators of pollution in the coastal waters of oceans and seas [6–8].

The purpose of this study is to identify patterns in the structure of the CDOM and TSM concentration fields of anthropogenic origin, analyze the statistical characteristics of their variability, determine the polluted areas of the Kerch Strait and their associated pollution sources, assess the linear scale of the identified sources' impact on the aquatic environment, and compare the results with existing water pollution data in the strait obtained through contact hydrochemical and satellite methods.

Initial data and research methods

The analysis is based on data collected from a series of expeditions to the Kerch Strait conducted between 2001 and 2014 by Marine Hydrophysical Institute (MHI), as well as joint expeditions involving MHI, the Southern Institute of Fisheries and Oceanography (YugNIRO), the Institute of Biology of the Southern Seas (IBSS), the Russian Federal Research Institute of Fisheries and Oceanography (VNIRO), the State Oceanographic Institute (GOIN), and the Southern Scientific Center (SSC) of the Russian Academy of Sciences.

The expeditions included comprehensive surveys of the entire Kerch Strait and targeted areas, specifically the northern and central parts of the strait and Kerch Bay, comprising 1,443 soundings conducted primarily from small vessels at drift stations. Additionally, a series of micro-surveys, including 83 stations, were performed in polluted areas of the studied water body. A detailed description of the dataset is available in [2]. Each sounding provides data on the vertical distribution of temperature, salinity, and concentrations of CDOM and TSM. These parameters were measured synchronously *in situ* with a depth resolution of 0.1 m.

In both international and domestic experimental research, CDOM concentrations are commonly measured in two units: optical (QSU) and weight (mg/L) (see the work [1] and [9–11]). These publications provide linear conversion formulas for these units across various regions, including the World Ocean, the Mediterranean Sea, and freshwater bodies, with high correlation coefficients ranging from 0.92 to 0.97. In this study, CDOM concentrations is expressed in QSU, with measurements taken across a depth range of 0.5–50 m. For analysis, 702 soundings from areas of the studied water body with depths greater than 2 m were selected.

All observations were conducted using the autonomous hydrobiophysical multiparameter optical sensing complex "Kondor" [2].

In this study, the term "pollution" encompasses two types of environmental contamination: *contamination* and *pollution*. C*ontamination* is defined as the presence of a substance in an environment where it is not naturally expected or where its concentration exceeds background levels. *Pollution* refers to contamination that causes or may cause adverse biological effects on local ecosystems.

A widely used method in global practice for identifying polluted areas in coastal waters of oceans, seas, and freshwater bodies relies on detecting local maxima (non-natural formations) in the concentration fields of studied substances [12]. In this study, CDOM and TSM of anthropogenic origin were identified in the horizontal distribution fields of their concentrations based on local maxima. The degree of anthropogenic impact on specific areas of the studied water body was assessed by calculating the ratio of maximum concentration to background concentration.

The analysis of the concentration fields of CDOM and TSM in polluted areas followed a systematic sequence. For each survey, areas with local maxima in surface layer concentrations of the studied substances were identified, and their vertical profiles, CDOM(z) and TSM(z), were selected and analyzed. Clusters of these profiles were then compiled across the entire dataset, and histograms of the frequency of CDOM and TSM concentrations in the surface layer were calculated. Subsequently, the most significant local maxima of CDOM and TSM concentrations were mapped, and their locations were correlated with the positions of industrial and economic facilities in the region to identify specific pollution sources for each area. The polluted areas and their associated sources were then

[1] Kraus, T., Bergamaschi, B., Pellerin, B. and Downing, B., 2011. What, Where, When and How Much? Combining Watershed NOM Source and Reactivity Studies with Real-Time Monitoring. In: USGS, 2011. *Proceedings of Fourth IWA Specialty Conference on Natural Organic Matter: From Source to Tap and Beyond, Costa Mesa, California, USA, 27-29 July 2011*, 42 p. [online] Available at: https://www.yumpu.com/en/document/view/24461784/presentation [Accessed: 01 July 2024].

[2] Ecodevice. *Ecodevice Catalogue. KONDOR "Multi*ZOND" Complex*. 2024. [online] Available at: http://ecodevice.com.ru/ecodevice-catalogue/multiturbidimeter-kondor [Accessed: 23 November 2024].

compared with findings from previous studies on pollution sources in the Kerch Strait, as reported in [1–5].

To evaluate the impact of shipping on anthropogenic suspended matter pollution in the strait, systematic monitoring of vessel wake trails along the main shipping channel was conducted. The expedition vessel was moored to a buoy marking the channel boundary, allowing water samples to be collected from the wake trail for TSM content analysis and visual assessment of trail composition and propagation velocity.

TSM concentrations during dredging operations at the Kerch Sea Trade Port were analyzed based on a micro-survey conducted by YugNIRO in the summer of 2000.

Discussion of results

Analysis of the structure of CDOM and TSM concentration fields for each survey revealed distinct characteristics in the Kerch Strait. Unlike the open waters of the Sea of Azov, the Black Sea, or unpolluted coastal areas, these fields are distorted by inhomogeneities – lenses of water with varying scales and volumes containing anthropogenic CDOM and TSM. These frequently observed formations appear as local maxima against the relatively homogeneous natural concentration fields of these substances (Fig. 1), which, according to [12], are not expected in natural settings.

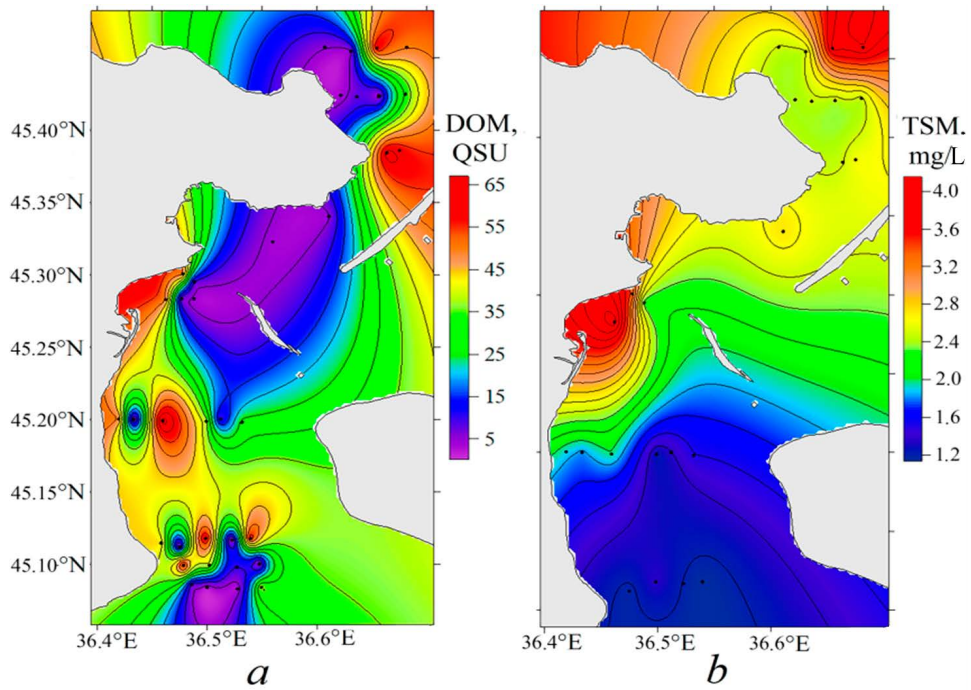

F i g. 1. Distribution of CDOM (*a*) and TSM (*b*) concentrations in the surface water layer, April 2008

Analysis of the vertical profiles, concentration distribution diagrams, and locations of the main local maxima in the Kerch Strait revealed the following. Both substances share similar vertical stratification characteristics. The CDOM(z) and TSM(z) profiles,

are non-monotonic function of depth, displaying a characteristic jagged shape that contrasts with the "smooth" profiles observed in unpolluted surrounding waters, indicating intrusions with elevated concentrations of these substances.

In the water column of polluted areas, distinct layers and interlayers with significantly elevated concentrations of CDOM and TSM are observed. These structural features, manifesting as local concentration maxima, indicate the presence of anthropogenic dissolved and suspended substances polluting the Kerch strait waters (Fig. 2).

The concentration distribution diagrams for CDOM and TSM in the surface water layer exhibit similar characteristics, displaying unimodal and right-skewed distribution. The most frequently occurring concentration for both substances is below the mean value, with modal concentration values having a similar frequency of approximately 30% (Fig. 2).

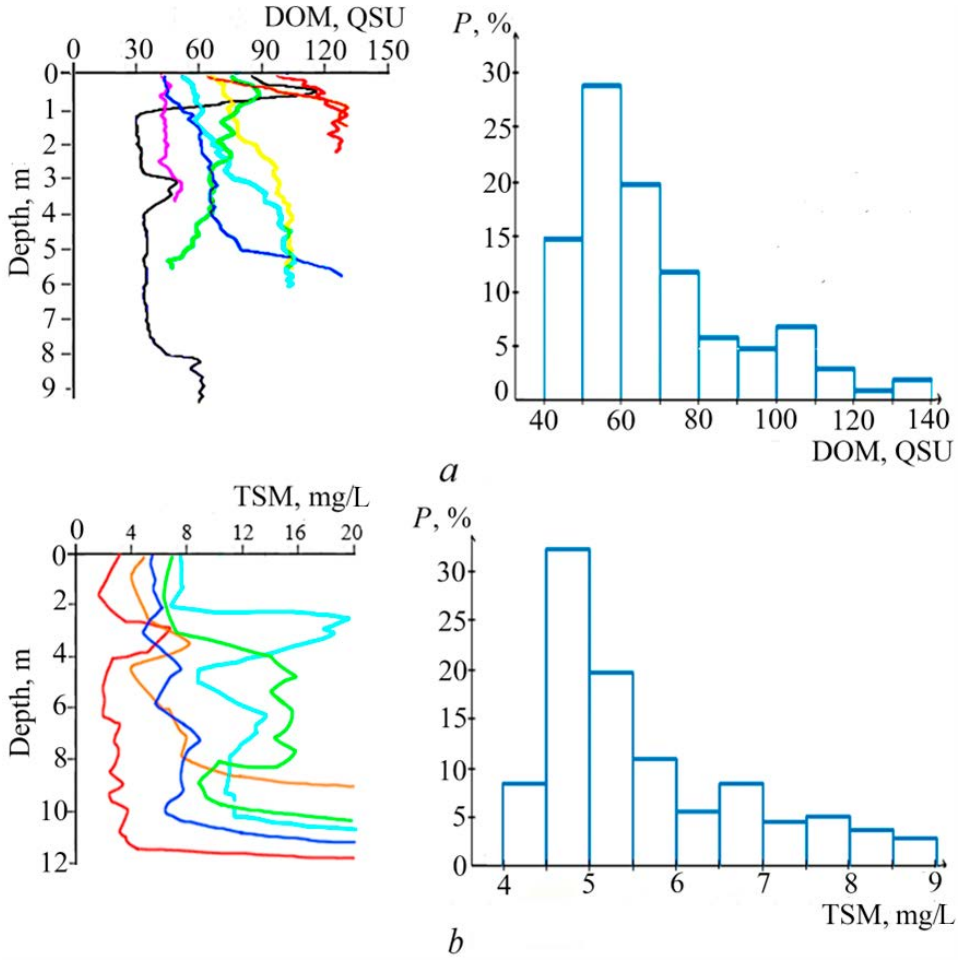

F i g. 2. Typical CDOM(*z*) profiles for the waters containing anthropogenic component (*left*), and histogram of CDOM concentration frequency in the sea surface layer (*right*) (*a*); the same characteristics for TSM (*b*)

Local maxima in the concentration fields of CDOM and TSM were observed in nearly all polluted areas of the Kerch Strait. This pattern is illustrated for three closed landfills of sediment from dredging operations (Fig. 3) and four polluted areas located near the wastewater treatment facilities of Kerch, in Kerch Bay, near the offshore transshipment site, and at the active sediment landfill near Cape Takil (Fig. 4). In the concentration fields of both substances, well-defined local maxima are evident, with their location closely aligned. The configuration and extent of these pollution patches vary.

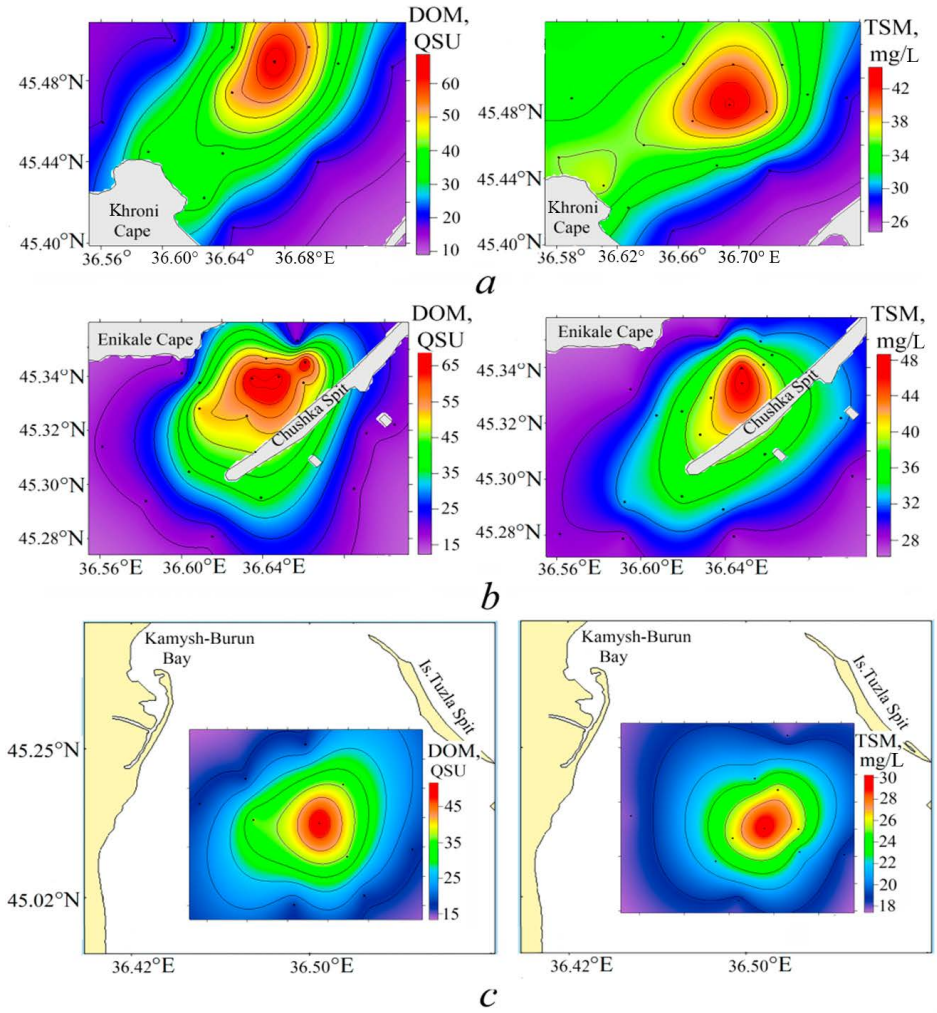

F i g. 3. CDOM (*left*) and TSM (*right*) concentrations in the bottom layer of dumping zones: *a* – landfill near Khroni Cape, May 2012; *b* – landfill near Chushka Spit, October 2013; *c* – landfill south of Tuzla Island, May 2005

The similarity in vertical structure, empirical concentration distribution characteristics (Fig. 2), and spatial alignment of local maxima (Figs. 3, 4) suggest that these “unnatural” structures in the Kerch Strait are formed under the influence of similar anthropogenic factors and sources polluting the aquatic environment.

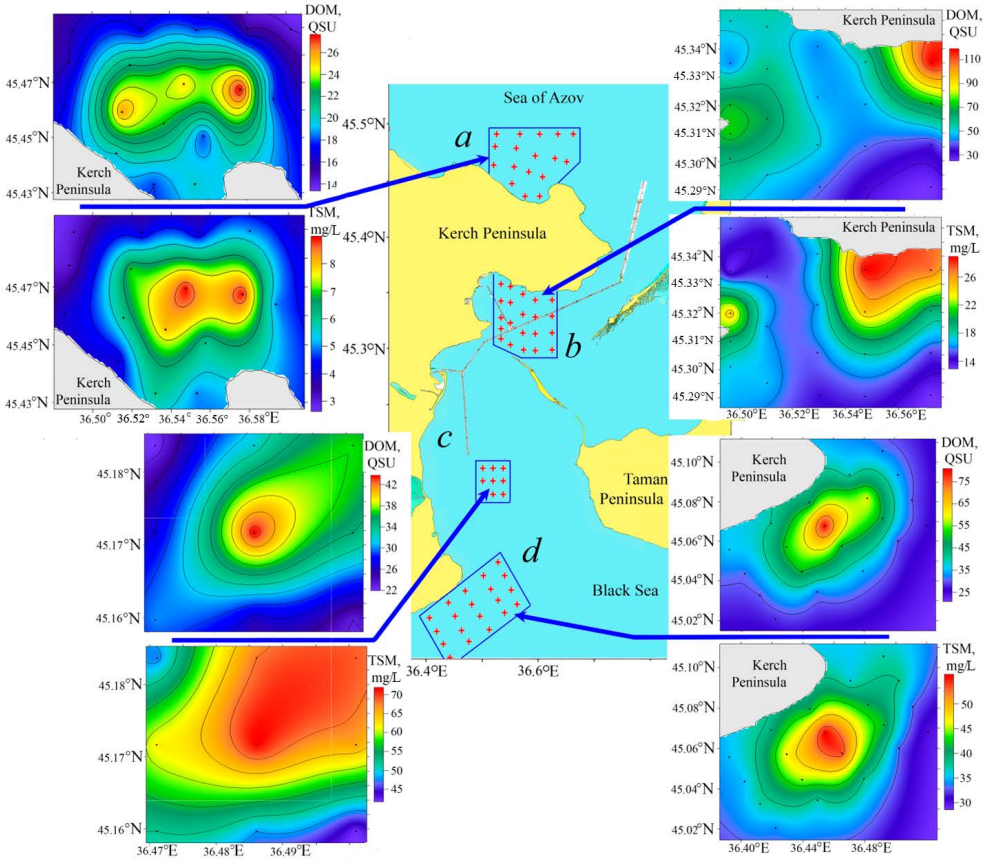

F i g. 4. CDOM and TSM concentrations in the polluted areas of the region under study: near treatment facilities, surface layer, May 2007 (*a*); Kerch Bay, the 3 m horizon, May 2005 (*b*); roadstead cargo handling site, bottom layer, September 2008 (*c*); operating landfill, bottom layer, June 2012 (*d*)

Water lenses containing anthropogenic CDOM and TSM were identified throughout the Kerch Strait and its adjacent areas. These lenses were mapped and presented as numbered patches in Fig. 5, while Fig. 6 illustrates the locations of the region's primary industrial and economic facilities, enabling the identification of pollution sources associated with each mapped area.

From all detected water lenses, 13 distinct large-scale lenses (horizontal extent of 1–6 nautical miles) contaminated with CDOM and TSM were identified and mapped (Fig. 5).

Lens *1*, located near the coast of the Azov pre-strait area in the vicinity of the Bondarenkovo wastewater treatment facilities for municipal wastewater from Kerch, exhibited a maximum CDOM concentration of 26 QSU, approximately twice the background level of 14 QSU, and a maximum TSM concentration of 8.8 mg/L, about three times higher than the background level of 2.8 mg/L (Figs. 4, *a*; 5, 6).

Lenses *2–5* are located in areas associated with sediment landfills (Figs. 3; 4, *d*; 5, 6). Sediment landfills, or dumping zones for sediment extracted during dredging, are known to cause significant harm to both living and non-living components of

marine ecosystems. The negative impacts of these landfills on marine ecology are actively studied globally. Contemporary literature addresses various aspects of this issue (e.g., [13–16]). Specifically, the impact of the active sediment landfill near Cape Takil as a source of pollution in the Kerch Strait and the adjacent Black Sea area has been investigated in [17].

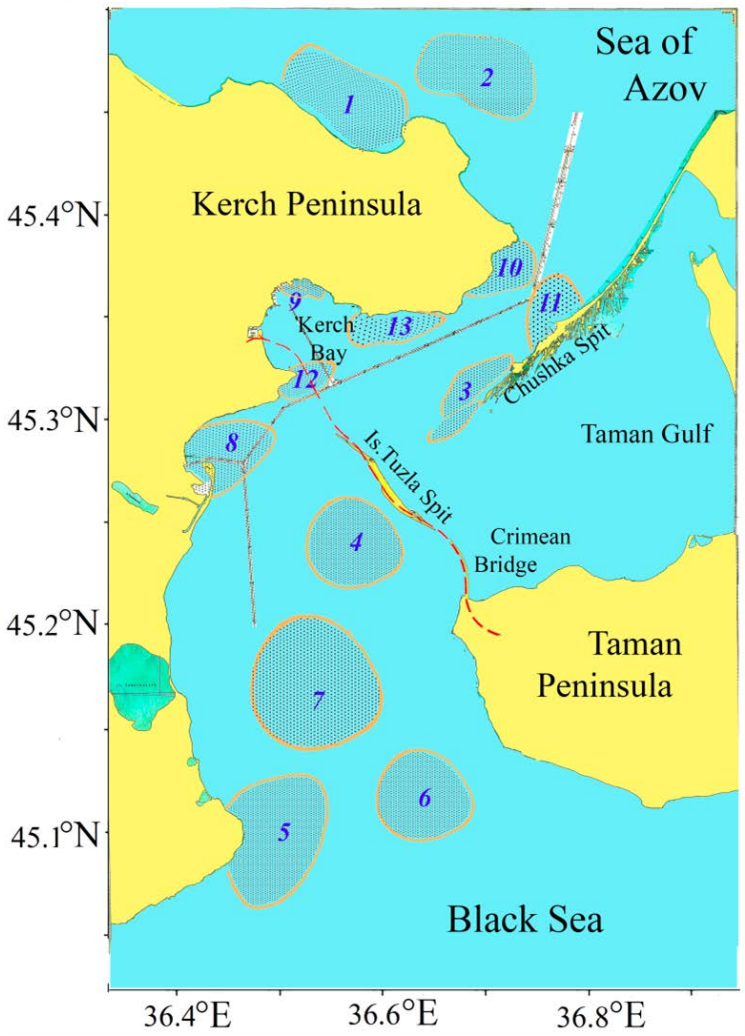

F i g. 5. Water lenses containing CDOM and TSM of anthropogenic origin

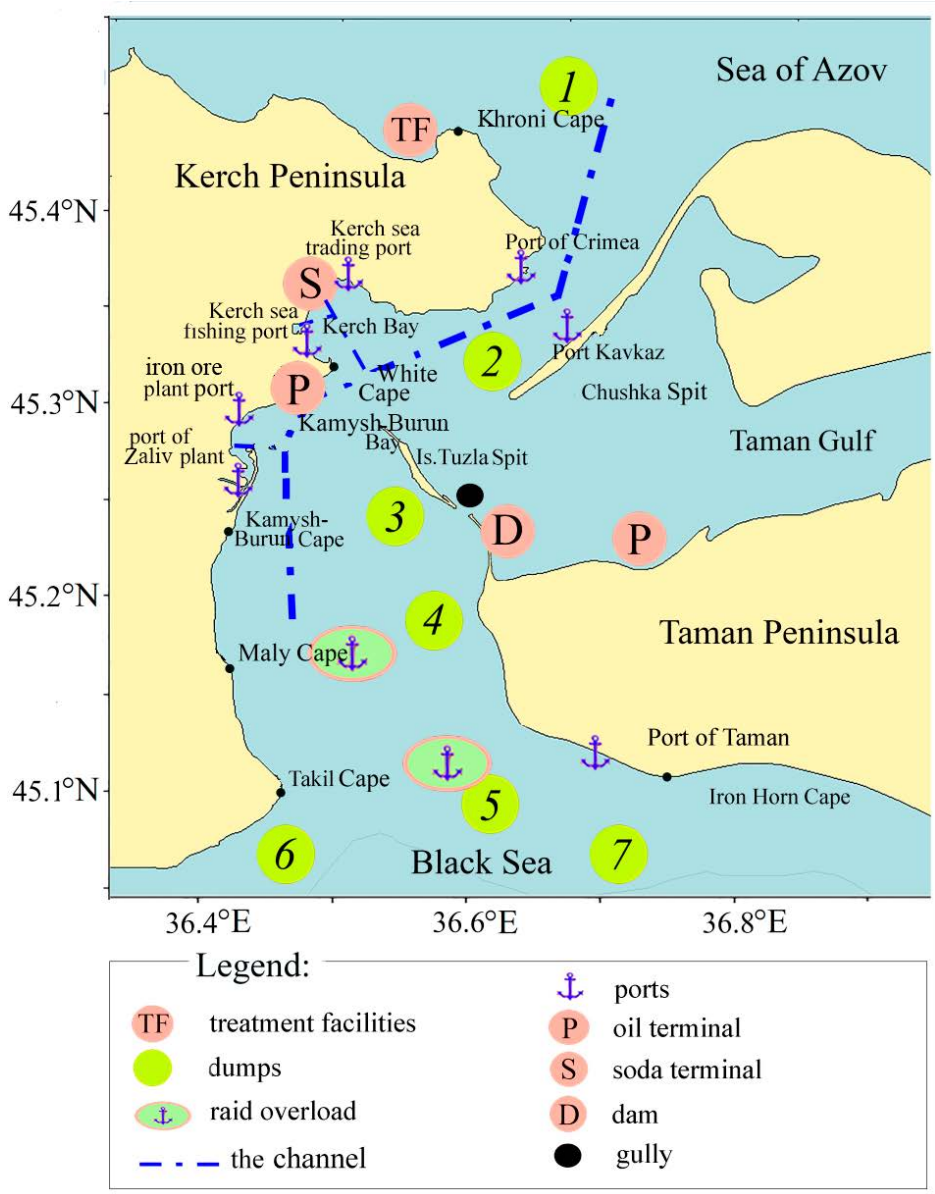

F i g. 6. Main objects polluting aquatic environment of the region

Micro-surveys were conducted in four of the seven known sediment landfill areas in the region (Figs. 3; 4, *d*), including two of the “oldest” landfills, closed in the 1970s, located northeast of Cape Khroni and south of Tuzla Island. Despite decades since the last sediment dumping, these areas exhibit persistent local maxima in the concentrations of CDOM and TSM in the bottom layer.

At the landfill near Cape Khroni, a maximum CDOM concentration of 60 QSU was recorded against a background level of 10 QSU, alongside a maximum TSM

concentration of 43 mg/L compared to a background of 25 mg/L (Fig. 3, *a*). Near the closed sediment landfill at the southern tip of the Chushka Spit, a local maximum CDOM concentration of 65 QSU was observed against a background of 15 QSU, with a maximum TSM concentration of 46 mg/L against a background of 28 mg/L (Fig. 3, *b*). Above the landfill south of Tuzla Island, corresponding concentrations were 50 and 15 QSU, 30 and 18 mg/L (Fig. 3, *c*).

The maximum CDOM concentrations in the studied closed landfills exceeded background levels by 3–6 times, while the ratio for TSM concentrations was significantly lower, approximately 2. This suggests that CDOM may be a more sensitive indicator of water pollution then TSM in these contexts.

According to [18], negative environmental consequences from dredging and dumping activities can persist long after operations cease, affecting both dredging sites and in dumping areas.

Lenses *6* and *7* were identified in areas corresponding to two offshore transshipment points (Figs. 4, *c*; 5, 6).

Micro-surveys conducted by YugNIRO and MHI at the western offshore transshipment point (site *451*) from 1997 to 2008 revealed the following. This site is a persistent source of anthropogenic suspended matter throughout the water column. In calm weather, the TSM concentration in this area was 1.5–3 times higher than the background level, with the polluted water lens estimated to have a horizontal extent of approximately 1 mile. Under strong southerly winds, the lens extended meridionally up to 6 miles, with TSM concentrations 5–6 times higher than the background level. Anthropogenic CDOM was also detected, with concentrations near the bottom reaching 45–52 QSU compared to a background level of 22 QSU (Fig. 4, *c*).

Lens *8* is located at the entrance to Kamysh-Burun Bay, corresponding to the polluted water area near the ports of the Zaliv plant and the iron ore plant. Anthropogenic CDOM and TSM were detected in this area during all large-scale surveys (Figs. 5, 6).

Lens *9* was identified in the western coastal part of Kerch Bay, associated with three adjacent facilities: the Kerch Sea Fishing Port, the soda terminal, and the Kerch Sea Trade Port (Figs. 5, 6).

Located between the trade and fishing ports of Kerch on the western shore of Kerch Bay, the soda terminal, commissioned in the late 20th century, has not been previously studied as a source of water pollution. This facility was identified as a pollution source based on visual observations during surveys in Kerch Bay, where a matte spot was consistently observed on the sea surface near the terminal. Single soundings in this area detected local maxima in the surface-layer concentrations of CDOM and TSM, with vertical profiles exhibiting shapes characteristic of polluted areas.

The small rivers Melek-Chesme, Bulganak, and Dzhardzhava, which flow into the western part of Kerch Bay, are significant sources of anthropogenic impact on the aquatic environment. The influence on CDOM concentration fields is discussed in [2].

Pollution in the Kerch Sea Trade Port and adjacent waters is associated with anthropogenic CDOM from the Bulganak River runoff, which flows through the industrial district of Kerch and enters the port's water area. Notably, in the port

approach channel, the highest CDOM concentration in the study region was recorded, ranging from 210–250 QSU [19].

Lenses *10* and *11*, located in the ferry crossing area near the approaches to the ports of Crimea and Caucasus (Figs. 5, 6), were consistently observed in the concentration fields of both analyzed variables across all surveys of the northern narrows of the Kerch Strait. A significant increase in background TSM concentrations, reaching up to ~ 10 mg/L, was also noted in this area during periods of intensive Kerch ferry crossing operations.

Lens *12* was discovered near Cape Beliy in the southeastern part of Kerch Bay, within the oil terminal area (Figs. 4, *b*; 5, 6). This lens extended throughout the water column, with a horizontal extent of ~ 3–4 miles. At a depth of 3 m, maximum concentration of CDOM reached 70 QSU and TSM reached 23 mg/L, compared to background levels of 30 QSU and 13 mg/L, respectively.

Lens *13*, *the* most extensive polluted water lens, was recorded in the northern part of Kerch Bay, having been transported into the strait from the Sea of Azov. Its origin and the concentration fields of CDOM, TSM, and dissolved petroleum products are detailed in [20] (Fig. 4, *b*; 5, 6).

The total area of lenses containing anthropogenic CDOM and TSM accounted for ~ 10–15% of the strait's water surface area, indicating a significant anthropogenic impact on the region's aquatic environment.

The construction of the Tuzla Dam in autumn of 2003, followed by artificial deepening of the bottom in the resulting ravine, emerged as a major anthropogenic source of TSM in the Kerch Strait (Fig. 6). This activity caused the collapse of the eastern part of Tuzla Island [21], leading to significant release of suspended matter due to intense erosion of the shore and seabed. The influence of this source extended across a substantial portion of the strait's waters.

According to the data from YugNIRO and reports from the Hydrographic Service, the completion of the Tuzla Dam led to a significant intensification of current systems and suspended matter flows in the Kerch Strait, accompanied by increased sedimentation in bays, ports, port approaches, and shipping channels. Approximately 5–10 years after the construction, when the morphometric characteristics of Tuzla Island shore and seabed had largely stabilized, the Tuzla ravine remained a significant source of TSM. Even under light to moderate winds, TSM concentrations near the island were several times (or even an order of magnitude) higher than background levels (Fig. 7). Prior to the construction of the dam, the waters in this part of the strait were noted for their high transparency and, according to long-term hydrochemical studies [1], were the cleanest in the region, classified as Class II marine water quality.

Despite significantly elevated TSM concentrations due to the influence of the Tuzla Dam, no anthropogenic CDOM was detected in the concentration field near Tuzla Island. Thus, unlike the other anthropogenic sources discussed, the Tuzla ravine did not contribute to anthropogenic CDOM pollution.

Globally, shipping and dredging, followed by the dumping of extracted sediment, are among the most significant sources (types of activity) of pollution in oceans, seas, and estuarine zones [22–25]. The evidence supporting this for the region under study is presented below.

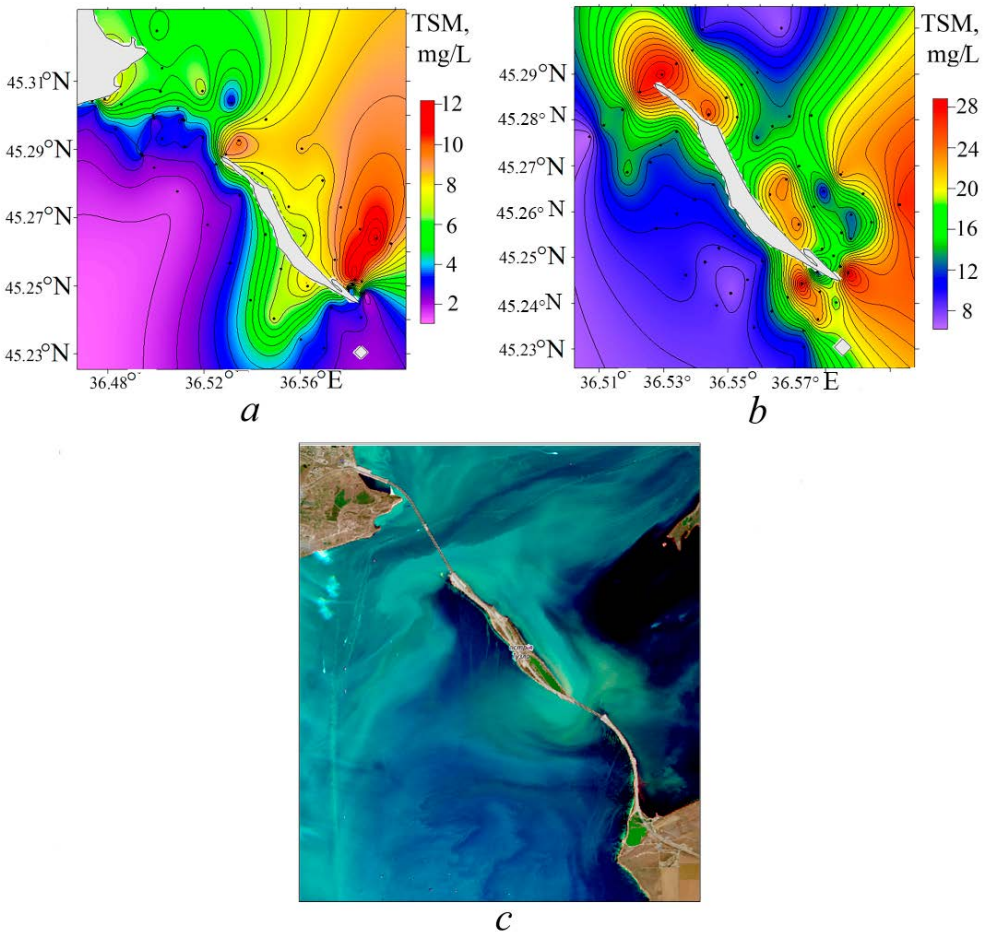

F i g. 7. Distribution of TSM, concentration in the sea surface layer in the region of Tuzla Island under weak and moderate south wind in April 2008 (*a*), and in April 2009 (*b*); satellite image of the Tuzla Island area on October 05, 2020 (*Sentinel*-2 *L2A* (4, 3, 2)) (*c*)

Water samples collected from the wake trails of large-tonnage ocean vessels (30–40 thousand tons) navigating shipping channels contained TSM concentrations of up to 270–300 mg/L, two orders of magnitude higher than background levels and the highest recorded during all expeditionary research. Visual observations revealed clumps of sediment, fragments of fishing gear (including broken floats, ropes, net pieces, wood fragments and planks), uprooted grass, and various debris, including plastic, rising and sinking in the water.

The wake trails of large-tonnage vessels generate powerful turbulent flows that expand behind the moving vessel and rapidly propagate toward the shores of the Kerch Strait, disturbing a significant portion of its waters. Additionally, alongside large-tonnage vessels, numerous smaller vessels of various types and purposes constantly navigate the strait.

During dredging operations in the Kerch Sea Trade Port in summer 2000 [19], a significant increase in TSM concentrations (210–260 mg/L) was recorded in

the port and adjacent waters, marking dredging as the second most significant pollution source after shipping.

Based on the characteristics of anthropogenic CDOM and TSM pollution sources in the Kerch Strait, combined with findings from prior studies [1–5], these sources can be ranked by significance as follows: fleet operations and supporting infrastructure, including shipping and shipping channels; dredging and dumping of extracted sediment; ports, offshore transshipment sites, cargo terminals, sediment landfills, polluted waters from the Sea of Azov, the Tuzla ravine, wastewater treatment facilities in Kerch, and polluted rivers flowing into the strait.

Comparison of our results with existing research on water pollution in the region demonstrates good agreement. Nearly all lenses containing anthropogenic CDOM and TSM correspond to polluted areas identified and studied in the long-term monitoring program by YugNIRO [2].

Exceptions include three previously unidentified areas, associated with the Tuzla Dam, the oil terminal, and the Port of Taman (Fig. 6). These facilities, as sources of water and sediment pollution in the strait, were investigated by YugNIRO [2], with the Port of Taman also studied by IO RAS [5]. In particular, the authors of [5] analyzed the propagation of suspended matter from dredging and dumping activities in the Port of Taman area, identifying these activities as the most significant source of anthropogenic suspended matter polluting in the southern Kerch Strait and the adjacent Black Sea pre-strait area.

Conclusion

Analysis of expedition data from 2001 to 2014 revealed the structure of concentration fields of anthropogenic CDOM and TSM in the Kerch Strait.

The analyzed substances are localized in distinct lenses with concentrations significantly exceeding background levels. The profiles of CDOM(z) and TSM(z) exhibit a characteristic intrusive shape, contrasting with the smooth profiles observed in unpolluted waters. Empirical distribution diagrams of CDOM and TSM concentrations in the upper water layer are similar, displaying unimodal, right-skewed distributions with comparable modal frequency.

The similarity in structural features of anthropogenic CDOM and TSM concentration fields, along with their empirical concentration distributions and spatial co-occurrence, indicates that these formations are driven by similar anthropogenic factors and pollution sources in the strait.

A total of 13 lenses, with horizontal extents of 1–6 miles, containing anthropogenic CDOM and TSM, were identified, covering 10–15% of the strait's water area. The sources of these lenses, including specific facilities and types of industrial and economic activities, were also determined.

The Tuzla ravine, a newly identified source of anthropogenic suspended matter, was analyzed separately. Unlike other anthropogenic pollution sources in the Kerch Strait, the Tuzla ravine did not contribute to anthropogenic CDOM concentrations. In the initial years following the dam's completion, anthropogenic suspended matter from the ravine dispersed across a substantial portion of the strait's waters, intensifying sedimentation in bays, shipping channels, port approaches, and ports. Even 5–10 years after its formation, the ravine remained a significant source of

anthropogenic suspended matter, maintaining TSM concentrations near Tuzla an order of magnitude higher than the surrounding background levels.

Analysis of the Kerch Strait revealed that the primary sources of pollution are associated with fleet operation and supporting infrastructure, including shipping and shipping channels, dredging and dumping of extracted sediment, ports, offshore transshipment sites, cargo terminals, and sediment landfills. Additional sources include polluted waters from the Sea of Azov, the Tuzla ravine, wastewater treatment facilities in Kerch, and runoff from polluted rivers flowing into Kerch Bay.

Comparison of these findings with existing studies on water pollution in the region shows strong agreement, with nearly all identified lenses containing anthropogenic CDOM and TSM corresponding to polluted areas previously documented and studied by YugNIRO through long-term hydrochemical monitoring programs.

REFERENCES

1. Shybaeva, S.A., Ryabinin, A.I., Ilyin, Y.P. and Lomakin, P.D., 2011. Kerch Strait Hydrochemistry Regime and Pollution in 1979–2009. *Morskoy Ecologicheskiy Zhurnal*, 10(4), pp. 77-87 (in Russian).
2. Lomakin, P.D., Zhugailo, S.S., Panov, B.N., Chepyzhenko, A.I. and Chepyzhenko, A.A., 2020. The Main Objects of Anthropogenic Impact on the Kerch Strait Water Environment According to Hydrooptical and Hydrochemical Observation Data. *Monitoring Systems of Environment*, 4, pp. 75-85. https://doi.org/10.33075/2220-5861-2020-4-75-85 (in Russian).
3. Kotelyanets, E.A. and Konovalov, S.K., 2012. Heavy Metals in Bottom Sediments of the Kerch Strait. *Morskoy Gidrofizicheskiy Zhurnal*, (4), pp. 50-60 (in Russian).
4. Zavialov, P.O., Zavialov, I.B., Izhitskiy, A.S., Izhitskaya, E.S., Konovalov, B.V., Krementskiy, V.V., Nemirovskaya, I.A. and Chasovnikov, V.K., 2022. Assessment of Pollution of the Kerch Strait and Adjacent Black Sea Area Based on Field Measurements of 2019–2020. *Oceanology*, 62(2), pp. 162-170. https://doi.org/10.1134/S0001437022020175
5. Ivanov, A.Yu., Khlebnikov, D.V., Konovalov, B.V., Klimenko, S.K. and Terleeva, N.V., 2021. Kerch Strait and Its Technogenic Pollution: Possibilities of Optical and Radar Remote Sensing. *Ecology and Industry of Russia*, 25(8), pp. 21-27. https://doi.org/10.18412/1816-0395-2021-8-21-27 (in Russian).
6. Eisma, D., 2011. *Suspended Matter in the Aquatic Environment.* Berlin, Heidelberg: Springer, 315 p. https://doi.org/10.1007/978-3-642-77722-6
7. Boss, E., Pegau, W.S., Zaneveld, J.R.V. and Barnard A.H., 2001. Spatial and Temporal Variability of Absorption by Dissolved Material at a Continental Shelf. *Journal of Geophysical Research: Oceans*, 106(C5), pp. 9499-9507. https://doi.org/10.1029/2000JC900008
8. Tedetti, M., Longhitano, R., Garcia, N., Guigue, C., Ferretto, N. and Goutx, M., 2012. Fluorescence Properties of Dissolved Organic Matter in Coastal Mediterranean Waters Influenced by a Municipal Sewage Effluent (Bay of Marseilles, France). *Environmental Chemistry*, 9(5), pp. 438-449. https://doi.org/10.1071/EN12081
9. Saraceno, J.F., Pellerin, B.A., Downing, B.D., Boss, E., Bachand, P.A.M. and Bergamaschi, B.A., 2009. High-Frequency in Situ Optical Measurements during a Storm Event: Assessing Relationships between Dissolved Organic Matter, Sediment Concentrations, and Hydrologic Processes. *Journal of Geophysical Research: Biogeosciences*, 114(G4), G00F09. https://doi.org/10.1029/2009JG000989
10. Downing, B.D., Pellerin, B.A., Bergamaschi, B.A., Saraceno, J.F., Kraus, T.E.C., 2012. Seeing the Light: The Effects of Particles, Dissolved Materials, and Temperature on in Situ Measurements of DOM Fluorescence in Rivers and Streams. *Limnology and Oceanography: Methods*, 10(10), pp. 767-775. https://doi.org/10.4319/lom.2012.10.767

11. Pugach, S.P. and Pipko, I.I., 2012. Dynamics of Colored Dissolved Matter on the East Siberian Sea Shelf. *Doklady Earth Sciences*, 448(1), pp. 153-156. https://doi.org/10.1134/S1028334X12120173

12. Chapman, P.M., Hayward, A. and Faithful, J., 2017. Total Suspended Solids Effects on Freshwater Lake Biota Other than Fish. *Bulletin of Environmental Contamination and Toxicology*, 99(5), pp. 423-427. https://doi.org/10.1007/s00128-017-2154-y

13. Stronkhorst, J., Ariese, F., Van Hattum, B., Postma, J.F., De Kluijver, M., Den Besten, P.J., Bergman, M.J.N., Daan, R., Murk, A.J. [et al.], 2003. Environmental Impact and Recovery at Two Dumping Sites for Dredged Material in the North Sea. *Environmental Pollution*, 124(1), pp. 17-31. https://doi.org/10.1016/S0269-7491(02)00430-X

14. Simonini, R., Ansaloni, I., Cavallini, F., Graziosi, F., Iotti, M., Massamba N'Siala, G., Mauri, M., Montanari, G., Preti, M. [et al.], 2005. Effects of Long-Term Dumping of Harbor-Dredged Material on Macrozoobenthos at Four Disposal Sites along the Emilia-Romagna Coast (Northern Adriatic Sea, Italy). *Marine Pollution Bulletin*, 50(12), pp.1595-1605. https://doi.org/10.1016/j.marpolbul.2005.06.031

15. Van der Wal, D., Forster, R.M., Rossi, F., Hummel, H., Ysebaert, T., Roose, F. and Herman, P.M.J., 2011. Ecological Evaluation of an Experimental Beneficial Use Scheme for Dredged Sediment Disposal in Shallow Tidal Waters. *Marine Pollution Bulletin*, 62(1), pp. 99-108. https://doi.org/10.1016/j.marpolbul.2010.09.005

16. Donázar-Aramendía, I., Sánchez-Moyano, J.E., García-Asencio, I., Miró, J.M., Megina, C. and García-Gómez, J.C., 2018. Impact of Dredged-Material Disposal on Soft-Bottom Communities in a Recurrent Marine Dumping Area near to Guadalquivir Estuary, Spain. *Marine Environmental Research*, 139, pp. 64-78. https://doi.org/10.1016/j.marenvres.2018.05.010

17. Petrenko, O.A., Sebakh, L.K. and Fashchuk, D.Ya., 2002. Some Environmental Consequences of Soil Dumping in the Black Sea as a Result of Dredging Operations in Kerch Strait. *Water Resources*, 29(5), pp. 573-586. https://doi.org/10.1023/A:1020338201171

18. Quan Tri, D., Kandasamy, J. and Cao Don, N., 2019. Quantitative Assessment of the Environmental Impacts of Dredging and Dumping Activities at Sea. *Applied Sciences*, 9(8), 1703. https://doi.org/10.3390/app9081703

19. Lomakin, P.D., 2019. Influence of Dredging and Dumping Zones on the Ecological Situation in the Kerch Strait. *Physical Oceanography*, 26(2), pp. 147-156. https://doi.org/10.22449/1573-160X-2019-2-147-156

20. Lomakin, P.D., Chepyzhenko, A.I., Panov, B.N. and Borovskaya, R.V., 2006. Hydrological Conditions and Characteristics of Pollution of Kerch Strait Water in May 2005 on Base of Contact Measurements and Satellite Observations. *Issledovanie Zemli iz Kosmosa*, (4), pp. 27-34 (in Russian).

21. Stepanyak, Yu.D. and Bashkirtseva, H.V., 2009. Morphology and Lythodynamics of the Tuzla Spit Island under the Data of Remote Observations. *Ecological Safety of Coastal and Shelf Zones and Comprehensive Use of Shelf Resources*, (20), pp. 100-107 (in Russian).

22. Zhang, C. and Yang, J.-q., 2024. Prevention and Control of Ship-Source Pollution in the Arctic Shipping Routes: Challenges and Countermeasures. *Environmental Science and Pollution Research*, 31(28), pp. 40436-40444. https://doi.org/10.1007/s11356-023-30817-w

23. Fan, L., Yang, H. and Zhang, X., 2024. Targeting the Effectiveness Assessment of the Emission Control Policies on the Shipping Industry. *Sustainability*, 16(6), 2465. https://doi.org/10.3390/su16062465

24. Aziz, H.A., Ariffin, K.S., Wang, M-H.S. and Wang, L.K., 2024. Dredging and Mining Operations, Management, and Environmental Impacts. Handbook of Environmental Engineering Series, vol. 28. In: L. K. Wang, M. S. Wang and Y. T. Hung, eds., 2024. *Industrial Waste Engineering. Handbook of Environmental Engineering*. Cham: Springer, pp. 333-396. https://doi.org/10.1007/978-3-031-46747-9_8

25. Wang, X.H., 2024. *Dynamic Response of Coasts and Estuaries to Human Impacts. Problems and Solutions*. Coastal Research Library Series, vol. 40. Cham: Springer Nature, 118 p.

Submitted 16.12.2024; approved after review 17.03.2025;
accepted for publication 15.05.2025.

About the authors:

Pavel D. Lomakin, Leading Research Associate, Marine Hydrophysical Institute of RAS (2 Kapitanskaya Str., Sevastopol, 299011, Russian Federation), DSc. (Geogr.), Professor, **ResearcherID: V-7761-2017**, **Scopus Author ID: 6701439810**, **SPIN-code: 5419-9884**, p_lomakin@mail.ru

Anna A. Chepyzhenko, Junior Research Associate, Marine Hydrophysical Institute of RAS (2 Kapitanskaya Str., Sevastopol, 299011, Russian Federation), **ORCID ID: 0000-0002-0789-4719**, **WOS ResearcherID: F-9651-2014**, **Scopus Author ID: 56536937200**, **SPIN-code: 4231-8711**, annachep87@yandex.ru

Alexey I. Chepyzhenko, Senior Research Associate, Marine Hydrophysical Institute of RAS (2 Kapitanskaya Str., Sevastopol, 299011, Russian Federation), CSc. (Tech.), **ORCID ID: 0000-0002-6763-7140**, **WOS ResearcherID: AAG-7929-2020**, **Scopus Author ID: 6504344211**, **SPIN-code: 3599-9653**, ecodevice@yandex.ru

Contribution of the co-authors:

Pavel D. Lomakin – formulation of research objectives and tasks, qualitative analysis and interpretation of results, discussion of findings, article text preparation, formulation of conclusions

Anna A. Chepyzhenko – preparation of graphical materials, processing and description of research results, participation in article discussion, final text revision

Alexey I. Chepyzhenko – methodology development, formulation of research objectives and tasks, qualitative analysis of results, description of research findings, discussion of results, formulation of conclusions

The authors have read and approved the final manuscript.
The authors declare that they have no conflict of interest.

ISSN 1573-160X, *PHYSICAL OCEANOGRAPHY*, Vol. 32, Iss. 4, pp. 508-523 (2025)

published in *Morskoy Gidrofizicheskiy Zhurnal*, 2025, Vol. 41, Iss. 4, pp. 484–500

Original article

Impact of Tide on Hydrological Conditions near the La Perouse Strait Based on Instrumental Measurements

G. V. Shevchenko [1, 2, ✉], V. E. Maryzhikhin [1]

[1] *Russian Federal Research Institute of Fisheries and Oceanography, Sakhalin Branch of VNIRO (SakhNIRO), Yuzhno-Sakhalinsk, Russian Federation*

[2] *Institute of Marine Geology and Geophysics, Far Eastern Branch of Russian Academy of Sciences, Yuzhno-Sakhalinsk, Russian Federation*

✉ *Shevchenko_zhora@mail.ru*

Abstract

Purpose. This study aims to investigate the influence of the tidal-driven Okhotsk Sea water inflow through the La Perouse Strait on the hydrological conditions along the western coast of the Krillon Peninsula (Southwestern Sakhalin) during the warm season.

Methods and Results. The material for investigation is based on the instrumental measurement data on sea current velocities, sea level fluctuations, and seawater temperature and salinity near the Gorbusha River mouth collected in May – October 2024. The results of oceanographic surveys performed in the coastal zone (up to the 20 m isobath) along transects perpendicular to the coast were also used. Additionally, the data on current velocities, water temperature, and salinity collected at the autonomous buoy station "Astarta", located in the central part of the La Perouse Strait (May – June 1999), as well as the meteorological observation data from the Nevelsk weather station (May – October 2024) were utilized. Against the backdrop of diurnal fluctuations, a semi-monthly cyclicity of the Okhotsk Sea water intrusion was identified: a 10–11-day phase of intensified inflow to the Southwest Sakhalin shelf during periods of tropical tides, followed by a 3–4-day period of marked weakening during equatorial tides. Standard methods of statistical and harmonic analysis were applied to the observation data.

Conclusions. The area off the western coast of the Krillon Peninsula is significantly influenced by the Okhotsk Sea water entering through the La Perouse Strait, driven by strong diurnal tidal currents. The diurnal temperature fluctuations can reach 10 °C, and salinity variations can reach 2 psu. An unexpected finding of this study was the identification of not only lower salinity but also higher temperature in the Okhotsk Sea water compared to those of the West Sakhalin Current, which flows southward along the southwestern coast of Sakhalin.

Keywords: La Perouse Strait, water exchange, cold water belt, seawater temperature, salinity, current, tide, West Sakhalin current

Acknowledgements: The authors express their gratitude to the staff of the Hydrobiology Laboratory and the leading researcher of Salmon Fish Laboratory, Dr. Sci. (Biol.) V. S. Labay, for their assistance in collecting observational materials and preparing certain illustrations (Fig. 7–9). This study was conducted within the framework of the assignment for implementation of NIOKR of the Sakhalin branch of FSBSI "VNIRO" ("SakhNIRO"): part II, section 7 of state assignment of FSBSI "VNIRO" 076-00001-24-01.

For citation: Shevchenko, G.V. and Maryzhikhin, V.E., 2025. Impact of Tide on Hydrological Conditions near the La Perouse Strait Based on Instrumental Measurements. *Physical Oceanography*, 32(4), pp. 508-523.

Introduction

Water exchange through the La Perouse Strait (defined here as the strait between the southwestern tip of Sakhalin Island, Cape Krillon, and the northernmost point of Hokkaido Island, Japan, Cape Soya) plays a crucial role in shaping the hydrological regime of the adjacent waters of the Sea of Japan and the Okhotsk Sea. During the warm season, warm, saline water from the Sea of Japan flow through the strait, giving rise to the Soya Current (an Okhotsk branch of the warm Tsushima Current). In contrast, during the cold season, an inflow of the Okhotsk Sea water is observed along the western coast of the Krillon Peninsula, characterized by lower temperatures and salinity compared to the Sea of Japan waters [1].

Water exchange processes through the La Perouse Strait, characterized by significant seasonal variability, are strongly influenced by tidal currents, which reach anomalously high velocities of up to 3 knots [2–4]. In study [5], analysis of seawater temperature measurements, obtained by attaching an instrument to a set net near Cape Kuznetsov, revealed significant fluctuations in this parameter caused by tidal influences. Studies [5, 6] established a correlation between the extent of the cold water belt off the western coast of the Krillon Peninsula (sometimes referred to as the “Makarov Spot”, named after the renowned Russian naval commander and oceanographer who first described its formation mechanism) and tidal phases, with notable expansion during tropical tides and contraction during equatorial tides. In regions dominated by diurnal tides, semi-monthly variations in sea level fluctuations are linked not to the relative positions of the Moon and Sun (as during syzygy and quadrature) but to changes in the Moon’s declination as it approaches the tropics or the equator.

Until recently, the specific pathways of the Okhotsk Sea water propagation along the southwestern coast of Sakhalin Island under tidal influence, as well as its characteristics and differences from the surrounding Sea of Japan waters, had not been described. Instrumental measurements of sea current velocities, water temperature, and salinity, conducted by the Sakhalin Branch of “VNIRO” from May to October 2024 near the Gorbusha River mouth (approximately 10 km north of Cape Kuznetsov and 30 km from the La Perouse Strait; Fig. 1), have provided new insights into these processes.

Thus, the study aims to investigate the influence of the tidal-driven Okhotsk Sea water inflow through the La Perouse Strait during the warm season on the hydrological conditions along the western coast of the Krillon Peninsula, Southwestern Sakhalin.

To achieve this goal, the following tasks were addressed:

– analyze instrumental measurements of sea level fluctuations and current velocities near the Gorbusha River mouth (western coast of the Krillon Peninsula) to determine the role of tidal components in their variability;

– examine variations in temperature and salinity during ebb and flood tides using instrumental measurements and coastal oceanographic surveys to identify the role of the Okhotsk Sea water in shaping hydrological conditions in the area;

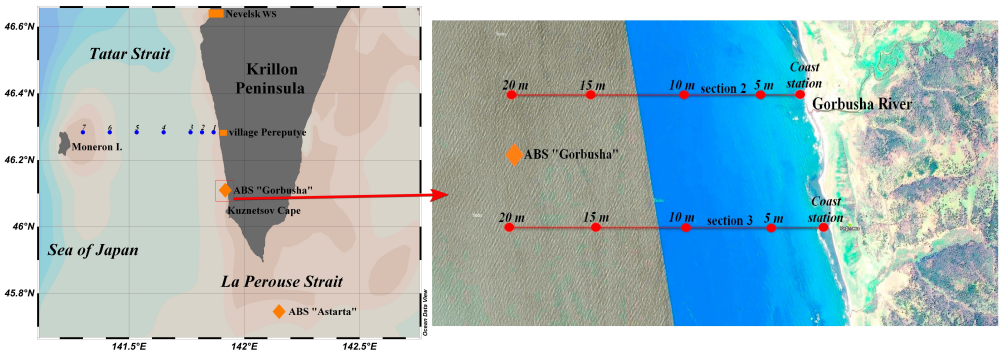

F i g. 1. Map of the study area. Diamonds indicate the locations of autonomous buoy stations, and dots represent stations along the standard oceanographic section from Pereputye village to Moneron Island (*on the left*) and coastal sections 2 and 3 (*on the right*)

– analyze historical instrumental measurements to identify the presence of the Okhotsk Sea water in the La Perouse Strait during tides and compare its temperature and salinity with oceanographic parameters along the western coast of the Krillon Peninsula;

– determine the thermohaline characteristics of the West Sakhalin Current (WSC) and compare them with those of the Okhotsk Sea water entering the southwestern shelf of Sakhalin Island during tides.

Observational data and analysis methods

The primary data for this study consisted of sea current velocity vectors, bottom hydrostatic pressure (sea level fluctuations), and seawater temperature and salinity recorded at the autonomous buoy station (ABS) “Gorbusha”, deployed near the mouth of the Gorbusha River (coordinates: 46°07′N, 141°54′E; location is shown in Fig. 1). The sea depth at the deployment site was approximately 20 m, with measuring equipment positioned in the bottom layer at approximately 18 m. The station was deployed from a motorboat on May 14 and retrieved on October 18, 2024, covering almost the entire warm season. The ABS was equipped with a Doppler acoustic current meter (Argonaut MD) and a SeaBird hydrological mini-probe. Hydrophysical parameters were recorded hourly, yielding 3,765 data points.

Harmonic constants for the amplitudes and phases of the main tidal waves (four diurnal: $Q1$, $O1$, $P1$, $K1$; and four semidiurnal: $N2$, $M2$, $S2$, $K2$) were calculated using the least squares method [7]. The length of the data series enabled direct computation of all harmonic parameters without corrections. A similar procedure was applied to the projections of measured current velocity vectors onto the parallel

and meridian axes. Residual components of sea level fluctuations and currents were determined by subtracting the predicted tide from the original sea level or current velocity projection series. Tidal, residual, and total fluctuations were analyzed using standard statistical methods.

Additional data included measurements of current velocities, water temperature, and salinity from the ABS "Astarta", deployed in the central part of the La Perouse Strait in 1999. The station was equipped with two AADERAA RCM-4 meters installed at depths of 15 m and 45 m (location is shown in Fig. 1). These data were previously analyzed [3, 8], but salinity was not examined in those studies. In this study, significant attention was given to salinity variations (or synchronous variations in temperature and salinity) to compare the thermohaline characteristics of the Okhotsk Sea water near the Gorbusha River mouth with those in the La Perouse Strait. Hourly measurements at 15 m depth from May 1 to July 15, 1999, were analyzed.

To investigate the water structure characteristics in the study area, oceanographic soundings were conducted along four cross-shore sections (from the shore to the 20 m isobath, approximately 2.4 km from the shoreline). Measurements were obtained using a portable ACTD-CMP probe deployed from a motorboat. Vertical sections were constructed using Surfer software. Results from two sections (2 and 3) near the Gorbusha River mouth (Fig. 1) are discussed below.

Meteorological conditions during the measurement period were characterized using data from the Nevelsk coastal weather station (May – October 2024), accessed from www.rp5.ru. Although the station is approximately 60 km north of the Gorbusha River mouth, it lies within the same orographic sector of the mountain range, suggesting similar wind flow characteristics. In contrast, the closer Cape Krillon weather station (20 km south of the study area) is separated by this range, resulting in different airflow patterns. Consequently, data from the Nevelsk station were preferred.

The characteristics of the WSC water were determined using long-term average temperature and salinity values along the standard oceanographic section from Pereputye village to Moneron Island (Fig. 1) for various months (March – December) [9, 1].

Results and discussion

Variations in hydrophysical parameters near the Gorbusha River Mouth. Fig. 2 represents graphs of total (measured) sea level variations and their residual component, obtained by subtracting the predicted tide from the original series. Tides play a dominant role in sea level fluctuations, accounting for over 76% of the variance (energy) of the measured series. Diurnal tides predominate in the study area, with the tidal character index, defined as the ratio of the summed amplitudes of the two main diurnal waves and two main semidiurnal waves:

$$R = (HO1 + HK1)/(HM2 + HS2) = 2.1.$$

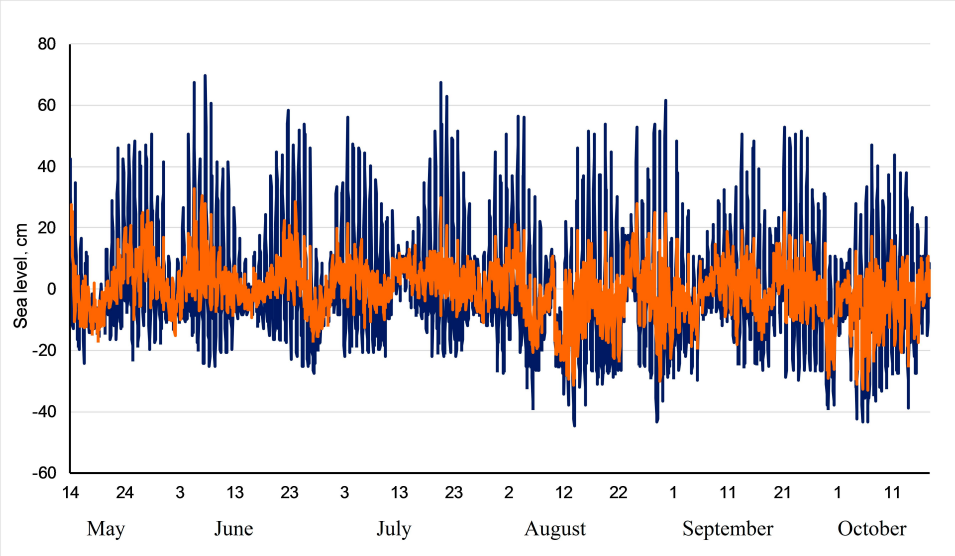

F i g. 2. Fluctuations of total level *L* (blue curve) and its residual component *L-rs* (orange curve) based on the ABS "Gorbusha" data, May – October 2024

The *O*1 wave exhibits the highest amplitude (approximately 14 cm), which is unusual as the main diurnal *K*1 wave typically dominates. Extreme tidal fluctuations were estimated by predicting a 100-year tidal series, revealing a maximum positive deviation of +49 cm and a negative deviation of −30 cm from the mean sea level, with a total fluctuation range of 79 cm – nearly twice that observed at the Nevelsk tide gauge station. This asymmetry between positive (flood) and negative (ebb) deviations indicates a shorter flood duration compared to ebb. Notably, the amplitude of the main diurnal *K*1 wave is smaller than that of the *O*1 wave, a rare observation.

Residual fluctuations are also significant, with extreme deviations from the mean sea level reaching ±33 cm. Synoptic-scale variations with a period of approximately two weeks and a notable presence of long-wave noise are evident in these fluctuations.

Fig. 3 shows graphs of total current variations and their residual component (projected onto the parallel). The shoreline in the study area is nearly meridional, resulting in relatively small zonal current components, particularly for eastward flows (maximum eastward flow velocity: 15 cm/s; westward: 26 cm/s). The tidal component's contribution was minimal, with wind-driven drift currents dominating. Synoptic-scale fluctuations (approximately two weeks) and long-wave noise are evident, consistent with the residual sea level component.

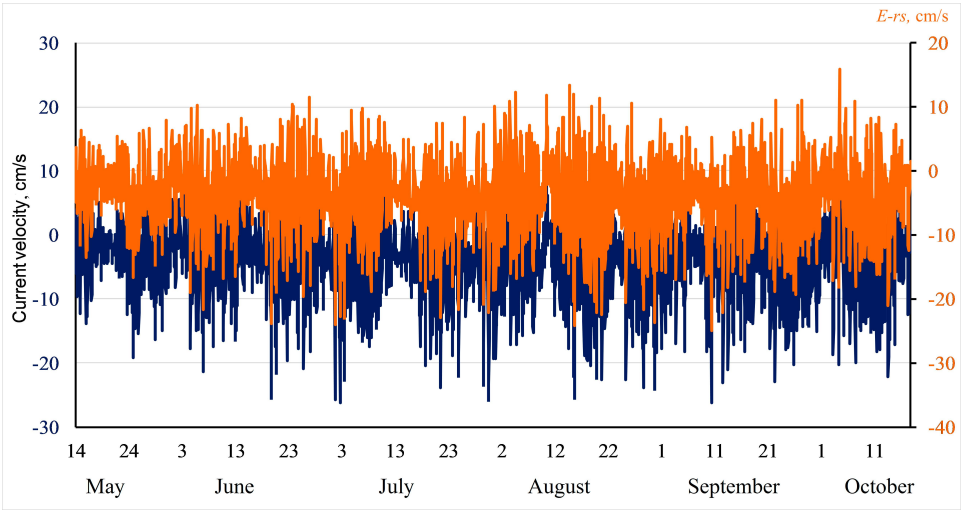

F i g. 3. Variations of projections of the vectors of total current *E* (blue curve) and its residual component *E-rs* (orange curve) onto the parallel based on the ABS "Gorbusha" data, May – October 2024

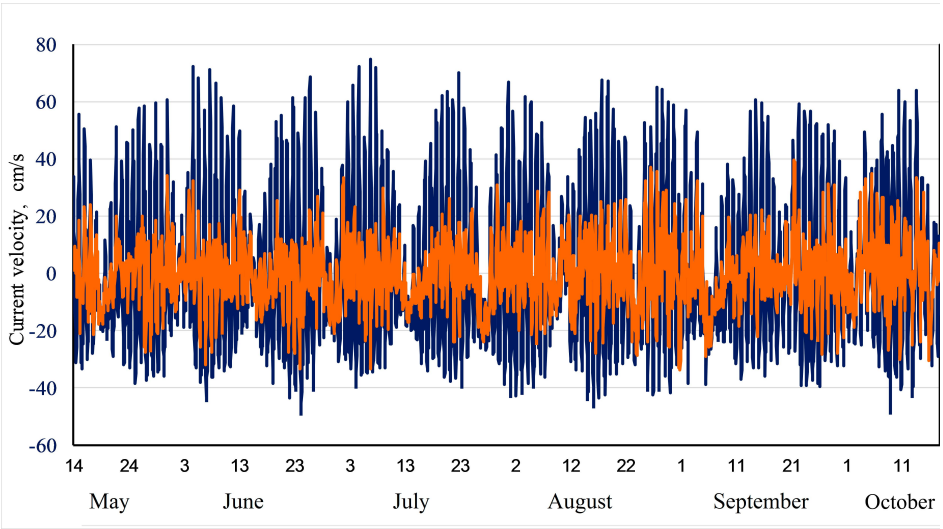

F i g. 4. Variations of projections of the vectors of total flow (blue curve) and its residual component (orange curve) onto the meridian based on the "Gorbusha" ABS data, May – October 2024

Fig. 4 presents similar graphs for the meridional current component. Total current velocities here are much higher than those of the cross-shore zonal component: the maximum northward velocity reaches 75 cm/s, and the maximum southward velocity reaches 49 cm/s. The alongshore component is dominated by tidal currents, accounting for over 82% of the time series variance. Diurnal waves play the predominant role in tidal currents: the amplitudes of the main diurnal waves are 18 cm/s for *K*1 and 21 cm/s for *O*1, with an amplitude ratio $R = 4.4$ (twice that

for sea level). Tidal currents are reversible, with ellipses of the main waves compressed and elongated along the meridian. The asymmetry between northward and southward currents is similar to that between positive and negative tidal level deviations: northward currents are stronger, while southward currents last longer.

Residual currents are also intense, with maximum northward and southward velocities of 40 cm/s and 34 cm/s, respectively. The observed variations additionally exhibit a synoptic component with a period of approximately two weeks, along with high-frequency noise producing distinct spikes. The frequency of these spikes increases notably during the autumn period.

The most unexpected result was the exact correlation between the maximum tidal level and the maximum northward current velocity (correlation coefficient between the total level series and the original meridional current component series: 0.78; for tidal components: 0.97). Unlike typical dynamics where the maximum level corresponds to weak currents (“still water”), an anomalous persistence of flow was observed near the Gorbusha River mouth. This phenomenon currently lacks a convincing explanation but suggests northward tidal energy transport, which is characteristic of areas with significant dissipation, highlighting the unique nature of tidal processes along the southwestern coast of Sakhalin.

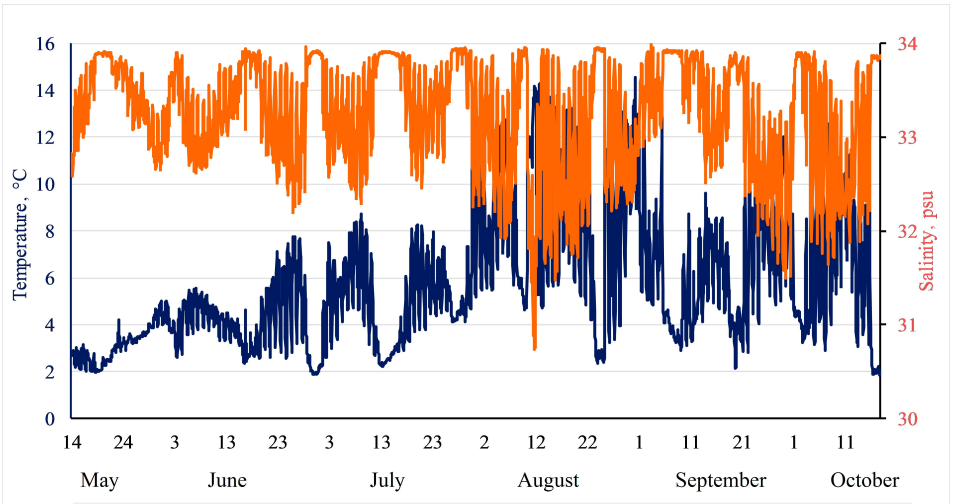

F i g. 5. Variations in seawater temperature (blue curve) and salinity (orange curve) based on the ABS “Gorbusha” data, May – October 2024

From the perspective of assessing the assimilative capacity of the water body, the most significant parameters of interest were the variations in seawater temperature and salinity (Fig. 5). These variations were substantial and complex. Temperature generally increased from May to late August or early September (the peak warming period) and then declined gradually. No similar variations were

observed in salinity. The remaining oceanographic parameters exhibited diurnal fluctuations that were strictly antiphased (correlation coefficient: −0.88).

The inverse relationship between temperature and salinity is surprising, as conventional wisdom states that water from the Okhotsk Sea entering the southern part of the Tatar Strait through the La Perouse Strait has lower temperature and salinity [1–4, 10–12]. We consider this in detail below.

Diurnal fluctuations in temperature and salinity, similar to variations in sea level and the meridional current, indicate a link between oceanographic parameters and tides. Semi-monthly fluctuations are also evident, with temperature rising and salinity decreasing during stronger tides (tropical tides). This reflects the semi-monthly cyclicity of the Okhotsk Sea water intruding into the ABS deployment area – a 10–11-day phase of intensified inflow onto the Southwest Sakhalin shelf during tropical tides, followed by a sharp weakening phase lasting 3–4 days during equatorial tides. During the latter period, the temperature decreases and the salinity increases, indicating a reduction in the impact of the Okhotsk Sea water. The station is usually affected by the WSC, so its characteristics should be examined in more detail. The most reliable data for this analysis are the long-term average temperature and salinity values at depths of 0, 10, and 20 m at station *1* (coastal) of the standard oceanographic section from Pereputye village to Moneron Island. Data from May to October, when the WSC is most active [1, 9], were selected (see Table). To compare with oceanographic conditions at the ABS deployment site, values at a depth of 20 m are relevant. As shown in the table, the WSC water temperatures can be very low, increasing from 2.7 °C to 3 °C from May to July and reaching only 4 °C in August. Higher values occur in September and October when the shift from summer to winter monsoons significantly alters coastal oceanographic conditions.

The WSC water is not only cold but also salty, with salinity increasing from 33.74 psu in May to 33.9 psu in August before returning to initial values by October. During equatorial tides, when tidal currents are weaker, salinity measurements at the ABS remain stable at 33.8–33.9 psu. Over the same period, temperatures ranged from 2 °C in May – June to 4.7 °C in August. These values indicate that the ABS was influenced by the cold WSC, while less salty and warmer Okhotsk Sea water entered the study area during tides. Diurnal variations in oceanographic parameters lagged behind the meridional current component, and this lag varied over the time interval under consideration. It was relatively stable within each two-week cycle, with salinity minima typically lagging behind peak northward currents by 2–4 hours. In some cases, however, the lag reached 6 hours, suggesting highly unusual water movement patterns under tidal forcing.

Diurnal temperature and salinity fluctuations varied throughout the measurement period. For example, salinity variations during the first month of observations were relatively small, at about 0.5 psu, but later increased to 1.5 psu. Large amplitude variations were observed for about 10 days during the period of

decreasing tides (equatorial tides), after which they decreased almost to zero. Maximum fluctuation values (approximately 2 and up to 2.4 psu) were recorded from August 12 to August 22. After this period, the clear two-week cyclicity was disrupted. In particular, during the period of decreasing tides, the amplitude of diurnal salinity variations was no longer close to zero.

Long-term average values of temperature *T* (°C) and salinity *S* (psu) on 0, 10 and 20 m horizons at station *1* of standard oceanographic section Pereputye village – Moneron Island (according to data from [9])

h, m	*T*	*S*	*h*, m	*T*	*S*
May			*August*		
0	3.51	33.41	0	13.61	33.44
10	2.85	33.50	10	6.65	33.67
20	2.69	33.74	20	4.13	33.90
June			*September*		
0	6.07	33.53	0	14.22	33.39
10	3.32	33.63	10	8.14	33.67
20	2.74	33.86	20	4.63	33.87
July			*October*		
0	9.41	33.48	0	7.88	33.15
10	4.71	33.64	10	6.62	33.49
20	3.08	33.88	20	5.28	33.74

The diurnal temperature variations were similar. At the initial stage, their magnitude was relatively small, at about 2 °C during tropical tides and nearly zero during equatorial tides. Then, the variations increased to 4 °C during large tides, remaining almost unchanged during weak tides. In August, the amplitude increased to 10 °C, and the duration of low values decreased. The intensity of daily variations decreased in September and increased again in October.

Semi-monthly variations linked to the “pumping” of the Okhotsk Sea water onto the southeastern Sakhalin shelf were also significant. The expansion and contraction of the cold “Makarov Spot” during tropical and equatorial tides was described earlier [6]. This occurs because not all of the Okhotsk Sea water entering the shelf during flood tides returns during ebb. Instead, some WSC water is exported through the La Perouse Strait. This effect strengthens and weakens with increasing and decreasing tidal currents, respectively. Two-week salinity variations were more stable, with a range of approximately 1 psu throughout most of the observation period. The temperature variability demonstrated a more complex pattern. During the first month, temperature fluctuations were relatively moderate, ranging from 2 to 4 °C, later increasing to 6°C. By August, both lower (up to 4 °C) and, particularly, upper

temperature extremes (10–12 °C) intensified significantly, accompanied by a notable loss of stability that persisted until autumn. From September to October, the range stabilized, with lower values around 4 °C and higher values around 8–9 °C.

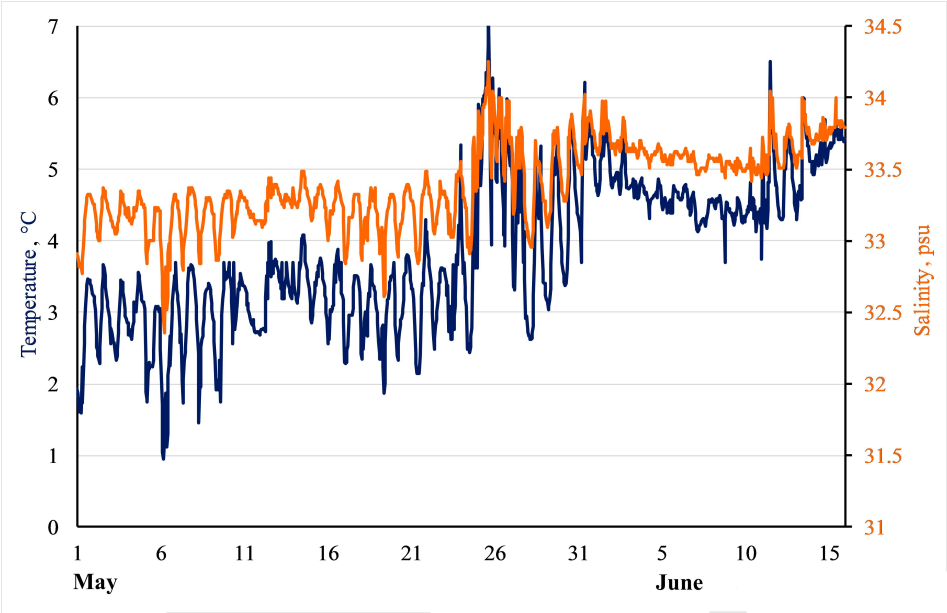

F i g. 6. Variations in seawater temperature (blue line) and salinity (orange curve) based on the ABS "Astarta" data, May – June 1999

For comparison, we are to examine the variations in seawater temperature and salinity recorded at the ABS "Astarta" mooring in the central part of the La Perouse Strait from May 1 to June 15, 1999 (Fig. 6). In May, the diurnal variations of both temperature and salinity were pronounced, with characteristic ranges of approximately 2 °C and 0.5 psu. Semi-monthly variations were also clearly evident, detected as weakened diurnal fluctuations during equatorial tidal phases – a pattern similar to that observed at the ABS "Gorbusha" station. A distinct relationship between hydrological parameters was observed exclusively in the strait: saltier water corresponded to higher temperatures, while fresher water corresponded to lower temperatures. This reflects the typical interaction between the Japan Sea water, carried here by the warm Soya Current, and the Okhotsk Sea water entering from the southwestern part of Aniva Bay. The characteristic values for the latter were 2.5 °C and 32.7 psu, closely matching the salinity readings recorded at the Gorbusha River estuary in May during periods of lowest salinity.

Pay attention that diurnal variations in oceanographic parameters decreased in June, likely due to seasonal strengthening of the Soya Current displacing the Okhotsk Sea water to the northern part of the strait, where it was no longer detected by the ABS "Astarta". Notably, the temporal patterns of oceanographic

parameter variations at the ABS “Gorbusha” in May were similar to those in the La Perouse Strait, highlighting the role of tides in temperature and salinity variations near the study area. The thermohaline characteristics of the Okhotsk Sea water in the strait and off the Krillon Peninsula were also similar, despite measurements being taken in different years.

Oceanographic soundings. The first oceanographic survey of four sections was conducted in mid-May 2024. Soundings at each section were taken at five stations: near the shore and at the 5, 10, 15, and 20 m isobaths. Near the shore, spring warming was evident, with water temperatures > 7 °C. At other stations, however, the water was much colder, ranging from 3 to 3.5 °C. Section 2, especially station *2* at a depth of 5 m, experienced sharp local salinity drops due to spring freshet. The lowest salinity was observed in the bottom layer: < 2 psu at station *2* and ~ 10 psu at station *3* at a depth of 10 m. A strong (5–8 m/s) southerly wind on May 14–15 may have contributed to the descent of freshened water.

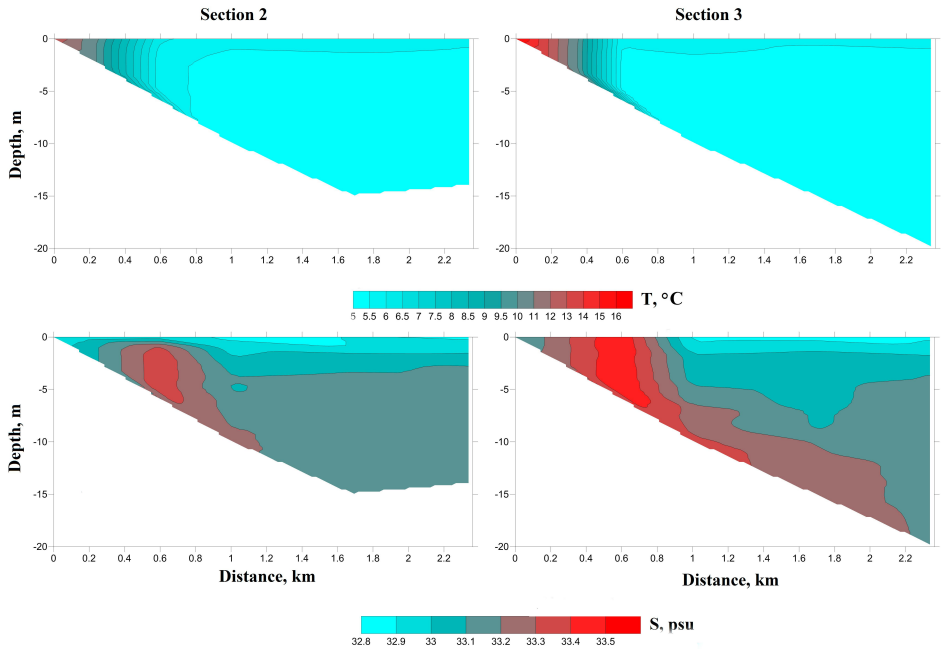

F i g. 7. Vertical distributions of temperature (*top*) and salinity (*bottom*) on sections 2 and 3 based on the results of oceanographic survey conducted in the first decade of June 2024

At other sections, salinity varied minimally (32.1–32.4 psu), which is a low value for Sakhalin’s southwestern coast (see Table). This indicates the influence of the Okhotsk Sea water, which is transported by tidal currents to the mouth of the Gorbusha River.

In early June (Fig. 7), the temperature of the coastal water increased significantly compared to May, reaching 12.8 °C at section 2 and 16.3 °C at section 3. At other stations, temperatures were uniform, ranging from 6 °C at the surface (5-m isobath) to 5.1 °C near the bottom at the offshore stations. Salinity ranged from 32.8 psu at the surface to 33.3 psu near the bottom. However, at station *2* on both sections, values were higher at ~ 33.4 psu at section 2 and 33.5 psu at section 3. The distribution of temperature and salinity suggests an effect of the Okhotsk Sea water over the shelf with a lesser impact on coastal shallows.

In mid-June (Fig. 8), temperatures were lower than two weeks earlier (~ 8 °C near the shore, 4.7–5.7 °C at the surface offshore, ~ 4 °C at 10 m, and ~ 3 °C at 15–20 m). Deep-water salinity was high (~ 33.9 psu), indicating a strong impact from the WSC water. This aligns with the graphs showing weak tidal and the Okhotsk Sea water influences, as well as temperature, salinity, and meridional current variations. Lower salinity (~ 33.2 psu) was observed only at the surface at a few stations. The two June surveys vividly demonstrate the abrupt alternation between the Okhotsk Sea water (lower salinity and higher temperature) and cold, salty WSC water.

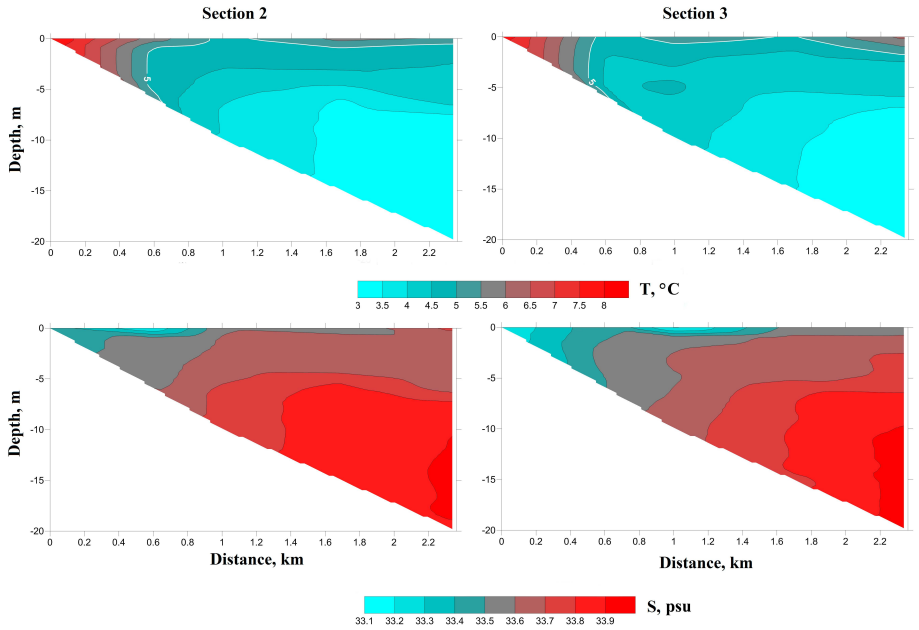

F i g. 8. Vertical distributions of temperature (*top*) and salinity (*bottom*) on sections 2 and 3 based on the results of oceanographic survey conducted in the second decade of June 2024

During the first ten days of July, conditions closely resembled those observed in early June (Fig. 9). Salinity values below 33 psu across the entire study area indicate the dominance of the Okhotsk Sea water. However, Fig. 6 shows that

the period of weak tides ended just two days prior to sampling. This suggests that the influence of this water mass was only beginning to intensify during the survey. This situation differed markedly from the observations made in early June, when saltier water was confined to the coastal shallows (from the shoreline to 5 m isobath). By early July, the Okhotsk Sea water had spread throughout the study area. Against this backdrop, a distinct freshened coastal band appeared along the shoreline above the 5 m isobath with salinity measurements of 19.4 psu at section 2 and 27.0 psu at section 3. This freshening likely resulted from the heavy rainfall recorded at the Nevelsk WS on July 1–2.

The temperature distributions were nearly uniform. Excluding the surface values, the temperatures ranged narrowly from 7.4–7.8 °C at 1 m to 6.7–6.9 °C near the bottom at deepwater stations. Higher values (up to 10.7 °C) occurred only at the surface.

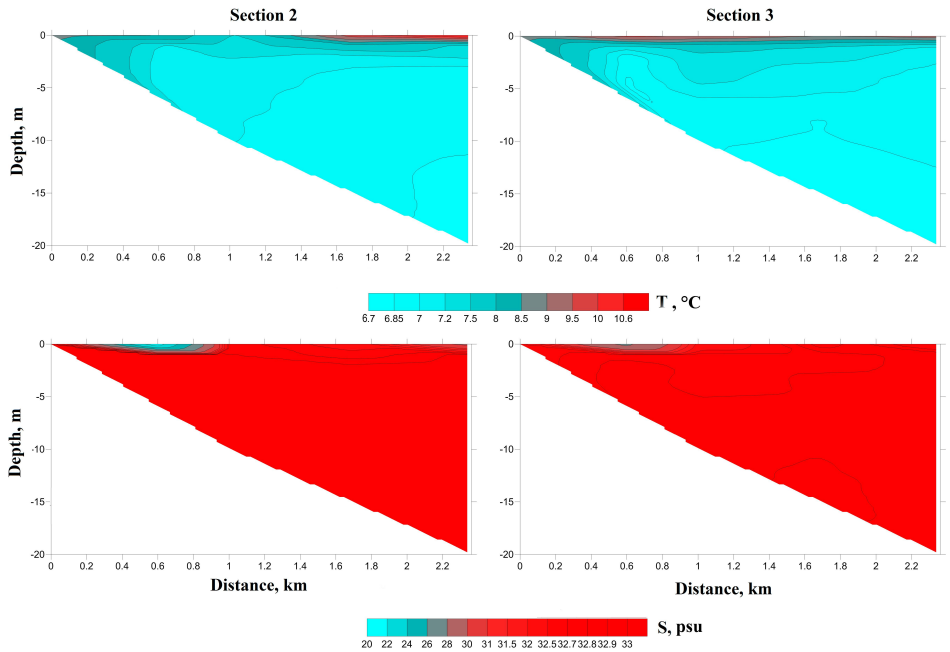

F i g. 9. Vertical distributions of temperature (*top*) and salinity (*bottom*) on sections 2 and 3 based on the results of oceanographic survey conducted in the first decade of July 2024

In late September, the temperature and salinity distributions were the most complex. Cold and salty WSC water (4.3–6.5 °C, 33.5–33.8 psu) dominated below 13 m. In the shallower layers, salinity was lower and temperature was higher, indicating the influence of water from the Okhotsk Sea (9–10 °C, 32.6–32.8 psu in the upper 5 m). A distinct freshened lens (28.6 psu) was observed at the surface at

the 15 m isobath, likely due to heavy rainfall. This survey highlights the complex interaction of waters with markedly different characteristics.

Conclusion

The study revealed that hydrological conditions near the Gorbusha River mouth during the warm season are significantly influenced by the Okhotsk Sea water propagating along the western coast of the Krillon Peninsula due to tidal forcing. Tidal current velocities in the study area can reach 66 cm/s northward and 45 cm/s southward under astronomical conditions. The absence of a time lag between tidal level fluctuations and currents indicates significant tidal energy dissipation on the southwestern Sakhalin shelf, further evidenced by the asymmetry between northward and southward alongshore flows. These findings highlight the atypical tidal dynamics in the study area.

A distinctive feature of this area is the significant temperature and salinity variations driven by the inflow of the Okhotsk Sea water through the La Perouse Strait during tidal cycles. Contrary to conventional understanding, the Okhotsk Sea water is not only less saline but also warmer than WSC water flowing southward along the southwestern coast of Sakhalin Island. The characteristics of the WSC, assessed through long-term average temperature and salinity measurements at a depth of 20 m at the coastal station of the Pereputye–Moneron Island standard oceanographic section, remain nearly constant throughout its duration.

In addition to diurnal variations in oceanographic parameters, with tidal currents exhibiting pronounced daily cycles, a significant accumulation of the Okhotsk Sea water masses occurs on the southwestern Sakhalin shelf. This phenomenon results from incomplete retreat of the Okhotsk Sea water from the shelf zone during ebb tides. The effect persists for 10–11 days within the two-week tidal cycle, becoming particularly pronounced during periods of enhanced tidal currents. Concurrently, the influx of less saline Okhotsk Sea water ceases for approximately 3–4 days during equatorial tidal phases. This mechanism was initially identified through satellite observations of sea surface temperature (SST) and subsequently validated by instrumental measurements.

Diurnal variations in oceanographic parameters are pronounced, with temperature fluctuations exceeding 10 °C and salinity changes reaching 2 psu. Variations over the two-week tidal cycle are also significant (up to 6 °C and 1 psu).

Oceanographic surveys of cross-shore sections indicate that warmer, less saline Okhotsk Sea water initially propagates offshore in the surface layer, subsequently displaces deeper water, and eventually influences coastal shallows.

The near-daily alternation between the Okhotsk Sea and the Sea of Japan waters is the primary defining feature of the hydrological regime in the study area.

REFERENCES

1. Shevchenko, G.V., Chastikov, V.N. and Maryzhikhin, V.E., 2018. Seasonal Variations in Marine Hydrological Characteristics off the Southwestern Coast of Sakhalin Island. *Russian Meteorology and Hydrology*, 43(12), pp. 865-870. https://doi.org/10.3103/S1068373918120087

2. Odamaki, M., 1994. Tides and Tidal Currents along the Okhotsk Coast of Hokkaido. *Journal of Oceanography*, 50(3), pp. 265-279. https://doi.org/10.1007/BF02239517

3. Shevchenko, G.V., Kantakov, G.A. and Chastikov, V.N., 2005. Results of Direct Measurements of the Currents in the La Perouse (Soya) Strait. *Izvestiya TINRO*, 140, pp. 203-227 (in Russian).

4. Shevchenko, G.V. and Maryzhikhin, V.E., 2024. The Effect of the Tide on Water Exchange through the La Perouse Strait. *Journal of Oceanological Research*, 52(3), pp. 95-115. https://doi.org/10.29006/1564-2291.JOR-2024.52(3).6 (in Russian).

5. Mitnik, L.M., Shevchenko, G.V., Sophienko, Yu.A. and Dubina, V.A., 2006. About Tidal Origin of Cold Water Belt in the Stone of Danger Area of the La Perouse Strait. *Issledovanie Zemli iz Kosmosa*, (5), pp. 86-96 (in Russian).

6. Bobkov, A.A. and Fux, V.R., 1997. Tidal Origin of Thermohalinic Anomalies in the La-Perouse Strait. In: Okhotsk Sea & Cold Ocean Research Association, 1997. The *Twelfth International Symposium on Okhotsk Sea and Sea Ice, 2-5 February 1997, Mombetsu, Hokkaido, Japan: Abstracts*. Hokkaido, Japan: Hokkaido University, pp. 242-247.

7. Godin, G., 1972. The *Analysis of Tides*. Liverpool University Press, 292 p.

8. Kantakov, G.A. and Shevchenko, G.V., 2001. Analysis of Nonperiodic Currents in the La Perouse (Soya) Strait due to Changes in Water Level and Wind Impact. In: IMGiG DVO RAN, 2001. *Dynamic Processes on the Sakhalin Shelf and Kuril Islands*. Yuzhno-Sakhalinsk: IMGiG DVO RAN, pp. 62-74 (in Russian).

9. Pishchal'nik, V.M. and Bobkov, A.O., 2000. *Oceanographical Atlas of the Sakhalin Shelf. Volume 2*. Yuzhno-Sakhalinsk: SakhGU, 107 p. (in Russian).

10. Makarov, S.O., 1950. Hydrological Studies Conducted in 1895 and 1896 in the La Perouse Strait and in Other Places. In: *Oceanographic Studies*. Moscow: Geografgiz, pp. 255-275 (in Russian).

11. Leonov, A.K., 1948. Water Masses of the Japan Sea. *Meteorologiya i Gidrologiya*, (6), pp. 61-78 (in Russian).

12. Danchenkov, M.A., Aubrey, D. and Riser, S., 1999. Oceanographic Features of the La Perouse Strait. In: North Pacific Marine Science Organization, 1999. *Proceedings of the Second PICES Workshop on the Okhotsk Sea and Adjacent Areas*. PICES Scientific Reports, no. 12. Sidney, Canada: PICES, pp. 159-171. [online] Available at: https://pices.int/outgoing/Julia/misc/PICES-2011%20USB/Scientific%20Reports/Rep12.pdf [Accessed: 10 July 2025].

Submitted 13.01.2025; approved after review 20.02.2025;
accepted for publication 15.05.2025.

About the authors:

Georgy V. Shevchenko, Head of Oceanography Laboratory, Sakhalin Branch of Russian Federal Research Institute of Fisheries and Oceanography (VNIRO) (196 Komsomolskaya Str., Yuzhno-Sakhalinsk, 693023, Russian Federation), Leading Research Associate of Tsunami Laboratory, Institute of Marine Geology and Geophysics, Far Eastern Branch of Russian Academy of Sciences (1B Nauki

Str., Yuzhno-Sakhalinsk, 693023, Russian Federation), DSc. (Phys.-Math.), **ORCID ID: 0000-0003-0785-4618**, **SPIN-code: 8230-2974**, shevchenko_zhora@mail.ru

Vsevolod E. Maryzhikhin, Head of Laboratory of Environmental Research and Anthropogenic Impact Monitoring, Sakhalin Branch of Russian Federal Research Institute of Fisheries and Oceanography (VNIRO) (196 Komsomolskaya Str., Yuzhno-Sakhalinsk, 693023, Russian Federation), **Scopus Author ID: 58453617900**, **SPIN 1923-5450**, **ORCID ID: 0000-0002-2775-4991**

Contribution of the co-authors:

Georgy V. Shevchenko – analyzing and summarizing the research results, paper preparation

Vsevolod E. Maryzhikhin – participation in field expeditions, data preparation and processing, discussion of the research results

The authors have read and approved the final manuscript.

The authors declare that they have no conflict of interest.

ISSN 1573-160X, *PHYSICAL OCEANOGRAPHY*, Vol. 32, Iss. 4, pp. 524-536 (2025)
Original Russian Text © V. V. Efimov, D. A. Iarovaia, 2025,
published in *Morskoy Gidrofizicheskiy Zhurnal*, 2025, Vol. 41, Iss. 4, pp. 501–514

Original article

Numerical Modeling of Cold Air Intrusion in the Crimean Region on January 22–24, 2010

V. V. Efimov ✉, D. A. Iarovaia

Marine Hydrophysical Institute of RAS, Sevastopol, Russian Federation
✉ *vefim38@mail.ru*

Abstract
Purpose. The purpose of the work is to numerically investigate the response of near-surface marine and atmospheric fields in the Crimean region to the cold air intrusion in January 22−24, 2010.
Methods and Results. A coupled mesoscale sea–atmosphere model NOW (NEMO-OASIS-WRF) with a 1 km resolution was used. The interaction of incoming airflow with the Crimean Mountains during the cold intrusion was reproduced, as well as the main changes in near-surface atmospheric and marine fields that occurred in the region of the Southern coast of Crimea during the cold air intrusion were analyzed. It is shown that the cold intrusion was characterized by a northeasterly wind throughout the region with maximum speeds up to 10 m/s over the land and up to 20 m/s over the sea. The sea surface temperature in the region decreased mainly by ~ 0.5 °C. To the south of peninsula, in the Rim Current area, a local decrease in sea surface temperature constituted ~ −1.5 … −1 °C. A distinctive feature of the considered case was a small thickness (less than 1 km) of the cold airflow incoming to the Crimean Mountains. On the over-land atmospheric profiles corresponding to the foothill region, a relatively thin cold surface layer with the increased wind speed and high values of stability frequency at its upper boundary is clearly pronounced.
Conclusions. Despite their short duration, winter intrusions of cold air across the northern boundary of the Black Sea region induce significant regional disturbances in the atmospheric and marine fields. The sea responds to cold air intrusions with a decrease in sea surface temperature, which can be explained by strong fluxes of sensible and latent heat from the sea surface, as well as by the entrainment processes at the lower boundary of the upper mixed layer. To the south of the Crimean Peninsula, there is an additional factor contributing to temperature decrease, namely the transport of colder water from the open sea towards the coast, which develops in response to the strengthening of along-coastal northeasterly winds over the sea. In the atmosphere, at its lower levels, the incoming cold flow is blocked by the coastal Crimean Mountains. As a result, the descending compensatory flows arise over the leeward slope of the mountains that leads to an increase in near-surface air temperature at the Southern coast of Crimea. Another consequence of the blocking is the absence of a cold gravity flow on the leeward slope of the Crimean Mountains, unlike other cases of cold air intrusions, such as the Yalta bora event in December 2013.

Keywords: mesoscale coupled modeling, cold air intrusion, Crimea region, near-surface current velocity fields in the sea, near-surface temperature fields in the sea, Black Sea

Acknowledgements: The study was conducted as part of the state assignment (No. FNNN-2024-0014).

For citation: Efimov, V.V. and Iarovaia, D.A., 2025. Numerical Modeling of Cold Air Intrusion in the Crimean Region on January 22–24, 2010. *Physical Oceanography*, 32(4), pp. 524-536.

Introduction

A notable feature of the local air circulation in the Black Sea region is the occurrence of cold air intrusion (CAI) during winter across the region's northern boundary into the atmospheric boundary layer over the sea. This extreme weather phenomenon is accompanied by a significant increase in surface wind speed of up to 10–15 m/s and a decrease in near-surface air temperature down to −10 … −15 °C [1]. At the same time, the sea surface temperature is approximately + 9 °C. Consequently, intense cloud convection develops over the sea, appearing on satellite images as cloud "streets" (Fig. 1).

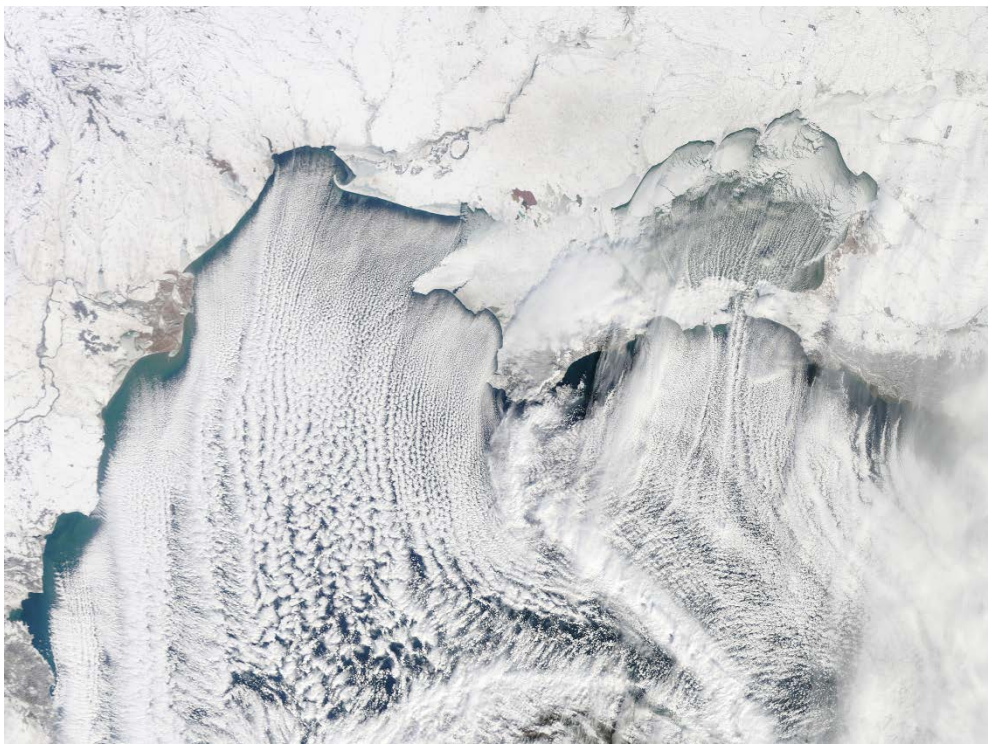

F i g. 1. Snapshot of cloudiness on January 25, 2010 obtained using the MODIS spectroradiometer installed on Terra satellite. Data source is website http://rapidfire.sci.gsfc.nasa.gov

Episodes of cold intrusions in the Black Sea region are mainly caused by winds from the north and northeast. There are two types of synoptic situations that lead to extreme cooling of the Black Sea during autumn and winter periods. Most often, an intense anticyclone is located north of the Black Sea. On the southeastern periphery of the anticyclone, a northeasterly flow of cold air forms, accompanied by high surface wind speeds [2]. In other cases, there is a less intense anticyclone north of the Black Sea and a cyclone to the south, centered in Asia Minor. The airflow on the southeastern periphery of the anticyclone increases due to the flow on the northwestern periphery of the cyclone, creating an intense Novorossiysk bora. This frontal-type bora is most frequent during the cold season when conditions for

the development of a true bora are met: wind speeds of at least 15 m/s and near-surface air temperatures no higher than – 10 °C [2, 3].

Relatively short-lived (usually no more than 2−3 days) but intense cold intrusions result in changes to the characteristics of the marine environment that stand out well against the background of synoptic variability. It should be noted that the cooling of the upper sea layer during cold intrusions occurs due to heat loss from the surface; however, the mixing of the upper layer has a different, non-convective physical mechanism. Interaction processes in the sea-atmosphere system for a characteristic CAI case were described in [4] using the coupled NEMO-WRF numerical model. Since cold intrusions are characterized by both low air temperatures and high surface wind speeds, a convective type of circulation (such as cellular convection in the atmospheric marine boundary layer) does not usually develop in the sea. Deep penetrating cooling of the upper sea layer during cold intrusions is mainly associated with turbulent mixing caused by the shear instability of currents and wind wave breaking [4]. Cold intrusions that recur during winter periods can influence the formation of the cold intermediate layer (CIL) in the Black Sea by determining the temperature of the surface layer at the end of seasonal winter cooling [4]. During these cold episodes, the upper quasi-homogeneous layer (UQL) can significantly deepen, merging with the CIL[1].

In addition to the general decrease in the sea surface temperature, which is most pronounced in the northern coastal region, specific local features appear in some areas of the sea during CAI. One such region is the northeastern area, where the Novorossiysk bora develops and leaves a significant mark on the temperature and velocity fields of the atmosphere and the sea [8, 9]. The second region where CAI causes specific disturbances in the boundary layers of the atmosphere and the sea is the Crimean region, where the influence of the relatively high Crimean Mountains is significant. During the autumn-winter period when cold air intrusions occur, the Yalta bora can develop in the Southern coast of Crimea (SCC), similar to the Novorossiysk bora [10]. Furthermore, the entire lower tropospheric circulation and, consequently, the temperature field south of the SCC are significantly influenced by the Crimean Mountains [11].

This paper uses the coupled sea-atmosphere NEMO-WRF numerical model to examine features of the temperature, wind speed, and surface current fields in the Crimean region during CAIs, taking the event of January 22–24, 2010 as an example (Fig. 1). This event has been previously studied in our works [1, 4]. Using the WRF atmospheric model, the structure of the convective atmospheric boundary layer over the western part of the sea on January 25, 2010, was reproduced. It was shown that convection occurred under quasi-stationary but substantially heterogeneous spatial conditions [1]. The convective cells in the atmosphere provided large fluxes of sensible and latent heat from the sea surface (up to 1000 W/m² in the northwest), which led to the rapid cooling of the sea surface layer by 1−2 °C [4].

[1] Blatov, A.S., Bulgakov, N.P., Ivanov, V.A., Kosarev, A.N. and Tuljulkin, V.S., 1984. *Variability of the Black Sea Hydrophysical Fields*. Leningrad: Gidrometeoizdat, 240 p. (in Russian).

This work aims to investigate the response of marine and atmospheric fields in the Crimean region to a characteristic case of CAI using a coupled mesoscale model.

Numerical model

The coupled sea-atmosphere model (NOW) [12] consists of the NEMO ocean model [2], the WRF non-hydrostatic atmospheric model [3], and the OASIS coupler (an application that handles data exchange between NEMO and WRF). The simulation used two computational grids: one with 3 km resolution covering all three seas (the Black Sea, the Azov Sea, and the Marmara Sea), and one nested grid with 1 km resolution covering the area (30−36°E; 43–47°N). The simulation results with 1 km resolution are considered further in the work.

The NOW model has been described in previous works (see, for example, [4]), so here we will only note that in the NEMO model, the GLS k-ε scheme [13] was used for parameterizing turbulent exchange. In this scheme, the exchange coefficients are defined as a function of two prognostic variables: turbulent kinetic energy k and turbulent kinetic energy dissipation rate ε. Additionally, the NEMO model accounts for surface wave breaking. To accomplish this, the following boundary condition is used: at the sea surface, the k and ε values are calculated as a function of wind stress.

Regional changes in velocity and temperature fields

Changes in parameters of the upper sea layer. Fig. 1 shows a satellite image of the studied CAI case. Over the western half of the sea, it is clearly visible that the cloud field consists of elongated cloud “streets” aligned with the northerly wind direction. The horizontal size of the cloud structures significantly increases with distance from the windward shore (from 1–2 km near the shore to ~ 10 km at a distance of 300 km from the shore). This is a characteristic feature of cloud fields that form during CAI [14].

Fig. 2 shows the temporal changes in surface wind speed and surface air temperature at the 34°E, 45°N point, which is located in the flat central part of Crimea. The CAI event itself, which lasted about two days (from the second half of January 22 to the first half of January 24), is well represented by increased wind speeds and a significant decrease in surface air temperature.

Fig. 3, a shows the surface wind speed and current velocity fields at 12:00 on January 23, when the wind speed over land was greatest. This cold air intrusion is characterized by northeasterly winds throughout the Crimean region, with maximum speeds of up to 10 m/s over land and up to 20 m/s over the sea. A significant aspect of water circulation in the Black Sea is the Black Sea Rim Current (RC), a year-round cyclonic alongshore current that reaches maximum intensity in late winter [15]. Large current velocities of up to 0.8 m/s are associated with the RC at a distance

[2] Skamarock, W.C., Klemp, J.B., Jimy, D., Gill, D.O., Barker, D.M., Duda, M.G., Huang, X-Y., Wang, W. and Powers, J.G., 2008. *A Description of the Advanced Research WRF Version 3. NCAR Technical Note*. NCAR/TN-475+STR, 113 p. https://doi.org/10.13140/RG.2.1.2310.6645

[3] NEMO Team, 2016. *NEMO Ocean Engine*. Note du Pôle de Modélisation de l'Institut Pierre-Simon Laplace, No. 27. France: IPSL, 412 p. https://doi.org/10.5281/zenodo.3248739

of 50−70 km south of Crimea. The response of the upper sea layer to the cold intrusion is also shown. This is evidenced by the decrease in SST (Δ*sst*) during the intrusion period from 12:00 on January 22 to 12:00 on January 24. Outside the RC area, Δ*sst* was ~ −0.5 °C except for coastal areas. Assuming the UQL thickness is 40 m, we can estimate the total (sensible + latent) heat flux $Q = \Delta sst \cdot \rho \cdot C_p \cdot H/(48\ \text{h})$, where $\rho = 1025$ kg/m³ and $C_p = 3900$ J/(kg·°C) are the density and specific heat capacity of seawater, respectively; H is the UQL thickness; Q is ~ 500 W/m², which is close to the modeled value.

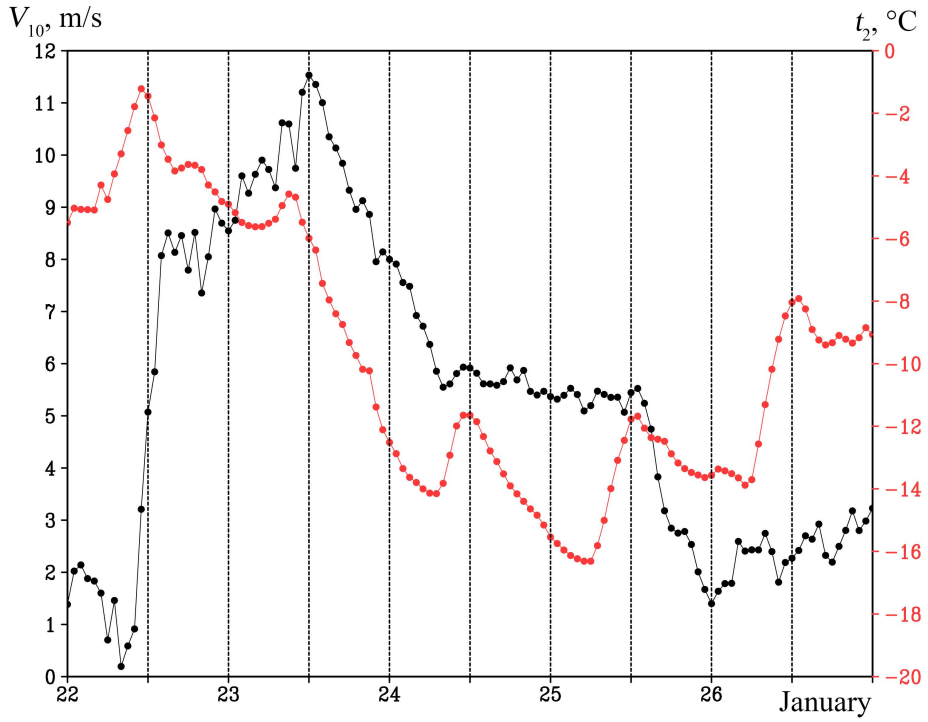

F i g. 2. Temporal variation of wind speed at the 10 m height (black curve) and air temperature at the 2 m height (red curve) at point 34°E, 45°N (point location is marked in Fig. 3, *a*)

An area of elevated negative Δ*sst* values stands out south of the peninsula, ranging from −1.5 to −1 °C. Fig. 3, *b* explains the origin of these values. This figure shows the SST field at the beginning of the cold intrusion, as well as the change in the surface current velocity field over the first 12 hours of the intrusion for a small area near the southeastern coast of Crimea. The SST field in this area exhibits strong spatial heterogeneity: relatively warm water with a temperature of 9−10 °C is found near the shore, while colder water with a temperature 1–1.5 °C lower is found farther offshore. After the CAI onset, an onshore-directed Ekman transport with velocities up to 0.2 m/s developed in the sea in response to the sharp intensification of the northeasterly alongshore wind. This led to an additional advective decrease in SST near the southeastern coast.

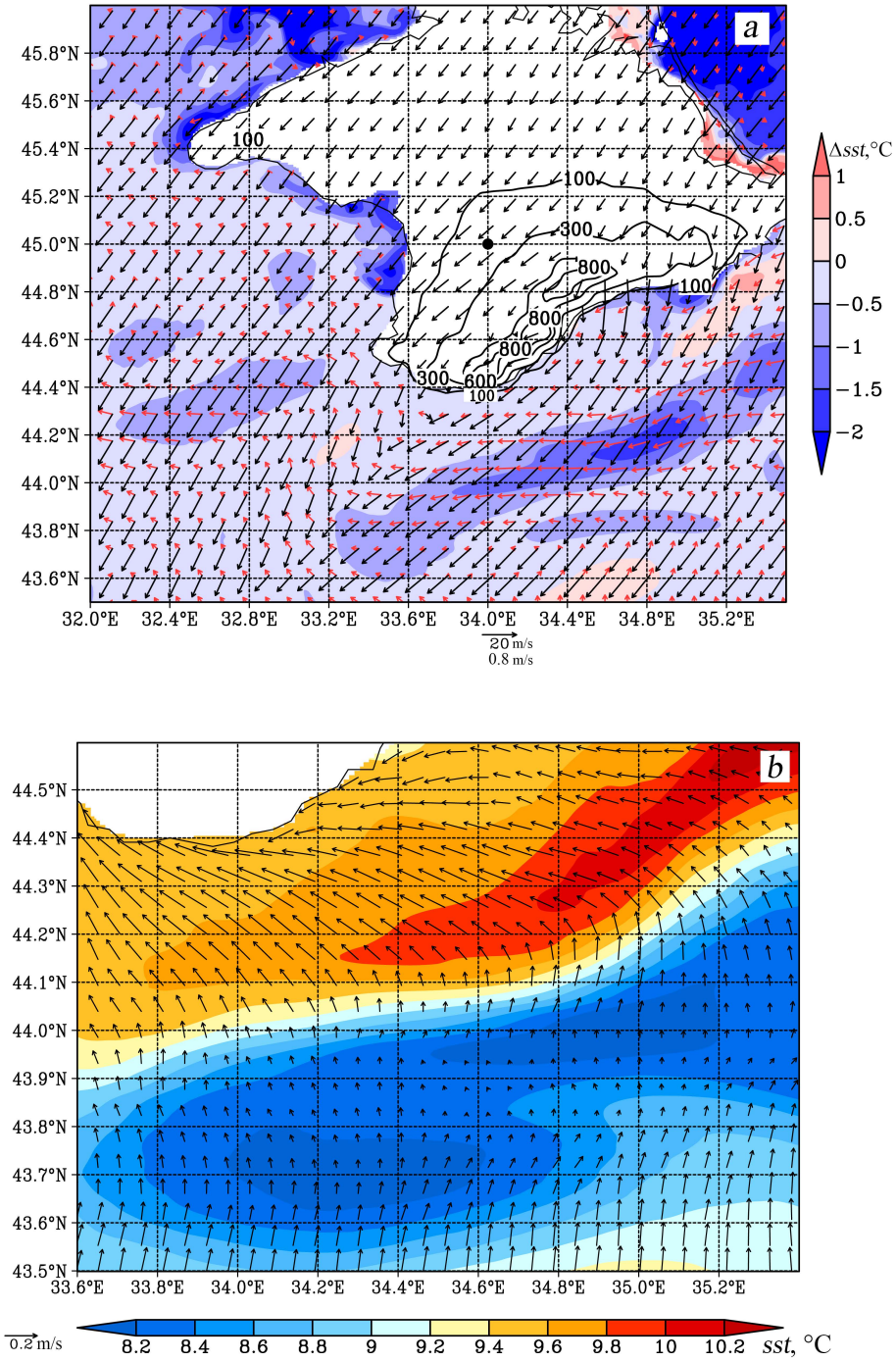

F i g. 3. Change in SST (Δ*sst*, °C) between 12:00, January 22 and 12:00, January 24, near-surface wind speed field (black arrows) and near-surface current velocity field (red arrows) at 12:00, January 23; relief height (m) is shown by isolines (*a*); SST field at 12:00, January 22, and change in the near-surface current velocity field between 12:00, January 22 and 00:00, January 23 (*b*)

Fig. 4 shows the vertical structure of the velocity and temperature fields in the sea on a meridian section at 34.55°E. It demonstrates the temperature field at the beginning of the cold intrusion and how it changes during the intrusion. There is a clear tendency for the UQL to deepen towards the shore: its thickness doubles from 30 to 60 m. The temperature decrease (Δt) in the RC area (44.0–44.3°N) reaches – 1.4 °C.

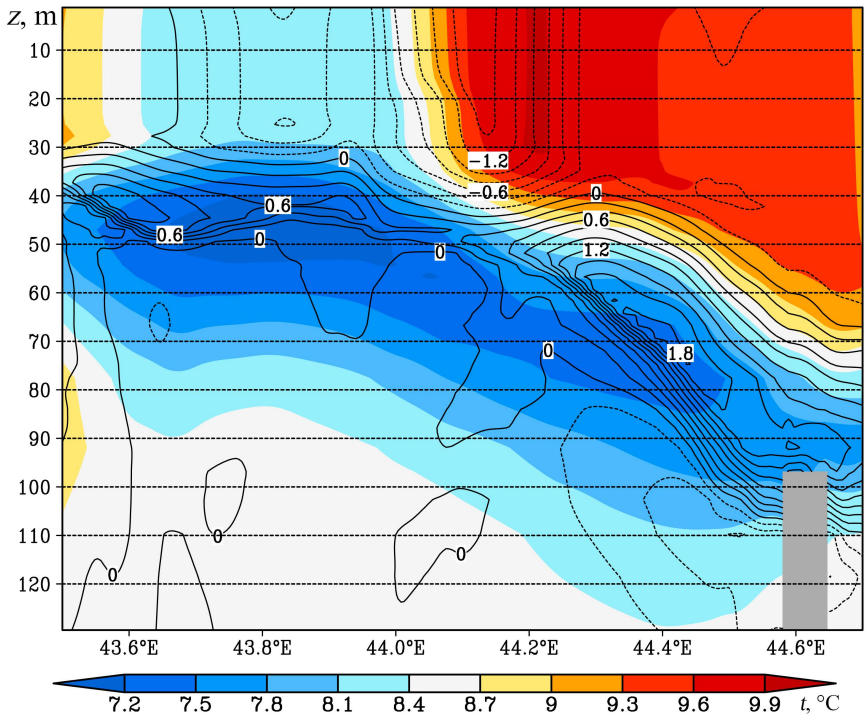

F i g. 4. Vertical structure of sea fields at meridional section along 34.55°E: sea temperature (color) at 12:00, January 22, and change in sea temperature (isolines) between 12:00, January 22 and 12:00, January 24

Fig. 5 shows the vertical temperature profiles in the upper sea layer at the beginning and end of the cold intrusion, as well as the temperature changes during the intrusion. CIL with a minimum temperature at a depth of ~ 50 m is visible. The upper sea layer response was cooling and deepening of the UQL. During the intrusion, the UQL temperature decreased by ~ 0.5 °C, and its thickness increased from 25 to 40 m. Meanwhile, the CIL thickness decreased accordingly. The physical reasons for these changes are well known: turbulent mixing of the UQL due to shear instability of currents and wind wave breaking, as well as its cooling due to sensible and latent heat fluxes from the sea surface and the entrainment of colder water from the CIL [4, 16].

Changes in atmospheric characteristics. Fig. 6 shows the surface wind speed fields at 10 m height at the beginning of the cold intrusion, as well as the change in

surface air temperature during the intrusion in the Crimean region. Note that changes in wind speed at one point in Crimea during the intrusion were shown earlier in Fig. 2. Without discussing the overall pattern of surface temperature changes related to the synoptic structure of meteorological fields, let us consider the features that are characteristic of the Crimean region. This region has sufficiently high coastal mountains that influence atmospheric and marine circulation. First, note the difference in temperature changes between the windward northwestern and leeward southeastern areas of the mountains. In the former, the air temperature decreases during cold intrusions, while in the latter, it increases. This phenomenon is associated with the physical process of a stably stratified airflow around the mountains.

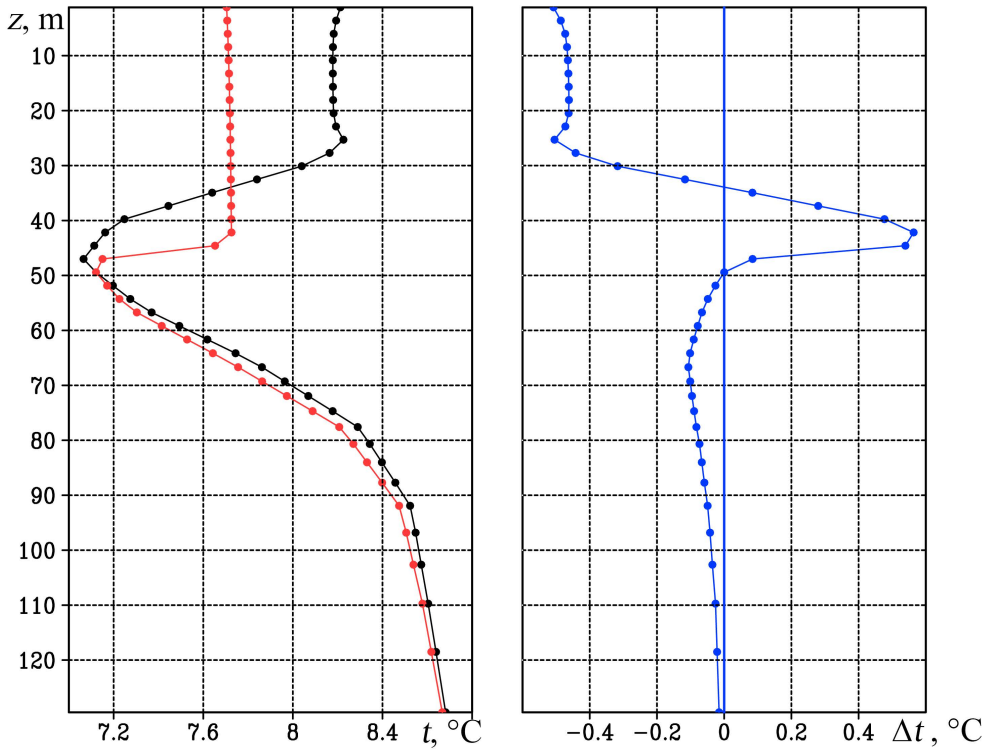

F i g. 5. Vertical profiles of sea temperature at 12:00, January 22 (black curve), 12:00, January 24 (red curve), as well as change in sea temperature (blue curve) between 12:00, January 22 and 12:00, January 24 at point (34.2°E and 43.8°N)

Fig. 7 illustrates the vertical structure of the potential temperature field and wind speed isolines on a meridional section along 34°E. The airflow mechanism around a mountainous obstacle is determined by the vertical structure of the density and flow velocity fields.

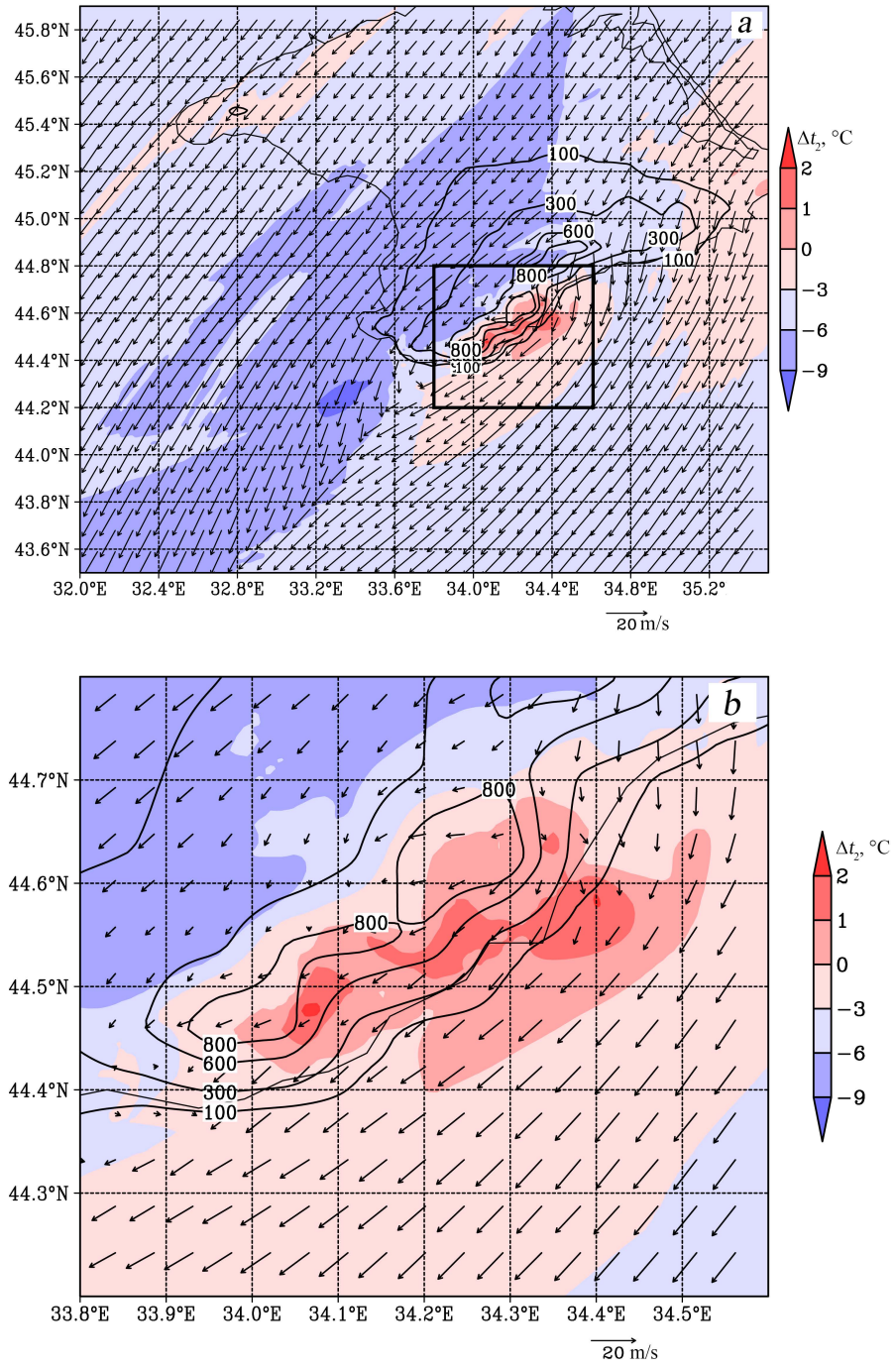

F i g. 6. Change in near-surface air temperature (Δt_2, °C) between 00:00, January 23 and 00:00, January 24, as well as near-surface wind field (black arrows) at 12:00, January 23; relief height (m) is shown by isolines (*a*); area (33.8−34.6°E, 44.2−44.8°N) highlighted by a rectangle in fragment *a*, is shown on fragment *b* on a larger scale

For our case, the vertical profiles of wind speed V and stability frequency N^2 are shown in Fig. 8. Stability frequency is equal to $(g/\rho)\cdot(\Delta\rho/\Delta z)$, where g is the acceleration due to gravity, ρ is air density, and z is height. The point in the flat land area is located at 34°E, 45°N. The most important feature of the vertical structure of the density field, and consequently the stability frequency N, determining the main properties of our intrusion case is the strong stability of the lower atmospheric layer at heights comparable to the height of the mountain ridge. The result of this is the airflow blocking effect over the windward slope of the mountains. As is well known, cold, stably stratified air flowing around a mountain ridge cannot rise above a height h equal to V/N [17, 18]. In our case, the blocking effect of cold air on the windward slope of the mountains is clearly visible as the intersection of the speed isolines with the windward slope and the concentration of cold air on the windward slope (Fig. 7). When considering velocity and temperature fields along a meridional section (such as in Fig. 7), it is necessary to consider the 3D characteristics of the mountain flow effects. The Crimean Mountain Ridge cannot be considered as a 2D obstacle because its length is only ~ 3 times greater than its width. Additionally, the wind direction is not strictly northerly and changes, albeit insignificantly, with height within the lower kilometer layer.

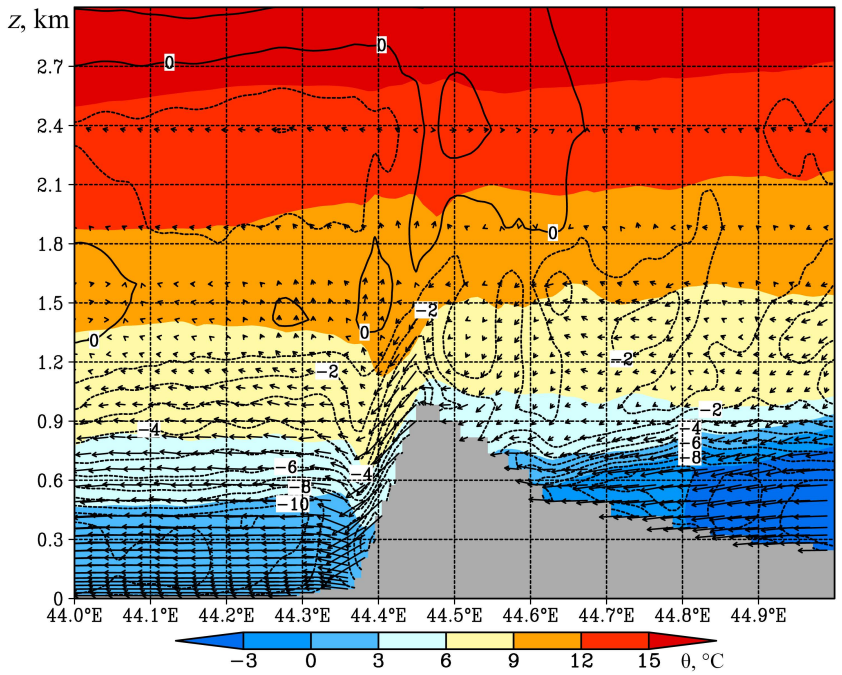

F i g. 7. Vertical structure of potential temperature θ (°C) and wind speed (m/s, isolines) fields on the meridional section along 34°E at 12:00 on January 23, 2010. Speed direction in the section plane is shown by arrows; for clarity, speed vertical component is enlarged by 10 times

Consequently, it can be concluded that the Crimean Mountains partially blocked the airflow – it went around the mountain ridge on both sides, and the northerly wind in the foothill area changed direction to northeasterly. The effect of temperature increase in the coastal area of the SCC is clearly visible in Figs. 6 and 7. Fig. 6, *b*

shows this effect as a local area of elevated surface temperature values, t_2, and low surface wind speeds. As is known, elevated potential temperature and temperature t_2 values over the leeward slope are a consequence of the mountain ridge partially blocking the airflow. This causes the surface air over the leeward slope to be replaced by potentially warmer air from higher altitudes [10]. This mechanism, which forms a local warm area over the SCC in winter, is described in [2].

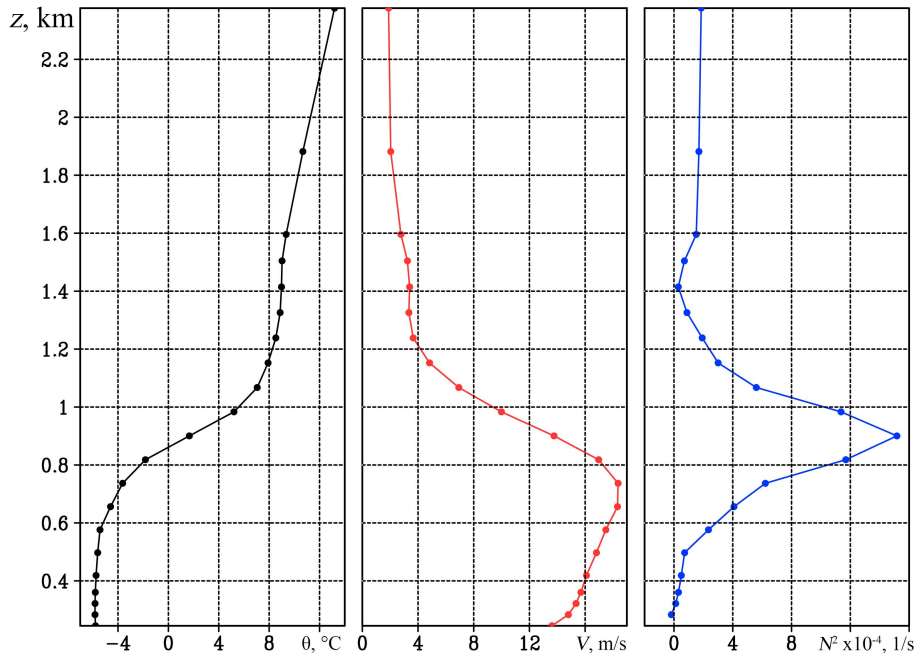

F i g. 8. Vertical profiles of potential temperature (black curve), meridional wind speed (red curve), and buoyancy frequency (blue curve) at point (34°E; 45°N) at 12:00 on January 23, 2010

Thus, a distinctive feature of the CAI event in January 2010 was the two-layer vertical structure of the troposphere, represented in Fig. 8 by the temperature and stability frequency profiles in the foothill plain part of Crimea. Anomalously cold air occupied only the lower part of the troposphere, extending up to a height of ~ 0.8 km. Above this level, wind speed decreased rapidly to a background value of 3 m/s, and stability frequency reached 0.0015 1/s. The low-tropospheric nature of the airflow distinguishes it from other CAIs in the northeastern part of the sea, which lead to the Novorossiysk bora [3] or, for example, the Yalta bora considered in [10]. Therefore, the absence of a strong downslope wind, such as a bora, in the SCC area is a distinctive feature of this intrusion in the Crimean region.

Conclusion

Despite their short duration, winter CAIs across the northern boundary of the Black Sea cause significant disturbances in atmospheric and marine fields of the region. These disturbances include strong convective instability in the atmospheric surface layer over the sea, which is visible as cloud “streets” on

satellite images, as well as sharp cooling of the upper sea layer. In some cases, CAIs can lead to the development of the Novorossiysk and Yalta bora.

This paper uses a coupled model with 1 km resolution to reproduce the interaction of the incoming air stream with the Crimean Mountains during the cold intrusion in January 2010. The main changes in the surface atmospheric and marine fields that occurred in the SCC area during the CAI were examined.

Outside the RC zone, it is shown that the decrease in SST is explained by strong fluxes of sensible and latent heat from the sea surface, as well as entrainment processes at the lower boundary of the UQL. Furthermore, south of the Crimean Peninsula, an additional factor contributing to the decrease in SST was identified: the transport of colder water from the open sea towards the shore. This phenomenon developed in response to the emergence of a strong northeasterly wind along the coast.

A distinctive feature of the considered event is the small thickness (less than 1 km) of the incoming cold airflow. Over the piedmont area, the atmospheric profiles clearly show a relatively thin cold surface layer with increased wind speed and high stability frequency values at its upper boundary. Hence, due to the incoming airflow being blocked, over the leeward slope of the Crimean Mountains and the SCC an area with a higher surface air temperature than the piedmont plain area of Crimea is formed. A gravity-driven flow, such as the Novorossiysk bora, did not reach speeds as significant as those during the CAI in December 2013.

REFERENCES

1. Efimov, V.V. and Yarovaya, D.A., 2014. Numerical Simulation of Air Convection in the Atmosphere during the Invasion of Cold Air over the Black Sea. *Izvestiya, Atmospheric and Oceanic Physics*, 50(6), pp. 610-620. https://doi.org/10.1134/S0001433814060073
2. Efimov, V.V., Savchenko, A.O. and Anisimov, A.E., 2014. Features of the Black Sea Atmosphere Heat Exchange Autumn-Winter Period. *Morskoy Gidrofizicheskiy Zhurnal*, (6), pp. 71-81 (in Russian).
3. Efimov, V.V., Komarovskaya, O.I. and Bayankina, T.M., 2019. Temporal Characteristics and Synoptic Conditions of Extreme Bora Formation in Novorossiysk. *Physical Oceanography*, 26(5), pp. 361-373. https://doi.org/10.22449/1573-160X-2019-5-361-373
4. Efimov, V.V., Yarovaya, D.A. and Komarovskaya, O.I., 2024. Deep Penetrating Cooling in the Black Sea as a Reaction to Cold Air Intrusions in Winter. *Izvestiya, Atmospheric and Oceanic Physics*, 60(5), pp. 667-679. https://doi.org/10.31857/S0002351524050081 (in Russian).
5. Piotukh, V.B., Zatsepin, A.G., Kazmin, A.S., Yakubenko, V.G., Stanichny, S.V. and Ratner, Yu.B., 2009. Impact of the Winter Atmospheric Forcing on the Variability of the Active Layer's Thermohaline Structure in the Black Sea. *Sovremennye Problemy Distantsionnogo Zondirovaniya Zemli iz Kosmosa*, 6(1), pp. 442-450 (in Russian).
6. Bayankina, T.M., Sizov, A.A. and Jurovskij, A.V., 2017. On the Role of Cold Invasion in the Formation of the Black Sea Winter Surface Temperature Anomaly. *Processes in GeoMedia*, (3), pp. 565-572 (in Russian).
7. Sizov, A.A. and Bayankina, T.M., 2019. Peculiarities of the Settling Temperature in the Upper Water Layer of the Black Sea during Invasions of Cold Air. *Doklady Earth Sciences*, 487(2), pp. 939-942. https://doi.org/10.1134/S1028334X19080105
8. Gavrikov, A.V. and Ivanov, A.Yu., 2015. Anomalously Strong Bora over the Black Sea: Observations from Space and Numerical Modeling. *Izvestiya, Atmospheric and Oceanic Physics*, 51(5), pp. 546-556. https://doi.org/10.1134/S0001433815050059
9. Ivanov, A.Yu., 2008. Novorossiysk Bora: A View from Space. *Issledovanie Zemli iz Kosmosa*, (2), pp. 68-83 (in Russian).

10. Efimov, V.V. and Komarovskaya, O.I., 2015. Spatial-Temporal Structure of Bora in Yalta. *Physical Oceanography*, (3), pp. 3-14. https://doi.org/10.22449/0233-7584-2015-3-3-14

11. Efimov, V.V. and Komarovskaya, O.I., 2019. Disturbances in the Wind Speed Fields Due to the Crimean Mountains. *Physical Oceanography*, 26(2), pp. 123-134. https://doi.org/10.22449/1573-160X-2019-2-123-134

12. Samson, G., Masson, S., Lengaigne, M., Keerthi, M.G., Vialard, J., Pous, S., Madec, G., Jourdain, N.C., Jullien, S. [et al.], 2014. The NOW Regional Coupled Model: Application to the Tropical Indian Ocean Climate and Tropical Cyclone Activity. *Journal of Advances in Modeling Earth Systems*, 6(3), pp. 700-722. https://doi.org/10.1002/2014ms000324

13. Umlauf, L. and Burchard, H., 2003. A Generic Length-Scale Equation for Geophysical Turbulence Models. *Journal of Marine Research*, 61(2), pp. 235-265. https://doi.org/10.1357/002224003322005087

14. Melfi, S.H. and Palm, S.P., 2012. Estimating the Orientation and Spacing of Midlatitude Linear Convective Boundary Layer Features: Cloud Streets. *Journal of the Atmospheric Sciences*, 69(1), pp. 352-364. https://doi.org/10.1175/jas-d-11-070.1

15. Ivanov, V.A. and Belokopytov, V.N., 2013. *Oceanography of the Black Sea*. Sevastopol: MHI, 210 p. (in Russian).

16. Zatsepin, A.G., Kremenetskiy, V.V., Piotukh, V.B., Poyarkov, S.G., Ratner, Yu.B., Soloviev, D.M., Stanichnaya, R.R., Stanichny, S.V. and Yakubenko, V.G., 2008. Formation of the Coastal Current in the Black Sea Caused by Spatially Inhomogeneous Wind Forcing upon the Upper Quasi-Homogeneous Layer. *Oceanology*, 48(2), pp. 159-174. https://doi.org/10.1134/S0001437008020021

17. Gill, A.E., 1982. *Atmosphere-Ocean Dynamics*. International Geophysics Series, vol. 30. New York: Academic Press, 662 p.

18. Lin, Y.-L., 2007. *Mesoscale Dynamics*. Cambridge: Cambridge University Press, 630 p. https://doi.org/10.1017/CBO9780511619649

Submitted 11.10.2024; approved after review 03.03.2025;
accepted for publication 15.05.2025.

About the authors:
Vladimir V. Efimov, Head of Atmosphere-Ocean Interaction Department, Marine Hydrophysical Institute of RAS (2 Kapitanskaya Str., Sevastopol, 299011, Russian Federation), DSc. (Phys.-Math), Professor, **SPIN-code: 4902-8602**, **ResearcherID: P-2063-2017**, **Scopus Author ID: 6602381894**, vefim38@mail.ru

Darya A. Iarovaia, Leading Researcher, Marine Hydrophysical Institute of RAS (2 Kapitanskaya Str., Sevastopol, 299011, Russian Federation), CSc. (Phys.-Math), **SPIN-code: 9569-5642**, **ResearcherID: Q-4144-2016**, **ORCID ID: 0000-0003-0949-2040**, **Scopus Author ID: 57205741734**, darik777mhi-ras@mail.ru

Contribution of the co-authors:
Vladimir V. Efimov – task setting, formulating conclusions

Darya A. Iarovaia – performing conclusions, interpreting simulation results, participating in the discussion of simulation results and formulating conclusions

The authors have read and approved the final manuscript.
The authors declare that they have no conflict of interest.

ISSN 1573-160X, *PHYSICAL OCEANOGRAPHY*, Vol. 32, Iss. 4, pp. 537-557 (2025)
Original Russian Text © A. A. Pavlushin, 2025,
published in *Morskoy Gidrofizicheskiy Zhurnal*, 2025, Vol. 41, Iss. 4, pp. 515–536

Original article

Numerical Simulation of Deep Currents in the Black Sea Using a Two-Layer Eddy-Resolving Model

A. A. Pavlushin

Marine Hydrophysical Institute of RAS, *Sevastopol*, *Russian Federation*
✉ *pavlushin@mhi-ras.ru*

Abstract
Purpose. The purpose of this study is to calculate and construct maps of deep currents in the Black Sea and to identify the key characteristics of deep-sea circulation.
Methods and Results. A two-layer eddy-resolving model incorporating actual bathymetry was used to simulate the currents. The motion was driven by wind shear stress with mean annual cyclonic vorticity. Long-term simulations yielded fields of current velocity and layer thickness for both upper and lower layers. The kinetic energy of mean and "eddy" currents was calculated and the parameters of wave oscillations in the current velocity field were determined.
Conclusions. The simulation results revealed a closed current system transporting water in a cyclonic direction in the deep layer of the Black Sea, driven by wind with cyclonic vorticity. The primary features of deep-sea circulation are eddies distributed across the continental slope and continental rise. The Rim Current instability, along with topographic and planetary β-effects, contributes possibly to the formation of eddy structures in the deep Black Sea.

Keywords: Black Sea, large-scale circulation, deep currents, mathematical modeling, topographic β-effect, planetary β-effect, Rossby waves

Acknowledgments: T he study was carried out within the framework of state assignment of FSBSI FRC MHI on themes FNNN-2023-0003 and FNNN-2024-0012.

For citation: Pavlushin, A.A., 2025. Numerical Simulation of Deep Currents in the Black Sea Using a Two-Layer Eddy-Resolving Model. *Physical Oceanography*, 32(4), pp. 537-557.

Introduction

The large-scale water circulation in the Black Sea is considered well-studied by the scientific community. Instrumental observations of currents span over a century. The circulation scheme, with the meandering Rim Current (RC) as its primary component encircling the deep-water part of the sea, was first described by Soviet scientist N. M. Knipovich in 1932 [1]. He proposed the existence of two separate large-scale cyclonic eddies within the RC, giving rise to the term "Knipovich's glasses." Since then, this circulation scheme has undergone only minor refinements [1].

In addition to the RC, the large-scale circulation in the Black Sea includes eddy formations, primarily anticyclones, forming in the meander troughs between the RC

[1] Knipovich, N.M., 1932. The Hydrological Investigations in the Black Sea Area. *Trudy Azovo-Chernomorskoy Nauchnopromyslovoy Ekspeditsii*, 10(10), p. 274 p. (in Russian).

and the coast. Typically, their spatial scale ranges from 30 to 150 km. In scientific literature these eddies are referred to as mesoscale vortices while the RC is classified as a large-scale current. However, according to A. S. Monin's classification [2], mesoscale vortices correspond to synoptic variability processes whereas the RC corresponds to seasonal variability. The most frequently observed anticyclonic vortices to the right of the RC are the quasi-stationary Batumi anticyclone located near the eastern coast and the Sevastopol anticyclone west of the Crimean Peninsula [1].

It is important to note that all the aforementioned elements of large-scale circulation exist only in the water layer above the main pycnocline [2]. The movement of water masses below the pycnocline to the seabed, which constitutes deep-water circulation, remains poorly understood despite long-term observations as direct measurements of currents at great depths over extended periods are labor-intensive and costly.

The lack of sufficient observational data has led to diverse and often conflicting hypotheses about the strength and direction of deep currents. Some hypotheses suggest the absence of such currents while others propose variable-direction currents. Notably, sporadic measurements of current parameters at great depths have been conducted. Results from analyzing multiyear observational data in the Oceanographic Data Bank (ODB) of Marine Hydrophysical Institute, reported in [3], indicate that variable-direction currents with velocities up to 25 cm/s can exist in the deep Black Sea.

In the 21st century, new methods have emerged for studying deep-sea currents in the Black Sea. First, Argo floats, deployed in the Black Sea since 1999, have been used to collect data. Although they do not directly measure current parameters, these floats enable the calculation of trajectories and mean velocities based on displacement at specific depths.

Analysis of a large dataset from Argo floats [4] revealed that deep-sea currents moved cyclonically along isobaths at mean velocities of 4–6 cm/s. Given the thickness of the water layer below the pycnocline, the mass of water transported by these currents exceeds that carried by the RC. This indicates that deep-sea currents are significant and not negligible.

In 2016, scientists from Shirshov Institute of Oceanology of RAS and Marine Hydrophysical Institute of RAS deployed a moored buoy station on the Black Sea continental slope. For one year, current parameters were measured at a depth of 1700 m using an Acoustic Doppler Current Profiler (ADCP) [5]. These measurements revealed horizontal velocity oscillations of ±15 cm/s indicating the presence of wave processes in the deep Black Sea waters.

Another important source of information about the Black Sea currents is mathematical modeling. Multiple simulations of the Black Sea circulation have been

[2] Monin, A.S., Kamenkovich, V.M. and Court, V.G., 1977. *Variability of the World Ocean*. New York: Wiley, 241 p.

conducted using various models [6–13]. Most models simulate key features of large-scale and mesoscale dynamics above the main pycnocline accurately. However, deep currents derived from these models are often described or analyzed in brief only. Moreover, results from different models show significant variability in current velocities and deep-sea circulation direction [11]. Additionally, data assimilation procedures influence simulated current patterns significantly.

Studies [14–16] using the MHI model to simulate deep-sea circulation in the Black Sea focus primarily on currents over the continental slope along the Caucasian coast. In this peripheral the deep-sea region, narrow jet currents opposing the main cyclonic circulation periodically occur. However, deep-sea currents in the central Black Sea remain understudied, despite their higher velocities and greater water layer thickness relative to the periphery.

This study aims to provide a detailed analysis of deep-sea current fields derived from numerical modeling with a two-layer eddy-resolving model incorporating actual bottom topography [17, 18]. Simulations using this model show strong agreement with observed large-scale circulation in the upper layer of the sea. This is attributed to the pronounced density gradient between surface and deep-sea waters, enabling the Black Sea to be modeled as a two-layer system [2]. Given the relatively stable water density below the main pycnocline [1], deep-sea currents derived from this model approximate reality likely closely.

The model incorporates bottom topography, which influences the formation of deep-sea circulation significantly. Furthermore, this simplified model provides a statistically stable solution enabling time-averaged estimates of circulation and current energy parameters.

Materials and methods

Two-layer model. Parameter selection. The model represents a closed water basin comprising two homogeneous fluid layers with different density ($\rho_1 < \rho_2$). The equations of the two-layer model are obtained by integrating the primitive equations of motion and continuity for the upper and lower layers in a Cartesian coordinate system with a downward-directed *Z*-axis:

$$\frac{\partial u_1 h_1}{\partial t} + \frac{\partial u_1^2 h_1}{\partial x} + \frac{\partial v_1 u_1 h_1}{\partial y} - f v_1 h_1 = g h_1 \frac{\partial \zeta}{\partial x} + \tau^x - R_L^x + A_B h_1 \Delta\left(\Delta u_1\right),$$

$$\frac{\partial v_1 h_1}{\partial t} + \frac{\partial u_1 v_1 h_1}{\partial x} + \frac{\partial v_1^2 h_1}{\partial y} + f u_1 h_1 = g h_1 \frac{\partial \zeta}{\partial y} + \tau^y - R_L^y + A_B h_1 \Delta\left(\Delta v_1\right),$$

$$\frac{\partial u_2 h_2}{\partial t} + \frac{\partial u_2^2 h_2}{\partial x} + \frac{\partial v_2 u_2 h_2}{\partial y} - f v_2 h_2 = g h_2 \frac{\partial \zeta}{\partial x} + g' h_2 \frac{\partial h_1}{\partial x} + R_L^x - R_D^x + A_B h_2 \Delta\left(\Delta u_2\right),$$

$$\frac{\partial v_2 h_2}{\partial t} + \frac{\partial u_2 v_2 h_2}{\partial x} + \frac{\partial v_2^2 h_2}{\partial y} + f u_2 h_2 = g h_2 \frac{\partial \zeta}{\partial y} + g' h_2 \frac{\partial h_1}{\partial y} + R_L^y - R_D^y + A_B h_2 \Delta\left(\Delta v_2\right),$$

$$\frac{\partial h_1}{\partial t}+\frac{\partial u_1 h_1}{\partial x}+\frac{\partial v_1 h_1}{\partial y}=0,$$
$$\frac{\partial h_2}{\partial t}+\frac{\partial u_2 h_2}{\partial x}+\frac{\partial v_2 h_2}{\partial y}=0,$$

where $(u_1,v_1),(u_2,v_2)$ are horizontal components of currents in the upper and lower layers, respectively (eastward *X*-axis, northward *Y*-axis); $f=f_0+\beta y$ is Coriolis parameter, $f_0=10^{-4}$ 1/s, $\beta=1.67\cdot10^{-11}$ 1/(m·s); g = 9.81 m/s^2 is gravitational acceleration; $g'=g(\rho_2-\rho_1)/\rho_2$ is reduced gravitational acceleration; ρ_1, ρ_2 are seawater density in the layers; R_L^x, R_L^y are interfacial friction components between layers, $\left\{R_L^x=r_1\left(u_1-u_2\right),\ R_L^y=r_1\left(v_1-v_2\right)\right\}$ when $h_2 > 0$, $\{R_L^x=\left(r_2+r_3\left|\mathbf{u}_1\right|\right)u_1$, $R_L^y=\left(r_2+r_3\left|\mathbf{u}_1\right|\right)v_1\}$ when $h_2 = 0$; R_D^x, R_D^y are bottom friction components in the lower layer $\left\{R_D^x=\left(r_2+r_3\left|\mathbf{u_2}\right|\right)u_2,\ R_D^y=\left(r_2+r_3\left|\mathbf{u_2}\right|\right)v_2\right\}$, r_1, r_2, r_3 are empirical coefficients; A_B is coefficient of horizontal turbulent viscosity; τ^x, τ^y are wind shear stress components; $\Delta=\frac{\partial^2}{\partial x^2}+\frac{\partial^2}{\partial y^2}$ is Laplace operator.

To close the system of equations, the integral continuity equation is applied using the rigid lid approximation:

$$U_x+V_y=0,$$

enabling the introduction of an integral streamfunction ψ at

$$U=-\psi_y,\ V=\psi_x,$$

where $U=u_1h_1+u_2h_2,\ V=v_1h_1+v_2h_2,$ are components of total flow.

Boundary conditions at the sea surface, the interface between layers and seabed are applied in deriving equations (1) – (4). Along the lateral boundaries, no-slip conditions and a zero velocity Laplacian are imposed:

$$u_k=v_k=0,\quad \Delta u_k=\Delta v_k=0,\quad k=1;2.$$

The Coriolis parameter is modeled using the β-plane approximation. The model incorporates bottom friction, friction between layers and horizontal turbulent viscosity modeled with a biharmonic operator. Circulation is driven solely by wind shear stress. Buoyancy fluxes at the sea surface and lateral boundaries are neglected, with buoyancy balanced by two layers of different density where the interface represents a constant pycnocline.

The two-layer model equations are discretized using finite differences on an Arakawa B-grid. Divergent terms in the equations of motion and continuity are discretized with central differences, and a semi-implicit scheme is employed for time integration [19].

In this study's experiments, the horizontal grid step and time integration step were $\Delta x = \Delta y = 2$ km and $\Delta t = 120$ s, respectively. For this time step, biharmonic turbulent viscosity coefficient $A_B = 1.5 \cdot 10^8$ m⁴/s was selected to ensure numerical stability.

Other model parameters were calibrated to observed Black Sea conditions. The reduced gravity acceleration $g' = g(\rho_2 - \rho_1)/\rho_2$ derived from the density difference between layers corresponding to a salinity difference ($\Delta S = 4$ ‰), was set to 0.032 m/s². The upper layer thickness at rest was set to $h_0 = 100$ m.

Bottom friction is modeled as proportional to the square of current velocity, with the friction coefficient calibrated to match observed deep-sea current velocities from [4, 5].

Model fields of wind shear stress on the sea surface were derived from empirical formulas accounting for spatial and temporal variability of observed wind fields [20]. The annual mean wind stress vorticity was consistent with observed values [1].

Spatially averaged kinetic energy values were used to monitor the numerical experiments in the upper $\langle K_1 \rangle$ and lower $\langle K_2 \rangle$ layers, defined by formulas

$$\langle K_1 \rangle = \rho \left\langle h_1 \frac{u_1^2 + v_1^2}{2} \right\rangle, \quad \langle K_2 \rangle = \rho \left\langle h_2 \frac{u_2^2 + v_2^2}{2} \right\rangle,$$

where angle brackets denote spatial averaging over the entire sea area; (u_1, v_1), (u_2, v_2) are horizontal velocity components in the upper and lower layers, respectively; h_1, h_2 represent layer thickness; ρ is mean sea water density.

Results of numerical experiments

The spatial and temporal variability of deep-sea current fields was analyzed using three numerical experiments (E1, E2, E3) conducted with the two-layer model. These experiments differed only in the amplitude and temporal variability of surface wind stress. In all experiments, calculations began from a state of rest, with the sea surface and interface between layers assumed horizontal and current velocities set to zero.

In experiment E1, the surface wind stress field was temporarily constant but incorporated spatial distribution features [20]. As demonstrated in [21], these features are critical for the accurate development of large-scale circulation. Experiment E1 aimed to trace the evolution of circulation from a state of rest to statistical equilibrium. Furthermore, the experiments revealed that under stationary external forcing conditions, the model reached statistical equilibrium faster. Algorithmically, constant wind stress field $\boldsymbol{\tau}$ $(x, y) = (\tau^x, \tau^y)$ was derived from the following formulas:

$$\tau^x(x,y) = -\tau_0^x \cos\left(\frac{\pi x}{L} + \pi\left(\frac{1}{2} - \alpha S\right)\right)\cos\left(\frac{\pi y}{B}\right)(1-S),$$
$$\tau^y(x,y) = -\tau_0^y \sin\left(\frac{\pi x}{L} + \pi\left(\frac{1}{2} - \alpha S\right)\right)(1-S)\left(\frac{(x/\Delta x)^2 + 20000}{(L/\Delta x)^2 + 20000}\right), \quad (1)$$

where τ_0^x, τ_0^y are constant amplitude values; $\alpha \in [0;1]$ is coefficient determining eastward propagation of anticyclonic vorticity zone; $S \in [0;\ 0.5]$ is parameter controlling temporal variability.

Fig. 1 shows the spatial distributions of fields $\boldsymbol{\tau}$ and $\mathrm{rot}_Z\ \boldsymbol{\tau}$ obtained in experiment E1. The calculation of $\boldsymbol{\tau}$ in equation (1) used the following parameters: $\tau_0^x = \tau_0^y = 0.05$ N/m^2, $\alpha = 0.85$, $S = 0.4$. Fig. 1 indicates maximum positive vorticity $\boldsymbol{\tau}$ (corresponding to a cyclone) in the eastern Black Sea and negative vorticity (anticyclonic) in the western Black Sea.

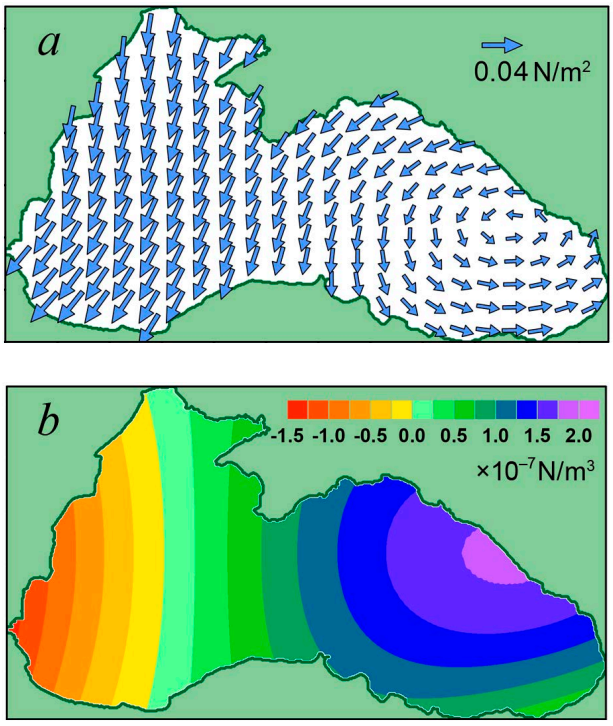

F i g. 1. Stationary fields $\boldsymbol{\tau}$ (*a*) and $\mathrm{rot}_Z\ \boldsymbol{\tau}$ (*b*) in experiment E1

Graphs of temporal variability $\langle K_1 \rangle$ and $\langle K_2 \rangle$ constructed for experiment E1 (Fig. 2, *a*, *b*) show that during the first year from the start of the calculations, the kinetic energy of the currents increases both in the upper and lower sea layers. At this time, under effect of the wind with cyclonic vorticity, the RC jet forms in the upper layer, which is located to the left of the distribution boundary of the lower (deep-water) layer (Fig. 3, *a*1). In the lower layer, Ekman pumping [22] drives the currents primarily along the isobaths (Fig. 3, *b*1).

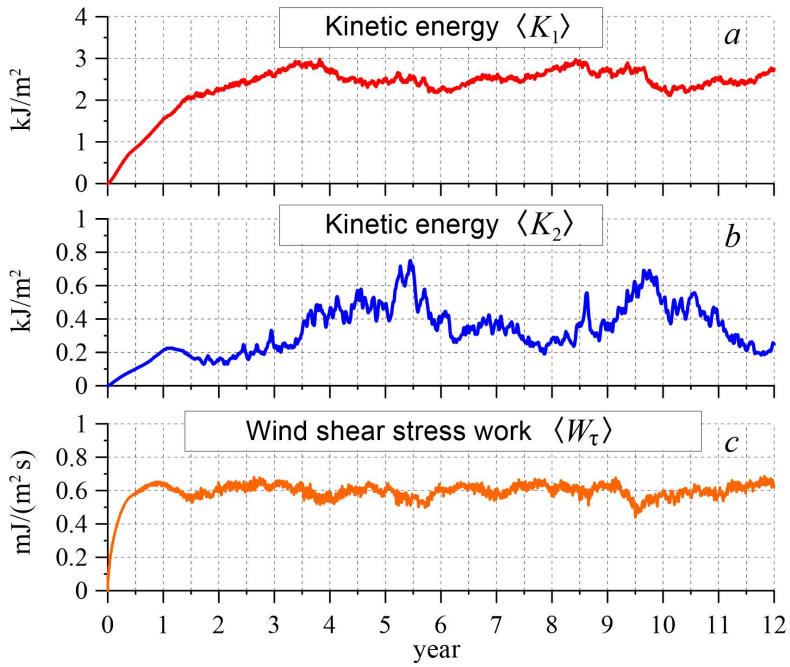

F i g. 2. Time dependence of $\langle K_1 \rangle$ (*a*), $\langle K_2 \rangle$ (*b*) and $\langle W_\tau \rangle$ (*c*) in experiment E1

Near the current velocity fields (Fig. 3, *a*1, *b*1), corresponding sea level ζ and function *M* fields are given (Fig. 3, *a*2, *b*2). Function *M* (similar to Montgomery potential in meteorology) represents the water pressure in the lower layer while ζ represents the pressure in the upper layer.

Scalar fields ζ and *M* facilitate visualization of currents as alternatives to vector fields u_1, u_2. Under geostrophic equilibrium, ζ isolines represent streamlines for upper-layer currents while *M* isolines represent streamlines for lower-layer currents with higher values of ζ and *M* to the right of the flow direction. The current velocity increases with decreasing spacing of ζ or *M* isolines.

To facilitate comparison of currents between layers, ζ isolines corresponding to the RC core are superimposed on the *M* maps in pink.

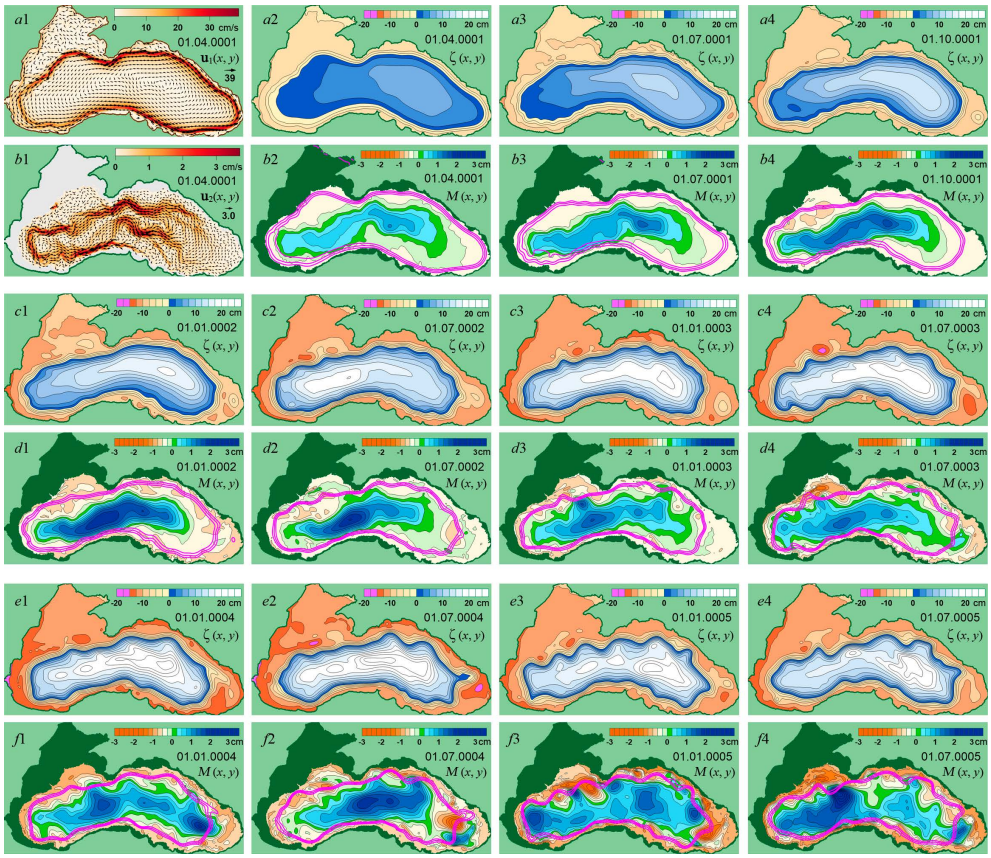

F i g. 3. Instantaneous fields u_1 (*a*1), u_2 (*b*1), ζ (*a*2 – *a*4, *c*1 – *c*4, *e*1 – *e*4) and M (*b*2 – *b*4, *d*1 – *d*4, *f*1 – *f*4) in experiment E1

Maps $\zeta(x, y)$ and $M(x, y)$ dated 01.07.0001–01.01.0002 (Fig. 3, *a*3, *a*4, *b*3, *b*4, *c*1, *d*1) demonstrate that currents in both upper (RC) and lower layers intensify during the first year, leading to increasing values of $\langle K_1 \rangle$ and $\langle K_2 \rangle$ (Fig. 2, *a*, *b*).

During the second year, the RC strengthens (Fig. 3, *c*2 – *c*4) and $\langle K_1 \rangle$ increases while circulation weakens (Fig. 3, *d*2 – *d*4) and $\langle K_2 \rangle$ decreases in the lower layer. This behavior results from a decrease in wind shear stress work $\langle W_\tau \rangle$ after its peak at the end of the first year (Fig. 2, *c*). Consequently, the uplift of the interface between layers driven by Ekman pumping slows down. The decrease in $\langle W_\tau \rangle$ is in turn associated with the alignment of the RC jet in the eastern Black Sea and its displacement from the region of maximum wind stress vorticity (Fig. 3, *a*4).

By the end of the second year, the wind energy input into the sea stabilizes at a steady level until the calculations end (Fig. 2, *c*) indicating a statistical equilibrium regime. The stabilization of $\langle W_\tau \rangle$ stems from increased velocity of surface currents and the onset of RC instability manifested through its meandering, which begins around the sixth month of the first year and evolves throughout the second and third years (Fig. 3, *a*3, *a*4, *c*1 – *c*4).

The intensified RC instability leads to the formation of eddy structures (ES) [3] at the periphery of the lower layer (beneath the RC). These structures move along the continental slope with cyclonic motion, aligned with the RC meandering (Fig. 3, *d*1 – *d*4, *f*1 – *f*4). This process is most pronounced in the northern Black Sea.

During the third and fourth years, the kinetic energy of currents increases in both layers (Fig. 2, *a*, *b*). In the lower layer, this energy growth results from the growing number and size of eddy structures forming along the continental slope and continental rise. By the fifth year, eddy formation in the lower layer reaches its peak (Fig. 3, *f*3) corresponding to the level of wind energy input under statistical equilibrium conditions.

The eddy structures emerging in the lower layer represent traveling waves in the current field, classified as gradient-vorticity waves [23] due to the conservation of potential vorticity [24]. For the lower layer of a two-layer fluid, this conservation law takes the following form:

$$\frac{d}{dt}\frac{f+\xi_2}{H}=0 \quad \text{or} \quad \frac{f+\xi_2}{H}=\text{const},$$

where $\xi_2=\frac{\partial v_2}{\partial x}-\frac{\partial u_2}{\partial y}$ is relative vorticity of current velocity in the lower layer.

According to this law, when a water mass moves, changes in the Coriolis parameter f or sea depth H (x, y) alter relative vorticity ξ_2 of the moving water. In the first case, planetary Rossby waves form, while in the second case, bottom-trapped topographic Rossby waves develop, with the continental slope and continental rise acting as the inclined topography.

Through the analysis of experiments E2 and E3, we examine the characteristics of deep circulation formation under statistical equilibrium conditions. These experiments used wind stress field $\boldsymbol{\tau}$ (x, y, t) with spatial and seasonal variability, achieved by specifying parameter S in equations (1) as a time-dependent function:

$$S(t)=0.5\cdot\sin^2\left(\frac{\pi}{8640}\cdot t\right),$$

where t is time in hours.

The wind stress intensity was adjusted by varying different amplitude values τ_0^x, τ_0^y in equations (1). In experiment E2, these values were set to 0.02 N/m², producing a basin-averaged annual mean wind stress vorticity $\overline{\langle \mathrm{rot}_Z \boldsymbol{\tau} \rangle}$ = $3.8\cdot10^{-8}$ N/m³. For experiment E3, reduced values τ_0^x, τ_0^y equal to 0.015 N/m², at which $\overline{\langle \mathrm{rot}_Z \boldsymbol{\tau} \rangle}$ = $2.6\cdot10^{-8}$ N/m³, were implemented. Both experiments maintained $\alpha = 0.75$.

[3] Ginzburg, A.I., Zatsepin, A.G., Kostianoy, A.G., Krivosheya, V.G., Skirta, A.Yu., Soloviev, D., Stanichny, S., Sheremet, N.A., Shiganova, T.A. [et al.], 2001. Anticyclonic Eddies in the Deep Eastern Black Sea in Summer-Autumn 1999 (Satellite and Ship-Borne Observations). *Issledovanie Zemli iz Kosmosa*, (5), pp. 3-11 (in Russian).

Varying wind stress intensities in experiments E2 and E3 was motivated by the existence of two distinct regimes of large-scale circulation in the Black Sea. As demonstrated in [25], the basin circulation exhibits a bimodal response to wind stress intensity. The first circulation regime emerges when the annual mean wind stress vorticity over the entire sea surface $T = \overline{\langle \mathrm{rot}_Z \boldsymbol{\tau} \rangle}$ exceeds threshold value T_{thr}. In this regime, the RC maintains a stable trajectory along the continental slope, forming continuous cyclonic circulation that encompasses the entire perimeter of the deep-sea basin. Conversely, when $T = \overline{\langle \mathrm{rot}_Z \boldsymbol{\tau} \rangle}$ falls below the threshold T_{thr}, the system transitions to the second circulation regime, characterized by periodic detachment (every 7–10 years) of the RC eastern branch from the coastline and its westward migration. This reorganization shifts the primary cyclonic gyre confining it primarily to the western Black Sea. This transition highlights the nonlinear response of the Black Sea dynamics to variations in atmospheric forcing.

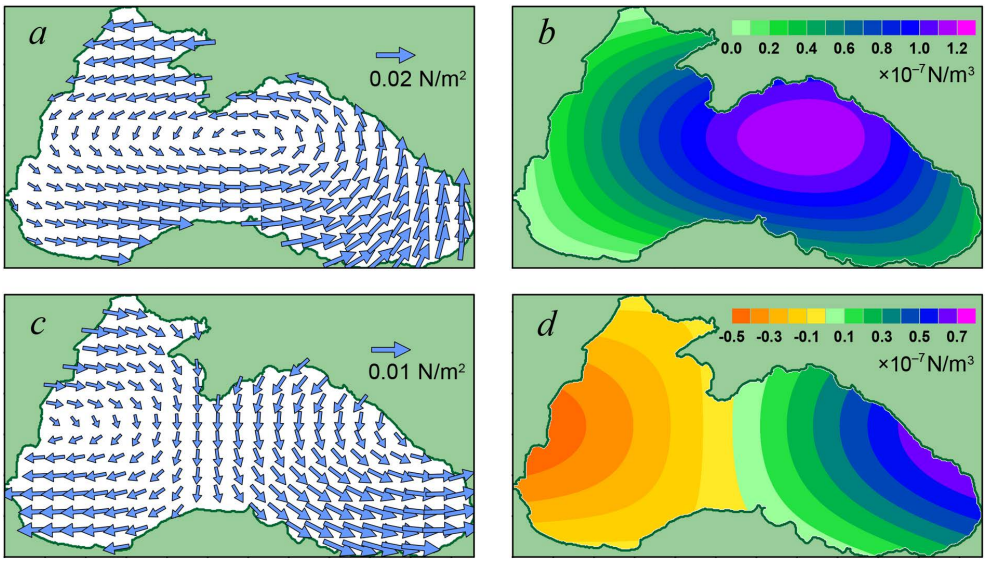

F i g. 4. Fields $\boldsymbol{\tau}$ and $\mathrm{rot}_Z\,\boldsymbol{\tau}$ in experiment E2 in January (*a*, *b*) and July (*c*, *d*)

Fig. 4 shows fields $\boldsymbol{\tau}$ and $\mathrm{rot}_Z\,\boldsymbol{\tau}$ for January 1st and July 1st in experiment E2. During winter months, cyclonic vorticity $\boldsymbol{\tau}$ dominates over the entire sea surface, peaking in the eastern Black Sea. In the first half of the year, this vorticity maximum shifts eastward gradually, while an area of anticyclonic $\boldsymbol{\tau}$ vorticity emerges in the western Black Sea. The second half of the year shows an opposite progression of $\boldsymbol{\tau}$ and $\mathrm{rot}_Z\,\boldsymbol{\tau}$ patterns, with the vorticity features shifting westward.

Graphs in Fig. 5 *a*, *b*, *c* illustrate the temporal evolution of $\langle K_1 \rangle(t)$, $\langle K_2 \rangle(t)$ and $\langle W_\tau \rangle(t)$ in experiment E2. The seasonal variability of wind stress fields drives corresponding oscillations in both wind energy input $\langle W_\tau \rangle$ and upper-layer

circulation intensity, as quantified by $\langle K_1 \rangle$. Notably, the seasonal cycle $\langle K_1 \rangle$ exhibits a phase lag of approximately three months relative to $\langle W_\tau \rangle$ variations, due to the inertial response of the dynamical system.

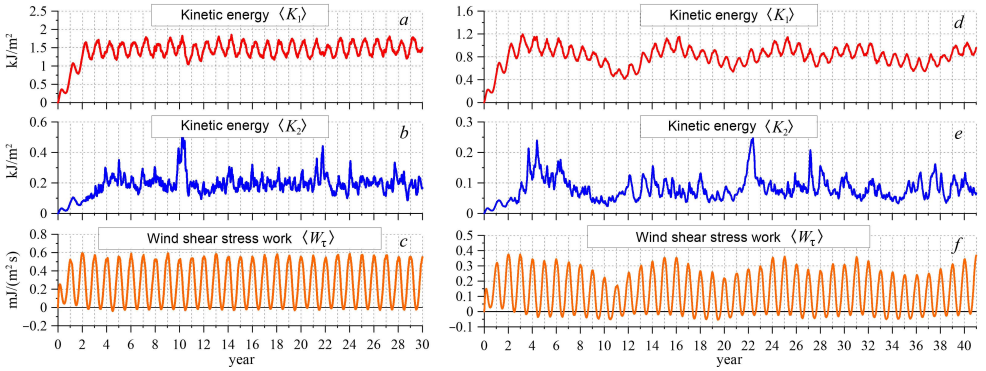

F i g. 5. Graphs of kinetic energy and work of wind shear stress in experiments E2 (*a, b, c*) and E3 (*d, e, f*)

The basin-averaged kinetic energy of lower-layer currents $\langle K_2 \rangle$ exhibits pronounced temporal variability (Fig. 5, *b*), with many energy peaks coinciding with maxima in wind energy input $\langle W_\tau \rangle$. However, establishing a direct correlation between $\langle K_2 \rangle$ and the seasonal cycles of either $\langle W_\tau \rangle$ or upper-layer energy $\langle K_1 \rangle$ would be methodologically unsound. Comparing the temporal evolution of $\langle K_1 \rangle$ and $\langle K_2 \rangle$ (Fig. 5 *a*, *b*) requires accounting for their distinct scale ranges and spatially averaged nature.

The circulation dynamics in the upper and lower layers can be traced through the sequential ζ (x, y) and M (x, y) fields shown in Fig. 6. The upper two rows demonstrate winter season, while the lower two rows depict summer months. In M field panels, additional ζ isolines marking the RC core are superimposed. The analysis reveals greater stability of the RC in the upper layer during winter months, indicated by fewer and smaller meanders compared to July when meanders are more frequent.

In the lower layer, January exhibits stronger currents in the central part of the deep-sea basin compared to July (Fig. 6, *b*1–*b*4, *d*1–*d*4), likely driven by enhanced Ekman pumping during winter. The propagation of more energetic eddies along the northeastern continental slope and continental rise contributes further, with eddies forming in the southeastern Black Sea near Trabzon, weakening as they move toward the Crimean Peninsula, and regaining intensity to strengthen currents in the western deep-sea basin (Fig. 6, *b*3, *b*4). The summer period demonstrates similar but weaker patterns of eddy generation and propagation along the northern continental slope.

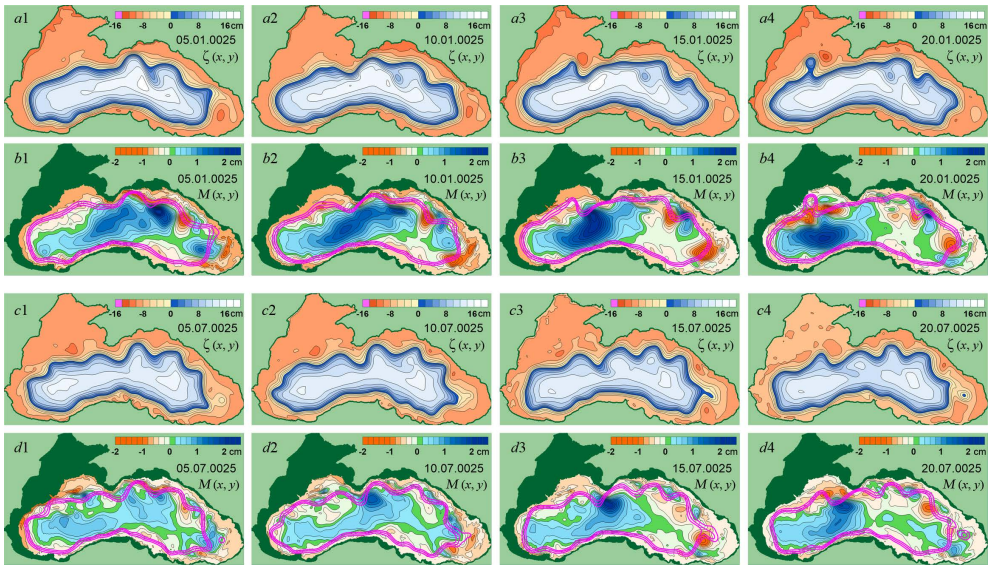

F i g. 6. Instantaneous fields ζ (*x, y*) and *M* (*x, y*) in experiment E2

During the summer period, eddies along the northern continental slope exhibit patterns of generation, propagation and transformation similar to those in winter months, but with lower intensity (Fig. 6, *d*3, *d*4).

Visual comparison of the RC jet position with lower-layer eddies (Fig. 6, *b*1–*b*4, *d*1–*d*4) reveals a consistent correlation. Typically, the RC jet shifts seaward over cyclonic eddies, while moving shoreward over anticyclonic ones. The phase propagation velocities of both RC meanders and eddies show complete synchrony.

In experiment E3, as previously mentioned, the wind stress field exhibited mean annual vorticity $T = \overline{\langle \mathrm{rot}_Z \boldsymbol{\tau} \rangle}$ below threshold value T_{thr} across the sea area, inducing distinct 7–9-year oscillations in circulation intensity, as shown in Fig. 5, *d*. In the $\langle K_2 \rangle$ graph (Fig. 5, *e*), no oscillations similar to $\langle K_1 \rangle$ are observed. However, significant amplitude spikes occurring predominantly during winter take place. As explained in [25], the $\langle K_1 \rangle$ oscillations result from variations in wind energy input $\langle W_\tau \rangle$ caused by the RC east-to-west displacement. The $\langle K_1 \rangle$ maxima correspond to periods when the RC flows along the entire perimeter of the deep-sea zone while $\langle K_1 \rangle$ minima occur when the it crosses the central Black Sea.

Fig. 7 presents the instantaneous ζ (*x*, *y*) and *M* (*x*, *y*) fields obtained in experiment E3. The upper two rows of panels correspond to periods when $\langle K_1 \rangle$ reaches maximum values when the circulation pattern resembles that in experiment E2 (Fig. 6, *d*1–*d*4).

The third and fourth rows in Fig. 7 show fields characteristic of periods with minimum $\langle K_1 \rangle$ values. During these phases, the RC demonstrates an anomalous cross-basin trajectory crossing connecting the Turkish coastal waters and the Novorossiysk area through the central eastern deep-sea basin. This displacement

from the eastern and northeastern Black Sea continental slope weakens lower-layer deep-sea circulation and halts eddy generation in the southeastern Black Sea.

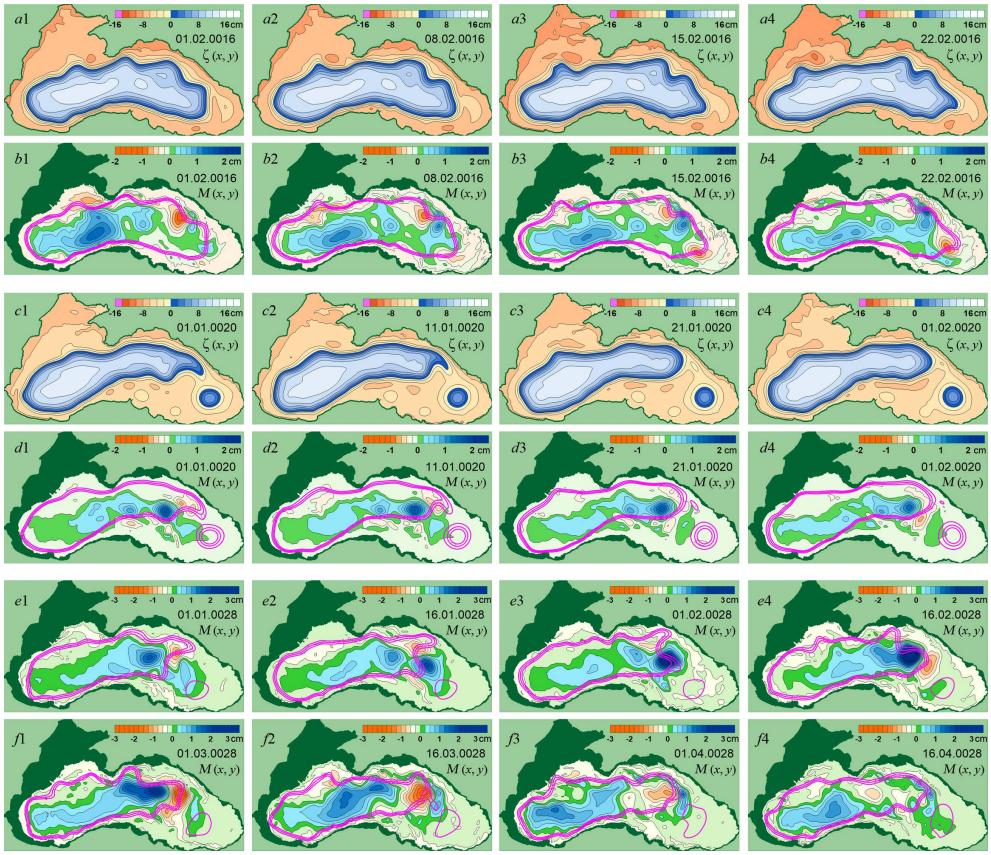

F i g. 7. Instantaneous fields ζ (*x, y*) and *M* (*x, y*) in experiment E3

The bottom two rows of Fig. 7 show the $\zeta(x, y)$ and $M(x, y)$ fields corresponding to the sharp intensification of $\langle K_2 \rangle$ observed in early February, year 28 (from the beginning of the calculations) (Fig. 5, *e*). This $\langle K_2 \rangle$ spike results from a strong cyclonic eddy forming and intensifying over the continental rise near the Caucasian coast (Fig. 7, *e*3, *e*4). After peaking, the eddy propagates along the continental rise, strengthening the cyclonic circulation in the western deep-sea basin.

The $\langle K_2 \rangle$ spikes resulting from intensifying eddies are a key characteristic of lower-layer dynamics. These energetic events manifest as direct consequences of hydrodynamic instability in large-scale currents. A detailed examination of the mechanisms generating lower-layer circulation will be explored in future research.

The features of the spatial distribution of currents in the lower layer of the sea obtained in the two-layer model show good agreement with modeling results in

[14, 15]. However, those studies do not analyze the dynamics of deep currents or explain the causes of eddy formation in the lower layer of the Black Sea adequately.

Mean and eddy currents

To analyze dynamic processes in the sea, we applied a statistical method, which consists in dividing real (instantaneous) currents into mean and deviations from the mean (pulsations). Visually, current pulsations most often have an eddy structure, so they are also called eddy currents. An important point in dividing currents into mean and eddy is the choice of the averaging period, which is determined based on the tasks and specific dynamics of the sea. When analyzing mean and eddy currents, it is necessary to remember that such a division is conceptual, as only total currents exist in reality.

We examine the results of applying statistical analysis to experiment E2. In the layered model, the flow is defined as the product of current velocity and layer thickness. This is expressed as $\mathbf{U}_1 = \mathbf{u}_1 h_1$ for the upper layer and $\mathbf{U}_2 = \mathbf{u}_2 h_2$ for the lower layer. Then mean currents are calculated as $\mathbf{U}_1^{\mathrm{m}} = \overline{\mathbf{u}_1 h_1}$, $\mathbf{U}_2^{\mathrm{m}} = \overline{\mathbf{u}_2 h_2}$, with deviations from the mean (pulsations) $\mathbf{U}_1^{\mathrm{p}} = \mathbf{U}_1 - \mathbf{U}_1^{\mathrm{m}}$, $\mathbf{U}_2^{\mathrm{p}} = \mathbf{U}_2 - \mathbf{U}_2^{\mathrm{m}}$. The overbar means averaging over time, superscript "m" is used to denote mean currents, "p" – for pulsations. We set the averaging period to be long enough (at least 20 years) to exclude temporal variability of mean currents.

Fig. 8 presents the fields of mean and eddy currents in the upper layer (first row) and lower layer (third row), along with their corresponding ζ (second row) and M (fourth row) fields. Mean current fields $\mathbf{U}_1^{\mathrm{m}}, \zeta^{\mathrm{m}}, \mathbf{U}_2^{\mathrm{m}}, M^{\mathrm{m}}$ are given in the first column, while columns two to four display eddy current fields $\mathbf{U}_1^{\mathrm{p}}, \zeta^{\mathrm{p}}, \mathbf{U}_2^{\mathrm{p}}, M^{\mathrm{p}}$.

The upper-layer mean currents propagate along the continental slope deviating from isobaths and follow sea surface isolines consistent with geostrophic balance. The core velocities of mean currents reach 20 cm/s and a flow width of 30–50 km. Over a 20-year averaging period, mean currents remain nearly stationary in both upper and lower layers.

Visually, upper-layer current oscillations appear as alternating cyclonic and anticyclonic eddies propagating counterclockwise along the mean RC core (cyclonic rotation). These eddies exhibit significantly larger amplitude in the northern Black Sea compared to the southern region. Upper-layer eddy generation and the RC meanders in the western boundary current both result from the hydrodynamic instability of the large-scale flow.

Lower-layer mean currents are strongly influenced by bathymetry, with streamlines (represented by M^{m} isolines) closely following isobaths.

The oscillating (eddy) component of deep currents similarly consists of alternating mesoscale eddy structures propagating cyclonically over the continental slope and continental rise. The likely generation mechanisms for these eddies include the RC instability, topographic and planetary β-effects.

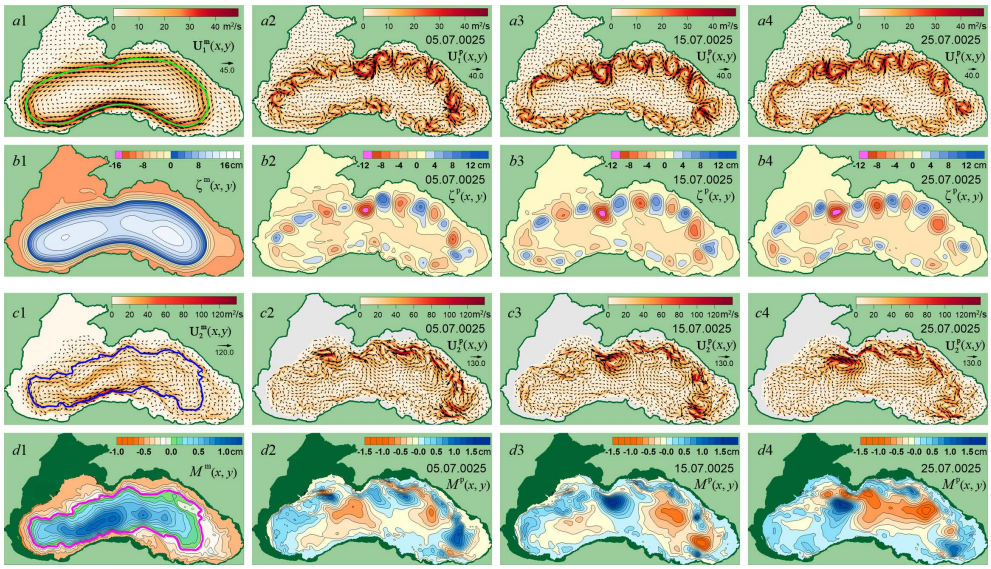

F i g. 8. Mean fields $\mathbf{U}_1^{\mathrm{m}}$ ($a1$), ζ^{m} ($b1$), $\mathbf{U}_2^{\mathrm{m}}$ ($c1$), M^{m} ($d1$) and instantaneous fields $\mathbf{U}_1^{\mathrm{p}}$ ($a2 – a4$), ζ^{p} ($b2 – b4$), $\mathbf{U}_2^{\mathrm{p}}$ ($c2 – c4$), M^{p} ($d2 – d4$) in experiment E2

Visually, the fields of eddy and instantaneous currents in the lower layer show strong similarity indicating a dominant eddy component in the total flow. To confirm this, we calculate the spatially averaged kinetic energy of mean $K_1^{\mathrm{m}}, K_2^{\mathrm{m}}$ and eddy $K_1^{\mathrm{p}}, K_2^{\mathrm{p}}$ components in the upper and lower layers:

$$\overline{K_1} = \sum_S \rho \frac{\overline{h_1 \mathbf{u}_1^2}}{2} = K_1^{\mathrm{m}} + K_1^{\mathrm{p}}, \quad K_1^{\mathrm{m}} = \sum_S \rho \frac{\mathbf{U}_1^{\mathrm{m}} \cdot \overline{\mathbf{u}_1}}{2}, \quad K_1^{\mathrm{p}} = \overline{K_1} - K_1^{\mathrm{m}},$$

$$\overline{K_2} = \sum_S \rho \frac{\overline{h_2 \mathbf{u}_2^2}}{2} = K_2^{\mathrm{m}} + K_2^{\mathrm{p}}, \quad K_2^{\mathrm{m}} = \sum_S \rho \frac{\mathbf{U}_2^{\mathrm{m}} \cdot \overline{\mathbf{u}_2}}{2}, \quad K_2^{\mathrm{p}} = \overline{K_2} - K_2^{\mathrm{m}}.$$

After averaging over the area, we obtain the following values:

$$\left\langle \overline{K_1} \right\rangle = 1.46 \text{ kJ/m}^2, \quad \left\langle K_1^{\mathrm{m}} \right\rangle = 1.04 \text{ kJ/m}^2 \ (71\%), \quad \left\langle K_1^{\mathrm{p}} \right\rangle = 0.42 \text{ kJ/m}^2 (29\%),$$

$$\left\langle \overline{K_2} \right\rangle = 0.20 \text{ kJ/m}^2, \quad \left\langle K_2^{\mathrm{m}} \right\rangle = 0.07 \text{ kJ/m}^2 (34\%), \quad \left\langle K_2^{\mathrm{p}} \right\rangle = 0.13 \text{ kJ/m}^2 (66\%).$$

Thus, the mean component accounts for 71% of the energy in the upper layer, with the eddy component contributing 29%. Conversely, in the lower layer, the eddy component dominates, accounting for 66% of energy, while the mean component contributes 34%.

Interestingly, decomposition into mean and eddy components reveals coherent eddies coinciding with the RC meanders in the upper layer. In contrast, averaging reveals mean deep currents following isobaths that remain visually obscured in instantaneous fields.

Parameters of wave oscillations of deep currents

To study the dispersion properties of wave processes in deep current fields, we constructed temporal variability diagrams of current characteristics along wave propagation trajectories.

As gradient-eddy waves involve oscillations of the horizontal current vector, the transverse component of the current velocity is a logical choice for constructing diagrams. However, since geostrophic balance governs large-scale and mesoscale dynamic processes, the fields $M(x, y, t)$ from experiment E2 were used as input data.

The core of the mean current, defined as the streamline with maximum flow velocity (Fig. 9, *a*), was selected as the reference level. Due to the geostrophic nature of the mean currents, zero isoline M^{m}, corresponding to this flow core, was used as the reference level (Fig. 8, *d*1), closely following the isobath at H = 1950 m (Fig. 9, *b*). Note that bathymetry results in several cores in the mean flow field.

To facilitate correlation between the temporal variability diagram and the Black Sea map, reference points were marked on it at regular intervals (Fig. 9, *a*).

Fig. 9, *c* demonstrates a high-resolution (1-day sampling) temporal variability diagram M^{p} along the zero isoline M^{m} over model years 23–25. Vertical dashed lines, numbered along the top axis, correspond to reference points shown in Fig. 9, *a*.

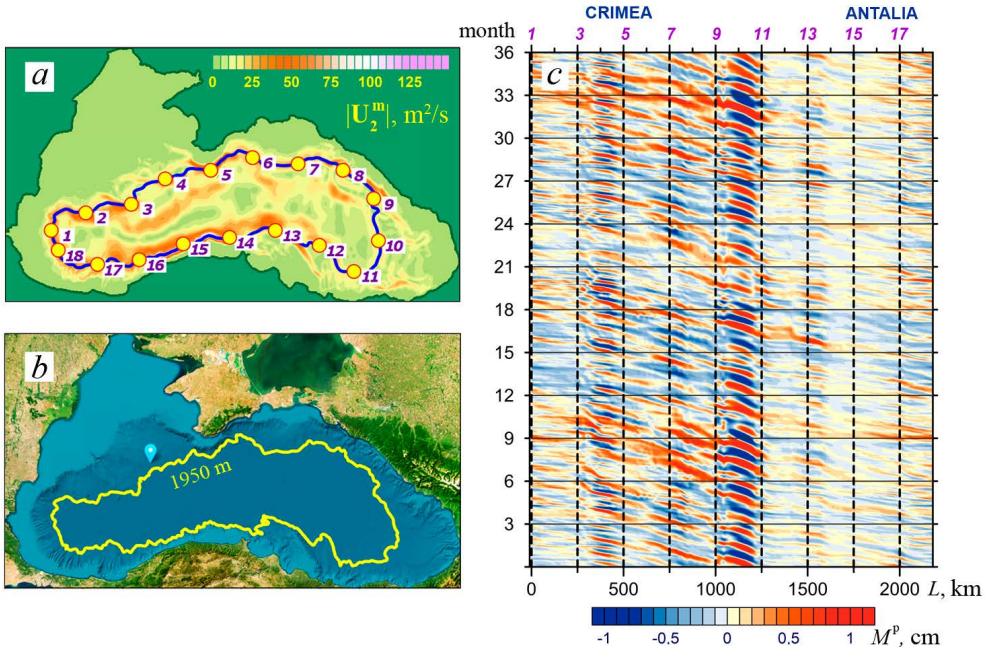

F i g. 9. Modulus of mean flow in the lower layer $\left|\mathbf{U}_2^{\mathrm{m}}\right|$ (*a*), isobath H = 1950 m (*b*), and time diagram M^{p} along isobaths M^{m} (*c*)

The diagram shows alternating oscillations in M^{p}, indicating wave motion along the selected trajectory in a counterclockwise direction. The phase velocity of these waves can be estimated from the slope of lines connecting identical oscillation phases, with notable variations across different segments of the trajectory. The fastest wave propagation occurs between reference points 18–11 in the southern part of the trajectory.

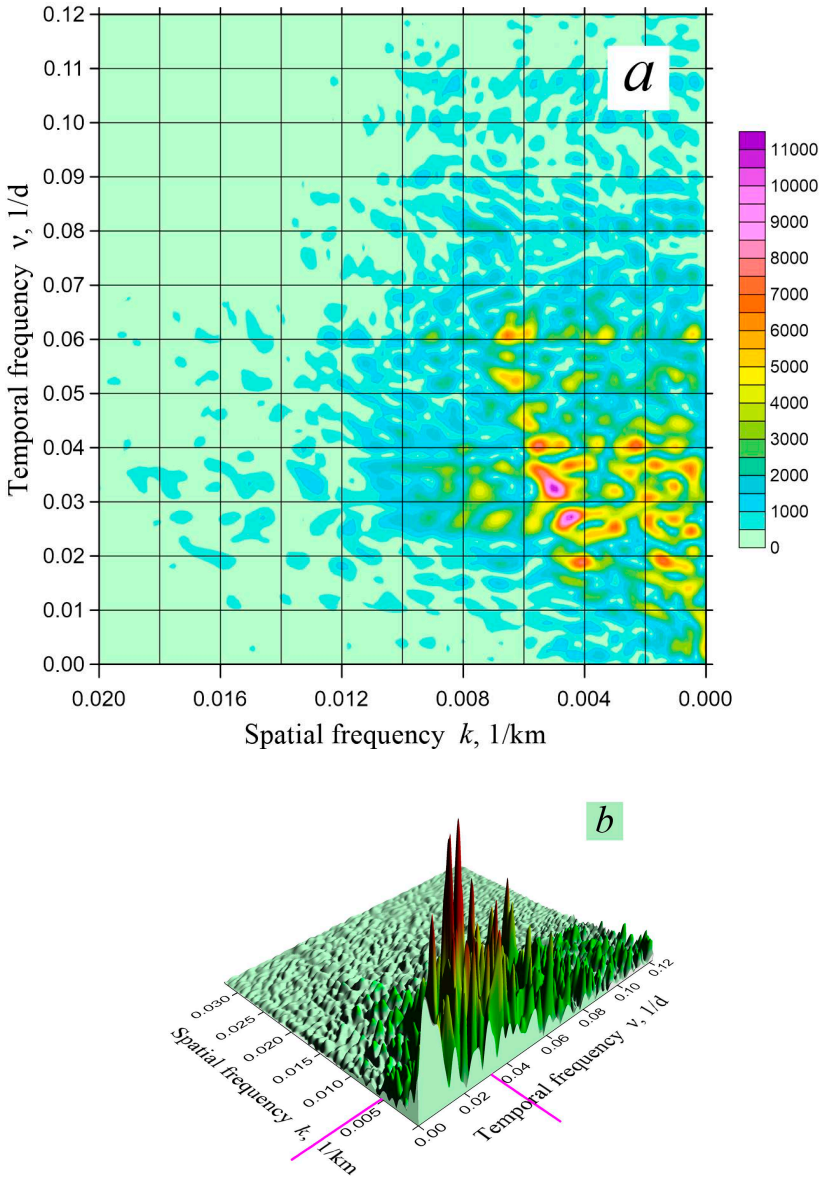

F i g. 10. Two-dimensional spectrum of wave oscillations in the field of deep currents in 2D (*a*) and 3D (*b*) formats

Wave activity intensifies significantly between reference points 11–9 in the eastern Black Sea, a generation zone for topographic Rossby waves (Figs. 6, 8). Additionally, amplified wave amplitudes occur between points 5 and 3 along the segment extending south of the Crimean Peninsula and westward.

The second stage of analyzing dispersion characteristics of wave oscillations involved computing a two-dimensional wave spectrum from the diagram (Fig. 9, *c*) using Fast Fourier Transform (FFT). The time diagram is a data array of 1080 daily samples of function M along trajectory L with a 2 km resolution.

Fig. 10 shows two-dimensional (in frequency and spatial frequency) spectrum $S = f(\nu, k)$ in 2D and, for clarity, 3D formats.

As we can see from Fig. 10, wave processes in the deep currents have the ranges of 0.01–0.06 1/day in frequency and 0.005–0.08 1/km in spatial frequency, corresponding to waves with periods of 17–100 days and lengths of 12–200 km. Such waves are classified as long as their shortest wavelength in the interval is several times greater than the sea depth.

The considerable variability in wave dispersion characteristics can be attributed to changing bottom slope along their propagation trajectory and multiple wave generation mechanisms. Nevertheless, the obtained dispersion properties, combined with observed wave features (vortical character, propagation direction and topographic dependence), align with previously identified waves trapped by the continental slope, accounting for planetary β-effects.

The derived spectrum shows peak energy concentration in waves with frequency ν = 0.033 cycles/day and wavenumber k = 0.0051 cycles/km, corresponding to wavelengths λ = 196 km and periods T = 30 days. These waves propagate along the selected trajectory (Fig. 9, *a*) with phase velocity C_{ph} = 0.078 m/s. Similar dispersion characteristics were previously reported in [26] concerning the RC meanders near Gelendzhik.

It should be emphasized that the analyzed spectrum (Fig. 10) only represents wave characteristics along a single trajectory. Spectral properties would likely differ for other trajectories across the region. Different wave dispersion characteristics can also be obtained for different sections of the same trajectory.

Conclusion

This study concludes that deep circulation in the Black Sea represents a combination of alternating eddy structures and mean currents flowing approximately along isobaths. These eddy formations propagate cyclonically (counterclockwise) around the deep-sea perimeter as long waves, with dispersion characteristics matching those of waves trapped by the Black Sea bathymetry comprising the continental slope and continental rise.

Eddy formations are the primary component of deep circulation, accounting for two-thirds of the kinetic energy of deep currents. In contrast, eddy currents in the upper layer contribute only one-third of the kinetic energy.

Deep circulation in the Black Sea exhibits a persistent cyclonic (counterclockwise) pattern, with both propagating phases of trapped topographic Rossby waves and mean currents following this dominant rotation. The observed phase velocities of long waves exceed the velocities of mean currents significantly.

Two possible sources generate deep currents in the Black Sea. Ekman pumping, a wind-driven mechanism, induces geostrophic currents. In the two-layer model, Ekman pumping manifests itself in the rise of the layer interface, which leads to the occurrence of currents in the lower (deep-sea) layer. Additionally, the RC instability generates eddy disturbances in both upper and lower sea layers.

The obtained results identify two distinct regions in the Black Sea where the formation and/or intensification of long waves occurs. These regions are located in the eastern Black Sea near Trabzon and southwest of the Crimean Peninsula.

This study of deep circulation raises several unresolved questions of significant scientific interest. First, the spatial distribution of dispersion characteristics of long waves remains unexplored. Second, the mechanisms of deep current generation require further investigation. Third, the relative influence of Rim Current instability, planetary β-effect and topographic β-effect on the formation of eddy waves in the deep sea needs quantification. These questions will be addressed in subsequent studies.

A further question concerns the agreement between the current pattern presented here for the lower layer and the observed circulation in the deep Black Sea. This requires validation through appropriate field experiments.

REFERENCES

1. Ivanov, V.A. and Belokopytov, V.N., 2013. *Oceanography of the Black Sea*. Sevastopol: ECOSI-Gidrofizika, 210 p.
2. Konovalov, S.K., Vidnichuk, A.V. and Orekhova, N.A., 2018. Spatio-Temporal Characteristics of the Hydrochemical Structure of Water in the Deep-Sea Part of the Black Sea. In: A.P. Lisitzin, ed., 2018. The *Black Sea System*. Moscow: Scientific World, pp. 106-119. https://doi.org/10.29006/978-5-91522-473-4.2018.106 (in Russian).
3. Ivanov, V.A., Plastun, T.V., Markova, N.V. and Bagaev, A.V., 2019. Statistical Parameters of the Black Sea Deep Currents Based on Measurement Data. *Fundamental and Applied Hydrophysics*, 12(4), pp. 49-58. https://doi.org/10.7868/S2073667319040063 (in Russian).
4. Markova, N.V. and Bagaev, A.V., 2016. The Black Sea Deep Current Velocities Estimated from the Data of Argo Profiling Floats. *Physical Oceanography*, (3), pp. 23-35. https://doi.org/10.22449/1573-160X-2016-3-23-35
5. Klyuvitkin, A.A., Ostrovskii, A.G., Lisitzin, A.P. and Konovalov, S.K., 2019. The Energy Spectrum of the Current Velocity in the Deep Part of the Black Sea. *Doklady Earth Sciences*, 488(2), pp. 1222-1226. https://doi.org/10.1134/S1028334X1910012X
6. Demyshev, S.G., Ivanov, V.A., Markova, N.V. and Cherkesov, L.V., 2007. Simulation of the Current Field in the Black Sea Based on Eddy-Resolving Model with Assimilation of Climatic Temperature and Salinity Fields. *Ecological Safety of Coastal and Shelf Zones and Comprehensive Use of Shelf Resources*, 15, pp. 215-226 (in Russian).
7. Zalesny, V.B., Diansky, N.A., Fomin, V.V., Moshonkin S.N. and Demyshev, S.G., 2012. Numerical Model of the Circulation of the Black Sea and the Sea of Azov. *Russian Journal of*

Numerical Analysis and Mathematical Modelling, 27(1), pp. 95-111. https://doi.org/10.1515/rnam-2012-0006

8. Zalesny, V.B., Gusev, F.V. and Moshonkin S.N., 2013. Numerical Model of the Hydrodynamics of the Black Sea and the Sea of Azov with Variational Initialization of Temperature and Salinity. *Izvestiya, Atmospheric and Oceanic Physics*, 49(6), pp. 642-658. https://doi.org/10.1134/S0001433813060133
9. Korotenko, K.A., 2015. Modeling Mesoscale Circulation of the Black Sea. *Oceanology*, 55(6), pp. 820-826. https://doi.org/10.1134/S0001437015060077
10. Dorofeev, V.L. and Sukhikh, L.I., 2016. Analysis of Variability of the Black Sea Hydrophysical Fields in 1993–2012 Based on the Reanalysis Results. *Physical Oceanography*, (1), pp. 33-47. https://doi.org/10.22449/1573-160X-2016-1-33-47
11. Korshenko, E.A., Diansky, N.A. and Fomin, V.V., 2019. Reconstruction of the Black Sea Deep-Water Circulation Using INMOM and Comparison of the Results with the ARGO Buoys Data. *Physical Oceanography*, 26(3), pp. 202-213. https://doi.org/10.22449/1573-160X-2019-3-202-213
12. Staneva, J.V., Dietrich, D.E., Stanev, E.V. and Bowman, M.J., 2001. Rim Current and Coastal Eddy Mechanisms in an Eddy-Resolving General Circulation Model. *Journal of Marine Systems*, 31(1-3), pp. 137-157. https://doi.org/10.1016/S0924-7963(01)00050-1
13. Gunduz, M., Özsoy, E. and Hordoir, R., 2020. A Model of Black Sea Circulation with Strait Exchange (2008–2018). *Geoscientific Model Development*, 13(1), pp. 121-138. https://doi.org/10.5194/gmd-13-121-2020
14. Demyshev, S.G., Dymova, O.A., Markova, N.V. and Piotukh, V.B., 2016. Numerical Experiments on Modeling of the Black Sea Deep Currents. *Physical Oceanography*, (2), pp. 34-45. https://doi.org/10.22449/1573-160X-2016-2-34-45
15. Dymova, O.A., Miklashevskaya, N.A. and Markova, N.V., 2019. Particularies of the Black Sea Deep-Water Circulation in Summer 2013. *Ecological Safety of Coastal and Shelf Zones of Sea*, (1), pp. 40-47. https://doi.org/10.22449/2413-5577-2019-1-40-47 (in Russian).
16. Markova, N.V. and Dymova, O.A., 2023. Conditions of Deep-Water Undercurrent Generation in the North-Eastern Black Sea. *Fluid Dynamics*, 58(5), pp. 852-863. https://doi.org/10.1134/S0015462823600591
17. Pavlushin, A.A., Shapiro, N.B., Mikhailova, E.N., and Korotaev, G.K., 2015. Two-layer Eddy-Resolving Model of Wind Currents in the Black Sea. *Physical Oceanography*, (5), pp. 3-21. https://doi.org/10.22449/1573-160X-2015-5-3-21
18. Pavlushin, A.A., Shapiro, N.B. and Mikhailova, E.N., 2017. The Role of the Bottom Relief and the β-effect in the Black Sea Dynamics. *Physical Oceanography*, (6), pp. 24-35. https://doi.org/10.22449/1573-160X-2017-6-24-35
19. Mikhailova, E.N. and Shapiro, N.B., 2014. Three-Dimensional Non-Hydrostatic Model of Submarine Discharge in the Sea Coastal Zone. *Morskoy Gidrofizicheskiy Zhurnal*, (4), pp. 28-50 (in Russian).
20. Efimov, V.V. and Yurovsky, A.V., 2017. Formation of Vorticity of the Wind Speed Field in the Atmosphere over the Black Sea. *Physical Oceanography*, (6), pp. 3-11. https://doi.org/10.22449/1573-160X-2017-6-3-11
21. Pavlushin, A.A., Shapiro, N.B. and Mikhailova, E.N., 2018. Influence of Seasonal Variability of the Wind Stress Vorticity on the Structure of the Black Sea Circulation. *Physical Oceanography*, 25(5), pp. 345-358. https://doi.org/10.22449/1573-160X-2018-5-345-358
22. Zatsepin, A.G., Kremenetskiy, V.V., Stanichny, S.V. and Burdyugov, V.M., 2010. Black Sea Basin-Scale Circulation and Mesoscale Dynamics under Wind Forcing. In: A. V. Frolov and Yu. D. Resnyansky, eds., 2010. *Modern Problems of Ocean and Atmosphere Dynamics. The Pavel S. Lineykin Memorial Volume*. Moscow: TRIADA LTD, pp. 347-368 (in Russian).

23. Belonenko, T.V., Foux, V.R. and Zakharchuk, E.A., 2010. *Gradient-Vorticity Waves in the World Ocean*. LAP Lambert Academic Publishing GmbH & Co. KG, 408 p.

24. Zhmur, V.V., Novoselova, E.V. and Belonenko, T.V., 2021. Potential Vorticity in the Ocean: Ertel and Rossby Approaches with Estimates for the Lofoten Vortex. *Izvestiya, Atmospheric and Oceanic Physics*, 57(6), pp. 632-641. https://doi.org/10.1134/S0001433821050157

25. Pavlushin, A.A., 2022. Self-Oscillations of Large-Scale Circulation Intensity in the Black Sea. *Physical Oceanography*, 29(6), pp. 587-601. https://doi.org/10.22449/1573-160X-2022-6-587-601

26. Zatsepin, A.G., Elkin, D.N., Korzh, A.O., Kuklev, S.B., Podymov, O.I., Ostrovskii, A.G. and Soloviev, D.M., 2016. On Influence of Current Variability in the Deep Black Sea upon Water Dynamics of Narrow North Caucasian Continental Shelf. *Physical Oceanography*, (3), pp. 14-22. doi:10.22449/1573-160X-2016-3-14-22

Submitted 23.12.2024; approved after review 23.01.2025;
accepted for publication 15.05.2025.

About the author:

Andrey A. Pavlushin, Junior Research Associate, Marine Hydrophysical Institute of RAS (2 Kapitanskaya Str., Sevastopol, 299011, Russian Federation), **ORCID ID: 0000-0002-2098-5068**, **Scopus Author ID: 57142406500**, **ResearcherID: R-4908-2018**, **SPIN-code: 1439-2290**, pavlushin@mhi-ras.ru

The author has read and approved the final manuscript.
The author declares that he has no conflict of interest.

ISSN 1573-160X, *PHYSICAL OCEANOGRAPHY*, Vol. 32, Iss. 4, pp. 558-576 (2025)

published in *Morskoy Gidrofizicheskiy Zhurnal*, 2025, Vol. 41, Iss. 4, pp. 537–556

Original article

Numerical Modeling of the Functioning of Oyster Farm in Donuzlav Bay and its Impact on Water Area

E. F. Vasechkina, T. A. Filippova✉, V. V. Fomin

Marine Hydrophysical Institute of RAS, *Sevastopol*, *Russian Federation*
✉ *filippovata@mhi-ras.ru*

Abstract

Purpose. This study aims to develop and apply a mathematical model for comprehensively assessing the ecological impact of an oyster farm on the coastal waters of the Black Sea through model experiments designed to investigate the interactions between marine farms and the environment.

Methods and Results. The oyster farm in Donuzlav Bay was simulated using a two-dimensional chemical-biological object-oriented marine ecosystem model. Numerical experiments simulated the operation of an oyster farm (capacity: ~ 100 tons of wet weight, area: 80 hectares) located in the central part of Donuzlav Bay. Calculations related to oysters in their first, second and third year of cultivation were performed for the period from May to October. Results indicate that during the first year of cultivation, when oyster wet weight of soft tissues ranges from 1.2 to 4.5 g, the farm's impact on the marine ecosystem is insignificant. In the second and third years of cultivation, an increase in the bottom sediments volume was observed, primarily attributed to the oyster plantation.

Conclusions. The simulation results highlight the need to optimize farm configuration and the number of cultivated mollusks to minimize negative impacts on the water area. The qualitative and quantitative characteristics of flat oyster life obtained from the model are consistent with the data from a previously developed one-dimensional mollusk growth model and field data from monitoring the European oyster cultivation in Donuzlav Bay.

Keywords: European oyster, Donuzlav Bay, chemical-biological model, coastal ecosystem, object-oriented modeling

Acknowledgments: The study was conducted within the framework of the state assignment of FSBSI FRC MHI FNNN-2024-0016 "Studies of spatial and temporal variability of oceanological processes in the coastal, near-shore and shelf zones of the Black Sea influenced by natural and anthropogenic factors on the basis of in situ measurements and numerical modelling"..

For citation: Vasechkina, E.F., Filippova, T.A. and Fomin, V.V., 2025. Numerical Modeling of the Functioning of Oyster Farm in Donuzlav Bay and its Impact on Water Area. *Physical Oceanography*, 32(4), pp. 558-576.

Introduction

Active mariculture cultivation raises numerous questions regarding the functioning of marine ecosystems in the coastal zone, which are characterized by a complex interplay of physical, chemical, and biological processes. Consequently, components of coastal ecosystems interact with each other and with the marine environment through multiple direct and feedback mechanisms. The success of a marine farm depends on how effectively mariculture species integrate into

the established ecosystem of the selected marine area. The exchange of matter and energy between mariculture and the environment must support sustainable growth of the cultivated species while avoiding degradation of the ecosystem and, where possible, enhancing its condition. These interaction processes can be evaluated using comprehensive ecological models that integrate physical, chemical, and biological components. This study considers several existing models that simulate the functioning of mariculture in relation to its environmental interactions.

The study [1] presents results on the impact of mussel (*Mytilus galloprovincialis*) mariculture on the marine environment, derived through mathematical modeling. The authors employed a population model based on dynamic energy budget theory, integrated with field data on seston content and the chemical composition of mussel tissues. These data were collected in 2006–2007 from three mussel farms located in Italy and Slovenia in the Adriatic Sea. The dynamics of carbon, nitrogen, and phosphorus fluxes were evaluated over a 10-month cultivation period. Calculations revealed that the nitrogen and phosphorus released by mussels as feces and pseudofeces during their life cycle are, respectively, two and five times greater than those incorporated into the mollusks' tissues. The obtained results underscore the need for a comprehensive approach to mariculture site selection, accounting for the environmental impact of marine farming.

The study [2] evaluates the influence of the Apalachicola River (Florida, USA) discharge on the population of the giant oyster *Magallana gigas*. The authors integrated a three-dimensional hydrodynamic circulation model with field data on the oyster life cycle to develop stochastic models. The results identify several environmental factors affecting oyster growth dynamics, with the hydrological regime of the Apalachicola River established as the primary factor. Although the influence of the marine environment on oyster population has been thoroughly studied, the impact of oyster farms on the water area ecosystem remains underexplored. A clearer understanding of the interactions between mariculture and the environment can be achieved by integrating a hydrodynamic model with a biological model.

The study [3] investigates the impact of an oyster farm on the ecosystem of the tidal zone in Marennes-Oléron Bay, France, with a primary focus on the structure of the bay's food chain. A carbon-based food chain model was employed to assess the influence of the oyster farm on the bay ecosystem. The analysis revealed that the presence of oysters alters the interactions between benthic and pelagic organisms, with benthic animals becoming the primary consumers of organic carbon. Doubling the area of the oyster farm increased secondary production, providing additional food for juvenile nekton. Through mathematical modeling, the authors demonstrated how bivalve mollusk mariculture affects the species composition of the tidal zone fauna. During growth, oysters release significant amounts of ammonium and phosphates; however, the direct impact of these compounds on the ecosystem was not investigated in the referenced study.

The efficiency of mariculture cultivation is often evaluated using the ecological carrying capacity of the water area as an indicator. Studies [4–6] describe several models developed to assess the ecological carrying capacity of water areas hosting mariculture operations. In [4], a two-dimensional physical-biogeochemical model applied to Sungo Bay, China, is presented. The findings from [4, 7], along with other studies, informed the strategic placement of a marine farm cultivating polyculture in Sungo Bay. Despite 60 years of active exploitation, the bay's ecosystems remain healthy due to the implementation of scientific recommendations for marine farm management [8].

Literature analysis reveals the widespread use of comprehensive ecological models for studying ecosystems that include mariculture. Studies [1, 3, 6, 8] demonstrate the potential of these models for assessing nutrient and carbon fluxes in ecosystems. Additionally, comprehensive ecological models enable evaluation of the influence of the hydrochemical regime on the productivity of cultivated species [2, 7, 9] and forecasting economic profitability [6, 8]. Analysis of the reviewed models indicates that they are geographically specific, with simulation results heavily dependent on local conditions. A promising approach involves using an individual-based model of the cultivated species as the core of the biological component in these models.

This study aims to develop a two-dimensional model of a marine coastal ecosystem incorporating European oyster mariculture. Using this model, numerical experiments are conducted to investigate and quantitatively assess the impact of an oyster farm on the ecosystem of Donuzlav Bay.

Materials and methods

Subject and object of research. The European oyster (*Ostrea edulis*), a commercially significant species in the last century, experienced a substantial decline in population, leading to the loss of its commercial importance [1]. The cultivation of *O. edulis* is of interest due to its relevance for restoring wild oyster population and supporting mariculture [2, 3] [10]. Donuzlav Bay was selected as the object of simulation modeling because it hosts several operational marine farms cultivating mussels and oysters [11]. The availability of field data on the dynamics of morphometric characteristics of the flat oyster in this region [3] further supported the choice of Donuzlav Bay as the location for the model plantation.

Model concept. The two-dimensional model of a marine coastal ecosystem is developed using object-oriented modeling (OOM) principles. The modeled ecosystem comprises the marine environment and marine plant and animal

[1] Krakatitsa, T.F., 1976. [*Biology of the Black Sea Oyster Ostrea edulis L. in Relation to Issues of Its Reproduction*]. Kiev: Naukova Dumka, 80 p. (in Russian).

[2] Kryuchkov, V.G., 2014. [*Oyster Farm. Explanatory Note and Economic Calculations*]. Kerch, 92 p. (in Russian).

[3] Sytnik, N.A., 2014. *Functional Ecology of the Flat Oyster (Ostrea edulis L., 1758, Ostereidae, Bivalvia) of the Black Sea*. Thesis Cand. Biol. Sci., Kerch, 174 p. (in Russian).

organisms. These components are represented as a set of objects or fields on a regular grid.

An object in the OOM framework is defined as a group of identical organisms and their immediate living space (ILS), such as a phytoplankton aggregation, a small area of the seafloor occupied by macroalgae of a certain species, a mussel collector, or an oyster cage. The ILS represents the area where exchange processes between organisms and the environment occur. Geometrically, model objects are represented as cylinders, the dimensions corresponding to the physical dimensions of the designated ILS for a given set of marine organisms. The model assumes a homogeneous distribution of biomass within each object. For cylindrical objects, the height and base radius are defined. The initial positions of objects in the model space can be specified or randomly distributed. When modeling marine farms, objects representing cultivated mariculture are positioned according to the farm's layout. Phytoplankton and phytobenthos objects are distributed randomly.

The sizes of objects may change over time. The maximum radius of an object's horizontal projection is set equal to the grid step. When this threshold is exceeded, the object splits into two new objects, with their combined volumes equaling that of the initial object. The mass is distributed equally between the new objects.

The biomass of an object can increase during growth and decrease due to a lack of resources. To save computational power, the program includes a procedure for removing objects with biomass below a threshold level from the calculation area. In this case, the object's biomass is transferred to the pool of particulate organic matter (POM).

The marine environment is represented by a set of hydrophysical and hydrochemical fields defined on a regular grid. The control variables in the model are air temperature, wind velocity, and illumination at the sea surface. The model calculates concentrations of inorganic compounds of nitrogen, phosphorus, and sulfur, POM, dissolved organic matter (DOM), and the concentration of dissolved oxygen in the water. The resource available to an object is calculated as a weighted average of the values in the grid cells partially or fully overlapped by the object's horizontal projection. Weight coefficients are proportional to the area of cell overlap by the object.

The developed simulation model of coastal ecosystem dynamics provides quantitative estimates of environmental characteristics and biological objects at any time. This representation enables the study of the dynamics of all parameters defining the state of the coastal ecosystem and the identification of relationships between its components. Quantitative assessment of material fluxes between ecosystem components allows for accurate determination of the degree and nature of the marine farm's impact on the coastal ecosystem.

OOM of a marine farm. Based on the principles outlined above, a two-dimensional chemical-biological OOM of a marine farm was previously developed [12]. To simulate the operation of an oyster farm and its interactions with the marine environment, a new method was incorporated into the "Mollusks" class, built upon

a one-dimensional dynamic energy budget (DEB) model for the European oyster [13]. This method mathematically describes the processes of filtration, feeding, respiration, excretion, growth, and reproduction of the oyster. Model verification results demonstrated strong agreement between the calculated values of linear and weight growth of oysters and those measured during a field experiment in Donuzlav Bay from 2001 to 2003. The structure of the OOM classes is examined in greater detail below (Fig. 1).

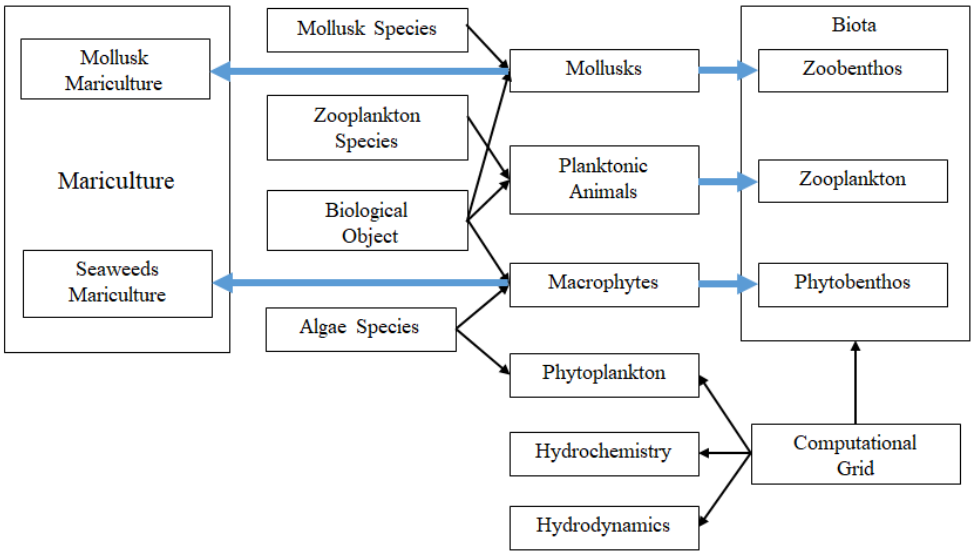

F i g. 1. Class diagram of the chemical-biological object-oriented model of marine ecosystem. Black arrows indicate heredity, blue ones – inclusion of multiple objects of one class into the properties of another higher class

The "Computational Grid" class defines the coordinates of the calculation domain and a regular grid, at the nodes of which hydrophysical and hydrochemical variables are specified. Class properties include water body depth (H), grid steps in the zonal (dx) and meridional (dy) directions, domain dimensions ($Ndx \times Mdy$), spatial boundaries of the water body, and the time step (dt).

The "Hydrodynamics" class is the inheritor of the " Computational Grid" class. Its primary method is a simplified integral model of the Black Sea's upper layer [14, 15], which describes the spatiotemporal dynamics of the upper mixed layer's temperature (T^0, °C) and depth (h, m), as well as the temperature of the lower layer (T^h, °C). These layers are assumed to be homogeneous in density. Given that the spatial variability of wind and air temperature fields over the sea, particularly in summer, exceeds the size of the computational domain, a one-dimensional version of the model is employed:

$$h\frac{\partial T^0}{\partial t} = \Gamma^0 - \Gamma^{h-0},$$

$$\Gamma^0 = a(T^0 - T_a),$$
$$\frac{\partial h}{\partial t} = \frac{1}{T^0 - T^h}(\Gamma^{h-0} - \Gamma^{h+0}),$$
$$G - D = 0.5\alpha g h \rho_w (\Gamma^0 + \Gamma^{h-0}), \quad (1)$$
$$G = C_g V_*^3,\ D = \rho V_*^3 \left(f\left(\frac{h}{L_1}\right) + \frac{a_2 h}{L|N|}\right),$$
$$f\left(\frac{h}{L_1}\right) = \begin{Bmatrix} \frac{a_1 h}{L_1} & \text{at } h \le \frac{C_g}{a_1} L_1 \\ C_g & \text{at } h > \frac{C_g}{a_1} L_1 \end{Bmatrix},$$

where Γ^0 is the heat flux through the sea surface; Γ^{h-0} and Γ^{h+0} are the heat fluxes at the lower boundary of the mixed layer and the upper boundary of the lower layer, respectively; T_a is the air temperature (°C); α is the coefficient of thermal expansion of water; ρ_w is the water density (kg/m^3); G, D represent the integral generation and dissipation of turbulent energy, respectively; $V_* = \sqrt{\frac{\tau_0}{\rho_w}}$ is the dynamic friction velocity in water; τ_0 is the wind stress at the surface; L is the Monin–Obukhov length scale (m); L_1 is the boundary layer thickness scale; $N = L/L_1$ is the dimensionless Kazansky–Monin stratification parameter; and C_g, a, a_1, a_2 are empirical coefficients.

Equation (1) defines the condition for switching between two regimes of upper layer dynamics: entrainment and detrainment of water mass into or from the upper layer. Entrainment occurs when $G - D - 0.5\rho_w \alpha g h \Gamma^0 > 0$, resulting in changes to the characteristics of the upper mixed layer while the lower layer remains unchanged. Otherwise, detrainment occurs, altering the characteristics of the lower layer while the upper layer remains unchanged. However, gas and heat exchange through the surface may modify the temperature and oxygen content in the upper layer. Thus, the two-layer model with a time-variable upper layer incorporates an additional term to the equations for hydrochemical variables of the upper layer [16]:

$$\frac{\partial Y_i^0}{\partial t} + U\frac{\partial Y_i^0}{\partial x} + V\frac{\partial Y_i^0}{\partial y} = K_x\left(\frac{\partial^2 Y_i^0}{\partial x^2} + \frac{\partial^2 Y_i^0}{\partial y^2}\right) + G_i^0 + A_i^0 + \frac{\Gamma^{h-0} - \Gamma^{h+0}}{(T^0 - T^h)h}(Y_i^h - Y_i^0) \quad (2)$$

and the lower layer:

$$\frac{\partial Y_i^h}{\partial t} + U\frac{\partial Y_i^h}{\partial x} + V\frac{\partial Y_i^h}{\partial y} = K_x\left(\frac{\partial^2 Y_i^h}{\partial x^2} + \frac{\partial^2 Y_i^h}{\partial y^2}\right) + G_i^h + A_i^h + \frac{\Gamma^{h-0} - \Gamma^{h+0}}{(T^0 - T^h)(H-h)}(Y_i^h - Y_i^0), \quad (3)$$

where Y_i^0 and Y_i^h represent variables of the "Hydrochemistry" block in the upper and lower layers (μM); U, V are the layer-averaged current velocities (m/s); G_i, A_i are source (sink) functions determined by chemical and biological processes, respectively; the superscripts "0" and "h" indicate association with the upper or lower layer, respectively; H is the basin depth (m); and K_x is the horizontal diffusion coefficient.

The “Hydrochemistry” class inherits from the “Computational Grid” class and is characterized by the following properties: concentrations of nitrates, nitrites, phosphates, dissolved oxygen, hydrogen sulfide, sulfates, sulfites, sulfur, and dissolved and particulate organic nitrogen at the nodes of the regular grid; coefficients in the parameterizing chemical reactions; and diffusion coefficients for suspended and dissolved substances. The class includes the following methods:

– a one-dimensional chemical-biological model that describes the coupled nitrogen and sulfur cycles under aerobic and anaerobic conditions, developed for modeling processes in the redox zone of the Black Sea (provides the setting of G_i functions in equations (2) and (3)). The chemical reaction equations and parameter values used in the calculations are detailed in [17];

– a procedure for calculating advection, diffusion, and vertical mixing at the boundary of two layers, with adjustments to hydrochemical variables;

– a procedure for incorporating the discharge and input of dissolved and suspended substances from the biological components of the model.

The “Phytoplankton” class is the inheritor of the “Computational Grid” and “Algae Species” classes. In the current model version, phytoplankton is represented as a passive tracer, simplifying the model and reducing computational time while maintaining acceptable error margins [18]. The primary method of this class is a model of phytoplankton field evolution, influenced by external conditions and interactions with mollusk mariculture objects. It is a two-dimensional adaptation of a previously developed and validated one-dimensional model [19]:

$$\frac{\partial B}{\partial t} + U\frac{\partial B}{\partial x} + V\frac{\partial B}{\partial y} = K_x\left(\frac{\partial^2 B}{\partial x^2} + \frac{\partial^2 B}{\partial y^2}\right) + (P_\mathrm{r}(1-k_\mathrm{r}) - k_\mathrm{e} - m)B - \sum A_i, \quad (4)$$

$$\frac{\partial Q_\mathrm{N}}{\partial t} + U\frac{\partial Q_\mathrm{N}}{\partial x} + V\frac{\partial Q_\mathrm{N}}{\partial y} = K_x\left(\frac{\partial^2 Q_\mathrm{N}}{\partial x^2} + \frac{\partial^2 Q_\mathrm{N}}{\partial y^2}\right) + V_{\mathrm{NO_3}}^{\max}\left(1 - f(Q_\mathrm{N})\right)\frac{[\mathrm{NO_3}]}{K_{\mathrm{NO_3}}+[\mathrm{NO_3}]} +$$
$$+ V_{\mathrm{NH_4}}^{\max}\left(1 - f(Q_\mathrm{N})\right)\frac{[\mathrm{NH_4}]}{K_{\mathrm{NH_4}}+[\mathrm{NH_4}]} - P_\mathrm{r}Q_\mathrm{N}, \quad (5)$$

$$\frac{\partial Q_\mathrm{P}}{\partial t} + U\frac{\partial Q_\mathrm{P}}{\partial x} + V\frac{\partial Q_\mathrm{P}}{\partial y} = K_x\left(\frac{\partial^2 Q_\mathrm{P}}{\partial x^2} + \frac{\partial^2 Q_\mathrm{P}}{\partial y^2}\right) + V_\mathrm{P}^{\max}\left(1 - f(Q_\mathrm{P})\right)\frac{[\mathrm{P}]}{K_\mathrm{P}+[\mathrm{P}]} - P_\mathrm{r}Q_\mathrm{P}, \quad (6)$$

$$P_\mathrm{r} = \mu \cdot \min(f(Q_\mathrm{N}), f(Q_\mathrm{P})),$$

where B represents phytoplankton biomass (mg/m^3); t is time (days); U, V are vertically averaged advection velocities (m/s); μ is the maximum specific rate of gross phytoplankton production (1/day); P_r is the realized specific rate of gross production (1/day); k_r is the coefficient determining energy expenditure on respiration; k_e is the coefficient of organic matter release (exudation); m is the phytoplankton cell mortality rate (1/day); Q_N and Q_P are the internal nitrogen and phosphorus content in phytoplankton cells, respectively (pmol/cell); $Q_\mathrm{N}^{\max}$, $Q_\mathrm{N}^{\min}$, $Q_\mathrm{P}^{\max}$, $Q_\mathrm{P}^{\min}$ are the maximum and minimum nitrogen and phosphorus content in phytoplankton cells (pmol/cell); [NO_3], [NH_4], [P] are the concentration of nitrates, ammonium, and phosphorus in water (μM); $V_{\mathrm{NO_3}}$, $V_{\mathrm{NH_4}}$, V_P are the uptake rates of

nitrates, ammonium, and phosphorus in water (pmol/(cell day)); $V_{NO_3}^{max}$, $V_{NH_4}^{max}$, V_P^{max} are the maximum nutrient uptake rates (pmol/(cell day); K_P, K_{NO_3}, K_{NH_4} are half-saturation constants (μM); and $\sum A_i$ represents the cumulative impact of oyster farm objects on the phytoplankton field. The number of phytoplankton cells per unit volume is calculated based on the carbon content in a cell Q_C, which is assumed to be constant, unlike Q_N and Q_P. For diatoms, Q_C = 12 pmol/cell. Given a phytoplankton biomass B = 0.083 mmol C/m^3, the number of cells $K = \frac{0.083}{12}\frac{B}{Q_C}10^9 = 6.9 \cdot 10^6 B(\text{cell/m}^3)$.

The numerical parameters of the phytoplankton species *Thalassiosira pseudo* used in this study are presented in Table 1.

Table 1

Numerical values of phytoplankton parameters

Parameter	*Thalassiosira pseudo*
Q_N^{max}, pmol/cell	0.286
Q_N^{min}, pmol/cell	0.050
Q_P^{max}, pmol/cell	0.020
Q_P^{min}, pmol/cell	0.001
$V_{NO_3}^{max}$, pmol/(cell day)	0.257
$V_{NH_4}^{max}$, pmol/(cell day)	0.744
V_P^{max}, pmol/(cell day)	0.210
K_P, μM	0.580
K_{NO_3}, μM	0.860
K_{NH_4}, μM	0.200
k_r, 1/day	0.150
k_e, 1/day	0.250
m, 1/day	0.250
P_{max}, mg O_2/g DW/h	1.250
R_d, mg O_2/g DW/h	0.310
α	0.110

The "Biological Object" class defines properties including the object's coordinates within the modeling domain, its vertical and horizontal dimensions, mass, and the range of possible variations in biomass and size.

The "Mollusk Species" class encompasses all parameters necessary for describing the energy balance of various mollusk species. The "Mollusks" class inherits from both the "Mollusk Species" and "Biological Object" classes, providing a comprehensive description of the carrier (collector or raft) and the group of cultivated mollusks. This includes parameters of the DEB model, which describes

their growth on the carrier and interactions with the environment. The primary method of the "Mollusks" class is the DEB model adapted to the specific mollusk species [13]:

$$K_{\mathrm{d}} \frac{dW_{\mathrm{d}}}{dt} = \left(P_{\mathrm{som}} + P_{\mathrm{gen}}\right),$$
$$P = P_{\mathrm{som}} + P_{\mathrm{gen}} + P_{\mathrm{sh}} = A_{\mathrm{e}} F K_{\mathrm{c}} C - R - E_{\mathrm{x}},$$

where K_{d} represents the caloric content of mollusk tissues (cal/(g dry weight)); W_{d} is the dry weight of soft tissues (g); P_{som} is the energy costs for somatic tissue growth (cal/h); P_{gen} is the energy costs for generative tissue growth (cal/h); P_{sh} is the energy expenditure for shell growth (cal/h); R is the energy expended on mollusk respiration (cal/h); E_{x} is the excreted energy (cal/h); F is the filtration rate (L/h); K_{c} is the caloric content of food suspension (cal/mg); C is the concentration of the food suspension (mg/L); and A_{e} is the food assimilation coefficient.

The current version of the ecological model incorporates two variants of the DEB model: one for the Black Sea mussel (*Mytilus galloprovincialis*) and one for the flat oyster (*Ostrea edulis*). This enables the model to simulate the operation of different mollusk species within a single area. Detailed DEB models describing the growth of oysters and mussels, along with approximations of their life processes, are provided in [13, 20].

The "Mariculture" class includes a set of objects from the "Mollusks" class. This class defines general and integral characteristics of the marine plantation, including its spatial configuration, length, volume, arrangement of collectors relative to the surface, total mass of cultivated mollusks, their production characteristics, and the quantities of consumed and released substances.

Similarly, an object of the "Mollusks" class can represent a group of identical bivalve mollusk individuals occupying a fixed area of the seabed with known dimensions and coordinates. In this case, a collection of such objects forms the "Zoobenthos" array.

The "Planktonic Animals" class inherits from the "Biological Object" and "Zooplankton Species" classes. A collection of such objects ("Zooplankton" in Fig. 1), together with the "Phytobenthos" and "Zoobenthos" arrays, is included in the "Biota" class, which is the inheritor of the "Computational Grid" class. The properties of the "Biota" class encompass fields of all biological components of the ecosystem on a two-dimensional grid, as well as averaged or integrated characteristics essential for analyzing system behavior. The methods of this class enable calculation of all listed characteristics and the conversion of object-based representations into two-dimensional fields suitable for analysis and visualization.

The "Macrophytes" class inherits from the "Algae Species" and "Biological Object" classes, and its object's properties include all necessary information for calculating the production and metabolic processes of macroalgae for a specific species. The primary method of the "Macrophytes" class is the DEB model developed in [21, 22]. For macroalgae and microalgae nearly identical models are

used, with minor differences reflecting the specific characteristics of available natural data. Based on these data, the following equations were formulated:

$$\frac{dB_{\mathrm{m}}}{dt} = (P_{\mathrm{r}} - k_{\mathrm{e}} - m)B_{\mathrm{m}},$$

$$\frac{dQ_{\mathrm{N}}}{dt} = V_{\mathrm{NO_3}}\frac{[\mathrm{NO_3}]}{K_{\mathrm{NO_3}} + [\mathrm{NO_3}]} + V_{\mathrm{NH_4}}\frac{[\mathrm{NH_4}]}{K_{\mathrm{NH_4}} + [\mathrm{NH_4}]} - P_{\mathrm{r}}Q_{\mathrm{N}},$$

$$\frac{dQ_{\mathrm{P}}}{dt} = V_{\mathrm{P}}\frac{[\mathrm{P}]}{K_{\mathrm{P}} + [\mathrm{P}]} - P_{\mathrm{r}}Q_{\mathrm{P}},$$

$$P(E) = \left(P_{\max}\tanh\left(\alpha\frac{E}{P_{\max}}\right) - R_{\mathrm{d}}\right)f(T),$$

$$E = E_0\exp(-\beta z),$$

$$P_{\mathrm{r}} = P(E)\,k_{\mathrm{DW}}\min\big(f(Q_{\mathrm{N}}), f(Q_{\mathrm{P}})\big)\,C_{\mathrm{w}},$$

$$f(Q_{\mathrm{N}}) = \frac{Q_{\mathrm{N}} - Q_{\mathrm{N}}^{\min}}{Q_{\mathrm{N}}^{\max} - Q_{\mathrm{N}}^{\min}},$$

$$f(Q_{\mathrm{P}}) = \frac{Q_{\mathrm{P}} - Q_{\mathrm{P}}^{\min}}{Q_{\mathrm{P}}^{\max} - Q_{\mathrm{P}}^{\min}},$$

$$V_{\mathrm{NO_3}} = V_{\mathrm{NO_3}}^{\max}\big(1 - f(Q_{\mathrm{N}})\big),$$

$$V_{\mathrm{NH_4}} = V_{\mathrm{NH_4}}^{\max}\big(1 - f(Q_{\mathrm{N}})\big),$$

$$V_{\mathrm{P}} = V_{\mathrm{P}}^{\max}(1 - f(Q_{\mathrm{P}})),$$

where E_0 (μmol photon/m^2/s) represents photosynthetically active radiation (PAR) at the water surface, E is the PAR at depth z (m); B_{m} is the biomass of the macrophyte object (g dry weight/m^3); P_{r} is the specific growth rate (1/day); $P(E)$ is the photosynthesis rate (mg O_2/g dry weight/h); $P_{\max}$ is the maximum photosynthesis rate; α is the slope of PE-curve at low light flux values; R_{d} (mg O_2/g dry weight/h) is the dark respiration rate, representing the oxygen consumed for respiration in the absence of PAR; Q_{N} and Q_{P} (μmol/g dry weight) are the concentrations of phosphorus and nitrogen in algal tissues; $Q_{\mathrm{N}}^{\max}$, $Q_{\mathrm{N}}^{\min}$, $Q_{\mathrm{P}}^{\max}$, $Q_{\mathrm{P}}^{\min}$ (μmol/g dry weight) are the minimum and maximum concentrations of phosphorus and nitrogen in algal tissues; $V_{\mathrm{NO_3}}$, $V_{\mathrm{NH_4}}$, V_{P} are the uptake rates of nitrates, ammonium, and phosphorus from water (μmol/g dry weight/h); $V_{\mathrm{NO_3}}^{\max}$, $V_{\mathrm{NH_4}}^{\max}$, $V_{\mathrm{P}}^{\max}$ are the maximum nutrient uptake rates; K_{P}, $K_{\mathrm{NO_3}}$, $K_{\mathrm{NH_4}}$ are half-saturation constants (μM); m is the mortality coefficient; k_{e} is the exudation rate; and k_{DW} is the conversion coefficient from O_2 mg to C mg.

The numerical parameters of phytobenthos, comprising two seagrass species (*Zostera noltii* and *Ruppia maritima*), used in this study are presented in Table 2.

A collection of objects of the "Macrophytes" class forms the "Phytobenthos" array, which is a property of the "Biota" class. Analogous to the "Mollusks" class, a collection of objects from the "Macrophytes" class can be included in an object of the "Mariculture" class, which describes a plantation of cultivated macroalgae. The top-level class "Ecosystem" includes instances of the classes "Hydrodynamics", "Hydrochemistry", "Phytoplankton", "Mariculture", "Biota".

Table 2

Numerical values of phytobenthos parameters

Parameter	*Zostera noltii*	*Ruppia maritima*
Q_N^{max}, μmol/g DW	4507	4507
Q_N^{min}, μmol/g DW	755	755
Q_P^{max}, μmol/g DW	118	118
Q_P^{min}, μmol/g DW	30	30
$V_{NO_3}^{max}$, μmol/g DW/h	3.0	14.1
$V_{NH_4}^{max}$, μmol/g DW/h	19.4	75.0
V_P^{max}, μmol/g DW/h	2.42	9.30
K_P, μM	1.5	1.5
K_{NO_3}, μM	7.0	9.2
K_{NH_4}, μM	12.3	12.3
k_e, 1/h	0.1	0.1
m, 1/day	0.005	0.005
P_{max}, mg O_2/g DW/h	6.85	15.94
R_d, mg O_2/g DW/h	1.70	1.43
α	0.046	0.060

Results and discussion

The configuration of the model oyster farm was designed based on recommendations for managing oyster farms in Donuzlav Bay [2]. The total area occupied by the oyster plantation is ~ 80 hectares. Oyster cages are suspended from rafts, with each raft designed to hold 500 kg of raw oyster mass (including shells) of marketable size. The rafts are organized into blocks of 8 units each, connected sequentially. The model oyster farm comprises 24 blocks, yielding ~100 tons of marketable products.

The initial conditions for model integration include the average dry weight of soft tissues of a single oyster, the total dry weight of all cultivated mollusks on a single raft (carrier), the vertical profile of water temperature, and fields of hydrochemical elements (nitrates, nitrites, ammonium, phosphates, POM and DOM), as well as phytoplankton biomass. The fields of chemical compounds were generated as random variables with specified mean and variance. Average concentrations were adopted from [11]: $[NH_4]$ = 3.6 μM; $[NO_3]$ = 3.0 μM; $[PO_4]$ = 0.25 μM; [POM] = 5 μmol N/l; [DOM] = 5 μmol N/l; B = 200 mg/m^3. At the grid nodes, with a temporal resolution

of three hours, vectors of vertically averaged current velocities were prescribed, calculated previously using a hydrodynamic nonlinear sigma-coordinate circulation model in the hydrostatic approximation [23]. In this model version, the zooplankton and zoobenthos components were disabled.

At each integration step, the exchange processes between objects and the environment were calculated. Phytoplankton and macroalgae assimilate carbon, nitrogen, and phosphorus compounds from the environment, releasing oxygen and DOM. Oysters consume phytoplankton and POM from the environment and release phosphates, ammonium, DOM, and POM, with a portion of the POM returning to the suspended matter pool in the water column and another portion contributing to biodeposits (SDM). At each integration step, objects calculate available resources based on the ecosystem's state, modified by prior calculations. This approach simulates competition for resources. When objects intersect or overlap, resource consumption by earlier-processed objects within the same time step can be significant, potentially causing nutrient deficiencies for subsequent objects. To avoid consistently disadvantaging certain objects, the order of calculations at each integration step was randomized.

Initial and boundary conditions. The integration step varied across the biological, chemical, and hydrodynamic components of the model. The dynamics of biological objects and chemical reaction equations were calculated with a time step of three hours, while advection and diffusion of fields were computed with a time step of 36 minutes. At the open boundaries of the computational domain, zero gradient conditions normal to the boundary were applied.

The phytoplankton field was represented as a collection of diatom microalgae objects with a high growth rate. The control variables of the model included surface illumination, air temperature, and wind velocity (Fig. 2). The time series of surface illumination was based on average insolation estimates for the Black Sea [24], with diurnal variability modeled using a sinusoidal function. Air temperature and wind velocity were derived from ERA-Interim data (2007) with a temporal resolution of three hours. The integration period spanned 5 months, from May to October, corresponding to the period of active oyster growth.

The time required for an oyster to reach marketable size from the moment it is placed in a cultivation cage is 27–33 months [2]. Consequently, calculations were performed for two size groups of oysters, corresponding to the second and third years of cultivation, with initial raw weights of soft tissues of 2.3 g and 18.4 g (shell heights of 22 mm and 48 mm, respectively). The impact of the oyster plantation on the ecosystem was evaluated through the dynamics of exchange processes between oysters and the marine environment. The following parameters were calculated: farm-averaged oyster shell height, oyster soft tissue mass, filtration rates, consumption, metabolic costs, excretion, mass of excreted ammonium and phosphates, and average concentrations of hydrochemical components across the entire computational domain and within the oyster farm area.

The conditions of the model marine environment for oyster cultivation are illustrated in Figs. 2 and 3. Fig. 3, a shows the evolution of the vertical temperature profile under the influence of heating and wind stress. The profile, determined by the upper mixed layer (UML) model variables T^0, T^h and h, evolves as follows: as heating intensifies, mixing extends to the seafloor, effectively eliminating the two-layer structure and establishing homogeneous conditions throughout the depth of the modeled water body. A new UML briefly forms during a sharp increase in wind stress but rapidly dissipates. Fig. 3, *b* depicts the dynamics of the average food suspension concentration across the computational domain and the ratio between its components – phytoplankton and POM. Phytoplankton accounts for approximately half of the mollusk' diet.

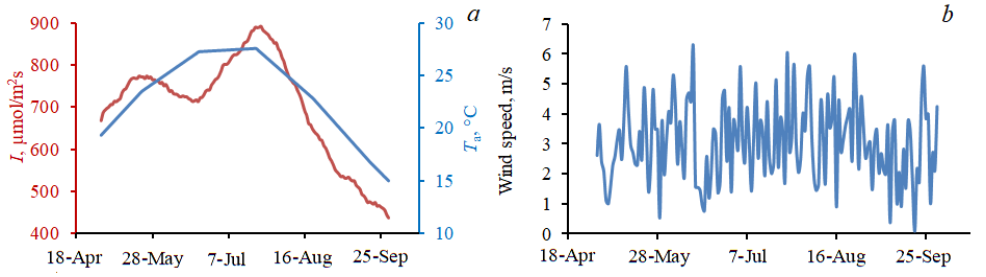

F i g. 2. Control variables of the model: insolation at midday (red curve), diurnal maximum air temperature (blue curve) (*a*); wind speed (*b*)

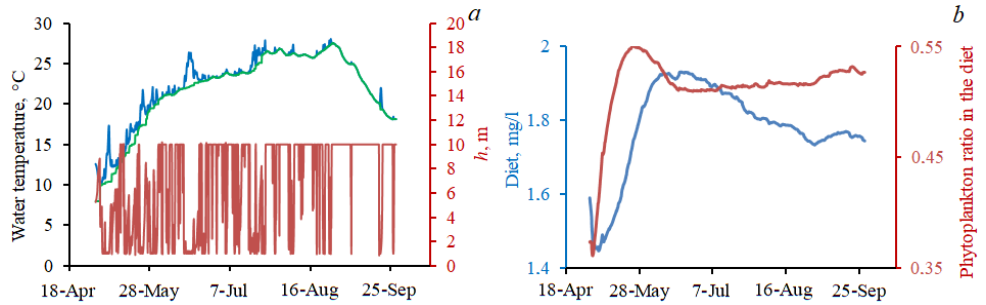

F i g. 3. Marine environment conditions: temperature of the upper (blue curve) and lower (green curve) layers, thickness of the upper layer (*a*); concentration of suspended food, and ratio between the mollusk diet components: phytoplankton and suspended organic matter (*b*)

Numerical experiments. The model was validated using the data from work [3], collected at an oyster farm in Donuzlav Bay during 2002–2003. The external conditions of the experiment, including water temperature and food suspension concentration, closely matched observed values. Fig. 4 presents a comparison of field data and model calculations for periods of active mollusk growth in the second and third years of cultivation.

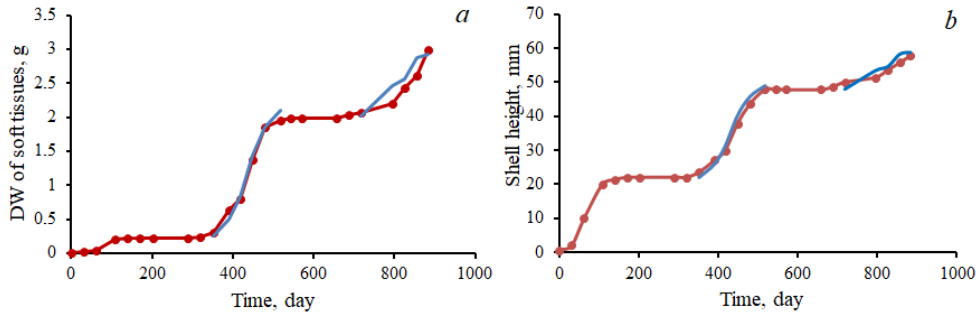

F i g. 4. Comparison of model (blue curve) and field (red curve) [3] data by two indicators: dry weight of oyster soft tissues (*a*) and shell height (*b*)

All graphs below refer to calculations for the third year of oyster cultivation, when ecosystem changes are more pronounced. Fig. 5 shows the average values of key hydrochemical characteristics across the computational domain, alongside model data on the growth of the total mass of cultivated oysters and the corresponding biodeposit accumulation over a 5-month period. The concentrations of nitrogen and phosphorus compounds in water, both organic and inorganic, exhibit quasi-stationary values that deviate slightly from those calculated for ecosystem dynamics in the absence of a farm. Within the immediate vicinity of the farm, concentrations differ by 10–20%, but across the entire computational domain, the difference is only 1–2%. The most notable differences in chemical component concentrations occur for organic matter, as inorganic compounds are rapidly assimilated by the plant components of the ecosystem, while POM and DOM persist as traces of autotroph activity.

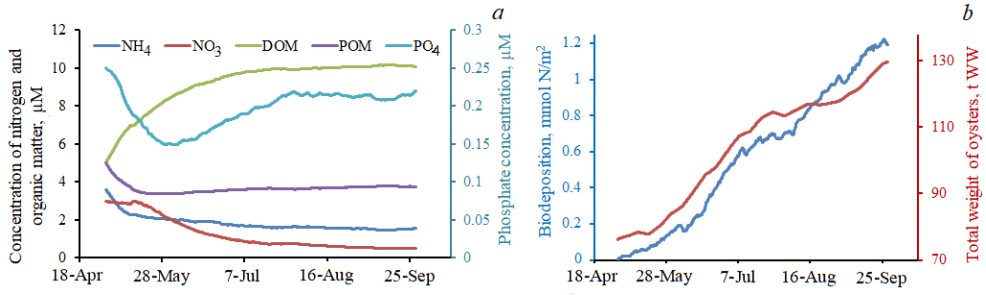

F i g. 5. Dynamic graphs of hydrochemical characteristics for the third year of oyster cultivation (*a*), biodeposits and total mass of cultivated oysters (*b*)

The operation of an oyster plantation with a total mass of ~ 100 tons results in increased biodeposit accumulation and seabed siltation, extending not only directly beneath the farm but also to a considerable distance (Fig. 6).

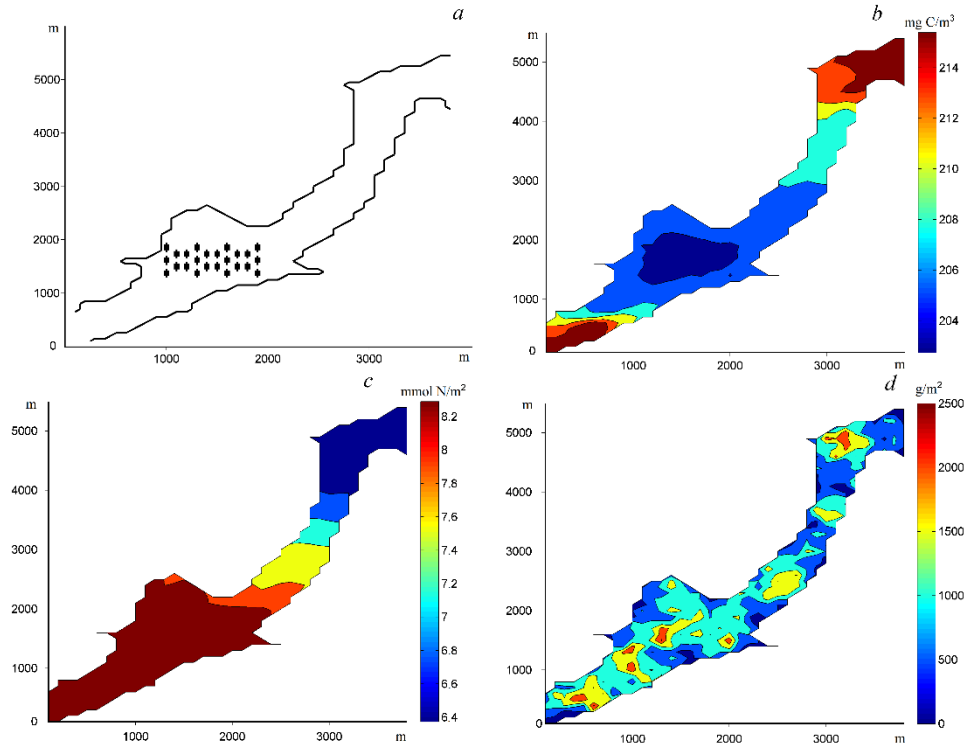

F i g. 6. Oyster farm scheme (*a*), phytoplankton biomass (*b*), biodeposits (*c*), phytobenthos biomass (*d*). The submitted fields correspond to the last day of calculation on 30.09.2007

As antisipated, phytoplankton biomass in the farm area is lower than in the surrounding waters, though this difference is minimal. The mass of biodeposits increases toward the southwest, likely due to the specific patterns of water circulation.

The impact of phytobenthos on oyster growth and the ecological state of the water area was investigated. Two scenarios were compared: one with phytobenthos (seagrasses *Ruppia maritima* and *Zostera noltii* with an average total biomass of 770 g raw weight/m^2) and one without. The results are presented in Fig. 7. The presence of bottom vegetation significantly reduces the concentrations of inorganic nitrogen and phosphorus compounds, DOM and POM in the water column. Concurrently, the biomass of farm production and the amount of biodeposits decrease slightly.

The beneficial impact of seagrass beds on the ecological state of coastal waters, particularly in areas with limited water exchange with the open sea, is well established. Primarily, phytobenthos ensures an adequate oxygen supply for benthic organisms, supporting their respiration and the oxidation of POM settling to the seafloor. As shown in Fig. 7, seagrass beds also significantly reduce the concentrations of nitrogen and phosphorus compounds in the water column.

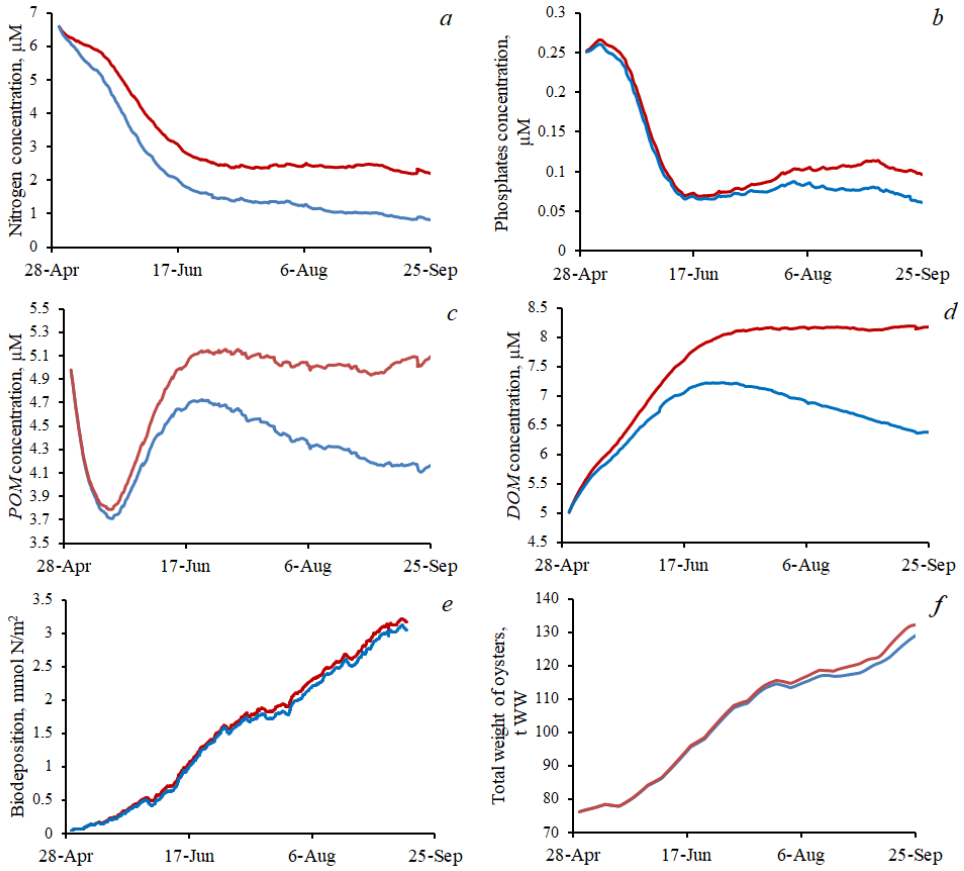

F i g. 7. Comparison of two numerical experiments – with (blue curve) and without (red curve) inclusion of macrophytobenthos: concentration of the sum of ammonium and nitrates in water (*a*), phosphates (*b*), POM (*c*), DOM (*d*), biodeposits in nitrogen units (*e*), mass of oysters cultivated at the farm (*f*)

Oysters release nitrogen in the form of ammonium at a rate of 0.3 to 0.83 mg N/(g dry weight day) and phosphorus in the form of phosphates at a rate of 0.06 to 0.1 mg/(g dry weight day), with organic nitrogen compounds released at a rate of 0.03 mg N/(g dry weight day). For the entire oyster farm, the total nitrogen release ranges from 0.33 to 1.35 kg N/day, and the total phosphorus release ranges from 0.04 to 0.18 kg P/day. These values double during spawning periods.

Conclusion

The proposed model yields results consistent with field monitoring data of flat oyster cultivation in Donuzlav Bay and a one-dimensional model (linear and weight growth rates, diet, respiration costs, excretion, and production). The dynamics of these characteristics are driven by external environmental conditions, such as water temperature and food suspension concentration, including POM and phytoplankton. Analysis of simulation results reveal the nature of interactions between the oyster

farm and the water body, quantifying exchange processes. The oyster farm is integrated into the carbon, nitrogen, and phosphorus cycles of the ecosystem; mollusks consume food suspension and release detritus, ammonium, and phosphates. Model data indicate that in the first year of cultivation (with an average raw weight of mollusk soft tissues of 1.2–4.5 g), the ecosystem impact is minimal. However, when mollusks exceed 45 mm (17 g raw weight of soft tissues), the farm's impact on the ecosystem becomes noticeable and intensifies as individuals grow.

Concentrations of dissolved compounds in the farm area exceed background levels by ~ 10–20%, but differences across the bay as a whole are negligible. The primary impact of the oyster farm is bottom siltation due to the sedimentation of biodeposits, such as mollusk feces and pseudofeces. The siltation area extends beyond the farm, with its size and configuration determined by the velocity and direction of prevailing currents. Phytobenthos positively affects water quality in the bay reducing ammonium and phosphate concentrations and competing with phytoplankton for nutrients, as confirmed by numerical modeling results.

REFERENCES

1. Brigolin, D., Maschio, G.D., Rampazzo, F., Giani, M. and Pastres, R., 2009. An Individual-Based Population Dynamic Model for Estimating Biomass Yield and Nutrient Fluxes through an Off-Shore Mussel (*Mytilus Galloprovincialis*) Farm. *Estuarine, Coastal and Shelf Science*, 82(3), pp. 365-376. https://doi.org/10.1016/j.ecss.2009.01.029

2. Livingston, R.J., Lewis, F.G., Woodsum, G.C., Niu, X.-F., Galperin, B., Huang, W., Christensen, J.D., Monaco, M.E., Battista, T.A. [et al.], 2000. Modelling Oyster Population Response to Variation in Freshwater Input. *Estuarine, Coastal and Shelf Science*, 50(5), pp. 655-672. https://doi.org/10.1006/ecss.1999.0597

3. Leguerrier, D., Niquil, N., Petiau, A. and Bodoy, A., 2004. Modeling the Impact of Oyster Culture on a Mudflat Food Web in Marennes-Oléron Bay (France). *Marine Ecology Progress Series*, 273, pp. 147-162. https://doi.org/10.3354/meps273147

4. Duarte, P., Meneses, R., Hawkins, A.J.S., Zhu, M., Fang, J. and Grant, J., 2003. Mathematical Modelling to Assess the Carrying Capacity for Multi-Species Culture within Coastal Waters. *Ecological Modelling*, 168(1-2), pp. 109-143. https://doi.org/10.1016/S0304-3800(03)00205-9

5. McKindsey, C.W., Thetmeyer, H., Landry, T. and Silvert, W., 2006. Review of Recent Carrying Capacity Models for Bivalve Culture and Recommendations for Research and Management. *Aquaculture*, 261(2), pp. 451-462. https://doi.org/10.1016/j.aquaculture.2006.06.044

6. Ferreira, J.G., Hawkins, A.J.S. and Bricker, S.B., 2007. Management of Productivity, Environmental Effects and Profitability of Shellfish Aquaculture – the Farm Aquaculture Resource Management (FARM) Model. *Aquaculture*, 264(1-4), pp. 160-174. https://doi.org/10.1016/j.aquaculture.2006.12.017

7. Nunes, J.P., Ferreira, J.G., Gazeau, F., Lencart-Silva, J., Zhang, X.L., Zhu, M.Y. and Fang, J.G., 2003. A Model for Sustainable Management of Shellfish Polyculture in Coastal Bays. *Aquaculture*, 219(1-4), pp. 257-277. https://doi.org/10.1016/S0044-8486(02)00398-8

8. Jian-guang, F., Hui-ling, S., Jing-ping, Y., Shi-huan, K., Feng, L., Newkirk, G.F. and Grant, J., 1996. Polyculture of Scallop *Chlamys Farreri* and Kelp *Laminaria Japonica* in Sungo Bay. *Chinese Journal of Oceanology and Limnology*, 14(4), pp. 322-329. https://doi.org/10.1007/BF02850552

9. Katrasov, S.V., Bugayets, A.N. and Zharikov, V.V., 2023. Evaluation of the Spatial Heterogeneity of the Pacific Oyster *Magallana Gigas* (Thunberg, 1793) Cultivation Conditions Using the FARM Marifarm Management Model in Voevoda Bay. *Russian Journal of Marine Biology*, 49(1), pp. 31-37. https://doi.org/10.1134/S1063074023010054

10. Zolotnitskiy, A.P., Orlenko, A.N., Kryuchkov, V.G. and Sytnik, N.A., 2008. On Organization of Large Scale Culture of Oysters in the Donuzlav Lake. *Trudy YugNIRO*, 46, pp. 48-54 (in Russian).

11. Dyakov, N.N., Belogudov, A.A., Levitskaya, O.V., Lipchenko, A.E., Malchenko, Yu.A., Martynov, E.S., Timoshenko, T.Yu., Fomin, V.V., Polozok, A.A. [et al.], 2021. *Modern Hydrometeorological and Hydrochemical Regimes of the Donuzlav Bay*. Sevastopol: Rosgidromet, 464 p. (in Russian).

12. Vasechkina, E.F., 2017. Coupled Physical Biological Model of Shellfish Mariculture. In: MEDCOAST, 2017. *Proceedings of the 13th International MEDCOAST Congress on Coastal and Marine Sciences, Engineering, Management and Conservation*, pp. 381-392.

13. Filippova, T.A. and Vasechkina, E.F., 2023. A Simulation Growth Model for the Cultured Oyster *Ostrea edulis* L. *Ecological Safety of Coastal and Shelf Zones of Sea*, (4), pp. 87-100.

14. Kraus, E.B. and Turner, J.S., 1967. A One-Dimensional Model of the Seasonal Thermocline. II. The General Theory and Its Consequences. *Tellus A: Dynamic Meteorology and Oceanography*, 19(1), pp. 98-106. https://doi.org/10.3402/tellusa.v19i1.9753

15. Vasechkina, E.F., Timchenko, I.E. and Yarin, V.D., 1988. Integral Dynamic-Stochastic Model of the Active Layer of the Ocean. *Morskoy Gidrofizicheckiy Zhurnal*, (1), pp. 16-22 (in Russian).

16. Eremeev, V.N., Vasechkina, E.F., Igumnova, E.M., Latun, V.S., Timchenko, I.E. and Yarin, V.D., 2007. Integrated Processes Modeling in Marine Ecosystems. *Marine Ecological Journal*, (1), pp. 5-30 (in Russian).

17. Yakushev, E.V. and Mikhailovskii, G.E., 1993. Modeling Chemical-Biological Cycles in the White Sea: Evaluating Seasonal Variations in Phosphorus, Nitrogen, and Oxygen. *Okeanologiya*, 33(5), pp. 695-702 (in Russian).

18. Vasechkina, E.F. and Yarin, V.D., 2009. Comparative Analysis of the Experiments Aimed at Modeling Marine Ecosystems by Using the Object-Oriented Approach. *Physical Oceanography*, 19(1), pp. 22-31. https://doi.org/10.1007/s11110-009-9033-y

19. Vasechkina, E.F., 2020. Nonlinear Relationships between Phytoplankton Nutrient Utilization Traits and Environmental Factors. *Ecological Modelling*, 433, 109233. https://doi.org/10.1016/j.ecolmodel.2020.109233

20. Vasechkina, E.F. and Kazankova, I.I., 2014. Mathematical Modeling of the Growth and Development of the Mussel *Mytilus galloprovincialis* on Artificial Substrates. *Oceanology*, 54(6), pp. 763-770. https://doi.org/10.1134/S0001437014060113

21. Vasechkina, E., 2020. Object-Based Modeling of Marine Phytoplankton and Seaweeds. *Journal of Marine Science and Engineering*, 8(9), 685. https://doi.org/10.3390/jmse8090685

22. Vasechkina, E.F. and Filippova, T.A., 2020. Simulation of Bottom Phytocenosis in the Crimean Coastal Zone. *Physical Oceanography*, 27(3), pp. 317-334. https://doi.org/10.22449/1573-160X-2020-3-317-334

23. Fomiv, V.V. and Ivanov, V.A., 2006. Combined Numerical Model of Currents, Waves, and Sediment Transport in Lake Donuzlav. *Physical Oceanography*, 16(2), pp. 107-127. https://doi.org/10.1007/s11110-006-0019-8

24. Finenko, Z.Z., Churilova, T.Y., Sosik, H.M. and Basturk, O., 2002. Variability of Photosynthetic Parameters of the Surface Phytoplankton in the Black Sea. *Oceanology*, 42(1), pp. 53-67.

Submitted 13.01.2025; approved after review 20.02.2025;
accepted for publication 15.05.2025.

About the authors:

Elena F. Vasechkina, Deputy Director for Scientific, Methodological and Educational Work, Marine Hydrophysical Institute of RAS (2 Kapitanskaya Str., Sevastopol, 299011, Russian Federation), DSc. (Geogr.), **ORCID ID: 0000-0001-7007-9496, Scopus Author ID: 6507481336, ResearcherID: P-2178-2017, SPIN-code: 2933-3834**, vasechkina.elena@gmail.com

Tatiana A. Filippova, Junior Research Associate, Marine Hydrophysical Institute of RAS (2 Kapitanskaya Str., Sevastopol, 299011, Russian Federation), **ORCID ID: 0000-0001-5762-5894, Scopus Author ID: 56190548500, ResearcherID: AAO-5512-2020, SPIN-code: 2922-1286**, filippovata@mhi-ras.ru

Vladimir V. Fomin, Head of the Department of Computational Technologies and Mathematical Modeling, Marine Hydrophysical Institute of RAS (2 Kapitanskaya Str., Sevastopol, 299011, Russian Federation), DSc. (Phys.-Math.), **ORCID ID: 0000-0002-9070-4460**, **Scopus Author ID: 34769824600**, **ResearcherID: H-8185-2015**, **SPIN-code: 6992-2688**, fomin.dntmm@gmail.com

Contribution of the co-authors:

Elena F. Vasechkina – statement of the problem, development of the biogeochemical model, numerical experiments with the developed model, critical analysis of the results obtained, revision of the text

Tatiana A. Filippova – statement of the problem, development of the biogeochemical model, numerical experiments with the developed model, qualitative and quantitative analysis of the results, preparation of the text and graphic materials for the article

Vladimir V. Fomin – numerical modeling of circulation in the Donuzlav Bay during the spring-summer seasons of 2007–2009, preparation of mean current fields for the biogeochemical model

The authors have read and approved the final manuscript.
The authors declare that they have no conflict of interest.

ISSN 1573-160X, *PHYSICAL OCEANOGRAPHY*, Vol. 32, Iss. 4, pp. 577-586 (2025)
Original Russian Text © A. L. Chikin, 2025,
published in *Morskoy Gidrofizicheskiy Zhurnal*, 2025, Vol. 41, Iss. 4, pp. 557–567

Original article

Numerical Study of Resonant Oscillations of Water Level in the Sea of Azov under the Impact of Weak External Forces

A. L. Chikin

Federal Research Center the Southern Scientific Center, Russian Academy of Sciences, Rostov-on-Don, Russian Federation
✉ *chikin1956@gmail.com*

Abstract
Purpose. The study is aimed at determining the frequencies of resonant oscillations of water surface level in the Sea of Azov.
Methods and Results. The computational experiments were performed using a mathematical model based on a system of equations for long waves in a homogeneous fluid. The wind of variable direction or strength and atmospheric pressure oscillations were considered to be an external force. The problem was solved by the finite-difference methods using the implicit difference schemes. The values of period lengths at which the resonant effect arises were obtained. The oscillation frequency values were determined by calculating the total energy of oscillations as a sum of potential and kinetic energy. Agreement between the values of resonant frequency (or periods) of sea level oscillations under conditions of variable wind load and changing atmospheric impact has been revealed. It has been established that stable resonant oscillations emerge after four to seven periods of external periodic forcing, after which the oscillatory motion stabilizes.
Conclusions. The applied mathematical model permits to conduct computational experiments for studying the process of formation of resonant oscillations of the Azov Sea water level. The results of investigation describe adequately the periodic external influence on the water surface of the Sea of Azov. The calculated resonance frequencies are consistent with the results obtained by other authors.

Keywords: shallow water equations, resonance, resonant oscillations, seiche, computational experiment

Acknowledgements: The article was prepared as part of the state assignment of SSC, RAS for 2025 (state registration No. 125012100503-4). The calculations were performed on the High-Performance Computing cluster (CCU) at the Southern Federal University.

For citation: Chikin, A.L., 2025. Numerical Study of Resonant Oscillations of Water Level in the Sea of Azov under the Impact of Weak External Forces. *Physical Oceanography*, 32(4), pp. 577-586.

Introduction

Oscillatory motions of water in enclosed or semi-enclosed water bodies can arise under relatively weak physical forcing on the water surface if this forcing resonates with the natural oscillations of the water body. The Sea of Azov belongs to such water bodies. Oscillations generated by setting the entire water mass of the Sea of Azov into motion affect its hydrological regime. In many studies, such resonant oscillations are identified as seiches and modeled by applying a disturbing force to the water surface followed by an analysis of free surface oscillations after the cessation of the forcing. Disturbances can be specified as either wind forcing or surface oscillations caused by atmospheric pressure changes. To identify seiches,

forced oscillations are calculated to identify resonance with the natural oscillations of the water body.

Seiches can occur when external forcing, even of small amplitude, coincides with the natural frequencies of a water body's oscillations, posing significant risks to anthropogenic infrastructure and ecosystems. The work [1] analyzes the long-term dynamics and recurrence of dangerous and adverse level oscillations in the Sea of Azov, leading to catastrophic rises in the water level, shoreline destruction, and the flooding of the Dolzhanskaya, Yeyskaya, Chumburskaya, and Ochakovskaya spits, and damage to coastal structures.

Using mathematical modeling, the work [2] investigates the influence of inhomogeneous moving atmospheric pressure fields on currents, free and forced level oscillations in the Sea of Azov caused by constant wind action and barometric disturbances. Free and forced oscillations in the Sea of Azov were studied using mathematical modeling with the three-dimensional sigma-coordinate POM (Princeton Ocean Model).

In [3], the water level oscillations (surge) near the Kerch Strait in the Sea of Azov are specified as the forcing. The resonant frequency is determined by the maximum total energy value observed while varying the frequency of the exciting oscillations. Total energy is defined as the sum of kinetic and potential energy.

In [4], the water level and current velocity oscillations are specified for the Balaklava Bay. Initially, the fluid is at rest. Then, a periodic disturbance begins acting on the open boundary of the basin. The objective is to determine the periods of the basin's natural oscillations and to study the structure of the level and current fields at the obtained period values.

The objective of the work [5] is to find an analytical solution to the seiche problem within the linear approximation for a rectangular basin of constant depth, which allows one to calculate the periods of seiche oscillation modes, free surface deviations, and wave current velocities. Using the obtained solution, seiche and seiche-like oscillations are then studied. The solution is sought in the form of time-periodic functions. Calculations were carried out for a rectangular basin 450 km long, 250 km wide, and 10 m deep, serving as an approximate model of the Sea of Azov, given its similar dimensions.

In [6], free sea level oscillations were modeled hydrodynamically, taking into account body forces, such as the Coriolis force and bottom friction. A nonlinear system of shallow water equations was used as the governing system. Above the sea, with initial values of level and currents set to zero, a uniform, constant wind blowing from different directions was specified. After 10 hours, the wind was switched off, and the free level oscillations were examined.

A similar approach to studying free water level oscillations in the Sea of Azov arising after the cessation of constant wind action is presented in [7]. This paper uses a sigma-coordinate model to determine the characteristics of seiche-like oscillations.

In [8], the speed and time of movement of the barometric field are determined based on the assumption that waves are generated with maximum amplitude. This occurs when the period of the forcing is similar to the period of the basin's natural oscillations. The time it takes the front to traverse the entire sea area is set equal

to the time it takes for the Sea of Azov level to rise to its maximum, which occurs during half the period of the fundamental mode of free oscillations.

Based on the analysis of numerical modeling results in [9], seiche-like level oscillations in the Sea of Azov within the field of atmospheric pressure disturbances were studied. In this case, the period of the atmospheric pressure disturbances equals the period of the fluid's natural oscillations in the basin.

This work aims to numerically investigate the occurrence of resonant oscillations of the Sea of Azov water surface resulting from weak periodic external forcing. This forcing could be a weak wind with variable direction or strength, or atmospheric pressure that changes with a specific period. Computational experiments were conducted using a mathematical model developed at the Southern Scientific Centre of the Russian Academy of Sciences [10].

Materials and methods

Calculations of level oscillations in the Sea of Azov are based on solving a system of equations for long waves in a homogeneous incompressible fluid subject to Coriolis force, while accounting for atmospheric pressure, as described in [11]:

$$\frac{\partial u}{\partial t}+u\frac{\partial u}{\partial x}+v\frac{\partial u}{\partial y}-\Omega v=-g\frac{\partial}{\partial x}\left(\zeta+\frac{P_a}{g\rho_0}\right)+\frac{\tau_{sx}}{H}-\frac{\tau_{bx}}{H},$$

$$\frac{\partial v}{\partial t}+u\frac{\partial v}{\partial x}+v\frac{\partial v}{\partial y}+\Omega u=-g\frac{\partial}{\partial y}\left(\zeta+\frac{P_a}{g\rho_0}\right)+\frac{\tau_{sy}}{H}-\frac{\tau_{by}}{H},$$

$$\frac{\partial \zeta}{\partial t}+\frac{\partial (Hu)}{\partial x}+\frac{\partial (Hv)}{\partial y}=0,$$

where $H=h+\zeta$; $h=h(x,y)$ is the water body depth; $u=u(x,y,t)$, $v=v(x,y,t)$ are velocities; P_a is the atmospheric pressure; ρ_0 is the mean density of the seawater; τ_{sx},τ_{sy} are the projections of the wind friction force against the water surface onto the *OX* and *OY* axes; τ_{bx},τ_{by} are the projections of the fluid friction force against the bottom onto the *OX* and *OY* axes. A similar approach to modeling marine floods in the Don River delta is presented in [12]. The values of the friction forces depend on the wind speed $\overline{W}_{\mathrm{B}}=\{W_x;W_y\}$ and current velocity $\overline{W}_{\mathrm{T}}=\{u_s;v_s\}$ and are determined as follows [13]:

$$\overline{\tau}_{\mathrm{s}}=\gamma\left|\overline{W}_{\mathrm{B}}\right|\overline{W}_{\mathrm{B}},\qquad \overline{\tau}_b=\beta\left|\overline{W}_{\mathrm{T}}\right|\overline{W}_{\mathrm{T}},$$

where $\left|\overline{W}_{\mathrm{B}}\right|=\sqrt{W_x^2+W_y^2}$, $\left|\overline{W}_{\mathrm{T}}\right|=\sqrt{u^2+v^2}$; β is the bottom friction coefficient; γ is the wind friction coefficient against the free water surface.

Slip conditions are specified at the solid boundary $\partial\Omega_b$:

$$\mathbf{V}_n\big|_{\partial\Omega_b}=0,\qquad \left.\frac{\partial \mathbf{V}_\tau}{\partial \overline{n}}\right|_{\partial\Omega_b}=0.$$

The problem was solved using finite-difference methods on a uniform grid with implicit difference schemes. The convective terms of the momentum equation were approximated using upwind differences. The water level difference was determined using the corresponding finite-difference analog. The grid spacing was Δx = 660 m and Δy = 685 m with 524 × 354 nodes. After indexing the cells in the computational domain, the number of unknowns for each variable was approximately 83,000. Although an analytical assessment of the permissible time step in the difference schemes was not performed, numerical calculations showed computational stability at Δt < 120 s. The program is written in FORTRAN; numerical implementation of the model was carried out on high-performance computing systems in an MPI environment using the Aztec package of parallel subroutines.

The resonant frequency of free and forced oscillations was determined by computing the time-averaged total energy as the sum of kinetic energy E_k and potential energy E_p. The total energy calculation followed the methodology from [3]:

$$E = E_k + E_p = \frac{\rho}{2T}\left(\iint\limits_{TS} (H+\zeta)\left(u^2+v^2\right) dSdt + g \iint\limits_{TS} \zeta^2 dSdt \right).$$

Here ρ is the density of seawater (assumed constant in the model and equal to 1000 kg/m³); T is the oscillation period; S is the computational domain area. When constructing graphs, the natural logarithm of the total energy $\ln(E)$ was considered.

Results and discussion

The range of variation of the forced oscillation period was studied over a time span of 2 to 30 hours. Resonance was observed at frequencies with a local maximum in total energy. The main scenarios considered for the occurrence of resonant water level oscillations in the Sea of Azov are as follows:

- wind direction changes from NE to SW at a constant speed of 2 m/s;
- an easterly wind action with a speed of 2 m/s alternates with calm;
- atmospheric pressure at the eastern and western boundaries of the Sea of Azov fluctuates alternately from 750 to 770 mm Hg.

In addition to the main scenarios, the wind directions NW–SE and N–S were also considered.

The period of forced oscillations changed every 0.2 hours (change in wind load or pressure). To obtain a more stable resonance pattern, the external forcing was modified 15 times for each period.

The most prominent local maximum energy was observed several times for period values of 6.4, 15.2, 19.2, and 26 hours (Fig. 1). This occurred with NE–SW winds, the alternation of an easterly wind and calm periods, and for atmospheric pressure oscillations. Furthermore, several smaller energy spikes were identified. These frequencies were observed for all wind directions and corresponded to both longitudinal and transverse forcing of the sea surface. The only difference was in the magnitude of the total energy.

The situation where a 2 m/s wind changed direction from SE to NW and alternated between easterly direction and calm was considered. The most

pronounced local energy maxima were observed at periods of 6.4, 15.2, and 26 hours, consistent with results obtained by other authors. For instance, work [14] shows that three oscillation modes can be distinguished in the level oscillations of the Sea of Azov: 23, 14.5, and 6–8 hours. Higher oscillation modes are less significant and not characteristic of the entire sea. Oscillations with a period of 23.7 hours are mentioned in [3], but the author attributes them to a two-node seiche.

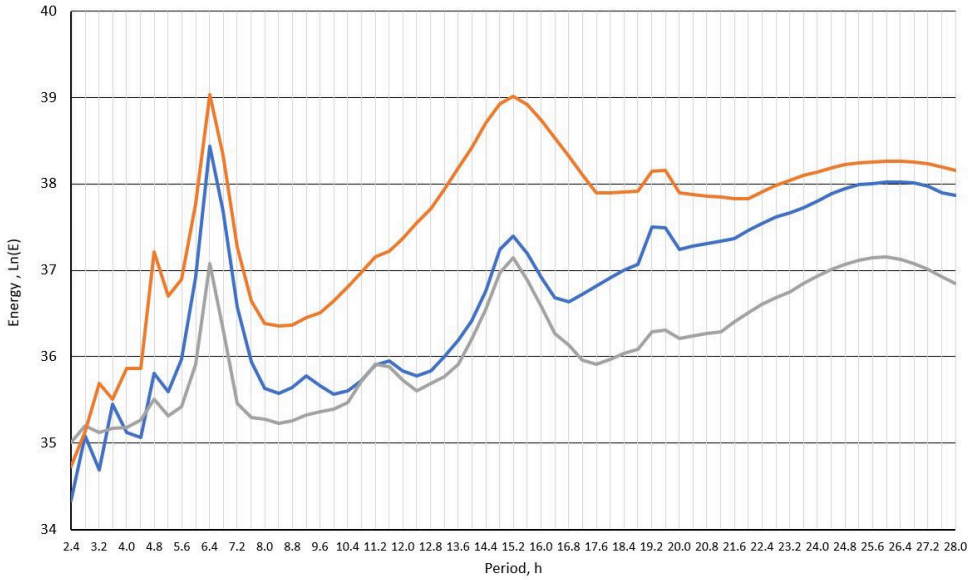

F i g. 1. Dependence of the energy logarithm on wind impact frequency at: changing the direction of constant wind (speed 2 m/s) from NE to SW (blue curve) (*a*), alternating action of east wind (speed 2 m/s) and calm (gray curve) (*b*), and fluctuations in atmospheric pressure at the eastern and western boundaries of the Azov Sea in the range 750–770 mm Hg (orange curve) (*c*)

The figures below illustrate the distribution of the sea surface elevation at the maximum total energy value.

With a wind oscillation period of 26 hours, water motion in the Sea of Azov exhibits a circulatory pattern, forming several circulation zones in both the Sea of Azov and Taganrog Bay. Fig. 2 shows the distribution of sea surface elevation and streamlines, displaying a maximum in Taganrog Bay (0.85 m) and a minimum near the Arabat Spit (−0.15 m), alternating with a minimum in Taganrog Bay (−0.74 m) and a maximum near the Arabat Spit (0.31 m). The seiche nodal line runs from the base of the Dolzhanskaya Spit to Berdyansk approximately. A similar result is described in [9].

Observations from meteorological stations and hydro-posts have shown that water level oscillations with a period of approximately 24 hours occur most frequently. Such water level oscillations with a period of 23–25 hours are described in [5, 7]. Work [7] indicates that the dominant longitudinal free oscillations of the Sea of Azov have a period of approximately 24 hours. One of this mode's antinodes is located in Taganrog Bay, and the other is near Genichesk. This situation closely resembles the pattern presented in Fig. 2.

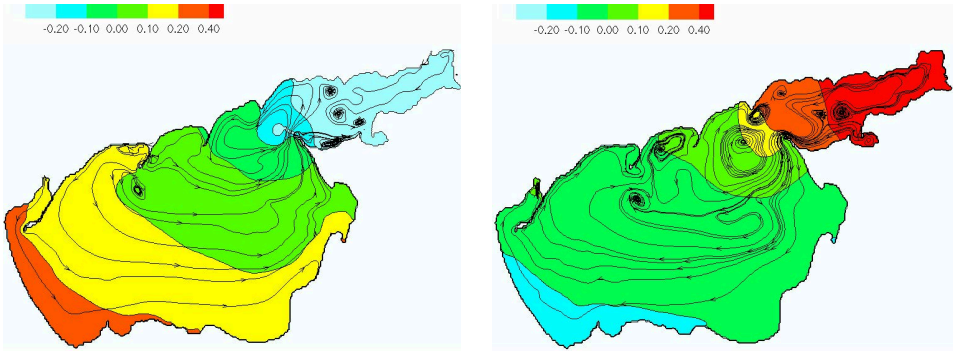

F i g. 2. Resonant oscillations at changing wind (speed 2 m/s) direction from NE to SW at the end of: *a* – period T = 26.0 h, and *b* – semi-period $T/2$ = 13.0 h

With a wind oscillation period of 19.2 hours, the Sea of Azov exhibits a circulatory pattern of water motion with the formation of several circulation zones, similar to the pattern observed with a 26-hour period. In this case, however, the oscillation amplitude is smaller, equaling 0.25 m at maximum and −0.45 m at minimum.

Wind oscillations with a period of 15.2 hours primarily cause translational water motion in the Sea of Azov (Fig. 3), revealing a two-node seiche. Two elevation maxima are observed in Taganrog Bay (0.39 m) and the Utlyuk Estuary (0.42 m), as well as a minimum in the Primorsko-Akhtarsk area (−0.44 m). These maxima and minima alternate with each other: a maximum in the Primorsko-Akhtarsk area and two minima in Taganrog Bay and the Utlyuk Estuary. One nodal line connects the Kerch Strait area with Berdyansk Bay. A second nodal line connects the Yeysk area with the Belosaraysk Spit.

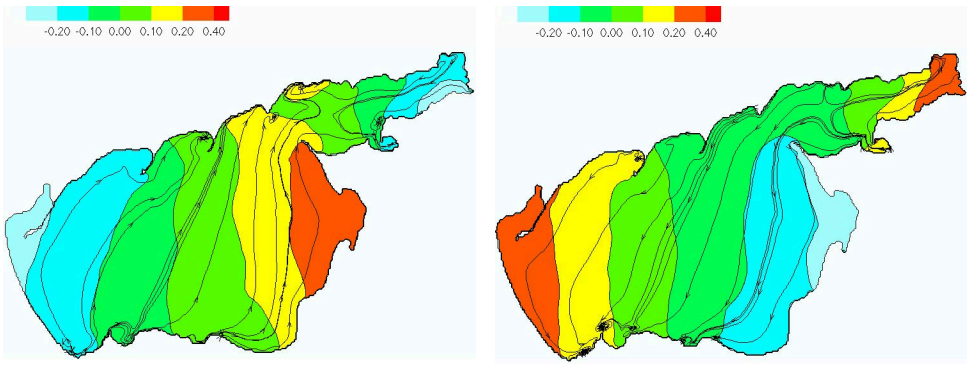

F i g. 3. Resonant oscillations at changing wind (speed 2 m/s) direction from NE to SW at the end of: *a* – period T = 15.2 h, and *b* – semi-period $T/2$ = 7.6 h

With a wind oscillation period of 6.4 hours (Fig. 4), the main water level oscillations occur ш т the Sea of Azov. The maximum level is recorded in the Primorsko-Akhtarsk area and Obitochny Bay (0.85–1.0 m), while the minimum

level is observed near the mouth of the Kuban River and the Arabat Spit (−0.55 m). After half the period (3.2 hours), the spatial distribution of level extremes reverses. One nodal line passes through the center of the Sea of Azov, stretching from the Primorsko-Akhtarsk area to Biryuchiy Island. The other two nodal lines are located at the boundary of Taganrog Bay and in its central part.

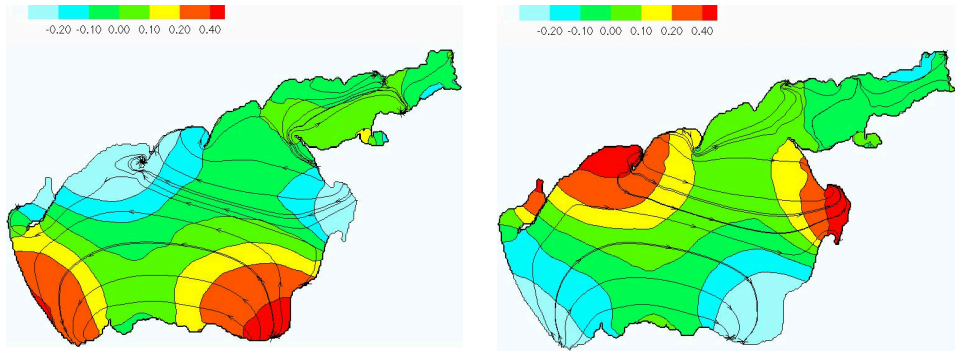

a *b*

F i g. 4. Resonant oscillations at changing wind (speed 2 m/s) direction from NE to SW at the end of: *a* – period T = 6.4 h, and *b* – semi-period $T/2$ = 3.2 h

Further investigation of oscillations at peak frequencies revealed that, for wind oscillations with a 26-hour period, a sharp increase in total energy begins as early as the fourth period of forcing. The difference in total energy values for subsequent periods does not exceed 1%. For 15.2-hour oscillations, the sharp increase in energy begins in the sixth period. For 6.4-hour oscillations, the sharp increase in energy begins in the seventh period.

With continued external oscillatory forcing at periods of 6.4, 15.2, 26, and 19.2 hours, the total energy value steadily increases, indicating a possible onset of resonance (Fig. 5). Note that the 19.2-hour frequency was not previously considered resonant. For frequencies with oscillation periods of 2.8 and 4.8 hours, continued external forcing leads to a decrease in total energy, indicating oscillation damping.

When wind action alternates with calm, the patterns of water surface level distribution in the Sea of Azov resemble those observed in the previous scenario.

Forced water level oscillations in the Sea of Azov were also generated using atmospheric pressure oscillations. It was assumed that there was no wind forcing. Different pressure values related by a linear dependence were specified at the western (Arabat Spit) and eastern (Don River delta channels) boundaries of the sea. Atmospheric pressure was set to 750 mm Hg at one end of the Sea of Azov and 770 mm Hg at the other. As expected, the peak values of total energy correspond to pressure change frequencies that coincide with the frequencies of wind forcing oscillations (see Fig. 1): 6.4, 15.2, 19.2, and 26 hours. Notably absent are total energy spikes for periods of 9.2 and 11.6 hours, as well as anomalous energy behavior for periods shorter than 6.4 hours.

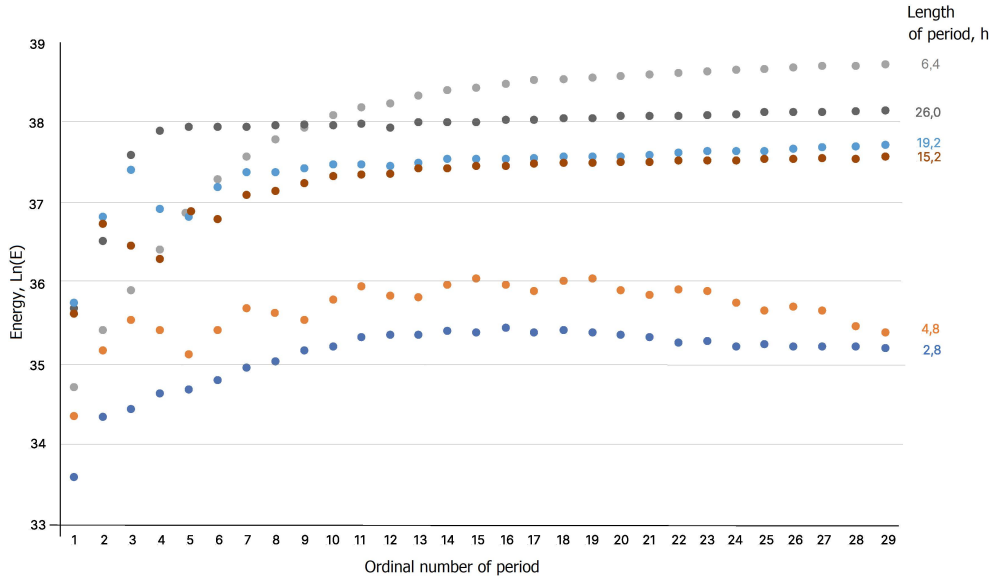

F i g. 5. Total energy for peak values of oscillation periods (h) under wind impact on the Azov Sea surface

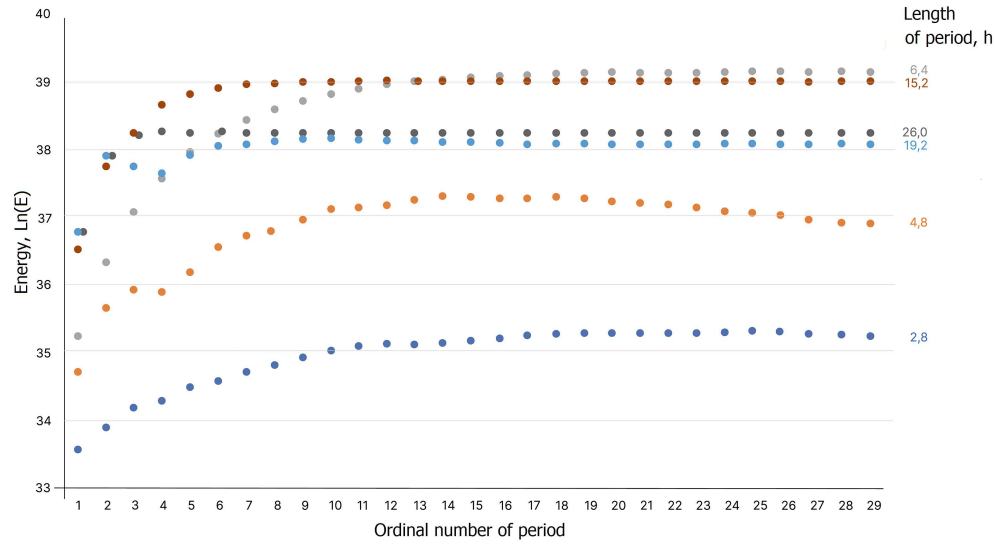

F i g. 6. Total energy for peak values of oscillation periods (h) under the influence of atmospheric pressure on the Azov Sea surface

With continued atmospheric pressure acting on the sea surface at peak frequencies for 6.4, 15.2, 19.2, and 26-hour periods, the total energy value stabilizes,

while for periods of 2.8 and 4.8 hours, the total energy decreases (Fig. 6). This confirms that the peak energy spikes for periods of 2.8 and 4.8 hours are not resonant.

Conclusions

The conducted numerical study demonstrated that significant water level oscillations in the Sea of Azov can be caused by relatively weak external forcing on the water surface. These oscillations are not necessarily resonant in nature, and significant disturbances to the water surface occur within the first four to seven periods of the external force's oscillation. Similar results were obtained for wind and atmospheric pressure forcing on the surface of the Sea of Azov.

The results of this study are consistent with those obtained by other authors, although they do not show exact correspondence. This discrepancy is due to the use of different mathematical models and differences in the approximation of the Sea of Azov itself, which affects the natural oscillation values of the model.

REFERENCES

1. Bespalova, L.A., Tsygankova, A.E., Bespalova, E.V. and Misirov, S.A., 2019. Dangerous Storm Surges and Destruction of Coast of the Sea of Azov. *Science in the South of Russia*, 15(2), pp. 29-38. https://doi.org/10.7868/S25000640190204 (in Russian).
2. Cherkesov, L.V. and Shul'ga, T.Ya., 2016. Investigation of the Effect of the Baric Formation Parameters on Free and Forced Oscillations of the Level and Flow in the Sea of Azov. *Physical Oceanography*, (4), pp. 12-24. https://doi.org/10.22449/1573-160X-2016-4-12-24
3. Matishov, G.G. and Inzhebeikin, Yu.I., 2009. Numerical Study of the Azov Sea Level Seiche Oscillations. *Oceanology*, 49(4), pp. 445-452. https://doi.org/10.1134/S0001437009040018
4. Fomin, V.V., Lazorenko, D.I. and Ivancha, E.V., 2017. Numerical Simulation of Seiches in the Balaklava Bay. *Ecological Safety of Coastal and Shelf Zones of Sea*, (3), pp. 32-39 (in Russian).
5. Maniliuk, Yu.V. and Cherkesov, L.V., 2016. Investigation of Free Liquid Oscillations in a Bounded Basin Representing an Approximate Model of the Sea of Azov. *Physical Oceanography*, (2), pp. 14-23. https://doi.org/10.22449/1573-160X-2016-2-14-23
6. Filippov, Yu.G., 2012. Natural Fluctuations of the Sea of Azov Level. *Russian Meteorology and Hydrology*, 37(2), pp. 126-129. https://doi.org/10.3103/S1068373912020082
7. Ivanov, V.A., Cherkesov, L.V. and Shul'ga, T.Ya., 2015. Studies of Free Fluctuations of the Sea of Azov Level Arising after the Termination of Prolonged Wind Effect. *Physical Oceanography*, (2), pp. 14-23. https://doi.org/10.22449/1573-160X-2015-2-14-23
8. Ivanov, V.A. and Shul'ga, T.Ya., 2018. Impact of Atmospheric Front Parameters on Free and Forced Oscillations of Level and Current in the Sea of Azov. *Journal of Applied Mechanics and Technical Physics*, 59(5), pp. 912-921. https://doi.org/10.1134/S002189441805019X
9. Cherkesov, L.V. and Shul'ga, T.Ya., 2016. Numerical Analysis of the Effect of Moving the Pressure Fields on the Flow Free and Forced Oscillations of Level in the Azov Sea. *Ecological Bulletin of Research Centers of the Black Sea Economic Cooperation*, 13(2), pp. 99-110 (in Russian).
10. Chikin, A.L., Kleshchenkov, A.V., Chikina L.G. and Korshun, A.M., 2017. Wind-Driven Water Level Variation of the Mouth Area of the Don: Numerical Modelling and Change Scenarios. *Science in the South of Russia*, 13(3), pp. 39-49. https://doi.org/10.23885/2500-0640-2017-13-3-39-49 (in Russian).
11. Luettich, R.A. and Westerink, J.J., 2004. *Formulation and Numerical Implementation of the 2D/3D ADCIRC. Finite Element Model Version 44.XX*. Notre Dame, 74 p.

12. Fomin, V.V., Alekseev, D.V., Lemeshko, E.M. and Lazorenko, D.I., 2018. Simulation and Analysis of Sea Floods in the Don River Delta. *Russian Meteorology and Hydrology*, 43(2), pp. 95-102. https://doi.org/10.3103/S106837391802005X

13. Filippov, Yu.G., 1970. [On a Method for Calculating of Marine Currents]. *Proceedings of N.N. Zubov State Oceanographic Institute*, (103), pp. 87-94 (in Russian).

14. Filippov, Yu.G., 2011. Modelling of Seiches Oscillations of the Azov Sea Level. *Proceedings of N.N. Zubov State Oceanographic Institute*, (213), pp. 146-154 (in Russian).

Submitted 19.03.2025; approved after review 02.04.2025;
accepted for publication 15.05.2025.

About the author:
Alexey L. Chikin, Chief Researcher, Federal Research Center the Southern Scientific Center, Russian Academy of Sciences (41 Chekhov Ave., Rostov-on-Don, 344006, Russian Federation), DSc. (Phys.-Math.), **SPIN-code: 3845-9760**, **ORCID ID: 0000-0002-4065-010X**, **Scopus Author ID: 8240627300**, chikin1956@gmail.com

The author has read and approved the final manuscript.
The author declares that he has no conflict of interest.